Title
Ultrafast Strong-Field Vibrational Dynamics Studied by Femtosecond Extreme-Ultraviolet Transient Absorption Spectroscopy

Author
Hosler, Erik Robert

Publication Date
2013

Ultrafast Strong-Field Vibrational Dynamics Studied by Femtosecond Extreme-Ultraviolet Transient Absorption Spectroscopy

By

Erik Robert Hosler

A dissertation submitted in partial satisfaction of the
requirements for the degree of
Doctor of Philosophy
In
Chemistry
in the
Graduate Division
of the
University of California, Berkeley

Committee in charge:
Professor Stephen R. Leone, Chair
Professor Daniel M. Neumark
Professor David T. Attwood

Spring 2013

Ultrafast Strong-Field Vibrational Dynamics Studied by Femtosecond Extreme-Ultraviolet Transient Absorption Spectroscopy

Erik Robert Hosler

Abstract

Ultrafast Strong-Field Vibrational Dynamics Studied by Femtosecond Extreme-Ultraviolet Transient Absorption Spectroscopy

Erik Robert Hosler

Doctor of Philosophy in Chemistry

University of California, Berkeley

Professor Stephen R. Leone, Chair

Femtosecond time-resolved extreme-ultraviolet core-level absorption spectroscopy has developed into a powerful tool for investigating chemical dynamics due to its sensitivity for detecting changes in electronic structure. By probing the core-levels of atoms and molecules, dynamics may be monitored with elemental specificity, as well as localized sensitivity to the oxidation state around the atomic absorber. Previous experiments with this technique demonstrated the capability to quantitatively resolve strong-field ionization dynamics including the complete $\left| j, m \right\rangle$ quantum state distribution of Xe^+ and the dissociative ionization of CH_2Br_2, both monitored in real-time with femtosecond resolution. In this thesis, the complete reconditioning of the experimental apparatus is described and its application to the study of vibrational wave packets created by strong-field ionization of Br_2 is discussed. Initially, the experimental apparatus was meant as a proof of principle demonstration for table-top extreme ultraviolet transient absorption spectroscopy based on a high-order harmonic generation source. To achieve the experiments discussed here, substantial changes were required to its construction concerning the high harmonic source and overall stability of the apparatus, which are discussed in terms of increasing the operation of the experiment to several days as opposed to a few hours, yielding an unprecedented spectral resolution after Fourier Transform of the signal versus pump-probe time delay for a table-top core-level spectrometer, better than 1.5 cm^{-1}. The improvements to the apparatus are exploited in terms of examining the vibrational wave packet dynamics in Br_2 induced by optical strong-field ionization.

First, extreme-ultraviolet transient absorption is established as a bond-length specific probe capable of resolving vibrational motion in Br_2 and Br_2^+ due to a change in the transition amplitude and energy versus bond length of the $3d_{5/2,3/2}$ core-level transitions to unoccupied molecular orbitals. Furthermore, the degree of coherence and beat composition of the ${}^1\Sigma_g^+$ ground state vibrational wave packet is established. Second, the preparation of vibrational wave packets by strong-field ionization of Br_2 is analyzed as a function of field intensity. At a field intensity near the threshold of ionization, selective depletion of the vibrational amplitude is observed near the inner turning point, corresponding to the minimum in the ionization energy for the unperturbed molecular potential energy curves. The observed superposition is determined to

be primarily composed of the $\nu_0\nu_1$ vibrational beat. As the field intensity is increased, perturbation of the potential curves results in preparation of the wave packet at longer internuclear separations, and the distortion of the potentials is directly observed by a shift in the Br_2^+ core-level transition energy within the intense laser pulse. Moreover, the composition of the wave packet is found to involve higher vibrational levels, indicating the involvement of a Raman pumping mechanism in the preparation of the superposition. Third, several ongoing experiments utilize the unique instrumental capabilities including the elemental specificity and polarization dependence of the absorption. The elemental specificity and nuclear motion dependence of the core-level probe is utilized to investigate the correlated detection of vibrational wave packet dynamics in IBr on the iodine *4d* and bromine *3d* core-level absorptions simultaneously. Also, polarization dependent absorption of Xe^{2+} looks to extend the quantitative measurements conducted for Xe^+ to determine the complete $\left| j, m \right\rangle$ state populations after sequential ionization. Lastly, polarization dependent measurements of the strong-field ionization of Br_2 suggest alignment between the molecular axis and the electric field of the ionizing pump at field intensities near the threshold for ionization, which is lost at higher field strengths. These studies expand the repertoire of capabilities for high-order harmonic generation beyond the proof of principle experiments and establish the technique as a practical tool for monitoring complex, ultrafast molecular dynamics by core-level probing.

The capabilities of femtosecond transient absorption have since been expanded here to include the investigation of strong-field generated vibrational wave packets in molecular bromine. To this end, a theoretical model for determining the sensitivity of XUV absorption to valence vibrational motion generated by strong-field ionization was developed utilizing Restricted Excitation Window Time-Dependent Density Functional Theory coupled with internuclear separation, vibrational state sensitive Ammosov-Delone-Krainov tunnel ionization rates. This theoretical model, including details of traditional Ammosov-Delone-Krainov tunnel ionization rates, is presented in Chapter 2. Chapter 3 describes the experimental changes incorporated into the apparatus for successful multi-day experiments for the determination of vibrational dynamics with ~1 cm^{-1} spectral resolution. Demonstration of the sensitivity of XUV transient absorption to non-stationary ground state vibrational dynamics is then presented in Chapter 4, investigating the vibrational superposition generated in Br_2 after irradiation with a 1.6×10^{14} W/cm^2 driving pump pulse. Chapter 5 expounds upon the dependence on field intensity to the observed vibrational dynamics in Br_2 as well as Br_2^+. Chapter 6 discusses the currently ongoing experiments being conducted for ground state vibrational wave packet preparation in iodine monobromide, the determination of the complete $\left| j, m \right\rangle$ quantum state population of Xe^{2+}, and the alignment of the molecular axis of Br_2 with the electric field of the ionizing 800 nm field following strong-field ionization. Chapter 6 also presents the conclusions of the experimental work presented here as well as the future outlook of XUV transient absorption spectroscopy in the broader perspective of investigating chemical reaction and dynamics.

Professor Stephen R. Leone
Chair, Dissertation Committee

To my parents

Contents

Chapter 6: Ongoing Experiments and Conclusions……………………………………. 157

List of Figures

List of Tables

Acknowledgements

First and foremost, I am grateful for my parents and all of the encouragement they provided as I grew up. Without them and their tenacity to drive me to bigger and better things than what I would typically settle for, I would never have made it to college let alone graduate school. I was always a kid with too much energy and imagination for his own good, and they were able to guide me to a productive outlet in science with my first experiment involving the construction of a highly inefficient hydroelectric power plant. From then on, I was hooked but still a troublemaker. The values and ambition they fostered in me when I was younger is the only reason I have been able to reach this point. I also owe a great deal to my older brother Chris, whom I spent most of my formative years trying to be like. Without his “brotherly” support, I would not have developed the work ethic I have always needed to succeed. I also appreciate that he keeps me in check when I am being an ass.

Throughout my education, I was constantly challenged and pushed by wonderful teachers and professors. In particular, I would like to thank Mr. Barcus for his “What’s-It” project in sixth grade science. The enthusiasm and praise he showed for the “Tinsel-eater” I created as well as the infectious exuberance for chemistry Mrs. McManus had every day in class are some of the key reasons I became a scientist.

Starting University at age 16 was not an easy thing for me, and I am grateful for all the support of the faculty there as I found my footing and began to earnestly pursue a career in chemistry. I am particularly grateful for the non-academic lessons and experiences imparted to me by the faculty. Dr. Holly Bevsek first sparked my interest in Physical Chemistry freshman year and got me on the right academic track to pursue that interest as my faculty advisor. Dr. Swarna Basu sealed my fate junior year in Quantum Mechanics, and I am indebted to him as he pushed me to not only apply to graduate school, but also apply to Berkeley. Dr. Geneive Henry was the first person to really challenge me academically and push me beyond my comfort zone in Organic Chemistry, though that could have been also the subject matter. Dr. Chris Janzen showed me that academia could be, and should be, fun. I am especially grateful for all the Ziploc bags Chris lent me during summer research so that we could pilfer the free food left by the teaching symposium. Dr. Fred Grosse taught me the value of simplicity in science, that pen, paper, and physical intuition is better than any simulation. Dr. Balwant Chohan gave me my first research opportunity exploring nickel dithiolate complexes and their oxidative pathways for two and a half years. I blew up, broke, and burned a large quantity of research material, and I am grateful for the leeway Bal afforded me in my failures, even when I came into his office covered in blue precursor material. I also owe a great deal to Dr. Wade Johnson; with whom I worked closely with on my sophomore Honor’s essay on J.R.R. Tolkien’s the Silmarillion. The essay may not have been fantastic, but I deeply appreciated our weekly conversations on life, the universe, and everything. Wade taught me the value of perseverance in academia and life. Lastly from Susquehanna, I must thank Dr. Richard “Koz” Kozlowski for turning me to the Dark Side, convincing me to become a Physics and Chemistry double major. Our 3 am conversations in the Knowledge Zone were most illuminating and inspiring. His approach to problems and his methodology for teaching are the basis for much of my way of thinking and mentoring.

The work presented here would not have been possible if my advisor Stephen Leone would not have taken a chance on an inexperienced, exuberant graduate student out of central Pennsylvania. I feel privileged to have had the opportunity to work with Steve these past six years. His mentorship and guidance has formed me into the scientist I am today, and for that I am grateful. Though we have never seen eye-to-eye on just about anything, I have greatly appreciated the time he has taken to work with me on even the craziest ideas I have proposed. Steve's commitment to Science and his students has truly been an inspiration for me.

At Berkeley, I have had the opportunity to work with some exceptional scientists, not least of which was my mentor Dr. Zhi-Heng Loh. Z taught me everything I know about lasers and modern science. Mottos such as "You can optimize it till it goes away," "Science is Hard," and "Wow-Wee-Wee-Wow," are seared into my brain thanks to him. Our daily lunches and conversations at House of Curries and afternoon Lemonade breaks were points of sanity in my life as I took classes, began research, and prepared for my qualifying exam.

Throughout my graduate work, I have had the distinct pleasure of collaborating with numerous exceptional scientists including Scott Sayres, Terefe Habteyes, Andrew Attar, Lorena Piticco, Alex Aguilar, and David Kilcoyne. Scott in particular has been a driving force behind my work over the past year and I am greatly appreciative of the time he has taken to review my manuscripts in depth as well as put up with my silly questions. Moving forward, I am proud that Andrew will be taking the reins of the experiment and running with it to new and exciting avenues of chemical research. I am also gratefully for the support and friendship of the entire Leone group, especially Phil Nagel, Ming-Fu Lin, and Teresa Bixby. To my friends outside of the Leone group – Hattie and Dru Ring, Pete Mustonen, Ian Ryu, Eita Tochigi, and Joe Zadrozny – I thank you for always being willing to meet me for a game of Beans.

Special thanks are due to Kathleen Fowler and Adam Bradford for administrative support, without which this research would not have been possible. The technical support provided by Eric Grunland of the Chemistry machine shop and the entire woodshop and electric shops has likewise been invaluable. Sincere thanks are also due to Professors Dan Neumark and David Attwood for taking time to sit on my qualifying exam and thesis committees.

Finally, I would like to thank Rebecca Stahl for her steadfast support of my single-minded pursuit of science. Her ability to keep my life at least somewhat organized as well as drag me out of the dungeon that is the D-level of Hildebrand on occasion to take a break has been greatly appreciated, though not always at the time. Her ability to cheer me up even on the worst days has been invaluable.

Erik R. Hosler

1888 Berkeley Way, Apt 216, Berkeley, CA 94703
(717) 215-4964 / hoslere@gmail.com

Education

University of California, Berkeley: PhD Physical Chemistry, May 2013
Susquehanna University, Selinsgrove**,** PA**:** B.S. Chemistry and Physics, May 2007

Employment and Research Experience

Graduate Research Assistant in physical chemistry, *Stephen R. Leone* Lab
University of California, Berkeley and Lawrence Berkeley National Laboratory (2007-Present)
Thesis Title: *Strong-field Dynamics of Vibrational Coherences and Hole Alignment studied by Femtosecond Extreme-Ultraviolet Transient Absorption Spectroscopy.*

Leadership and Teamwork

Collaborated with a team of 26 people to conduct landmark experiments at the Linac Coherent Light Source at the SLAC National Accelerator Laboratory, which lead to a groundbreaking **publication**

Proposed, managed , and **conducted** seven experiments at the Advanced Light Source, **leading** teams of 2-4 people

Coordinated with teams of 2-3 people in the development and troubleshooting of several complex **extreme-ultraviolet** and **soft x-ray** experimental apparatuses

Mentored three high school seniors and one graduate student in independent research

Communication and Public Speaking

Vice-President of the Student Leadership Council for the Extreme Ultraviolet Engineering Research Center, in charge of conducting and presenting **SWOT** analysis for NSF review team

Wrote reports on conducted research for grant renewals as part of the Extreme Ultraviolet Engineering Research Center (EUV ERC)

Presented seminars at six Extreme Ultraviolet Engineering Research Center retreats and four NSF renewal reviews, as well as six Leone group meetings and the annual Divisions of Atomic, Molecular, Optical Physics Conference in 2012

Technical Skills

To improve the effectiveness of the existing extreme ultraviolet transient absorption spectrometer, I employed my skills in **instrument design** and **fabrication** to develop a novel light source into a viable experimental tool, increasing photon flux by two orders of magnitude, reducing data collection time by 75% and opening new scientific avenues

Expert in **operation** and **maintainance** of high power femtosecond Titanium:Sapphire **laser systems, high vacuum apparatus,** and **electronics** (oscilloscopes, high voltage supplies, picoammeters, x-ray CCD cameras, lock-in amplifiers, etc...)

Adept in the use of ultrafast **extreme-ultraviolet** sources, optics, and detectors

Performed spectroscopy with infrared and **extreme-ultraviolet** light on gas phase and condensed matter samples

Fabricated custom apparatus parts in a precision machine shop, which were designed in **SolidWorks**

Developed **data analysis** subroutines for daily review of collected experiment results employing **Origin**, **LabView**, and **Python** subroutines

Established Standard Operating Procedures (**SOP**s) for use of home-built EUV transient absorption spectrometer and femtosecond laser system as well as **safety protocols** for use of hazardous gasses and materials.

Graduate Student Instructor in general and physical chemistry laboratory classes
University of California, Berkeley (2007-2010)

Instructed laboratory and recitation sections of 20-35 undergraduates for three semesters
Developed and **taught** lecture curriculum for two semesters of physical chemistry laboratory

Undergraduate Research Assistant in theoretical chemistry
Rice Quantum Institute, (summer 2006)

In order to interpret complex spectra of DNA attached to gold nanoparticles I taught myself Python to **develop** code for plasmonic electromagnetic field simulations, which lead to an understanding of the orientation dynamics of the DNA strands
Presented at three internal group meetings and one regional conference
Awarded best presentation at Institute summer colloquium

Undergraduate Research Assistant at **17 years old** in synthetic chemistry
Susquehanna University, (2004-2007)

In order to support my undergraduate research, I **independently wrote** and **applied** for a grant from Sigma Xi: Grants in Aid of Research, which resulted in $1,000 per year in operational funding for three years for myself and two additional students
Trained and **supervised** two undergraduate students in Schlenk and glove box anaerobic techniques
Consistently **developed** independent research projects
Published and **presented** independent research at four **national** conferences
Awarded 2nd best presentation at the Intercollegiate Student Chemists' Conference 2006
Supervised seven undergraduate labs of 15-20 students in general and organic chemistry as well as Newtonian physics

Publications

E.R. Hosler, S.R. Leone. Characterization of Vibrational Coherences by Core-Level High Harmonic Transient Absorption. Submitted to Physical Review Letters.

E.R. Hosler, S.R. Leone. Field-Dependence on the Formation of Electronic Ground State Coherences in Br_2 Probed by EUV Core-Level High Harmonic Transient Absorption Spectroscopy. In Preparation for the Journal of Chemical Physics.

E.R. Hosler, S. Sayres. S. R. Leone. Xe^{2+} Quantum State Distribution from Strong-Field Ionization. In Preparation.

E.R. Hosler, S. Sayres. S. R. Leone. Molecular Hole Alignment from Strong-Field Ionization in Br_2^+. In Preparation.

E.R. Hosler, R.W. Herbst, M.J. Maroney, B.S. Chohan. Exhaustive Oxidation of a nickel dithiolate complex: some mechanistic insights en route to sulfate formation. Dalton Transactions. 41.804. 2012.

M. Hoener, L. Fang, O. Kornilov, O. Gessner, S.T. Pratt, M. Guhr, E.P. Kanter, C. Blaga, C. Bostedt, J.D. Bozek, P.H. Bucksbaum, C. Buth, M. Chen, R. Coffee, J. Cryan, L. DiMauro, M. Glownia, **E. Hosler**, E. Kukk, S.R. Leone, B. McFarland, M. Messerschmidt, B. Murphy, V. Petrovic, D. Rolles, N. Berrah. Ultraintense X-Ray Induced Ionization, Dissociation, and Frustrated Absorption in Molecular Nitrogen. Physical Review Letters. **104**. 253002. 2010.

Chapter 1

Strong-Field Dynamics and Femtosecond Extreme-Ultraviolet Transient Absorption Spectroscopy

The development of the LASER[1] following the successful demonstration of the MASER[2,3] has led to a revolution in chemical dynamics studies, allowing access to the fundamental timescales of molecular reactions and most recently, electron dynamics. The breaking and forming of chemical bonds is the foundation of chemistry, and chemical reactions occur on the timescale of tens to hundreds of femtoseconds (10^{-15} seconds). Prior to the laser, chemical reactions could be examined by crossed molecular beam experiments[4-6] and infrared emission studies,[7-10] allowing inference of activated collision complexes and transition states.[11] In the past three decades, the advent of ultrafast lasers[12-14] and the development of commercially available femtosecond laser systems has facilitated the routine interrogation of femtochemistry,[15,16] as well as the real-time observation of chemical reactions and dynamics,[17] at a global scale. An invaluable experimental procedure for investigation of chemical reactions and dynamics is the pump-probe technique. Typical femtochemistry pump-probe experiments involve the absorption of a single femtosecond photon, often leading to excitation to a non-stationary excited state, which is subsequently probed via a second femtosecond pulse to elucidate the excited state characteristics. In particular, the investigation of real-time non-stationary state dynamics was observed through dynamic white light absorption, in which a broad-band sub-10 fs probe was utilized to observe wave packet dynamics in complex molecular systems.[18] By monitoring the absorption spectrum in time, the chemical dynamics of the molecular system could be observed directly by the change in the magnitude and wavelength of absorption. This examination of femtochemistry via transient absorption spectroscopy has since been extended by our group[19] to the investigation of atomic[20,21] and molecular[22,23] dynamics as well as attosecond (10^{-18} seconds) electronic dynamics employing core-level extreme-ultraviolet absorption.[24]

High-order harmonic generation (HHG)[25,26] has facilitated the investigation of femtosecond extreme-ultraviolet (XUV) absorption on a table-top scale in a variety of chemical systems and states of matter. XUV/soft x-ray experiments had previously only been accessible at large government light source facilities, such as the Advanced Light Source, on picosecond timescales or the few hundred femtosecond timescales at pulse slicing beamlines.[27,28] The limitation of the temporal resolution at synchrotrons stems from the electron bunch length in the storage ring, which generates the coherent x-ray radiation. Slicing beamlines are able to reduce the pulse duration to the femtosecond timescale by selecting a subsection of the electron bunch, sacrificing substantial photon flux. High harmonic generation is accomplished by tunnel ionization of a valence electron in a target medium, subsequently followed by recombination of the electron with the ion core on the timescale of half a cycle of the laser pulse later, resulting in emission of a photon corresponding to the electron's excess energy. The very nature of the high harmonic process lends itself to the generation of ultrashort, high photon energy pulses in the 10's to 100's of electron volts, since the process occurs on the optical sub-cycle timescale.[29-31] High harmonic generation has been used as both a source of XUV light[32-36] and a probe of dynamics and orbital structure due to its sensitivity to the electronic subtleties of the generation medium.[37-39] The utility of XUV light as a probe stems from the accessible core-level states encompassed by the spectral bandwidth of the pulses from high harmonic generation, which may be availed to permit elementally specific probing of complex molecular systems. For example, in bromoiodomethane the bromine and iodine atoms may be probed separately at their respective $M_{4,5}$ and $N_{4,5}$ edges (~ 20 eV separation) during and after excitation.

Natural photochemical[40,41] processes occur via single photon absorption, where excitation from the ground state to an excited state leads to a fundamental change in the chemical structure of the absorbate. This process is well characterized by such pillars of quantum mechanics including time-dependent perturbation theory,[42] the Born-Oppenheimer approximation,[43] and Fermi's Golden Rule.[44,45] These obelisks of quantum mechanics pertain particularly to the purview where only absorption of a single photon is likely. The genesis of ultrafast high energy femtosecond laser systems has paved the way for investigating photochemical processes in a non-perturbative regime, where multiphoton absorption is likely and the interaction of the laser's electric field with the atomic or molecular Coulombic potential must be considered.[46] This field intensity is achieved when the electric field of the laser approaches the potential energy experienced by valence electrons, approximately 10^8 V/cm, characterizing the onset of the strong-field regime at a laser intensity of approximately 10^{13} W/cm^2.

The non-perturbative interaction of high intensity laser pulses distorts the effective atomic or molecular potential resulting in ionization on the sub-cycle timescale by either multiphoton absorption or tunnel ionization as illustrated in figure 1.1. Within the multiphoton regime, the strong-field interaction requires a non-perturbative treatment to account for even the direct effects at high field intensities, such as the shifting of above threshold ionization (ATI) structures observed in photoelectron spectroscopy with field intensity. Intuitively, ATI structures result from the successive multiphoton absorption of light beyond the minimal number of photons required to ionize the target. Each successive peak corresponds to an additional absorption of a photon.[47] The quantization of the energy eigenstates is conserved, although AC-stark shifting of the levels may occur at field intensities close to the tunnel ionization limit, resulting in the necessity for the non-perturbative treatment of the effect. The AC-Stark shifting of the levels results in the change of the ATI structures' energies. Multiphoton ionization occurs during the entirety of the driving laser pulse. Therefore, there is only a weak dependence of the ionization rate on the phase of the laser electric field.[48] As the field intensity is increased, tunnel ionization becomes dominant and a strong dependence of the ionization rate on the phase of the driving laser electric field is observed. The phase dependence originates from the interaction of the intense laser field with the Coulombic barrier of the valence electron. The rate of ionization is the fastest at the peak of the laser field when the Coulomb barrier is the most suppressed. In the regime of strong-field ionization, the quasistatic approximation is valid, which relies on the assumption that the tunneling electron wavefunction arrives at a quasistatic state before the electric field varies significantly. The insignificant variation in the electric field during tunnel ionization implies the Coulombic barrier also remains constant on the ionization timescale; consequentially, the tunneling electron must react instantaneously to the laser electric field. This permits the calculation of tunnel ionization rates employing a static electric field, utilizing namely Keldysh[49] and Ammosov-Delone-Krainov theories.[50] At even higher field intensities (>10^{15} W/cm^2), the Coulombic barrier may be completely suppressed such that the valence level becomes unbound and ionization may occur directly over the barrier.[51]

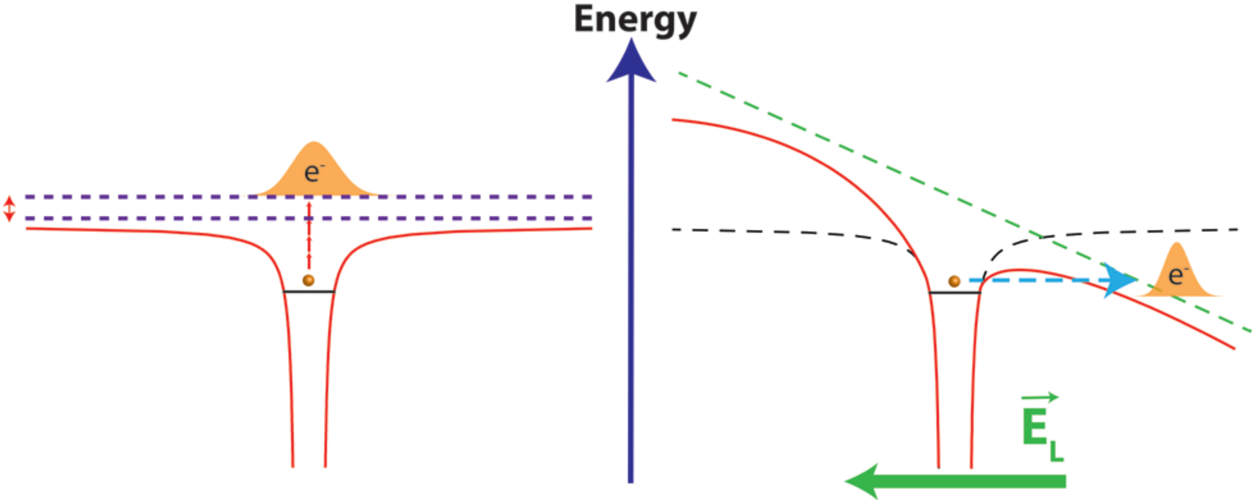

Figure 1.1: Strong-field interaction of an intense laser pulse with the Coulomb potential of an atom. (Left) Multiphoton ionization occurs via the absorption of several successive photons to overcome the ionization potential of the atom. AC-Stark shifting of the excited state (dashed purple lines) may result due to the strong-field non-perturbative interaction. (Right) Tunneling ionization results from the interaction of the electric field of the intense laser pulse (dashed green line) and the binding potential (dashed black line) of a valence electron (orange sphere), resulting in the suppression of the Coulombic barrier (red curve) of the atom allowing a valence electron to tunnel ionize into the continuum. If the field intensity is strong enough, the barrier may be suppressed completely, directly field stripping the electron. It is possible that multiple valence electrons may undergo tunnel ionization.

Once ionized, the liberated electron from an atom accelerates in the strong laser. The phenomena resulting from the ionization process are then dictated by the interaction of the electron with the ion core in accordance with the “Simple Man’s” or “three-step” model.[52] Elastic scattering of the electron on the ion core results in ATI,[47,53] while inelastic scattering leads to double non-sequential ionization or excitation of the ion.[54,55] High harmonic generation may occur if the returning electron wave packet radiatively recombines with the ion core.[26]

In addition to the before mentioned strong-field phenomena in atoms, molecules undergo an additional set of phenomena due to the additional nuclear degrees of freedom. Molecular systems may undergo symmetric or asymmetric[56] dissociative ionization, resulting in charged reaction products.[22,57-61] Non-sequential or sequential ionization of a molecule or cluster could facilitate Coulomb explosion of the resulting highly charged ion. Lastly, the strong-field interaction with molecules may deform the ground state potential energy surface in accordance with the magnitude of the interaction with the intense laser electric field, consequentially, causing bond-softening or hardening.[58,59,62-65] Enhanced ionization may also occur due to coupling of the ground state potential surface with high lying ionic states, resulting in a decrease in the ionization potential at a particular internuclear separation.[62,64,66-69] Ground state vibrational wave packets may also be produced due to the asymmetric ionization rate around the molecular equilibrium geometry.[61,70,71]

The remainder of this chapter is divided into four sections, providing the relevant material for understanding the experiments presented in the following chapters. Section 1.1 elaborates on the strong-field ionization phenomena, which are omnipresent when a molecule is exposed to an intense laser field of $\geq 10^{14}$ W/cm^2, including tunnel ionization, enhanced ionization, dissociative ionization, and Coulomb Explosion. Section 1.2 details the high harmonic generation process with particular emphasis on aspects relevant to the development of the experimental apparatus into a robust instrument, covering the “three step” model, HHG in a capillary waveguide, HHG in a semi-infinite gas cell, and field symmetry breaking for even harmonic generation. Section 1.3 describes the mechanisms for strong-field wave packet formation by impulsive stimulated Raman scattering, critical internuclear separation ionization, and the Lochfraß mechanism. Lastly, section 1.4 explains the development of femtosecond extreme-ultraviolet transient absorption spectroscopy. The experimental work presented in the following chapters demonstrates the applicability of femtosecond XUV transient absorption spectroscopy to investigate vibrational dynamics via core-level spectroscopy, providing a weakly interacting probe of strong-field dynamics. In particular, the phase of Lochfraß vibrational wave packets are be explored as a function of field intensity to determine the ionization pathway along with the superposition composition and localization. Also, previous work investigating the alignment quantum state distribution of the strong-field generated hole in Xe^+ is expanded to Xe^{2+} as well as Br_2^+. The strong-field ionization dynamics of heteronuclear diatomic iodine monobromide (IBr) is also explored in the context of observing dissociative ionization timescales and wave packet motion relative to the iodine *4d* and bromine *3d* core-level absorptions.

1.1 Molecular Dynamics in the Strong-Field

The ready availability of high energy, femtosecond pulse duration sources has allowed access to atomic and molecular interactions with strong-electric fields greater than the Coulombic binding potential of valence electrons. Modern, commercially available laser systems can easily obtain field intensities greater than 10^{15} W/cm^2 (pettawatt), while advanced exawatt and zettawatt systems are being developed at National user facilities world-wide to investigate fusion and relativistic dynamics.[72] Laser dressing of potential energy surfaces may be controlled at such field intensities, allowing direct control of quantum dynamics and ionization processes.[73,74] In particular, strong-field interactions permit barrier-suppression of the Coulombic potential of a valence electron, resulting in tunnel ionization, which can lead to the formation of highly charged species.[51] Moreover, the strong-field interaction in molecular species need not only present itself as a barrier suppression interaction, but may also result in the coupling between states previously isolated in absence of the field. This potential energy surface perturbation has been observed to result in coupling of the ground state surface with a higher lying ionic state potential, resulting in enhanced ionization at internuclear separations greater than the static equilibrium geometry as well as dissociative ionization.[22,57-61,67] Strong-field ionization of molecules and clusters may result in the formation of highly charged states, which may undergo rapid dissociation as a result of charge repulsion given by the classical Coulomb's Law, known as Coulomb explosion.[58,59,75,76] Short descriptions of these strong-field effects are presented here as a reference for the discussion of experiments to follow, but a more detailed explanation is contained in the relevant chapters. Moreover, an introduction to strong-field generated vibrational superpositions is presented in section 1.3; including impulsive stimulated Raman scattering, critical internuclear separation ionization, and the Lochfraß mechanism.

1.1.1 Tunnel Ionization

A theoretical structure for tunnel ionization is discussed thoroughly in Chapter 3, including the development of internuclear separation, vibrational level sensitive tunnel ionization rates in terms of Keldysh and Ammosov-Delone-Krainov theories. As previously mentioned, tunnel ionization is a product of the interaction of a strong-electric field with the Coulomb potential of a valence electron, each of which has an electric field strength on the order of the 10^8 V/cm. If the applied electric field is greater than the Coulomb potential, the ionization barrier of the valence electron may be completely suppressed, allowing the electron to exit the barrier classically.[77] It is under these field intensities that a non-perturbative description of dynamics is required. Tunnel ionization requires a quantum mechanical description. Below the field intensities relevant to tunnel ionization, multiphoton absorption (where $E_p < I_P$) is the dominant mechanism by which atoms and molecules ionize. In the multiphoton regime, (lowest-order) perturbation theory may still describe the observed dynamics such that an ionization rate may be calculated according to:

$$W_{multiphoton} = \sigma_N I^N \tag{1.1}$$

where σ_N is the N photon absorption cross-section and the ionization rate is proportional to the laser field intensity to the power of N, I^N. Therefore, the rate of ionization should increase linearly with field intensity on a Log-Log plot. This solution inherently does not account for sub-cycle ionization dynamics occurring at high field intensities, but instead it incorporates the electric field of the driving laser via the pulse envelope.

Originally, tunnel ionization was observed under static electric fields,[49] but the advent of high energy, ultrashort laser systems has allowed tunnel ionization to be observed on the sub-cycle timescale as the Coulombic potential constantly flip-flops, following the applied vector of the laser electric field. As a result, tunnel ionization in an AC field occurs on the few femtosecond to attosecond timescale, which affords the ultrashort pulse duration of XUV light generated by high harmonic generation discussed later.[78] Given the typical use of many-cycle optical pulses in tunnel ionization experiments, an adiabatic ionization potential may be utilized for tunnel ionization calculations, the quasi-static approximation. For few-cycle pulses, the quasi-static approximation is no longer valid since the average electric field vector is no longer zero over the pulse envelope. Therefore, the electron may no longer be assumed to react instantaneously to the laser electric field. The process of tunnel ionization has been observed to occur within 100 attoseconds.[79] Once the electron has tunnel ionized, it may be treated as a free-particle in a time-evolving electric field, which is a function of the Coulomb potential of the remaining ion and the applied laser electric field.

After an electron has tunnel ionized, a possibility exists that the electron wave packet will revisit the ion core once the field has changed sign. Initially, the tunnel ionized electron accelerates away from its originating ion core. A quarter of an optical cycle after ionization, the ionized electron reverses trajectory in the continuum, as the vector potential of the electric field has changed sign, and accelerates back toward the ion core. A half-cycle after tunneling out, the electron is in the vicinity of the ion core. At this moment, the electron may either scatter elastically, inelastically, or recombine resulting in above-threshold ionization, non-sequential double ionization, or high harmonic generation, respectively. The latter will be explored in great detail in the following section. When one electron is ionized from an atom, the remaining electrons move closer to the nuclei due to the decrease in the effective shielding caused by the loss of the first electron, raising the ionization potential of the remaining electrons. Non-sequential ionization may occur through two separate pathways; simultaneous and delayed ionization. Simultaneous, non-sequential double ionization may occur when the field intensity is sufficient to remove two electrons before the second electron has a chance to adjust to the new effective potential caused by the loss of the first electron. This is considered to occur only at field intensity regimes where the dominant ionization mechanism occurs by a complete suppression of the tunneling barrier.[80] Delayed, non-sequential double ionization requires the scattering electron to provide the necessary energy to overcome the strengthened ionization barrier experienced by the second electron bound to the ion core. Typically, reencounter must happen on the first or second pass lest the free electron wave packet diffuse into the continuum and no longer have the necessary overlap with the ion core for a strong interaction to occur on successive revisits. Lastly, sequential ionization may also occur as successive single electron ionization events, where the field intensity to ionize the second electron must overcome the second ionization barrier as sufficient time has passed to allow the second valence electron to adjust to the new Coulombic field.[81]

1.1.2 Enhanced Ionization

For the strong-field ionization of molecules, the degree of freedom afforded by the vibrational modes of the species permit access to unique ionization dynamics. In particular, it is possible that highly charged states may be accessed due to enhanced ionization resulting from motion of the nuclei during the tunnel ionization process. Most simply, the field interaction model for tunnel ionization may be applied to the potential energy landscape of diatomics. Barrier suppression of a diatomic molecule’s Coulomb potential leads to augmented barrier suppression at one nucleus over the other. Tunnel ionization may then occur directly to the continuum over the internal Coulomb barrier, bypassing the outer barrier as seen in figure 1.2. As the barrier is suppressed in a diatomic, the internuclear separation is observed to elongate, leading to enhanced ionization at large internuclear separations. Also, as the strong-field interacts with the potential energy landscape of a molecule, a higher lying state with ionic character may couple via the driving laser field to the perturbed neutral state. This coupling may facilitate an avoided crossing between the states as seen in figure 1.2, causing consecutive ionization processes resulting in highly charged states of the target molecule.[64] This process is known as charge resonance enhanced ionization (CREI), where the higher lying state is lowered by the same energy as the lower state is raised, allowing nonadiabatic population transfer.

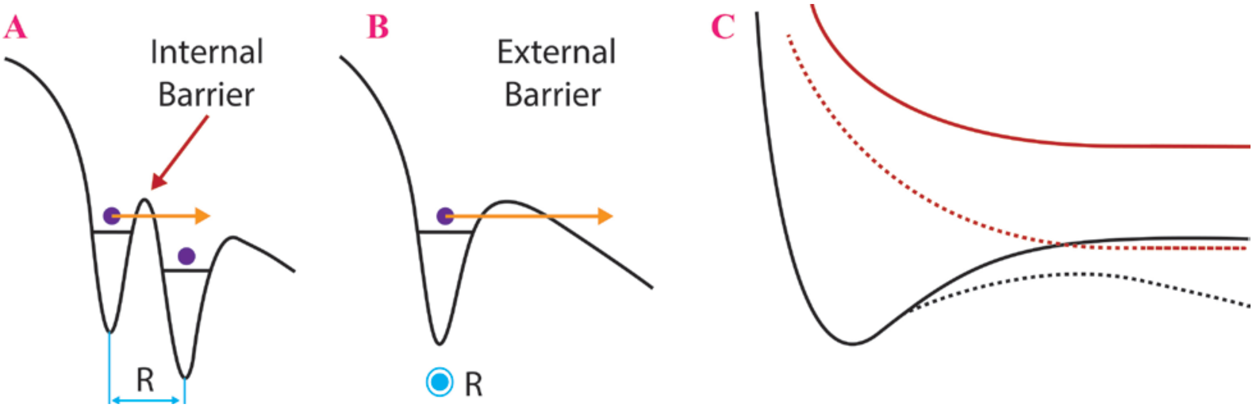

Figure 1.2: Perturbed Coulomb potential of a diatomic molecule in the presence of a strong-electric field as viewed along the internuclear axis (A) and perpendicular to it (B). As the field intensity increases, the internuclear separation elongates to a point where the perturbed barrier minimizes the ionization potential at one atomic site in the molecule, facilitating tunnel ionization across the internal molecular potential barrier to the continuum.[67] (C) State coupling in molecules permits barrier suppression and enhanced ionization at large internuclear separations. The resulting avoided crossing facilitates CREI. The solid lines represent the potential energy curves for the molecular ground state (black) and a higher lying repulsive state of opposite symmetry (red). The dotted lines represent the field distorted states and the resulting avoided crossing.

Enhanced ionization has been observed in detail for diatomic systems of H_2, I_2, and N_2.[56,62,64,69,71,82-84] For each diatomic system, a critical internuclear separation is attributed to the enhanced ionization rate in terms of CREI. For N_2, the individual internuclear separations relevant to ionization are determined for multiple charge states in terms of the measured kinetic energy of the ions related to accurate potential energy curves. The trend of increasing ionization with increasing internuclear separation is identified for both symmetric and non-symmetric charged atomic site pathways, indicating that the ionization to high charged states occurs through an expanding internuclear separation instead of a fixed critical distance.[84] Examining the strong-field ionization of I_2 demonstrates that enhanced ionization is specific to the orientation of the molecular axis with the laser electric field, dictating the necessity for electron localization in the ionization process.[67] As the internuclear separation is increasing with CREI, dissociative ionization may occur for the ions and the ground state, facilitated by the relaxation of the molecular potential. Furthermore, once highly charged states have been accessed by enhanced ionization, Coulomb explosion leads to a rapid dissociation of ion pairs within a molecule or cluster, yielding ion kinetic energies determined by a Coulomb repulsion field.

Additionally, molecular interactions with intense laser fields have the tendency to align the target gas dipole (permanent or transient) moment with the applied field's polarization. This alignment is achieved via an impulse torque on the molecule resulting from the applied force of the laser electric field on the dipole moment of the molecule. For such alignment, it is not necessary for the target molecule to be polar, as nonpolar molecules are aligned in accordance with their second-order polarization response to the intense laser field and subsequent formation of an induced dipole moment. Alignment of molecules in this fashion requires only that the polarizability be anisotropic.[85] For the strong-field alignment of a diatomic molecule, the Schrödinger equation may be written for a linear rotor subject to a time-dependent electric field of $E(t)=E_0\cos[\omega t+\varphi]$, where E_0 is the peak intensity of the field:

$$\left[BJ^2+V_\mu(\theta)+V_\alpha(\theta)\right]\Psi=E\Psi \tag{1.2}$$

with J^2 being the squared angular momentum operator, *B* the rotational constant of the target molecule, *E* the eigenenergy, *Ψ* the eigenvector, and *θ* the polar angle between the molecular axis and the electric field polarization. $V_\mu(\theta)$ and $V_\alpha(\theta)$ characterize the interaction of the electric field with the permanent dipole moment and molecular polarizability, respectively. Each field interaction term may then be written as:

$$V_\mu(\theta)=-\mu\cos[\theta] \tag{1.3}$$

where *μ* is the permanent dipole moment along the molecular axis, and:

$$V_\alpha(\theta)=-\tfrac{1}{2}E(t)^2\left(\alpha_\parallel\cos^2[\theta]+\alpha_\perp\sin^2[\theta]\right) \tag{1.4}$$

with $\alpha_\parallel$ and $\alpha_\perp$ being the polarizability of the molecule parallel and perpendicular to the molecular axis, respectively. For ultrashort pulses and nonresonant alignment frequencies, the laser frequency is typically much greater than the inverse of the pulse duration; therefore the dipole response of the molecule to the electric field averages out due to the AC vector oscillation, leaving only the polarization response. $V_\alpha(\theta)$ now also becomes:

$$V_\alpha(\theta)=-\tfrac{1}{2}\frac{E_0^2}{2}\left(\alpha_\parallel\cos^2[\theta]+\alpha_\perp\sin^2[\theta]\right) \tag{1.5}$$

and the time averaged Schrödinger equation may be reduced to an oblate spheroid wave equation since $\alpha_\parallel>\alpha_\perp$.[86]

Clearly, laser alignment of polar and nonpolar molecules is possible through impulsive, strong-field irradiation. Moreover, angle dependent tunnel ionization experiments have revealed that ionization occurs predominantly from molecules that are aligned (intrinsically or methodically) with the polarization of the applied laser field.[87,88] Specifically, the strong-field ionization of D_2 is observed to be 1.15 times more probable when the laser electric field is aligned parallel to the molecular axis rather than orthogonal, as compared to circularly polarized experiments.[89] Experiments involving the strong-field ionization of small molecules can then be assumed to both partially align the target molecular axis to the electric field of the driving laser as well as selective ionize those molecules inherently aligned with the laser polarization.

Photoelectron angular distribution measurements have been conducted for both diatomic[90] and large molecules,[91] demonstrating the dependence of the outgoing electron trajectory on the shape of the originating orbital as well as field intensity. This is a direct correlation of the tunnel ionization rate relative to the alignment of the molecular axis and the laser polarization. Ionization to higher charge states beyond the first cationic state were found to be weakly dependent on molecular orientation due to the rescattering nature of the process. The rescattering electron is also affected by the molecular orientation relative to the electric field as it has been observed that above-threshold ionization emission is minimized in diatomics when ionization occurs perpendicular to the molecular axis.[92] Rescattering of the returning electron may also be employed in molecular orbital tomography to provide attosecond information about the ion core subsequent to ionization.[93]

1.2 High-Order Harmonic Generation (HHG)

High-order harmonic generation was originally discovered during the investigation of few-order (2nd, 3rd, …) harmonic generation in solid aluminum targets irradiated by intense 10.54 μm light from a pulsed CO_2 laser at the National Research Council in Canada.[25] Integral harmonics up to the 11th order were observed due to the lack of inversion symmetry in the target, but the theoretical framework at the time, focusing solely on second/third harmonic generation, was unable to explain the phenomena. Later, studies by McPherson, Rhodes, et al. examined high harmonic generation in rare gas targets produced by a pulsed gas jet, discovering the impact of ionization potential on the maximum harmonic energy observed.[26] A large plateau of equally intense harmonics was observed that was not readily explainable in terms of perturbation theory, which predicts exponentially decreasing harmonics as a function of the increasing harmonic order. Several explanations for high harmonic generation were offered in the late 1980's and early 1990's. Specifically, L'Hullier, Schafer, and Kulander explained the trend of high harmonic spectra generated in inert gases by solving the time-dependent Schrödinger equation for a laser-excited gas medium.[94] It was not until 1993 though that Paul Corkum[52] offered an encompassing explanation for high harmonic production in terms of the "Simple Man's" or "three step" model, describing the harmonic generation process as an ionization of an electron, at each peak of the driving laser electric field, followed by an electron-ion interaction. Until this point, the electron was treated as a bound particle. Since this explanation, high harmonic generation has continued to blossom into a field of rich new physics and chemistry pertaining to molecular orbital structure, attosecond spectroscopy, and novel XUV light sources. Here, we provide an overview of the high harmonic process and the generation techniques necessary for effective transient absorption spectroscopy.

1.2.1 Three-Step Model

The three step model is an elegant, semi-classical solution to high-order harmonic generation for a single particle response, illustrated in figure 1.3. In the first step of the model, the electron tunnel ionizes into the continuum as a result of the suppression of the effective atomic binding potential at the peak of the intense laser electric field. Maximum suppression of the binding potential is achieved at the minimum magnitude of the vector potential, $\vec{A}(t):\vec{E}(t)=\frac{-\partial\vec{A}}{\partial t}$, of the driving laser.[95] The laser electric field then changes sign a quarter of an optical cycle later, accelerating the electron back toward the ion core. In the final step, at the maximum vector potential of the electric field (zero-crossing of the electric field), the electron has arrived back at the ion core and may recombine with a finite probability to emit a photon. The emitted photon energy is equal to the kinetic energy gained in the continuum by the acceleration of the electron plus the ionization potential (IP) of the particle. Typically the photon energy is in the XUV regime (10's to 100's of electron volts). When considering multiple single emitters, it is necessary to incorporate phase matching of the macroscopic collection of emitters for the coherent buildup of the XUV emission. Here, we will discuss each step of the harmonic emission process at the microscopic level only, saving elaboration of phase matching for the next section as well as for the discussion on the merits of different high harmonic generation methods.

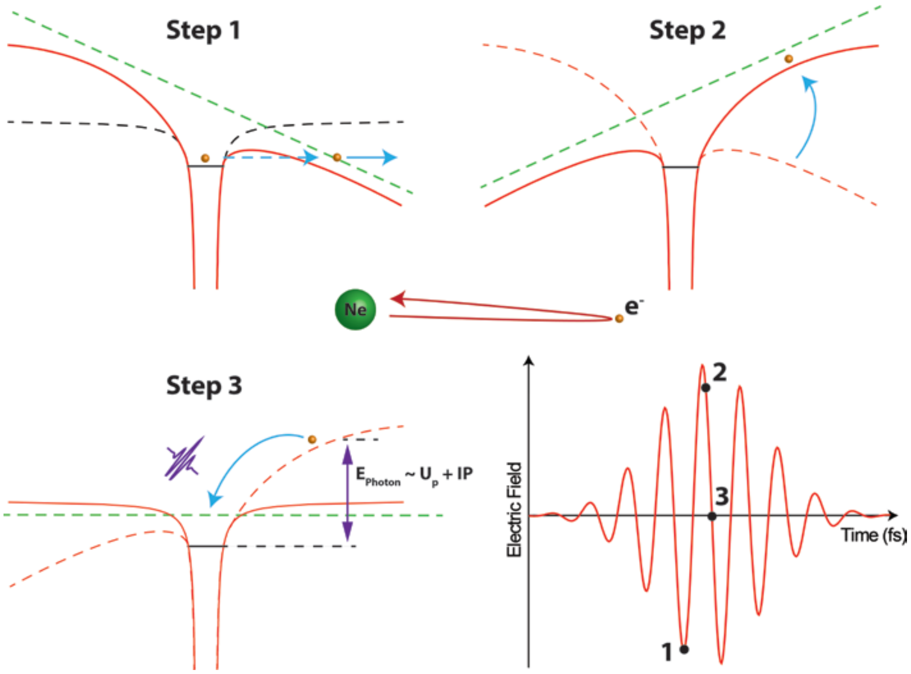

Figure 1.3: The "three step" model for high harmonic generation in an atomic gas medium (neon) as a function of the optical cycle of the driving electric field (bottom right). In step 1, the intense laser field, near the peak of an optical sub-cycle, interacts with the effective binding potential of a valence electron, resulting in a deformation of the potential proportional to the strength of the electric field. At this point, the electron may tunnel ionize into the continuum instantaneously with respect to the time evolution of the laser electric field and the suppressed barrier. Step 2 occurs when the electric field of the driving laser changes sign relative to step 1, causing the electron to be accelerated back toward the ion core. At the zero crossing of the electric field, step 3, the electron is in the vicinity of the ion core with high kinetic energy and may interact with the ion releasing its excess energy through photoemission equal in energy to the ionization potential of the atom plus the kinetic energy gained in the continuum, typically 10's to 100's of electron volts.

In the first step of high harmonic generation, the effective binding potential of a valence electron is suppressed such that electron tunneling under the barrier, or complete barrier suppression and subsequent stripping of the electron, becomes likely. As noted earlier, a theoretical structure for this process will be outlined in Chapter 3 in terms of Keldysh and Ammosov-Delone-Krainov (ADK) theories. The effective potential may be determined by the strength of the electric field of the laser acting on the harmonic generation target and the binding potential experienced by a valence electron. The time varying electric field of the laser is given as:

$$E(t)=E_0\cos[\omega t+\varphi] \tag{1.6}$$

and the effective binding potential of the valence electron is determined via Coulomb's law:

$$V_{Coulomb}(\vec{r})=\frac{-e^2}{4\pi\varepsilon_0\vec{r}} \tag{1.7}$$

where E_0 is the intensity of the electric field of the laser, ω is the laser frequency, φ is the phase of the electric field at the time of ionization, e is the fundamental electric charge, $\vec{r}$ is the position vector of the electron relative to the effective charge of the atomic core, and ε_0 is the electric permittivity of vacuum. The instantaneous potential of the laser's electric field may be treated as a linear function around the vicinity of a sufficiently small target (an atom) and is simply: $V_{Electric\ Field}(\vec{r},t)=e\vec{E}(t)\vec{r}$. When the laser electric field strength approaches the intratomic field strength, a valence electron may become directly field ionized, but even before this field strength is reached, the probability of tunnel ionization is quite large as determined by ADK theory. The field strength experienced by a valence electron is then simply given as:

$$V_{valence\ electron}(\vec{r},t)=e\vec{E}(t)\vec{r}-\frac{e^2}{4\pi\varepsilon_0 r} \tag{1.8}$$

The time it takes for the electron to tunnel under the ionization barrier is finite and must be considered in attosecond electron dynamics,[79,96,97] but for high harmonic generation on the 10's of femtosecond timescale, the quasistatic approximation is valid. Therefore, the tunneling of the electron under the barrier may be considered instantaneous with respect to the time evolving laser electric field and suppression of the ionization barrier. At the moment of ionization, the electron finds itself outside of the Coulomb barrier with some initial kinetic energy, v_0.

As the electric field is evolving from the time of ionization, the electron is accelerated away from the ion core until a quarter of an optical cycle later at which point the sign of the laser electric field has changed sign. The motion of the electron may at this point be treated completely classically as a point charge interacting with a time evolving linear electric field. The trajectory of the electron may be determined by solving the classical Newtonian equations of motion.[81] The velocity of the electron is then given in one-dimension as:

$$\mathrm{v}_{electron}(t)=\int_0^t \frac{e}{m_e}E'(t')dt'+\mathrm{v}_0 \tag{1.9}$$

$$\mathrm{v}_{electron}(t)=\frac{E_0 e}{m_e\omega}\left(\sin[\omega t+\varphi]-\sin[\varphi]\right)+\mathrm{v}_0 \tag{1.10}$$

The average kinetic energy gained by an electron, $\overline{T}_{electron}$, in the continuum is then given as (ignoring the phase of the laser electric field momentarily):

$$\overline{T}_{electron}=\frac{1}{2}m_e\left(\overline{\mathrm{v}}_{electron}\right)^2=\frac{1}{2}m_e\left(\frac{E_0 e}{m_e\omega}\right)^2=\frac{E_0^2e^2}{4m_e\omega^2}=U_p \tag{1.11}$$

where U_p is the ponderomotive potential, or the quiver energy of the ionized electron, and the initial kinetic energy is zero ($v_0 = 0$). It is important to note that the ponderomotive potential is proportional to electric field strength squared, indicating that the kinetic energy of the accelerated electrons in the continuum increases linearly with field intensity.

Considering the phase of the electric field, φ, relative to ionization, the velocity of the position of the ionized electron relative to the ion core ($x_0 = 0$, $v_0 = 0$) is determined to be:

$$x(t)=\int_0^t \mathrm{v}'_{electron}(t')dt' \tag{1.12}$$

$$x(t)=\frac{E_0 e}{m_e\omega^2}\left(\left(\cos[\omega t+\varphi]-\cos[\varphi]\right)+\sin[\varphi]t\right) \tag{1.13}$$

This solution determines the electron trajectories in the continuum after ionization and the dependence of those trajectories on the phase of the electric field in terms of the ponderomotive radius: $a_0=\frac{E_0 e}{m_e\omega^2}$. Iterating various phases of the electric field, it is seen in figure 1.4 that an electron wave packet launched at a phase of 0° oscillates around a fixed point (the ion core) in accordance with the ponderomotive radius, while the other trajectories reencounter the ion core several times before being lost to the continuum. At this point, it is necessary to consider the quantum mechanical repercussions of a free electron accelerating in a continuum. Once the electron is removed from the Coulomb binding potential it behaves as a free particle wave packet. No longer confined to the Coulombic potential well, the electron wave packet will begin to progressively disperse in the continuum proportional. As the electron wave packet spreads, the likelihood of recombination at each successive encounter with the ion core will decrease as a result of diminishing overlap with the atom upon each successive reencounter event.[98]

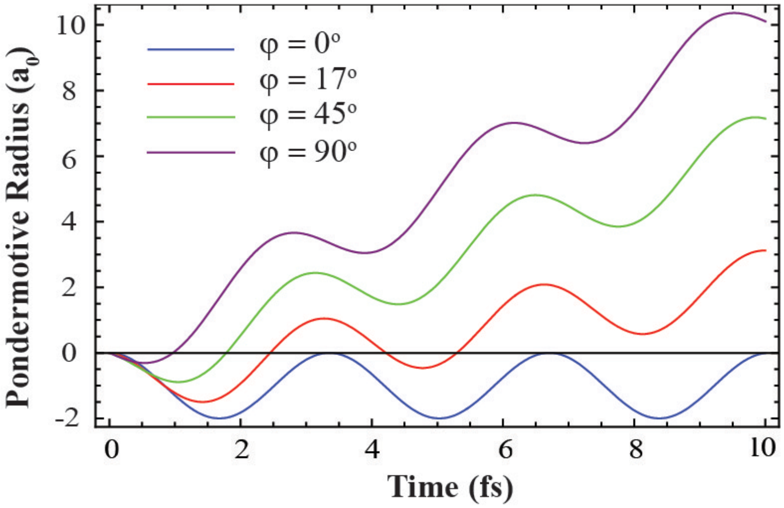

Figure 1.4: Electron trajectories dependent upon the phase of the laser electric field relative to ionization of a valence electron. It can easily be seen that an electron ionized at a phase of 0° oscillates around a fixed point, while an electron ionized at 90° is lost to the continuum. The slope around x = 0 is the velocity of the electron at 't' and is indicative of the kinetic energy the electron has gained in the continuum and is directly proportional to the photon energy emitted from recombination.

The final step of the high harmonic process is the recombination with the ion core. Each time the electron wave packet encounters the ion core there is a finite possibility the electron will interact, with one possible interaction being recombination and emission of an XUV photon. The probability of recombination is proportional to the location of the electron to the ion core, the diffusion of the electronic wave packet in the continuum, and the overlap of the electron wave packet with the positive hole in the ion core of the target atom. The energy of the emitted photon is:

$$\hbar\omega_{XUV} = IP + \overline{T}_{electron} \tag{1.14}$$

The highest kinetic energy to be gained by an electron accelerated in the continuum can be determined by solving x(t) = 0 for various phases of the laser electric field. The slope of the plot in figure 1.4 around x = 0 at time 't' is indicative of the velocity of the electron at the point of encounter with the ion core and therefore represents the kinetic energy available. It is found that $3.17U_p$ is the maximum kinetic energy to be acquired occurs when the electron has been ionized at a phase of the laser electric field of 17°. From 0° to 17°, the kinetic energy is increasing and then falls off beyond an electric field phase of 17°. The cut-off frequency of the high harmonic spectrum is then expected to be:

$$\hbar\omega_{XUV,\max} = 3.17U_p + IP \tag{1.15}$$

which has been confirmed experimentally and has been termed the "cut-off" law for high harmonic generation. An electron ionized at a laser electric field phase of 90° will gain the most kinetic energy in the field, 8 U_p, but that trajectory does not return to the vicinity of the ion core.

There are possible two trajectories that may impart the same kinetic energy to the free electron ionized at phases of the same change in angle from 17º. Trajectories of the free electron acquiring the same kinetic energy in the electric field are the so-called long and short trajectories, which as the names indicate correspond to the amount of time the ionized electron spends in the continuum. These trajectories will interfere constructively or destructively, depending on the relative dipole phase acquired during the electron's propagation in the continuum. The ratio of the long and short trajectory contribution to a particular high harmonic photon energy determines the spectral width of a given harmonic as a result of the quantum path interference, i.e. an increase in the contribution of the long trajectory will increase the spectral bandwidth of a harmonic, while preferential selection of the short trajectory will narrow the spectral bandwidth. Selection of a particular electron trajectory can be accomplished by adjustments to the intensity[99] and chirp[100] of the driving strong-field laser. The different trajectories also contribute uniquely to the temporal and spatial coherence of the generated XUV beam; the phase front curvature of the short trajectory is smaller than the long trajectory, leading to a reduced divergence angle with propagation of the beam and higher spatial coherence.[101] Coherence of the XUV beam is defined by the correlation of the electric field phases within the pulse at different points in space and time. Partial coherence would imply there is some correlation between the measured phase values, while perfect coherence occurs when all measured phase values are the same regardless of the spatial or temporal coordinates. The coherence of the XUV light is directly determined by the ability of the beam to exhibit interference effects.[102]

The basic principles of tunnel ionization and recombination have been laid out under the guise of an explanation for high harmonic generation, but this is only one of the possible outcomes as outlined earlier. If the electron scatters off of the ion core as opposed to recombining, above-threshold ionization or non-sequential double ionization may be the result if the collision is elastic or inelastic, respectively. Moreover, the high harmonic generation process itself is a means to an end for XUV light generation, and it may also provide a unique method for examining electron dynamics involving the ion core as a result of the collision event, especially when high harmonic generation is conducted in a molecular medium. Significant research is currently being conducted in relation to high harmonic generation as a novel avenue for investigating electron and hole dynamics via the collision event.[37]

High harmonic generation is a robust technique that is relatively insensitive to the method in which the process is conducted, in the sense that it is quite easy to obtain XUV light. In order to obtain bright, high photon energy XUV light a variety of sources and phase matching conditions have been explored. For brevity, only high harmonic generation from a capillary waveguide and a semi-infinite gas cell will be examined here due to their relevance to the experimental apparatus employed in the following scientific investigations.

1.2.2 Phase Matching

At this point, it must be noted that the three step model relates to the high harmonic generation process in terms of single emitters. In order to produce bright XUV sources from inert gas media, it is necessary to maintain the same electric field phase between many single atom emitters at the macroscopic level. This process is known as phase matching, in which the dispersion of the XUV generated high harmonics is matched to that of the driving laser field within the generation medium. Due to the significant difference in wavelength between the driving laser and the XUV emissions, there is an inherent mismatch in the dispersion between the two light fields, which may be compensated for by the physical condition of the target media.

Phase matching was originally introduced for the efficient generation of low-order harmonic generation (second, third, …) from a driving laser. Nonlinear effects such as second and third harmonic generation were only possible with the advent of the laser. Second harmonic generation (SHG) was originally accomplished in 1961 by Franken at the University of Michigan by focusing the output of a Ruby laser onto a quartz crystal.[103] The efficiency was so poor that when the report of SHG was published, the editor of Physical Review Letters removed the experimental evidence from the print as he thought it was a speck of dust. For efficient second harmonic generation of the fundamental, it is necessary that both wavelengths travel with the same phase through a nonlinear crystal, allowing the second harmonic to be generated in phase as a function of the polarization interaction of the fundamental with the crystal. The dielectric polarization, $\vec{P}$, of a medium may is given as $\vec{P} = \varepsilon_0 \chi \vec{E}$, where χ is a second-rank tensor, and may be expanded in a Taylor series:

$$P_i^n = \varepsilon_0 \sum_n \chi^n E_n^{\omega_n} = \varepsilon_0 P_i^0 + \varepsilon_0 \chi_{ij}^{(1)} E_j^{\omega_1} + \varepsilon_0 \chi_{ijl}^{(2)} E_j^{\omega_1} E_l^{\omega_2} + \varepsilon_0 \chi_{ijlk}^{(3)} E_j^{\omega_1} E_l^{\omega_2} E_k^{\omega_3} + \cdots \qquad (1.16)$$

where ε_0 is the vacuum electric permittivity, χ^n is the electric susceptibility of a given order n (χ^1 is the linear electric susceptibility), and $E_n^{\omega_n}$ is the electric field of frequency ω_n in Cartesian coordinates [j,l,k]. From the equation of the dielectric polarizability, it can clearly be seen that the fundamental electric field perturbs the target medium that generates the second harmonic in accordance with the electric susceptibility. Phase matching of the two laser colors propagating in the crystal may be achieved through generation of the harmonic of the incident light along an extraordinary axis of the non-linear crystal employed, where the difference in the index of refraction for one color verses the ordinary crystal axis minimizes the phase mismatch between the fundamental and harmonic light. With the fundamental and the second harmonic phase matched, efficient harmonic generation may be accomplished.

For high harmonic generation, the inert gas medium typically employed does not have an extraordinary axis in which to phase match the XUV light to the fundamental driver. Instead, the phase mismatch may be corrected employing the difference in dispersion caused by the inert gas between the low-energy fundamental and the high-energy harmonic light. The k-vector for the fundamental driving laser is given as:

$$k_L \approx \left[\frac{2\pi}{\lambda_L}\right]_{vacuum} + \left[p\eta N_{atm} r_e \lambda_L\right]_{Plasma} - \left[p(1-\eta) N_a \frac{2\pi}{\lambda_L}\left(n_L^p I_L\right)\right]_{Neutral\ gas} \qquad (1.17)$$

where there is a term relating to the dispersion of the vacuum, the strong-field generated plasma (ions and electrons), and the neutral gas. Here, η is the fraction of ionization of the inert gas, N_{atm}

is the gas number density per atmosphere, r_e is the classical electron radius, n_L^p is the refractive index of the gas at the fundamental driving laser wavelength, λ_L, and intensity, I_L, at a given pressure, p. The k-vector for the high-order harmonics is then likewise:

$$k_q \approx \left[\frac{2\pi}{\lambda_q}\right]_{vacuum} + \left\{ \left[p\eta N_{atm} r_e \lambda_q\right]_{Plasma} - \left[p(1-\eta) N_a \frac{2\pi}{\lambda_q}\left(n_q^p I_L\right)\right]_{Neutral\ gas} \right\} \tag{1.18}$$

given that q is the order of the high harmonic. The vector (phase) mismatch between the XUV harmonics and the driving fundamental will then be:

$$\Delta k = k_q - qk_L \tag{1.19}$$

with $\Delta k_{q,L} = 0$ being full phase matching. This equation may be simplified if λ_q is replaced with $q\lambda_L$:

$$\Delta k = \left[qp\eta N_a r_e \lambda_L\right]_{Plasma} - \left[qp(1-\eta) N_a \frac{2\pi}{\lambda_L}\left(\Delta\delta[\lambda_L] + n_L^p I_L\right)\right]_{Neutral\ gas} \tag{1.20}$$

where $\Delta\delta[\lambda_L]$ is the difference in the refractive index between the high harmonics and the fundamental laser wavelengths.

The equations for the phase matching of high harmonics illuminate several key points relating to macroscopic high harmonic generation.

1) For any experimental geometry and high harmonic generation gas target, phase matching may be achieved by adjusting the neutral gas pressure and the percentage of ionization (by adjusting the field intensity either by input energy, pulse duration, chirp, focal spot size, etc…)
2) There is a fundamental limit to the possible photon flux that may be generated given a certain set of experimental conditions. Once full phase matching is accomplished, any additional alterations to the high harmonic process will only decrease the output photon flux. (Not considering systematic flaws, i.e. insufficient differential pumping of gas media outside of the harmonic generation region)
3) Additional phase matching terms may be incorporated to aid in achieving full phase matching, thus extending the photon flux and energy generation possible. Geometric restrictions on the high harmonic generation process will alter the phase matching condition such as in a capillary waveguide or self-guiding laser-based filamentation.

1.2.3 HHG in a Capillary Waveguide

The first insight into structures for the guided propagation of waves was originally proposed by J.J. Thompson in 1893 and experimentally tested by Oliver Lodge in 1894, but it was not until the 1960s that the communication industry began to proceed in earnest with research into their applications. Since then, waveguides have been instituted into a myriad of applications in telecommunications or any instance where energy transfer needs to be efficient and directional. Typical solid-core dielectric waveguides operate on the principle of confining the expansion of traveling waves in the direction perpendicular to propagation due to total internal reflection, preventing dispersion as a function of path length. For the coupling of intense femtosecond light into a capillary for the purposes of high harmonic generation, the capillary must have a hollow core, such that the dielectric material is the glass tubing and either vacuum or air/HHG gas medium. For a hollow core waveguide, the restriction of the expansion of the traveling waves is accomplished by Fresnel reflections at the inner wall of the capillary. Coupling into a hollow core waveguide may result in a higher-order modal structure, but for the purposes of applying high harmonic generation to spectroscopy a Gaussian type profile is preferred, although high-order modes result in higher coupling efficiency.[104] The lowest order modal profile that may be obtained is the EH_{11} hybrid mode for cylindrical dielectric waveguides,[105] which minimizes the field loss rate α_{FLR}[106]:

$$\alpha_{FLR} = \left(\frac{u_{nm}}{2\pi}\right)^2 \frac{\lambda_L^2}{a^3} \mathrm{Re}\left[\nu_{EH}^2\right] \tag{1.21}$$

$$\nu_{EH}^2 = \frac{\nu^2 + 1}{\sqrt{2\left(\nu^2 - 1\right)}} \tag{1.22}$$

where u_{nm} is the modal constant for the azimuthal (m) and radial (n) modal indices given by the Bessel function (EH_{11}: $u_{11} = 2.405$), a is the hollow core radius, and ν is the ratio of the refractive index of the capillary material to that of its contents. For short length hollow capillaries, the coupling efficiency for perfect Gaussian beams may be as high as 98%, while under experimental conditions coupling efficiencies approaching 85% are observed.[34,107,108]

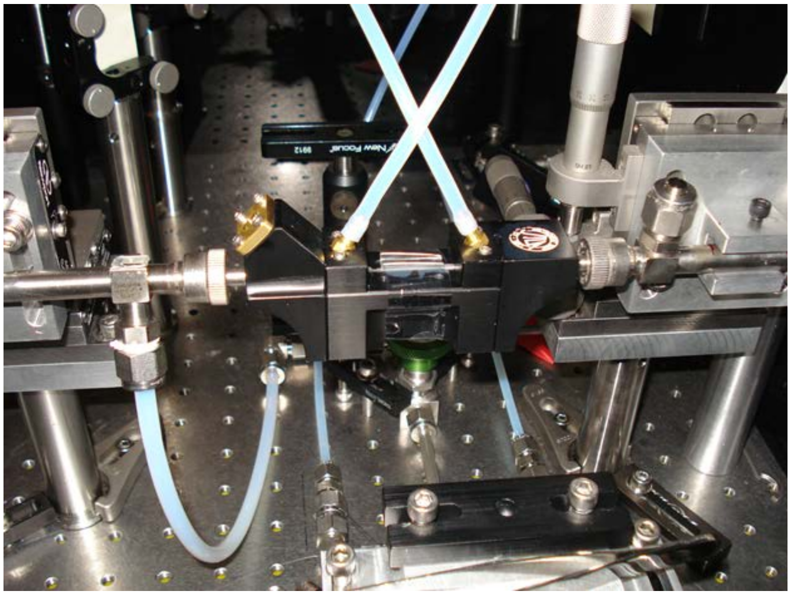

Figure 1.5: Installation of a third generation JILA v-groove for high harmonic generation employing a 5 cm long fiber. The four-fold manipulation optomechanics of the fiber may be seen at the front and the back of the v-groove as well as the inert gas inlets at the top of the fiber. The differential pumping connection at the front of the v-groove prevents plasma distortion of the driving laser before coupling to the waveguide.

The optimal focal spot size for maximum coupling efficiency of a free space TEM_{00} laser beam to a hollow core capillary waveguide into the EH_{11} hybrid mode is determined to be:

$$\omega_{optimal} = 0.6435a \tag{1.23}$$

since:

$$f_{optimal} = 0.6435\frac{\pi a D_{col}}{2\lambda_L} \tag{1.24}$$

The optimal beam waist ($\omega_{\mathrm{optimal}}$) and focal distance ($\mathrm{f}_{\mathrm{optimal}}$) may then be chosen for the largest coupling efficiency of a collimated driving laser beam of a given wavelength (λ_{L}).[109] Then, only the positioning of the hollow core waveguide to the driving laser beam needs to be optimized to obtain maximum coupling efficiency into the EH_{11} hybrid mode. Positioning of the capillary is typically accomplished by first noting the position of the driving laser and then introducing the waveguide while the energy of the laser is quite low to prevent burning of the waveguide. The waveguide may then be adjusted such that the beam path is unaltered from its original alignment and a clean spatial mode is obtained. The set-up for coupling the laser beam to the fiber is typically accomplished with an XY actuator at both the front and the rear of the waveguide, giving four axes of manipulation of the fiber for the alignment as seen in figure 1.5. The position/pointing of the driving laser is not adjusted at all; this would decrease the coupling efficiency be changing the angle of the incoming beam relative to the normal of the capillary face. This allows for vertical and horizontal positioning of the fiber, as well as pitch and azimuthal rotation relative to the beam axis. Adjustment of the front actuators for the capillary typically optimize the coupling efficiency of the capillary since that is the point of control for the entrance aperture, but also the azimuthal and planar rotation determine the coupling efficiency as a result of minimizing bending loss (loss to capillary cladding due to curvature of the fiber) and optimizing the acceptance angle as explained below. The rear actuation points control mainly the beam pointing as well as the mode of the outgoing beam. During experimental operation, adjustments to the front of the waveguide improve coupling efficiency with little effect on the beam pointing.

The equations presented above assume a perfect Gaussian beam able to produce a near diffraction limited spot. For most Ti:sapphire femtosecond laser systems, this is nearly impossible. Instead, a figure of merit is assigned to each laser system, which dictates its deviation from a diffraction limited focal spot known as the beam product parameter (M^2), i.e. a laser yielding a diffraction limited spot size has an M^2 of unity and a laser producing a focal spot size twice the diffraction limit has an M^2 of 2, etc… This provides a means for determining the coupling efficiency of a laser system to a capillary waveguide in terms of the numerical aperture of the fiber. Optimal coupling of the incoming driving laser beam of beam waist ω to the fiber is obtained by matching the numerical aperture of the fiber (NA_{fiber}) to that of the laser beam (NA_{beam}):[110]

$$NA_{fiber} \geq NA_{beam} = \sin\left[\frac{M^2\lambda_L}{\pi\omega}\right] = \sin\left[\frac{\omega}{f}\right] \tag{1.25}$$

given by the acceptance angle ($\theta_{a,fiber}$) of the fiber, and the refractive indices of the fiber core and cladding:

$$NA_{fiber} = \sqrt{\left(n^2_{fiber\,core} - n^2_{cladding}\right)} = \sin\left[\theta_{a,fiber}\right] \tag{1.26}$$

From the equations above, it can be seen that as the M^2 of a system deviates from a diffraction limited spot size, the coupling efficiency into the capillary decreases, resulting in losses to the capillary cladding material.

Additionally, bending losses may occur in the waveguide since no capillary is completely straight. Each capillary is drawn from a molten batch of fused silica, and as a result there is a large radius of curvature for each capillary, typically greater than six meters. The loss due to bending (R_{BL}) from the EH_{1m} mode may be given in terms of the radius of curvature:

$$R_{BL} = \frac{2}{\sqrt{3}}\left(\frac{2\pi}{u_{nm}}\right)^2 \frac{a^3}{\lambda_L^2}\sqrt{1 + \frac{1}{u_{nm}^2} + \frac{3\left(\nu^2 - 1\right)}{4\left(\nu^2 + 1\right)}\cos[2\theta_0]} \tag{1.27}$$

where θ_0 is the orientation of the laser electric field polarization with respect to the waveguide curvature. At $\theta_0 = 0°$, the face of the capillary waveguide is matched to the plane of curvature and if the polarization of the laser electric field is also perpendicular to the plane of curvature, bending losses are minimized. This implies that if coupling of the laser beam to the capillary waveguide is to be maximized, the fiber should be held as rigidly and straight as possible and coupling should be to the EH_{11} mode, since R_{BL} is only dependent (for a given set of physical parameters of the fiber) upon the coupling mode and the angle with respect to the incident laser beam; high order modes lead to less bending loss.

Hollow core capillaries have been developed rapidly over the past decade as an efficient source of fully coherent XUV light as a result of the additional geometric dispersion term for the phase matching of high harmonics to the driving laser. The geometric dispersion term arises from the wavelength dependent interaction of the coupled light to the cladding of the capillary through Fresnel reflection. The complete phase matching term for a capillary is then:

$$\Delta k = \left[qp\eta N_a r_e \lambda_L\right]_{Plasma} - \left[qp(1-\eta)N_a \frac{2\pi}{\lambda_L}\left(\Delta\delta[\lambda_L] + \widetilde{n_{atm}}I_L\right)\right]_{Neutral\ atom} + \left[q\frac{u_{11}^2\lambda_L}{4\pi a^2}\right]_{geometric} \tag{1.28}$$

The additional geometric term allows balancing of the phase-mismatch to higher photon energies, while also yielding a fully coherent XUV beam, even at hard x-ray wavelengths, due to the wave guiding nature of the structure. This allows a coherent build-up of harmonic along a long interaction length (figure 1.6), akin to using a thick non-linear crystal for second harmonic generation except the capillary suffers no significant loss of pulse duration over the extended interaction length.

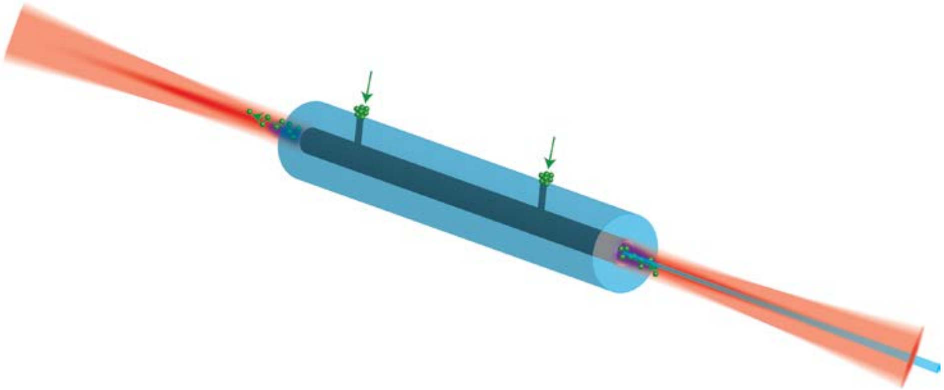

Figure 1.6: High harmonic generation in a gas filled hollow core fiber waveguide allows coherent addition of successive XUV generation events over several centimeters, resulting in increased photon flux over tight, free focusing geometries. The use of a hollow core waveguide also relaxes the gas flow requirement for XUV generation since the geometry is typically confined to 150 μm entrance and exit apertures. Since the capillary is a waveguide, the resulting XUV beam is fully coherent and has a very small divergence angle in relation to the driving laser, an appealing attribute for imaging and spectroscopic applications.

As was mentioned previously, the phase matching condition between the fundamental laser and the high harmonics may be met by pressure tuning until $\Delta k_{q,L} = 0$. Clearly, as the ionization fraction is increased the overall sign of the phase mismatch becomes positive. Therefore, there is a critical ionization percentage ($\eta_{critical}$) in which phase matching is achieved:

$$\eta_{critical} = \left[1 + \frac{N_{atm} r_e \lambda_L^2}{2\pi\left(\Delta\delta\left[\lambda_L\right]\right)}\right]^{-1} \tag{1.29}$$

As a result, the pressure tuning of the high harmonics is limited by the critical ionization percentage, which is typically <5% for harmonic photon energies < 100 eV.[104]

The original construction process for capillary waveguides for high harmonic generation involved placing three sections of 1.2 mm outer diameter, 150 μm internal hollow diameter fiber into an outer glass casing. Three sections were used to allow separation between a main middle segment and the entrance/exit segments such that the gas could be introduced to the center of the fiber. This therefore prevents pre-ionization before the fiber and reabsorption after the fiber, which would have resulted had the gas been introduced at the respective ends of the fiber. Typically capillary lengths resulting in an optimal number and length of coherence regions were on the order of less than 10 centimeters, 5 cm or 7 cm usually. Capillaries of 5 cm total length yielded high photon flux, but relatively poor XUV beam quality, and vice versa for 7 cm capillaries. This was due in part to the difficulty in aligning and gluing the three sections into the outer glass cladding effectively. To resolve the inconsistencies in construction, a CO_2 laser drilling platform designed by Ariel Paul[104] was constructed to create two 100 μm diameter gas inlet holes in each capillary as seen in figure 1.7. Once optimized, the set-up could routinely punch holes in fibers consistently on target with the same characteristics.

Figure 1.7: (Left)100 μm diameter CO_2 laser drilled gas inlet for a fused-silica capillary waveguide viewed through a stereoscope.[104] (Right) Third generation capillary waveguide holder oriented such that the driving laser enters from the right side. The fiber is pressed into an aluminum block v-groove with a piece of flexible plastic tubing to minimize bending losses and a viewing window is situated such that laser coupling to the entrance of the fiber may be optimized through minimization of scattering off the fiber cladding. The gas inlets of the fiber are sealed to the aluminum gas blocks (black, with brass tube fittings) via a hand cut 2 cm section of 1 mm diameter silicone tubing, sectioned lengthwise to make a gasket for each end. A 500 μm hole is punched with a syringe in each gasket to allow the gas to flow from the aluminum block to the fiber. The ends of the capillary are sealed to the v-groove via #002 silicone O-rings.[111]

In addition to the laser drilling of the gas inlets, the capillary waveguide mount design evolved from an outer glass casing to the third generation aluminum v-groove as seen in figure 1.7. This v-groove allows the capillary to be held rigidly straight, yielding improvements in the mode of shorter length fibers and overall flux enhancements at all lengths. This allowed the production of high flux, high coherence, and high energy XUV light from relatively short fibers (5 cm). Due to the very hands on nature of the capillary construction, there is much likelihood of error on the part of the experimentalist, especially relating to gas leaks (air in the fiber during harmonic generation). Much care must be taken in the cutting and fitting of the homemade gaskets as well as in the laser drilling of the fiber gas inlets themselves. Over drilling or off center drilling results in the ablation of material into the inner bore of the fiber, reducing the lifetime and the effectiveness of the structure.

1.2.4 HHG in a Semi-Infinite Gas Cell

High harmonic generation from a semi-infinite gas cell is not a particularly new idea, having been researched as an efficient means for XUV light production since the turn of the Millennia by Midorikawa et al. at RIKEN in Japan. Conversion efficiencies as high as 10^{-5} have been observed in argon, matching results of capillary waveguides without the need for a complex alignment apparatus.[33,112-114] Recently, the groups of Peatross[36,115,116] and Kovačev[35,117] have investigated in detail the dynamics of high harmonic generation within quasi-static focusing geometries, determining the effects of the focal spot size through aperaturing, the gas pressure, and focal spot position on the obtained XUV flux and photon energies. One of the major advantages of the semi-infinite gas cell though is the simplicity of the design, as is illustrated in figure 1.8. A semi-infinite gas cell is typically a 1” diameter, 0.5 meters long vacuum tube with a thin metal foil (~1/32” thick) on the vacuum side of the tube and a laser grade window on the atmospheric side. The exit aperture for the XUV light and inert gas may be created via laser ablation of the vacuum side foil, or a prefixed aperture may be installed of a greater thickness and variable diameter exit slit. The advantage of the laser ablation technique is the insensitivity of the foil position for alignment, but the prefixed exit slit spatial filters the harmonics at the risk of ablating material, which may coat the entrance window. A long focal length lens is then employed to drive high harmonic generation, which allows the support of laser based filamentation in the high harmonic generation medium, increasing photon flux and the average photon energy. A high degree of coherence is also observed, rivaling that of the capillary waveguide for high harmonic generation. The full degree of spatial coherence is obtained as a consequence of the loose focus geometry and the subsequent creation of a laser filament.

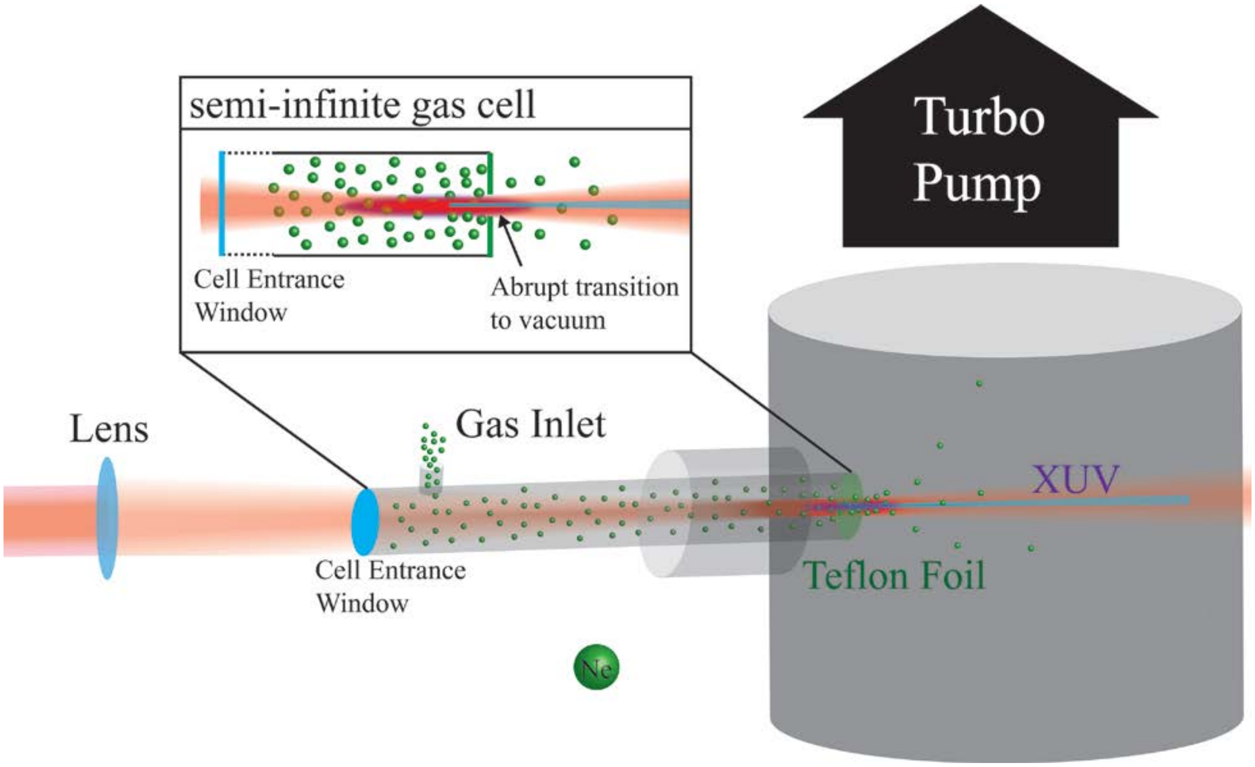

Figure 1.8: Typical schematic design for a semi-infinite gas cell high harmonic source. The semi-infinite gas cell itself is nothing more than a long (~0.5 meter) vacuum tube (< 1” diameter), pressurized with a high harmonic generation medium, with a laser entrance window and a laser ablated thin metal foil or prefixed pinhole as the XUV exit aperture. This design creates a quasi-static gas cell for high harmonic generation.

The semi-infinite gas cell affords a degree of tunability in the average XUV photon flux obtained via positional tuning of the focal plane relative to the exit foil. Starting with the focal volume symmetric around the exit foil aperture, tuning the lens position of the driving laser pulse along the direction of propagation translates the focal volume inside or outside of the semi-infinite gas cell. Translating the focus into the gas cell tends to shift the average XUV photon energy to shorter wavelengths due to the longer interaction length and the growth of the plasma filament. Choice of the focal length lens also affects the average photon energy obtained as a longer focal length lens yields a longer plasma filament. Translation of the focal plane outside of the semi-infinite gas cell yields brighter, longer wavelength XUV light. The XUV intensity increases outside of the foil as a result of reduction in the bandwidth supported by the generation process, i.e. harmonics are generated over a smaller energy range. Tuning of the focal plane position relative to the exit foil of the semi-infinite gas cell therefore allows selection of the XUV photon energy and spread for a given application. It is important to note here that in imaging or spectroscopic applications, when employing a refocusing mirror for the high harmonics the output will also have its focal plane shifted in accordance with the translation of the driving laser focal plane (object plane of the refocusing mirror).

As was demonstrated by Zhi-Heng Loh with a capillary waveguide high harmonic source, wavelength tuning of high harmonics may also be accomplished by pressure tuning, which was also demonstrated by the group of Kovačev.[19,35] The similarity between the capillary waveguide and the semi-infinite gas cell is best observed in the trend of harmonic flux between the low-order harmonics and high-order harmonics as a function of gas pressure. The low harmonics are observed to drop-off in intensity with increasing gas pressure due to reabsorption effects, while the more transparent high-order harmonics continue to increase in flux. Also, it may be seen that as the pressure is increased, the spectral features in a semi-infinite gas cell become quite broad and the spectral profile begins to break apart from the typical Gaussian distribution. The high harmonics are also driven to shorter wavelength with increasing pressure as is also observed in a capillary waveguide. The tunability of the harmonic wavelength is a critical function in a transient absorption experiment. Though all spectral transitions are observed within the bandwidth covered by the XUV pulse train, the greatest signal-to-noise is obtained at those optical transitions falling along the peaks of the harmonic flux. Tunability of the individual XUV harmonics allows selection of the molecular or atomic resonances to be interrogated with greatest signal-to-noise. This tunability comes at the expense of the XUV focal mode. The distortion of the spectral signatures of the harmonics is a direct result of plasma defocusing of the XUV mode within the harmonic generation region. Similar effects have been observed during transient absorption experiments of the strong-field ionization of xenon by pressure tuning the target density, resulting in the deformation of the individual harmonic modes after spectral dispersion.

High harmonic generation by a semi-infinite gas cell is by far the simplest iteration of an XUV source, requiring minimal user alignment when utilizing a laser ablated exit aperture. Very little if anything, is lost in terms of XUV photon energy, flux, or coherence for this simplicity of use, and stability of the source is gained given a robust incident driving laser. The experiments presented here represent the first application of this source to XUV transient absorption spectroscopy, and the details of operation are presented in Chapter 3.

1.2.5 Even High Harmonic Generation

Typical high harmonic generation in an inert gas by a single wavelength intrinsically generates only odd order high harmonics as a result of the inversion symmetry of the generation medium and of the driving laser electric field. XUV bursts are generated ever half cycle of the laser period ($\tau/2$). The Fourier transform of the XUV generation period easily predicts that a pulse train with frequency $2f$ of the driving laser is generated. To generate both even and the odd order harmonics, either the symmetry of the generation medium or the driving laser must be broken. Since high harmonic generation from inert gases is the most robust and established method for producing XUV light it is easiest to alter the driving laser parameters. By introducing a small amount of the second harmonic to the driving laser field, the symmetry of the electric field may be broken as seen in figure 1.9.

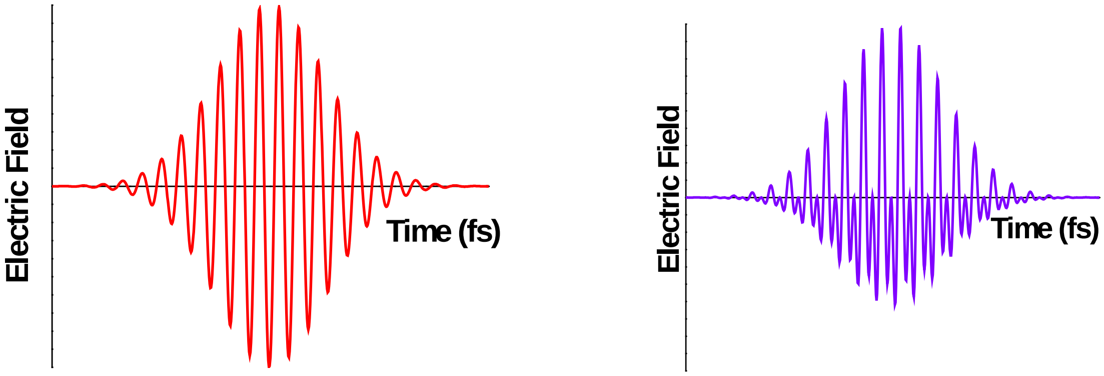

Figure 1.9: Calculation of the electric field of the driving laser pulse for high harmonic generation demonstrating symmetry breaking for even harmonic generation. (Left) Electric field envelope of an 800 nm laser pulse. (Right) The electric field pulse envelope of a two color driving laser pulse after mixing 800 nm (1.6 mJ) and 400 nm (25 µJ) light.

Even harmonic generation has been explored by several research groups[33,118-122] in terms of a breaking of the symmetry of the driving electric field and as a four-wave frequency mixing mechanism in the XUV. The difference between the two mechanisms is based on the input power of the second harmonic beam. Given a sufficiently large proportion of second harmonic light to the fundamental, 1:16 or 2:15 (second harmonic pulse energy:fundamental pulse energy), high energy frequency (ω_n is the angular frequency of the n^th^ harmonic) mixing may be observed including: four-wave sum frequency generation ($\omega_{20} = \omega_{17} + \omega_1 + \omega_2$), four wave difference frequency generation ($\omega_{20} = \omega_{21} + \omega_1 - \omega_2$), or high-order sum/difference frequency generation ($\omega_{20} = 18\ \omega_1 + \omega_2$ or ($\omega_{20} = 22\ \omega_1 - \omega_2$)). These processes are typically observed when the intensity of the second harmonic is capable of generating odd harmonics of frequency $2\omega_1$.[121,122]

Additional experiments conducted at second harmonic field intensities equivalent or greater than 50% of the fundamental intensity showed discrepancies in whether harmonic generation was more enhanced at parallel or perpendicular relative polarizations of the second harmonic to the fundamental. The results were conclusive in that a two-color laser field leads to an overall harmonic emission increase over that of a single color generation process. The general increase of harmonic emission from two-color over one-color may be understood in terms of trajectory selection by the driving electric field. A two-color field preferentially selects the short over the long trajectory (time the electron spends in the continuum during step two of the harmonic generation process), and therefore the electron wave packet dispersion is much less, allowing for a higher conversion efficiency. Enhancement of harmonic yield resulting from an electric field with the second harmonic orthogonal to the fundamental is accounted for only when the second harmonic field intensity is as high as the fundamental. These conditions yield a high ionization percentage (confirmed by ADK tunnel ionization calculation), which is a disadvantage for phase-matching. Therefore, when the second harmonic field intensity is on the same order as the fundamental, orthogonally polarized fields will yield the highest XUV photon flux.[118,123]

Even harmonic generation is also observed when the second harmonic is incapable of generating its own harmonics. Under these conditions, harmonics are generated solely as a function of the total electric field (fundamental + second harmonic), where the second harmonic pulse energy is on the order of 1:60 to the fundamental. Sum frequency and difference frequency generation at these pulse energy ratios is unlikely. Even harmonic intensity relative to the odd harmonics of the driver is then dictated by the polarization of the second harmonic field relative to the fundamental. Examining the single atom response at these intensity ratios predicts that parallel polarized electric fields of the fundamental and the second harmonic should yield the most intense XUV flux and smallest ratio between even and odd order harmonics (~1:1). This may intuitively be expected as a small component of the second harmonic electric field parallel to that of the driving field, which should not greatly affect the ionized electron trajectory. This is in contrast to the previously discussed scenario where essentially the even harmonics are being generated orthogonally to the odd harmonics. Driving high harmonics with a weak second harmonic field orthogonal to the fundamental field yields no even harmonics, while parallel polarizations of the fields yield not only an enhancement in the overall harmonic flux, but also a 1:1 ratio between odd and even harmonics as is experimentally demonstrated in Chapter 3.[33,119,124]

It is important to note the impact of generating the even harmonics for XUV transient absorption spectroscopy. Not only does it increase the overall photon flux by generating equal intense even harmonics, but it also increases the spectral coverage through efficient continuum generation. The amount of continuum between harmonics is a direct indication of the number of XUV pulses generated within the driving laser field in the high harmonic generation medium. Each XUV burst interferes with the other pulses in the XUV pulse train, and is evident by the resulting periodic interference pattern observed in the energy resolved high harmonic spectrum. A long driving pulse has many XUV burst and therefore very discrete harmonics while a single isolated XUV burst is of attosecond duration and completely continuous. Even two XUV bursts exhibit a weak interference pattern. By generating even harmonics, the effective number of XUV bursts is reduced in half, leading to enhanced continuum between pulses. An increase in continuum can also be achieved by chirping the incoming pulse thereby limiting the number of optical cycles capable of generating XUV bursts.[124] Ionization gating is also an effective means to bolster continuum generation or create an isolated attosecond pulse.[125] Even harmonic generation itself is also an effective means for obtaining an isolated attosecond pulse for the exact reasons outlined here expanded to optical[126] and double optical gating.[127] Even harmonic generation, though maybe somewhat counter-intuitive, is therefore an effective tool for high harmonic and attosecond spectroscopy.

1.2.6 High Harmonic Scaling

As scientific applications of table-top XUV sources becomes more demanding, it is not only necessary to improve the overall photon flux of XUV sources, but also to increase the spectral coverage, range, and subsequently the bandwidth of these methods. In particular, the creation of ultrashort attosecond pulses requires bandwidth of 10’s of electron volts, while the infant field of zeptosecond pulse generation is just beginning to bud and requires 100’s of electron volts of bandwidth in the XUV, soft x-ray, and hard x-ray regimes to support such pulse durations. While pulse duration is of key interest, sufficient photon flux at these energies is required to conduct reliable spectroscopy to gain insight into fundamental chemical and physical dynamics. Luckily, the three-step single atom response model provides avenues for source improvement along both of these aspects.

The maximum photon energy obtainable from high harmonic generation was discussed in section 1.2.1 as:

$$E_{\max} = 3.17 U_p + IP \tag{1.30}$$

Here, it can be seen that there are two options for increasing the photon energy. The most obvious is the ionization potential (IP) of the target medium. Typical, inert gases are employed for high harmonic generation and have the following ionization potentials: helium (24.58 eV), neon (21.56 eV), argon (15.76 eV), and xenon (12.13 eV). Clearly, changing the target gas is not an effective avenue for increasing the XUV average photon energy into the hundreds of electron volts. Even though changing the IP does not drive the cut-off photon energy substantially higher, it does drive the overall photon flux. Increasing the target ionization potential allows for higher field intensities to be accessed before the electron tunnel ionizes (lower ionization fraction at high intensities), leading to a dramatic enhancement of the kinetic energy gained by the electron in the continuum. This comes at the expense of typically the decrease in the recombination cross section of the returning electron wave packet, i.e. the higher the ionization potential the smaller the ion core. Likewise, by decreasing the ionization potential, the overall XUV photon flux will increase at the expense of photon energy, allowing high photon fluxes to be obtained in the 10-100 eV range.

The second possible avenue for driving the maximum XUV photon energy higher is contained in the ponderomotive potential, the kinetic energy that the electron wave packet gains in the continuum. The ponderomotive potential may be written as:

$$\mathrm{U_p} = 9.33\mathrm{x}10^{-14}\,\mathrm{I_L}\lambda_{\mathrm{L}}^{2} \tag{1.31}$$

where I_L is the intensity of the driving laser centered at a wavelength of λ_L. Obviously, there are two different avenues to pursue in terms of driving E_{max}: increasing the driving laser intensity or wavelength. Since most high harmonic sources employ a commercial Ti:sapphire laser system, it is typically easier to increase the driving laser intensity (changing the focal spot size, the pulse duration, pulse energy), allowing a linear increase in the maximum photon energy until the critical ionization point is reached for phase matching. Increasing the driving laser wavelength is the most effective method for increasing the maximum obtainable photon energy as E_{max} goes as the square of the driving laser center wavelength. Employing an optical parametric amplifier or nonlinear parametric amplifier optical line easily allows conversion of 800 nm to longer wavelength, but at the expense of efficiency. More direct techniques of optical parametric chirped pulse amplification are more efficient, but more costly as well. Additionally, at longer driving wavelengths the single atom emitter efficiency begins to drop as $\lambda^{-5.5}$,[128] indicating that shorter driving lasers lead to an overall increase in high harmonic generation efficiency. This progression is outlined in table 1.1, given that the photon energy and flux for a given set of laser parameters (field intensity, pulse duration, …) for a driving laser remains constant while only the wavelength is adjusted.

Table 1.1: Scaling of XUV photon flux and maximum photon energy with wavelength.

λ_L	E_{max}	**Photon Flux**
> 800 nm	Higher	Lower
800 nm	(Baseline)	(Baseline)
< 800 nm	Lower	Higher

Increasing the wavelength of the driving laser may suffer from a detrimental single atom emitter efficiency scaling, but the transparency of the single atom emitter also increases with wavelength. This allows for high pressures to be employed for the high harmonic target as well as high laser field intensities. Great success has been achieved by the Kapteyn-Murnane labs, in particular, utilizing long wavelength driving lasers and high pressure waveguides at >30 atm of helium gas. Photon energies higher than 1 kiloelectron volt have been realized with a 4 μm driving laser with full phase matching. The bandwidths of the XUV pulses generated by few micron wavelength drivers are capable of supporting zeptosecond pulse durations.[30,31,128,129]

1.3 Wave Packet Formation from Strong-Field Ionization

Wave packets, by their basic definition, originate from the superposition of waves of different frequencies. The phase between each of the wave components of the packet defines the degree of temporal and spatial coherence of the superposition. For a light source, a wave packet is generated by a coherent pulsed source, where the probability of finding a photon from the source is contained within the envelope of the pulse. The superposition of the emitted light waves creates the wave packet, but for a chemical system a wave packet is created by the superposition of the quantum energy states. For atomic and molecular systems, stationary states are given by the eigenstate and eigenenergy solutions of the time-independent Schrödinger equation. Non-stationary states on the other hand are solutions to the time-dependent Schrödinger equation, consisting of the superposition of time-independent energy eigenstates which are known as wave packets. Wave packets may exist, for example, between rotational, vibrational, or electronic states, resulting from the superposition of at least two distinct states. Each quantum particle, such as an electron or proton, may also be treated as a wave packet where the squared amplitude of the wave packet is proportional to the probability of determining a set of complimentary variables at any given point in space and time.[130]

The interaction of an intense laser field with a molecule may facilitate the formation of vibrational wave packets on either excited/ion state potentials or the ground molecular state. The vibrational wave packets may be generated by coherent ionization, potential surface perturbation, or Raman coupling/impulsive driving. Each of these processes proceeds via a different mechanism, but each may occur in coincidence within a strong-field excitation and will be elaborated on here as well in the related experiments to follow.

1.3.1 Impulsive Stimulated Raman Scattering

Coherent vibrational motion may be achieved at field intensities insufficient to ionize a molecular system either by strong-field or multiphoton interactions by impulsive excitation. Simultaneously, impulsive absorption and impulsive stimulated Raman scattering may occur. The former results in the excitation of a molecule to an (or several) excited state(s) resulting in coherent motion due to subsequent transition of the excited probability density to other additional states after propagation on the first excited state, i.e. excitation to an excited state, propagation, excitation to a second excited state, or relaxation/stimulate emission to ground state. Impulsive stimulated Raman scattering results from the pure excitation of ground state vibrational motion due to the action of the applied force of the driving electric field on the molecule. A classical analogy would be the quick compression of a spring attached to two masses by an external force, which would result in the periodic motion of the system.

For describing the Raman excitation process, the total Hamiltonian is given as:

$$\widehat{H} = \widehat{H_0} + \widehat{H_1} + \widehat{H_2} + \cdots \tag{1.32}$$

where $\widehat{H_2}$ relates to the light scattering process by a molecular system with oscillator modes *q* with polarization indices *i,j*. Light scattering by the system is then:

$$\widehat{H_2} = -\sum_{i,j}\sum_{q}\delta\alpha_{ij}(q,t)F_{ij}(-q,t) \tag{1.33}$$

with $\delta\alpha_{ij}(q,t)$ describing the change in polarizability, and the effective force applied to an oscillator mode *q* of a molecule is given as:

$$F_{ij}(q,t) = \frac{1}{8\pi}E_i(q,t)E_j(q,t) \tag{1.34}$$

The impulsive excitation of a vibrational mode of a molecule is clearly proportional to the square of the applied electric field strength and the polarizability of a mode within that field. Examining impulsive excitation in terms of second-order perturbation theory, the contributions of ν_0 and ν_1 within the generated superposition are overstressed in the calculation, leading to a false impression of the structure of the observed quantum beat. In actuality, impulsive stimulated Raman scattering involves a superposition of all populated vibrational energy levels, but in the weak-field limit, contributions from $\nu > \nu_1$ are vanishingly small. This is not the case as the field intensity is increased owing to the $\left|E(q,t)\right|^2$ relation to the impulsive force. As the field intensity is increased, the contribution of higher lying vibrational levels to the superposition composition increases due to population redistribution to those states.[131] The process of redistribution of vibrational state population to higher lying states is well demonstrated for successive impulsive stimulated Raman scattering pump pulses, which is analogous to increasing the overall field intensity given a zero time delay between the pulses.[132] Furthermore, similar Raman pumping may be accomplished by non-resonant chirped adiabatic Raman passage. Chirped adiabatic Raman passage is a method by which the rate of chirp in a Raman pump pulse evolves within its duration such that progressive transfer of population to higher lying vibrational levels is achieved, either causing a population inversion or progressive ladder climbing.[133] Each of these processes lead to a progressive increase in the vibrational energy of a molecule with increasing field intensity beyond the impulsive limit and into the strong-field regime.

1.3.2 Lochfraß Mechanism

The Lochfraß mechanism is a general class of strong-field wave packet formation, implying that the ionization rate is highest where the ionization potential is at a global minimum.[61,70] This could easily be interpreted for field free potentials as well as field-dressed states, where enhanced ionization would dominate. "Lochfraß" is German for "biting corrosion" or more simply "eating a hole away," which in the strong-field ionization regime implies very selective ionization in accordance with the internuclear (R-)separation. Therefore, a portion of the probability density of a molecular state may be selectively depleted. The result is a residual wavefunction which is no longer an eigenstate of the ground state potential Hamiltonian, resulting in wave packet formation. Goll et al. represented the Lochfraß process in the time-dependent Schrödinger equation via an imaginary potential, $W(R,t)$, equal to the ionization rate due to a strong static laser electric field:

$$\left(H_0 - i\frac{W(R,t)}{2}\right)\Psi(R,t) = i\frac{\partial}{\partial t}\Psi(R,t) \tag{1.35}$$

where $\Psi(R,t)$ is the time-dependent nuclear wavefunction. If W is R-independent, then $\Psi(R,t)$ remains an eigenfunction of H_0 after ionization, but since W is R-dependent a non-stationary state is formed.[70] For the case of H_2/D_2, the minimal ionization rate is at large internuclear separations due to the geometry of the neutral potential surface relative to the ion, and consequently the ground state vibrational wave packet is formed at the inner turning point, i.e. the vibrational amplitude is initially localized at the outer turning point. This represents coherent wave packet dynamics generated by strong-field ionization at $R \neq R_e$ in the fastest molecular system, and illustrates the breakdown of traditional Franck-Condon ionization in the strong-field regime.[134]

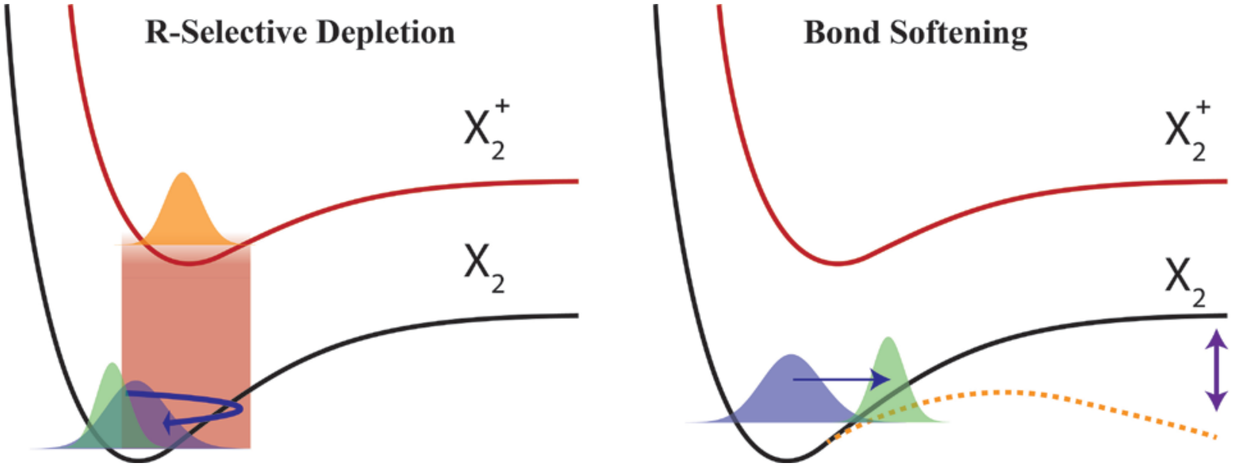

Figure 1.10: Illustration of the difference between R-selective depletion via ionization (left) and bond-softening (right) for ground state wave packet formation.

Lochfraß ionization was determined to be the dominant mechanism for wave packet formation in "hot" Boltzmann ensembles since it is a dissipative effect, preferentially ionizing at higher vibrational states.[135] Typically, a large manifold of populated vibrational states is detrimental to the formation of strongly coherent, localized wave packets. The selective ionization of higher lying vibrational states effectively reduces the average vibrational state population distribution energy, concentrating the population to lower lying states. Experiments also showed that increasing field intensity extends the vibrational state population median reduction, localizing the vibrational amplitude and narrowing the range of internuclear separations explored.[136] Bond-softening predicts a similar trend in the reduction of higher vibrational state populations with field intensity, except there is no R-dependence on the ionization rate except for a motion of the overall probability density with the time evolving deformation of the molecular potential energy surface with the field interaction.[62] These findings are contrary to the trend of impulsive stimulated Raman scattering, which tends to increase the vibrational energy of a molecule on average. Raman scattering is concurrently driving vibrational state populations to higher lying levels (progressively so, as field intensity increases), while Lochfraß is selectively ionizing the higher lying states.

1.3.3 Critical Internuclear Separation Ionization

By definition, critical internuclear separation ionization (R-critical) requires field perturbation of the active potentials, i.e the occupied states and the CREI accessed states, by Stark shifting. The magnitude of the Stark shifting of the potentials is determined by the strength of the perturbing electric field. The Stark shifting of the potentials facilities enhanced ionization at elongated molecular geometries, the hallmark of R-critical ionization. The R-critical distance in angstroms may be calculated according to the ionization potential in electron volts of a molecule as:[137]

$$R_c = \frac{40.7}{I_p} \qquad (1.36)$$

determined from the CREI condition:

$$V_{out}\left(R_c\right) \leq V_{in}\left(R_c\right) \leq \varepsilon_+\left(R_c\right) \qquad (1.37)$$

where $V_{out}\left(R_c\right)$, $V_{in}\left(R_c\right)$, and $\varepsilon_+\left(R_c\right)$ are the inner, outer, and Stark shifted barriers, respectively. Neglecting stark shifting of the upper lying state yields R-critical as $3/I_p$, defining electron localization within the two center Coulomb potential due to insignificant electron tunneling between the wells.

Extensive studies have been conducted on I_2 exposed to an intense laser field and the resulting electronic ground state wave packet.[56,68,83,135,136,138] The ground state wave packet generated via strong-field ionization of I_2 $\widetilde{X}$ to the I_2^+ $\widetilde{A}\,{}^2\Pi_{u,3/2}$ state was subsequently probed via a second strong-field ionization interaction to the directly asymmetric dissociative I_2^{2+} surface. From the kinetic energy release of the ion, the average intermolecular distance and maximum displacement were retrieved, as well as the period of the wave packet. The formation of the vibrational wave packet was attributed to Lochfraß R-critical ionization in accordance with the retrieved phase factor. The origin of the superposition was further confirmed by projection of the ground state wave packet I^{2+} signal onto a time dependent positional subspace determined by a weighting of the standard molecular hydrogen potentials. [48, 60, 72, 104-106] These experiments and calculations further supported the D_2 results of Ergler et al. that bond softening does not contribute significantly to coherent vibrational motion.[139] Significant contribution of bond-softening to the ground state wave packet would lead to a weighted phase shift of $\pi/2$, which was observed to be minor in both experiments. Furthermore, the R-dependent ionization of I_2 was investigated with a vibrational population distribution centered at higher lying levels ($\nu=33$) to engage a larger range of internuclear separations. Subsequent ionization from the HOMO, HOMO-1, and HOMO-2 revealed preferential ionization of the inner orbitals, with preference to the σ orbitals aligned with the laser electric field at large R over the π type orbitals. No evidence of R-selective ionization was observed beyond R-critical.[66,140]

An additional effect of enhanced ionization on the vibrational state distribution after interaction with the strong-field results from the counterpoint of bond-softening (barrier suppression by the field interaction), bond hardening. If a molecular potential may be suppressed, it may also be enhanced as is observed in high harmonic generation within the three step-model as illustrated in Fig. 1.11.[58,62] This is the basis for enhanced ionization and CREI, where the higher potential surface is suppressed. After population transfer at the critical internuclear separation, the excited state barrier is heighted a quarter of an optical cycle later, hardening the bond. At this phase of the electric field oscillation, it is possible for vibrational trapping to occur.[65] This effect is typically observed to form stable trapped populations when the laser field interaction is longer than several vibrational periods of the molecule, i.e. for hydrogen (vibrational period of ~ 11 fs) a 100 fs, 10^{13} W/cm^2 laser pulse generates stable, bond-hardened vibrational populations after the field interaction, while a 50-fs pump does not. Concurrently, bond-softening results in molecular dissociation at such pulse duration and intensities.

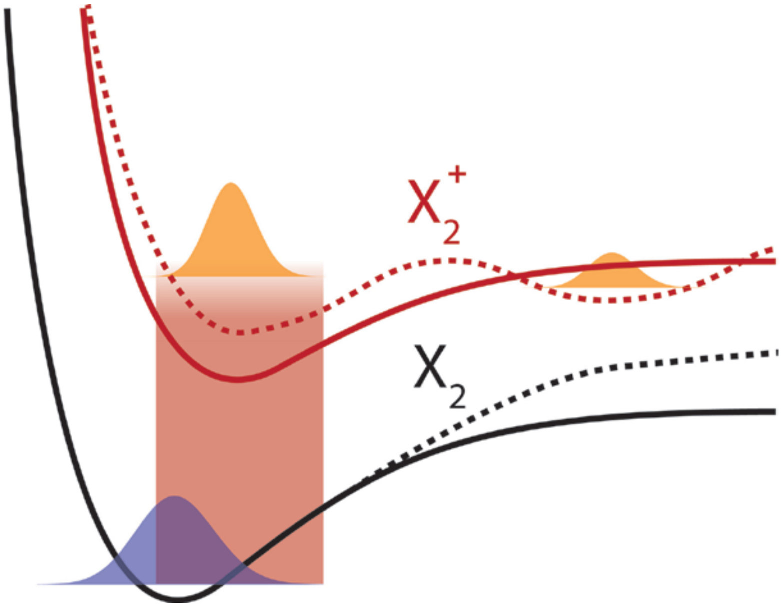

Figure 1.11: Illustration of vibrational trapping from the interaction of a diatomic molecule with a strong laser field. Field intensity dictates the location of the minima produced allowing vibrational trapping during the field interaction, which subsequently populates high lying vibrational states of the ion after exposure.[65]

1.4 Transient Absorption Spectroscopy

Spectroscopy of time-dependent process is an invaluable tool for the investigation of chemical and physical dynamics, facilitating comprehension of fundamental processes in nature otherwise inaccessible to frequency resolved techniques. Transient absorption spectroscopy affords experimentalists the ability to observe dynamics in real-time, limited only by the spectral and temporal resolution of their instruments. Early absorption techniques with limited temporal resolution still permitted investigation of kinetic processes in chemistry due to the inherent sensitivity of the absorption of light at a given wavelength to the concentration of a chemical species.[141] Here, a description of absorption spectroscopy in terms of the Beer-Lambert law is presented, followed by brief explanations of dynamic transient absorption spectroscopy as pioneered by the group of Richard Mathies and the development of femtosecond XUV transient absorption spectroscopy by the Leone group.

1.4.1 Absorption Spectroscopy

Absorption spectroscopy is based on the Beer-Lambert law for the transmission of light at a particular wavelength through a sample of a given length containing a concentration of an analyte with a given cross-section for absorption. The theory for the exponential absorption of light absorption related to cross-section and path length was determined by Pierre Bouguer in the early 1700's, but was attributed to Johann Lambert, who cited Bouguer's work. Later, the theory of light absorption was extended by August Beer to include the sample concentration. The principle is simple; the more absorbate of a given wavelength that is encountered during the propagation of light through a sample, the less light is likely to emerge from the sample. This is illustrated in figure 1.12:

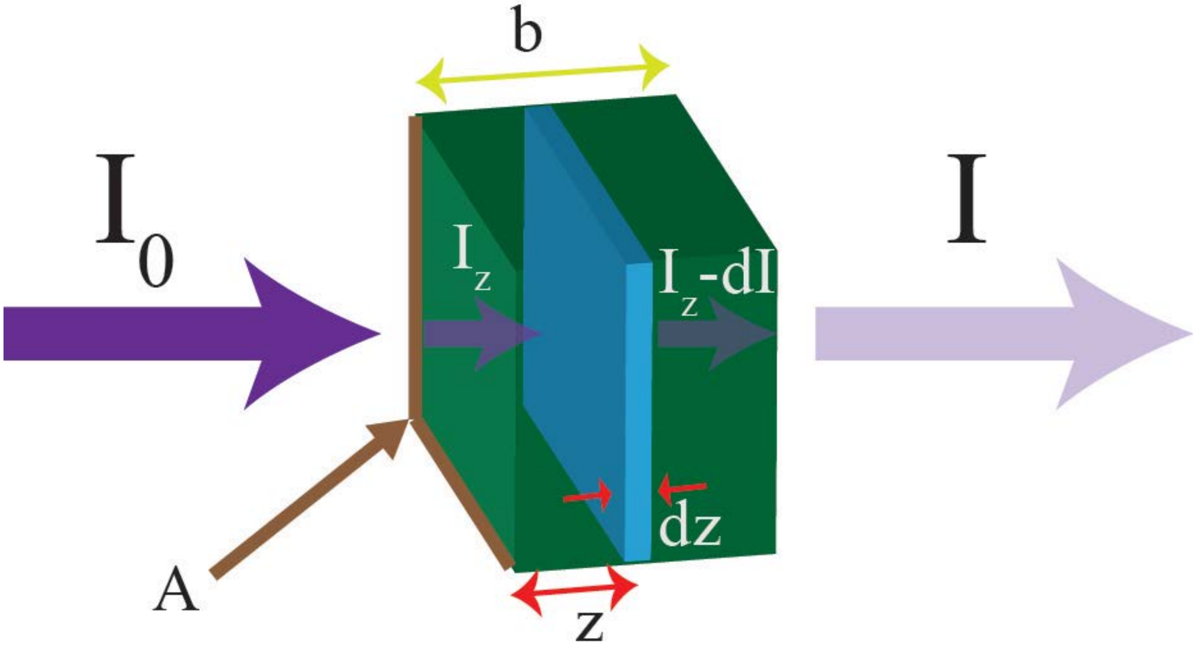

Figure 1.12: Typical absorption schematic according to the Beer-Lambert Law. Initially, radiation of intensity I_0 is incident on a sample of length b and total area A. For a subsection of the sample of width dz, z deep into the sample along the propagation axis of the incident light (arriving at z now with intensity I_z), a certain amount of light (dI) is absorbed by the sample ($n(z)$ particles) with absorption cross section σ. Finally, the light emerges from the sample with intensity I.

Absorption by a sample may be derived starting with a small subsection of the total sample. Given that light of initial intensity I_0 is incident on a sample of interaction length b, over an incremental section dz, dI light is absorbed from the initially incident light intensity, I_z (at some position (z) within the sample such that some light has already been absorbed from I_0), on the subsection of area A:

$$\frac{dI}{I_z} = -\sigma * n(z) * dz \tag{1.38}$$

The total number of absorbers illuminated by the incident light source within the subsection of volume Adz is $n(z)$ and each absorber has a cross-section for absorption of σ. Then, integrating over the total volume of the sample illuminated by the light source the total change in absorption may be calculated:

$$\int_{z=0}^{z=b}\frac{dI}{I_z}=-\int_{z=0}^{z=b}\sigma*n(z)*dz \tag{1.39}$$

$$\ln[I]-\ln[I_0]=\ln\left[\frac{I}{I_0}\right]=-\sigma*n_{eff}*b \tag{1.40}$$

Here, the effective number density, n_{eff}, accounts for the pressure gradient encountered in gas phase experiments across the aperture of the target cell. Essentially, n_{eff} reflects the total analyte molecules along the path length of the incident light, which is more accurate than the absolute number density. The total absorbance of the sample in terms of the incident and transmitted light intensities is then:

$$Absorbance=-\ln\left[\frac{I}{I_0}\right]=\sigma*n_{eff}*b \tag{1.41}$$

where transmittance is given as:

$$Transmission=e^{-\sigma*n_{eff}*b} \tag{1.42}$$

The optical density of a sample may then be written as:

$$OD_{measured}(E)=-\log_{10}\left[e^{-n_{eff}\sigma(E)b}\right] \tag{1.43}$$

By utilizing the Beer-Lambert law optical density in base$_{10}$ a direct comparison may be made between the absorbed light and the incident light, i.e. if a sample of a given density and absorption cross section initially has an optical density of 0.5 and subsequently has an optical density of 0.25 after some perturbation, it may be said that 50% of the population was removed from its initial state by the perturbation. Therefore, absorption spectroscopy provides a unique method for monitoring chemical dynamics in real-time given sufficient temporal resolution relative to the investigated phenomena.

1.4.2 Dynamic Non-Stationary State Transient Absorption Spectroscopy

Richard Mathies of the University of California, Berkeley, originally pioneered the field of dynamic white light absorption spectroscopy with femtosecond sources in the late 1980's and early 1990's. Together with Thomas Pollard and Soo-Y. Lee, a large collection of literature was produced relating to the theory of dynamic absorption and the experimental implementation for the study of Bacteriorhodopsin.[18,142,143] The technique was made possible through the large spectral width of the ultrafast optical pulses, delivering unprecedented temporal and spectral resolution. Previously, narrow (essentially monochromatic) wavelength sources had been employed in the investigation of chemical dynamics, granting access to the dynamics only by monitoring the change in absorption at a defined energy in time, preventing observation of the evolving absorption wavelength in real-time. Dynamic absorption spectroscopy allowed a physically intuitive approach to interrogating wave packet dynamics in accordance with time-dependent quantum coherence theories. Initial experiments involved several excitation pathways, including impulsive stimulated Raman scattering, transition to the excited state and stimulated emission, resonance Raman, and nonlinear absorption. As a result, perturbative density matrix theory for a third-order susceptibility of a multilevel system and four-time correlation functions are required for interpreting the dynamic absorption spectra when the pump and the probe pulses are overlapped. If the pump and probe pulse are well separated in time, the third-order perturbation theory polarization response may be recast to a first-order interpretation of the probe interacting with the induced polarization in the analyte by the pump, which is quite tractable. In this way, a direct connection may be made between the dynamics and the change in the probe pulse spectrum and intensity. Figure 1.13 shows a for a ground state vibrational wave packet primarily composed of a beat between the first and second vibrational levels of a 1-dimensional harmonic oscillator. Clearly, an oscillation in both frequency and amplitude of the dynamic absorption may be observed and directly correlated to the motion of the ground state probability density with time.

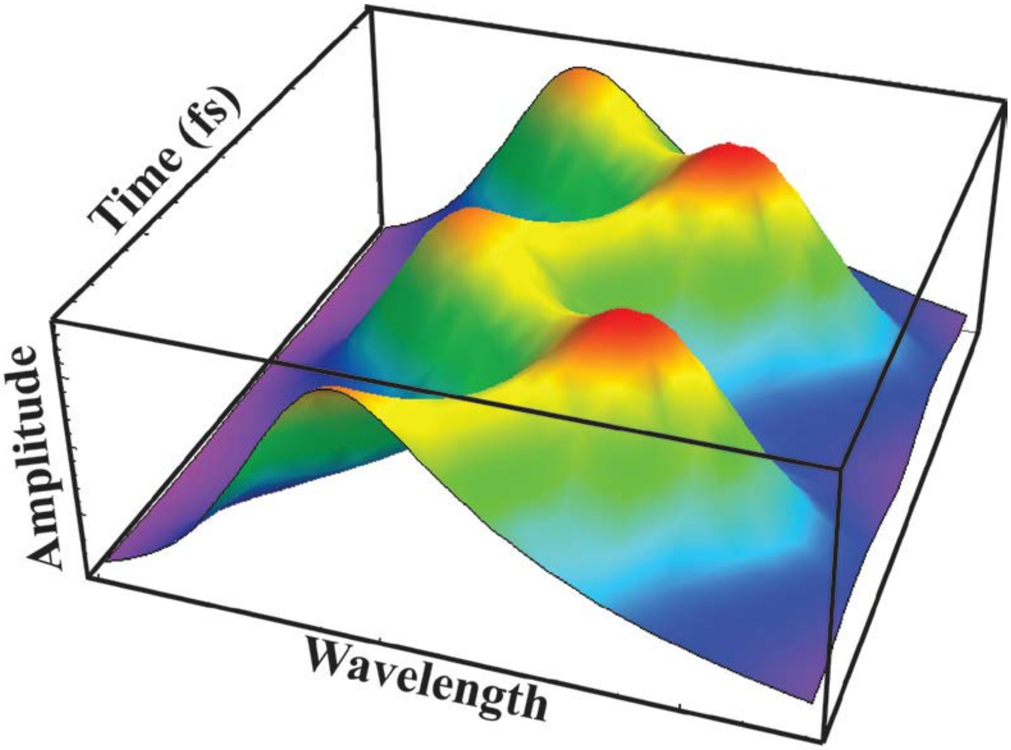

Figure 1.13: Simulated dynamic absorption spectrum of the ground state of a model 1-dimenisional harmonic oscillator system following preparation of a wave packet primarily composed of a beat between the first and second vibrational levels. Oscillations can clearly be observed in the amplitude and wavelength of the absorption in time.

Femtosecond dynamic absorption exemplified for the first time the ability to conduct direct, real-time measurements of chemical dynamics via time evolving probability densities. By employing a broadband probe, information on the ground state, excited state, or even previously inaccessible transition states along the potential surfaces, which govern reactivity, may be detected and interpreted directly. The direct detection and preparation of nuclear wave packets allows the investigation of vibrational superpositions and their interplay with reaction dynamics across multiple electronic surfaces, helping in the elucidation of the role of the potential energy landscape, such as intersystem crossings and conical intersections, in chemical processes.

1.4.3 Femtosecond Extreme-Ultraviolet Transient Absorption Spectroscopy

XUV absorption studies allow insight into the complex coupled ionization dynamics resulting from excitation/ionization by a high energy photon, including Auger decay and autoionization. These XUV studies facilitate the analysis of fast correlated electron dynamics at unprecedented temporal resolution. The examination of the autoionization of oxygen as a function of internuclear separation revealed a delay in the ionization process of superexcited states created by an ultrafast XUV pump until the O_2 molecule reaches a bond length of 30 Å, which was confirmed by state coupling calculations following XUV absorption.[144] Of recent importance has been the understanding of nonlinear x-ray absorption at Free-Electron laser facilities such as Stanford's Linac Coherent Light Source, which is capable of field stripping atoms[145,146] and molecules[147] from inner core levels due to successive sequential and non-sequential x-ray absorptions accompanied by cascading Auger decay. Interestingly enough, simple rate equations tend to account for the intense x-ray interaction and the main features measured in the charge distributions. The rate equations include Hartree-Fock-Slater type calculations to account for the one-photon absorption cross-section including temporal and focal averaging as well as the Auger decay process. Additional theoretical formalism has been developed to distinguish the two photon absorption processes that result in either the formation of double core-holes or those associated with a core-hole formation followed by immediate Auger decay.[148]

The group of Stephen R. Leone has developed in recent years a novel application of dynamic non-stationary state absorption spectroscopy to femtosecond XUV sources. XUV absorption up until that point had focused on employing high harmonic pulses as an excitation or ionization pump method to investigate highly excited states or to quickly ionize an analyte. By employing XUV light as a probe of dynamics, the elemental and chemical specificity of the source was utilized to its full advantage. Prior to the development of XUV transient absorption spectroscopy, absorption experiments of this type were limited to synchrotron facilities with large, scanning monochromators and picosecond time resolution. Initially, high-order harmonic absorption spectroscopy was applied to measuring the $M_{2/3}$ edge absorption features of first-row transition metal thin films and even up into the keV range.[149,150] At this point, XUV absorption stood to bridge the dynamic spectroscopic capabilities of transient, non-stationary techniques with the elemental specificity of XPS.[151]

Broadband absorption first and foremost permits XUV absorption spectroscopy to be conducted instantaneously by spectrally dispersing the probe light after interaction with the sample, eliminating the need for a monochromator before the interaction region. Also, by accessing the core-level states of atoms and molecules, elementally specific information can be acquired due to the large separation in the absorption features, even between elements of similar electronic structure, i.e. the iodine $^2P_{3/2} \rightarrow {}^2D_{5/2}$ absorption line is at 46.2 eV[152] and the Xe^+ $^2P_{3/2} \rightarrow {}^2D_{5/2}$ transition is at 55.4 eV.[153] Moreover, by promoting core electrons to unoccupied valence states (possibly dynamically vacated) information may be realized about the chemical bonding environment, such as vibrational dynamics or the oxidation state of the analyte, as demonstrated in the following experiments.

For an XUV transient absorption measurement the optical density may be determined in a similar fashion as presented in section 1.4.1, except additional terms must be included that incorporate the resolution of the XUV spectrometer:

$$OD_{measured}(E) = -\log_{10}\left[e^{-n_{eff}\sigma(E)b} * \sqrt{\frac{4*\ln[2]}{\pi*\Delta^2}} * e^{\frac{-4*\ln[2]*E^2}{\Delta^2}}\right] \tag{1.44}$$

where Δ is the spectral resolution of the spectrometer, independently measured as a convolution of a Gaussian function with the lifetime of an optical transition, and E is the photon energy. The change in optical density ($\Delta OD_{measured}(E,\Delta t)$) may then be measured by collecting two spectra, one when the pump is 'on' and then one when the pump is 'off', yielding:

$$\Delta OD_{measured}(E,\Delta t) = -\log_{10}\left[\frac{I_{on}(E,\Delta t)+I_b}{I_{off}(E,\Delta t)}\right] \tag{1.45}$$

The specifics of XUV transient absorption spectroscopy in relation to the instrumental apparatus employed for the following experiments are discussed in more detail in Chapter 3.

The technique of XUV transient absorption has successfully been implemented in several experiments prior to those presented here, with the intent of demonstrating the technique as a flexible platform for interrogating a variety of physically relevant scientific problems previously inaccessible. The majority of the effort was expended in the group of Stephen Leone by Zhi-Heng Loh, first investigating the strong-field ionization of xenon and the resulting quantum state distribution of the hole in the 5p ($^2P_{3/2,1/2}$) state as probed from the 4d core level at 55.4 and 56.1 eV. It was determined that the strong-field generated a vacancy in the 5p state that is partially aligned with the ionizing laser field as observed through the anisotropy in the $^2P_{3/2} \rightarrow {}^2D_{5/2}$ transition.[20] Next, the femtosecond induced transparency and absorption of XUV light in helium was observed by an Aulter-Townes doublet resulting from the coupling of the He 2s2p ($^1P_0$) and $2p^2$ (^1S_e) double excited states monitoring the Fano resonance profile at 60.15 eV.[21] Next, the strong-field dissociative ionization of dibromomethane was investigated, revealing the ionization dynamics and products resulting from interaction with a 10^{14} W/cm^2 pump pulse. Dibromomethane was observed to be metastable even after being double ionized, while the singly charged species dissociated on the 130 fs and 75 fs timescale for the formation of atomic ground and spin-orbit excited state bromine, respectively.[22] Lastly, in collaboration with the Ferenc Krausz group in Munich at the Max Planck Quantum Institute, the attosecond spin-orbit wave packet from the strong-field ionization of krypton was observed to have the expected 6.3-fs period by XUV transient absorption; this is the first direct, real-time observation of valence electron motion.[24]

Chapter 2

Theory of Dynamic Extreme-Ultraviolet Transient Absorption Spectroscopy of Strong-Field Dynamics

The investigation of chemical dynamics in the strong-field regime by femtosecond XUV transient absorption branches into two distinct fields of theory: strong-field atomic/molecular interactions and XUV absorption. Since the advent of high harmonic generation and above-threshold ionization in early 1990's, extensive research has been conducted into strong-field dynamics, some of which have been presented in Chapter 1. One dynamic and experiment of particular relevance to the investigations presented here is the strong-field ionization of an inert atomic gas (krypton/xenon) and subsequent alignment of the m_j quantum state populations. Through the investigation of the m_j alignment phenomena, a theoretical framework was established for the XUV probing of strong-field generated coherences on the attosecond timescale, which provide the theoretical structure for determining the internuclear-separation-dependent XUV transient absorption and strong-field formation of ground state vibrational wave packets investigations presented here.

Strong-field ionization dynamics, including ground state vibrational wave packet formation, has been the focus of much theoretical research and modeling.[61,64,71,82,148,154-157] A possible avenue for determining the dynamics of some strong-field responses focuses on the impact of ionization rates through the application of Keldysh[49] and Ammosov-Delone-Krainov (ADK)[50] tunneling rates formulations. The effect of strong-field ionization on the resulting quantum state distribution of an atomic ion was principally outline within ADK theory by Robin Santra. Successive one-electron models employing a square-integrable, flexible finite-element basis set utilizing a complex absorbing potential demonstrate that the uncoupled m_l, m_s basis is inappropriate for describing the resulting Kr^+ states populated by strong-field ionization. Therefore, the spin-orbit interaction is revealed to be necessary to accurately account for the ion population distribution, but most importantly indications were presented for time resolved experiments in the fs and sub-fs regime, paving the way for direct monitoring of electron dynamics resulting from strong-field ionization.[20,24,156]

The initial experimental investigation of quantum state alignment was conducted by the group of Linda Young at the Advanced Photon Source synchrotron.[158] Successive table-top experiments by the Leone lab confirmed the orbital alignment of strong-field ionized atoms, employing xenon as the target and femtosecond XUV transient absorption as the probe.[20] This was the first table-top femtosecond XUV transient absorption experiment utilizing a high-harmonic source and demonstrated the experiment's temporal and spectral capabilities.[19] This was followed by a series of experiments in helium[21] and dibromomethane,[22] which culminated in the attosecond XUV transient absorption of the electronic spin-orbit wave packet generated by few-cycle strong-field ionization of krypton.[24] Strong-field ionization calculations recast to include multichannel coherences[155] coupled with the previous calculated polarization response of dynamic absorption spectroscopy[143] allows the direct determination of transient absorption features in the XUV domain.

For high harmonic core-level spectroscopy, a detailed theoretical model for the ultrafast XUV transient absorption of attosecond dynamics has been outlined by Santra, Yakovlev, Pfeifer, and Loh.[159] Though the theory for XUV transient absorption is outlined in order to account for few-cycle electron dynamics, it may easily be extended to the femtosecond regime for vibrational wave packets. Essentially, the XUV transient absorption signal boils down to the sub-cycle polarization response of the target medium in the strong-field dictated by the time varying electronic dynamics.[159] A time-dependent absorption cross section may then be elucidated, and thereby the XUV transient absorption. This stems from the original formulation by Pollard and Mathies in which dynamic white light absorption was described as a function of the polarization response of the target medium due to the time-dependent vibrational dynamics. For the attosecond investigation of the strong-field ionization of krypton with a few-cycle pulse, the full first-order XUV absorption cross section, $\sigma^{(1)}(\omega)$, was determined to be:[159]

$$\sigma^{(1)}(\omega)=4\pi\frac{\omega}{c}\mathrm{Im}\left\{\begin{array}{l}
\dfrac{\left|\left\langle 4p_{3/2}^{-1}\right\|D\left\|3d_{5/2}^{-1}\right\rangle\right|^2}{I_{3d_{5/2}}-i\dfrac{\Gamma_{3d}}{2}-I_{4p_{3/2}}-\omega}\left[\rho_{3/2,3/2}^{(3/2)}\dfrac{2}{15}+\rho_{3/2,3/2}^{(1/2)}\dfrac{1}{5}\right]\\
+\dfrac{\left|\left\langle 4p_{3/2}^{-1}\right\|D\left\|3d_{3/2}^{-1}\right\rangle\right|^2}{I_{3d_{3/2}}-i\dfrac{\Gamma_{3d}}{2}-I_{4p_{3/2}}-\omega}\left[\rho_{3/2,3/2}^{(3/2)}\dfrac{3}{10}+\rho_{3/2,3/2}^{(1/2)}\dfrac{1}{30}\right]\\
+\dfrac{\left|\left\langle 4p_{1/2}^{-1}\right\|D\left\|3d_{3/2}^{-1}\right\rangle\right|^2}{I_{3d_{3/2}}-i\dfrac{\Gamma_{3d}}{2}-I_{4p_{1/2}}-\omega}\left[\rho_{1/2,1/2}^{(1/2)}\dfrac{1}{3}\right]\\
+\dfrac{1}{3\sqrt{10}}\left\langle 4p_{3/2}^{-1}\right\|D\left\|3d_{3/2}^{-1}\right\rangle\left\langle 4p_{1/2}^{-1}\right\|D\left\|3d_{3/2}^{-1}\right\rangle *\\
\left[\dfrac{\rho_{3/2,1/2}^{(1/2)}\left(t_{XUV}\right)}{I_{3d_{3/2}}-i\dfrac{\Gamma_{3d}}{2}-I_{4p_{1/2}}-\omega}+\dfrac{\left[\rho_{3/2,1/2}^{(1/2)}\left(t_{XUV}\right)\right]^*}{I_{3d_{3/2}}-i\dfrac{\Gamma_{3d}}{2}-I_{4p_{3/2}}-\omega}\right]
\end{array}\right\} \tag{2.1}$$

where $\left\langle 4p_j^{-1}\right\|D\left\|3d_j^{-1}\right\rangle$ is the reduced dipole matrix element[160] with total angular momentum *j*, $\rho_{j,j'}^{(m)}$ is the hole population between j and j' with any coherence in the system given by the off-diagonal, time-dependent elements of the density matrix where $j \neq j'$, Γ_{3d} is the decay width of the core-hole state in the 3d orbital, I_{4p_j} is the ionization potential of the *4p_j* state, and ω is the frequency of the XUV pulse. The final term of the XUV absorption cross-section is the sum of both the absorptive and dispersive lineshape terms, reliant on the time-dependent $\rho_{3/2,1/2}^{(1/2)}(t_{XUV})$ coherence. Though this formulation is robust, it is too cumbersome to employ directly in the formulation of vibrational dependent XUV transient absorption calculations of a molecular system, i.e. there is no direct method to obtain the reduced dipole matrix elements for the core-hole excitation of various molecular states, the linewidth is equally undetermined for molecular ions, and the angular momentum algebra for heavy molecular systems is not as straight forward as in the atomic case.

All is not lost. Equation 2.1 clearly shows that the time-dependent XUV absorption spectrum is simply a function of a time-dependent absorption feature (there, the evolving spin-orbit state distribution) and the static absorption features. Therefore, the model may be overhauled into a simpler form, neglecting the quantitative detail of the formulation in exchange for qualitative analysis of time-dependent XUV absorption features.

As mentioned earlier, to calculate the time-dependent XUV transient absorption signal of a ground state vibrational wave packet the core-hole excited state transition energy and strength must be determined at all internuclear separations sampled by the dynamic to be probed, and the time-dependence of the vibrational wave packet created by the strong-field interaction must also be unraveled. NWCHEM 6.1[161] has recently incorporated Restricted Excitation Window Time-Dependent Density Function Theory (REW-TD-DFT),[162] which allows the calculation of core-hole excited states with minimal computational resources. By scanning the internuclear separation along the coordinate of a molecule and conducting successive REW-TD-DFT calculations, the general shape of the core-hole excited state may be solved relative to the ground state.

Of particular importance to this research is the interaction of the strong-field with molecular potentials and the ensuing ionization mechanisms relevant to ground state vibrational wave packet formation including bond-softening, R-Critical ionization, and Lochfraß. Bond softening has been discussed in Chapter 1 as a cycle-averaged suppression of the ground state molecular binding potential at internuclear separations longer than the equilibrium geometry.[59,63] This leads to the ground state probability density moving toward longer bond lengths within the strong-field pulse. When the strong-field is no longer present, the ground state potential returns to the field-free shape causing coherent vibrational motion as a result of the displaced probability density. R-critical ionization and the Lochfraß mechanism invoke an ionization pathway for vibrational wave packet formation but are modeled within two different theoretical frameworks of ionization as a function of bond length in diatomics. R-critical involves enhanced ionization as a result of the field coupling of the ground state potential surface to a higher lying repulsive state. The coupling of these two states results in a shifting of the states akin to CREI,[163] allowing ionization to occur predominately at large internuclear separations. This results in a deformation of the vibrational probability density of the ground state, localizing the density and creating a wave packet as a result of the coherent ionization mechanism.[164] R-critical ionization always results in wave packet formation at internuclear separations smaller than the equilibrium geometry as a result of the field depletion of vibrational state population at large separation. The Lochfraß ionization mechanism considers only the ionization rate with internuclear separation calculated from the field unperturbed potentials, i.e. the potential energy curves of the ground and ion states govern the ionization potential of each molecular orbital.[61,70,71] Therefore, each molecule's potential energy landscape must be treated as a unique case when determining the initial localization of the strong-field ionization generated ground state vibrational wave packet. These mechanisms are not inherently different, but simply discern between the degree of coupling between the driving laser field and the various potential energy curves with respect to the impact on the ionization rate with bond length. The implementation of quantum Volkov states,[165] which directly incorporate the electric field coupling into the molecular potentials presents the most accurate formalism for interpreting strong-field dynamics, but is inherently computationally intensive. The wave packet formation and time dependence may also be found by conducting novel tunnel ionization calculations via Ammosov-Delone-Krainev (ADK) theory incorporating internuclear (R-)separation and vibrational level population sensitivity[166] (R_v-ADK).

By combining these two computational methods, REW-TD-DFT and R_v-ADK ionization, the total XUV transient absorption signal may be calculated. The REW-TD-DFT results provide the XUV absorption signal at all R according to the probability density distribution on the ground state found by R_v-ADK ionization modeling coupled with the standard evolution operator at all times, probed relative to the non-coherent initial probability density on the ground state. This formulation provides a simple, qualitative determination of the XUV transient absorption signal at all probed times.

In this chapter, the basic framework for calculating the femtosecond XUV transient absorption signal of ground state vibrational wave packets in Br_2 generated by strong-field ionization is described. The basic solutions for a Morse potential is presented first, which is later employed in the calculation of the tunnel ionization rates according to the R_v-ADK theory derived here. The basic application of REW-TD-DFT is then explained in terms of the core-hole excitation of molecular bromine at various internuclear separations. The combination of R_v-ADK and REW-TD-DFT for the modeling of ground state vibration wave packet formation and subsequent detection by XUV transient absorption spectroscopy is then demonstrated for bromine.

2.1 Morse Potential

The solutions for a Morse oscillator[167] provide a convenient method for the determination of the vibrational wavefunctions of a diatomic, which is later utilized in tunnel ionization calculations of Br_2. The Morse potential, an adequate representation of the anharmonicity of ideal diatomic molecules, is given as:[168]

$$V(R)=D_e\left(1-e^{-\alpha(R-r_e)}\right)^2 \tag{2.2}$$

where D_e is the well depth (defined relative to the dissociation energy, different from the dissociation energy defined relative to the zero-point energy, D_0), r_e is the equilibrium bond length, and α is related to the force constant, k_e, of the bond:

$$\alpha=\sqrt{\frac{k_e}{2D_e}} \tag{2.3}$$

The eigenvalues and eigenvectors of the Morse potential may then be determined by solving the Schrödinger equation:

$$\left(-\frac{\hbar^2}{2m}\frac{\partial^2}{\partial r^2}+V(R)\right)\psi_\nu(R)=E(\nu)\psi_\nu(R) \tag{2.4}$$

yielding eigenvalues:

$$E(\nu)=-\frac{a^2\hbar^2}{2m}\left(\lambda-\nu-\tfrac{1}{2}\right)^2 \tag{2.5}$$

where:

$$\lambda=\frac{\sqrt{2mD_e}}{a\hbar} \tag{2.6}$$

and eigenvectors:

$$\psi_\nu(R)=N_\nu z^{\lambda-\nu-\frac{1}{2}}e^{-\frac{1}{2}z}L_\nu^{2\lambda-2\nu-1}[z] \tag{2.7}$$

with:

$$z=2\lambda e^{-\alpha(R-r_e)} \tag{2.8}$$

and:

$$N_\nu=\nu!\sqrt{\frac{\alpha(2\lambda-2\nu-1)}{\Gamma(\nu+1)\Gamma(2\lambda-\nu)}} \tag{2.9}$$

given $\Gamma(x)$ is the gamma function of x, and $L_\nu^{2\lambda-2\nu-1}[z]$ is a Laguerre polynomial:

$$L_\nu^{2\lambda-2\nu-1}[z]=\frac{\Gamma\left[(2\lambda-2\nu-1)+\nu+2\right]\Big/\Gamma\left[(2\lambda-2\nu-1)+2\right]}{\Gamma[\nu+1]}\,{}_1F_1\left[-\nu,(2\lambda-2\nu-1)+1,z\right] \tag{2.10}$$

where ${}_1F_1\left[-\nu,(2\lambda-2\nu-1)+1,z\right]$ is a hypergeometric function.

The vibrational wavefunction for diatomic molecular bromine may then be simulated by employing spectroscopic determined values for the anharmonic terms of the potential presented in table 2.1:

Table 2.1: Br_2 and Br_2^+ potential parameters[169-171]

	$Br_2^{79\text{-}81}$ $\tilde{X}$ $^2\Sigma^+_g$	**Br_2^+ $^{79\text{-}81}$ $\tilde{X}$ $^2\Pi_{3/2,g}$**	**Br_2^+ $^{79\text{-}81}$ $\tilde{X}$ $^2\Pi_{1/2,g}$**	**Br_2^+ $^{79\text{-}81}$ $\tilde{A}$ $^2\Pi_{1/2,g}$**
D_0 (cm^{-1})	15893	26292	23472	9672
$\chi_e\omega_e$ (cm^{-1})	1.064	1.13	1.10	1.31
ω_e (cm^{-1})	323	364	361	204
r_e (Å)	2.28	2.18	2.18	2.54

The energies of each vibrational state may be directly determined from the spectroscopic values given:

$$E(\nu)=\hbar\omega_e\left(\nu+\tfrac{1}{2}\right)-\hbar\omega_e\chi_e\left(\nu+\tfrac{1}{2}\right)^2 \qquad (2.11)$$

2.2 Internuclear-Separation-Dependent Ammosov-Delone-Krainov Theory

Tunnel ionization rates were initially calculated in terms of a static applied electric field to helium by Keldysh in the 1960s. As was discussed in Chapter 1, tunnel ionization involves the distortion of the Coulomb potential proportional to the strength of the applied electric field such that the ionization barrier of a valence electron is suppressed, allowing the electron to escape into the continuum. Faisal[172] and Reiss[173] later expanded the tunnel ionization calculations to determine the final state of the electron after ionization via the incorporation of a translation operator into the Schrödinger equation and exclusion of the effect of the atomic Coulomb potential on the final state of the tunneled electron (the strong-field approximation), respectively. Perelomov, Popov, and Terent'ev then extended the tunnel ionization model to average the ionization rate over multiple electric field cycles for an optical laser in the case of the ionization of hydrogen,[174] which was finally further extended by Ammosov, Delone, and Krainov to include complex atomic systems, yielding ADK theory.[50,51] Later, ADK theory was expanded to cover molecular tunnel ionization by incorporating the shape of the molecular orbitals as well as their alignment with respect to the polarization of the laser field, which is determined by varying the angle relative to the laser electric field vector via a Wigner rotation matrix.[175] MO-ADK facilitates the determination of tunnel ionization rates within multiple valence level orbitals, which illuminates the possibility of increased ionization from HOMO-N orbitals (N=1, 2, 3, …) at particular orientations of the molecule to the laser electric field, an essential point for multielectron ionization dynamics.[38,176,177] For the experiments described here, it is assumed that the majority of the ionized electrons emerge from the HOMO along the laser polarization axis, and owing to the symmetry of the diatomic molecular orbitals along the molecular axis, standard ADK calculations are determined, by independent calculation, to be sufficient over the more cumbersome MO-ADK.

2.2.1 Ammosov-Delone-Krainov Theory

As mentioned above, Keldysh originally calculated tunnel ionization rates, *W*, as a function of a static applied electric field to an atom, given as (utilizing atomic units: $m=\hbar=e=1$):

$$W=\frac{\pi}{2^{3/4}}I_p\sqrt{\frac{3E_0}{\pi\kappa^3}}e^{\frac{-2\kappa^3}{3E_0}} \tag{2.12}$$

where $\kappa=\sqrt{2I_p}$ is the electron velocity after ionization, and E_0 is the laser's electric field amplitude in atomic units. Historically, equation 2.12 was thought to provide an effective means for determining if a given field intensity results in tunnel ionization of a valence electron or multiphoton ionization in terms of the ionization potential of the target and the ponderomotive potential of the laser:

$$\gamma=\sqrt{\frac{I_P}{2U_p}} \tag{2.13}$$

where,

$$U_p=\frac{E_0^2e^2}{4m_e\omega^2} \tag{2.14}$$

If γ is much greater than unity, then the target medium with ionization potential (I_P) undergoes multiphoton ionization, while if γ is smaller than unity the system is said to be within the tunneling regime.[49,51] The Keldysh parameter may be considered more generally as a measure of the tunneling time verses the wave period of the applied field:

$$\gamma=\frac{(tunneling\ \ time\ \ through\ \ barrier)}{(wave\ \ period\ \ of\ \ the\ \ applied\ \ field)} \tag{2.15}$$

Since Keldysh's original parameter was specified for quasistatic electric fields, it is not directly applicable to plane-wave electric fields generated by lasers, which are fundamentally different. As a result, the direct applicability of the Keldysh parameter to the determination of the ionization regime accessed in an experiment is not as clear as typically applied in the justification of strong-field experiments.[178] Even so, tunnel ionization rates may still be obtained from modifications of Keldysh's original framework.

Ammosov, Delone, and Krainov formulated the modern framework for tunnel ionization of complex atomic systems, and the static tunneling ionization rate was determined to be:[50]

$$W_{static} = \frac{\kappa^2 \left[C_{n^* l} Q(l,m) \right]^2}{2^{|m|} (|m|)!} \left(\frac{2\kappa^3}{E_0} \right)^{2n^* - |m| - 1} e^{\frac{-2\kappa^3}{3E_0}} \tag{2.16}$$

$$C_{n^* l} = \left(\frac{2}{n^*} \right)^{n^*} \frac{1}{\sqrt{2\pi n^*}} \tag{2.17}$$

$$Q(l,m) = (-1)^{(m+|m|)/2} \sqrt{\frac{(2l+1)(l+|m|)!}{2(l-|m|)!}} \tag{2.18}$$

where $n^* = Z_c / \kappa$ is the effective principal quantum number, Z_c represents the charge state after the electron departs, and *l* is the orbital angular momentum quantum number with its projection *m*. The cycle averaged ionization rate for the oscillating laser field may then be calculated from:

$$W = \sqrt{\frac{3E_0}{\pi\kappa^3}} W_{static} \tag{2.19}$$

where the laser intensity may be converted to the atomic units of electric field from:

$$I = \frac{cn\varepsilon_0}{2} |E|^2 = I\left(W / cm^2 \right) = 3.51 \text{x} 10^6 E_0^2 \tag{2.20}$$

given the index of refraction *n* for the target medium, the speed of light *c*, and the electric permittivity of vacuum ε_0. From this series of equations, the tunnel ionization rate of atoms may be calculated, and it has been shown to accurately predict the saturation intensity and tunnel ionization rate of the noble gases.[51]

It is straightforward to recast the tunnel ionization rate in terms of a tunnel ionization probability. The probability, *P*, for an electron to be tunnel ionized within the pulse width of the laser with a given pulse shape defined by *T(t)* may be represented as:

$$P = 1 - e^{-\int_{-\infty}^{\infty} WT(t)dt} \tag{2.21}$$

If the laser electric field is assumed to be a square wave, the integral of the probability of tunnel ionization simplifies to $W\tau$, where τ is the pulse width of the laser. As a result, the tunnel ionization probability is dependent on the same parameters as the tunnel ionization rate and provides an effective binary model for tunnel ionization, which is attractive for the presented experiments. The tunnel ionization rates for atoms described by *Z, l, and m* with various ionization potentials to singly charged states may then be calculated for a given set of laser parameters. For example, the tunnel ionization probability for atoms (*Z*=1; *l*,*m* = 0) of various ionization potentials to singly charged states as a function of field intensity is presented in figure 2.1

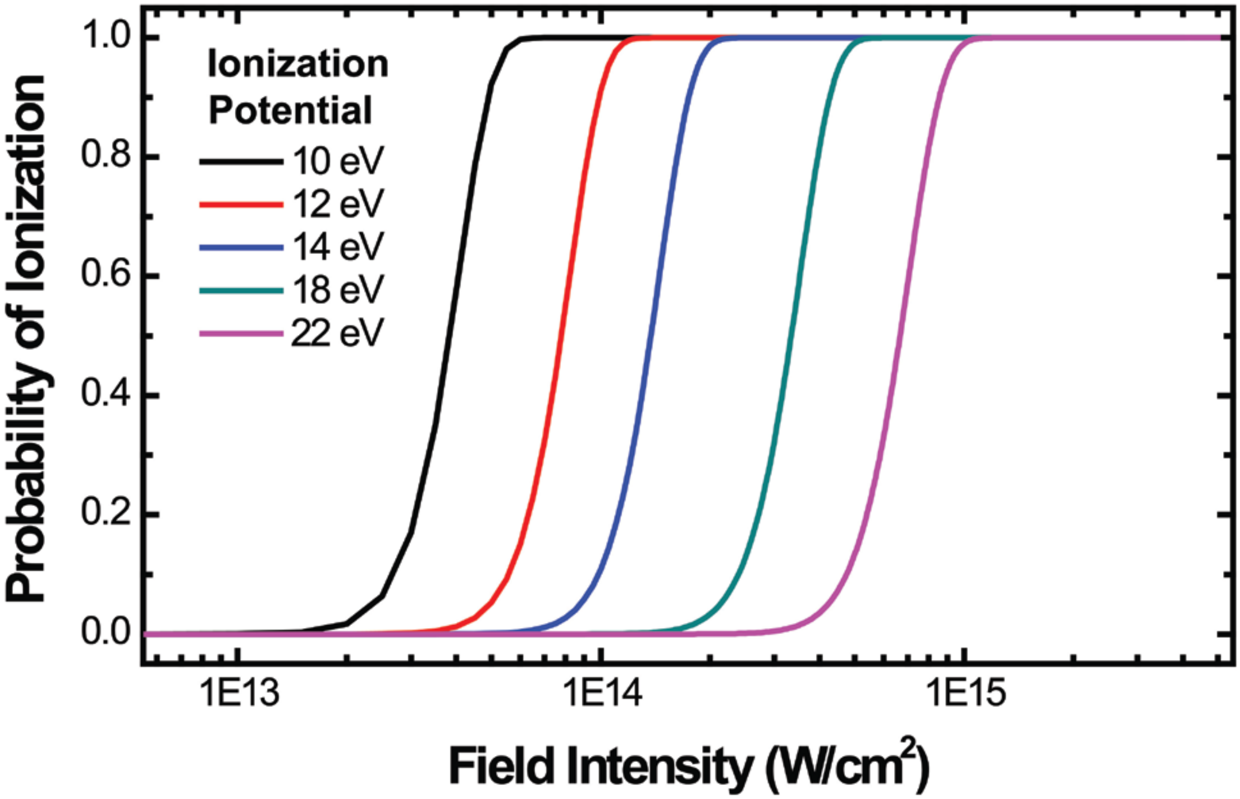

Figure 2.1: Ionization probabilities of atoms (Z=1; l,m = 0) with various I_P's (in legend) as calculated via ADK theory for a 40 fs pulse width as a function of various field intensities.

2.2.2 Internuclear Separation and Vibrational Level Sensitive Ionization Rates

ADK theory may be expanded to include an internuclear-separation-dependent ionization potential given by either the static or field-perturbed electronic structure, as well as the probability density distribution in the vibrational levels on the ground state potential. For simplicity, only the unperturbed potential energy surfaces are considered. The electron velocity, κ, may be recast to include the R dependent ionization potential, yielding:[166]

$$W_{ADK}\left(R,I\right)=\sqrt{\frac{3E_0}{\pi\kappa\left(R\right)^3}}\frac{\kappa\left(R\right)^2\left[C_{n^*l}Q\left(l,m\right)\right]^2}{2^{|m|}\left(|m|\right)!}\left(\frac{2\kappa\left(R\right)^3}{E_0}\right)^{2n^*-|m|-1}e^{\frac{-2\kappa(R)^3}{3E_0}} \qquad (2.22)$$

where,

$$\kappa(R)=\sqrt{2I_P(R)} \tag{2.23}$$

All other terms remain unchanged. At this point, it may be prudent to engage MO-ADK theory instead of traditional atomic ADK, but as long as the orbital in which the ionized electron originates remains sufficiently symmetric around the laser polarization axis, ADK is an effective model for tunnel ionization.[166]

The tunnel ionization rate as a function of vibrational state may be calculated taking into consideration the probability density of the occupied vibrational energy levels of the unperturbed initial state of the target molecular system. This is akin to determining the internuclear separation averaged vibrational state ionization rate:

$$W_{ADK}^{\nu}(R,I)=\int\left|\psi_{\nu}(R)\right|^2 dR\ W_{ADK}(R,I) \tag{2.24}$$

where the difference in ionization potential with vibrational state may also be taken into account, i.e. $I_p^{\nu}=I_p^0-E_{\nu}$, given the energy of a vibrational level ν E_{ν}. A more effective tunneling rate for determining internuclear separation and vibrational state, $\psi_{\nu}(R)$, dependence involves bypassing the R averaging of the ionization rate and instead evaluating $W_{ADK}^{\nu}(R,I)$ over a finite element, ΔR, of each vibrational state, i.e.:

$$W_{ADK}^{\nu}(R,I)=\int_{R}^{R+\Delta R}\left|\psi_{\nu}(R)\right|^2 dR\ W_{ADK}(R,I) \tag{2.25}$$

or the entire probability density, with $\Psi=c_0\psi_{\nu=0}+c_1\psi_{\nu=1}+c_2\psi_{\nu=2}+\cdots$, where $\left|c_n\right|^2:\ \{n=0,1,2,\cdots\}$ is the population in each vibrational level n given the condition $\sum_n\left|c_n\right|^2=1$:

$$W_{ADK}^{\nu}(R,I)=\int_{R}^{R+\Delta R}\left|\Psi(R)\right|^2 dR\ W_{ADK}(R,I) \tag{2.26}$$

The final formulation of R-dependent, vibrational level sensitive ADK tunnel ionization in equation 2.24 is recast to tunnel ionization probabilities in equation 2.25. This is the framework utilized to determine the resulting vibrational state populations in the following experiments.

$$P_{ADK}^{\nu}(R,I)=1-e^{-\int_{R}^{R+\Delta R}\left|\Psi(R)\right|^2 dR\ W_{ADK}(R,I)\tau} \tag{2.27}$$

The depletion of various vibrational states may be calculated for molecular bromine utilizing equation 2.25, starting with initially equal populations in all vibrational levels of the Morse potential eigenstates. The results are shown in figure 2.2. Clearly, at low field intensities, ionization is most probable at the inner turning point, R less than the ground state equilibrium geometry for neutral Br_2 (2.28 Å), and higher lying vibrational states due to the minimum in the ionization potential. Ionization actually occurs fastest at the equilibrium geometry of Br_2^+, 2.18 Å. As the field intensity increases, this dependence becomes less significant and ionization becomes equally probable at all internuclear separations and vibrational states as is seen at 6 x 10^{14} W/cm^2, and instead becomes solely dependent on the probability density distribution. A maximum in ionization probability is observed at the outer turning point (determined by integration of the vibrational amplitude near the outer turning point) of all vibrational states $\nu > 0$ due to the anharmonicity of the potential. The remaining population in the ground state may then be determined by:

$$\left|\Psi_{coherence}\left(R\right)\right|^2 = \left|\Psi_{neutral}\left(R\right)\right|^2\left(1 - P_{ADK}^{\nu}\left(R,I\right)\right) \tag{2.28}$$

where $\left|\Psi_{coherence}\left(R\right)\right|^2$ is the remaining probability density in the ground state after strong-field ionization, which was initially given as $\left|\Psi_{neutral}\left(R\right)\right|^2$.

Initially before ionization, the vibrational state populations of the neutral molecule are an incoherent mixture of states. The vibrational state population distribution in the ion and the neutral may become coherent after the strong-field interaction due to the ionization coupling of the states resulting in asymmetric depletion around the center of the vibrational wavefunction probability distribution. The coherence may then be simulated by introducing the time-evolution operator, $e^{-i\omega_\nu t}$, to the wavefunction of the vibrational states.

$$\psi_\nu(R) \Rightarrow \psi_\nu(R,t) = \psi_\nu(R)e^{-i\omega_\nu t} \tag{2.29}$$

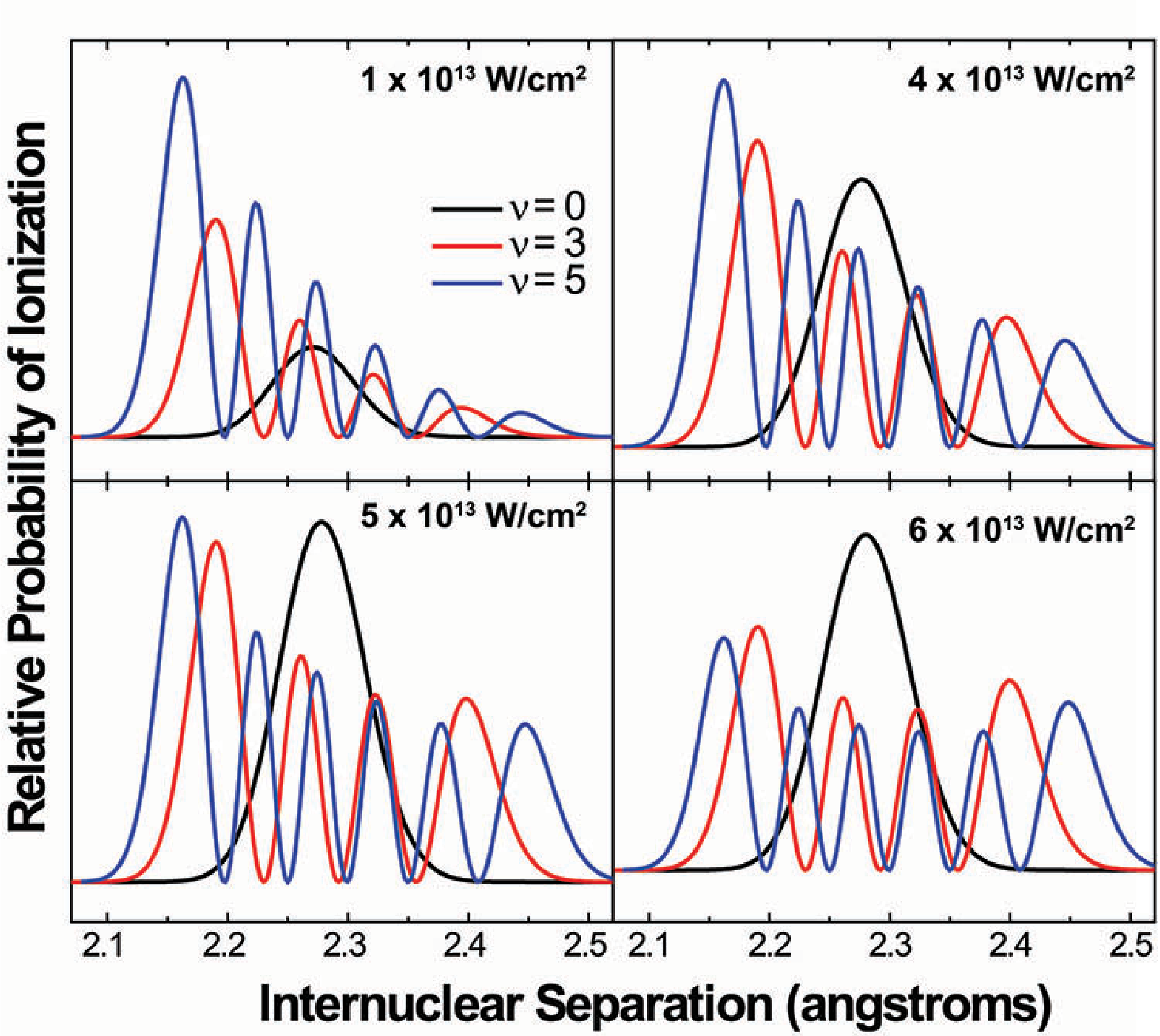

Figure 2.2: Probability of ionization of select vibrational energy levels of Br_2, assuming equal initial population of all states. Obviously, at low laser peak intensities the most probable ionization occurs around the equilibrium geometry of the Br_2 cation (2.18 Å) at R less than R_e of Br_2 (2.28 Å). As the laser intensity increases, the selectivity of ionization is lost as the field is strong enough to ionize equally at all R, leading instead to a broader distribution of vibrational final states in the ion.

Lastly, the ionization of the Br_2 vibrational states to the vibrational level of the cation may be predicted in terms of the Franck-Condon factors. Figure 2.3 illustrates these results. Unique coupling of the vibrational states of the neutral and the ion is observed in terms of the ionization pathway when each vibrational state is populated equally, but once the Boltzmann distribution at 300 K is included to provide the vibrational wavefunction coefficients, the predominant ionizing state is $\nu = 0$ for the neutral, which populates a broad distribution in the ion. As a result, it may be expected that the ion vibrational wave packet from strong-field ionization of the unperturbed potentials involves a large superposition of vibration levels. Moreover, it is seen that Franck-Condon ionization does not predict an overall decrease in the vibrational energy of Br_2, contrary to R_ν-ADK theory.

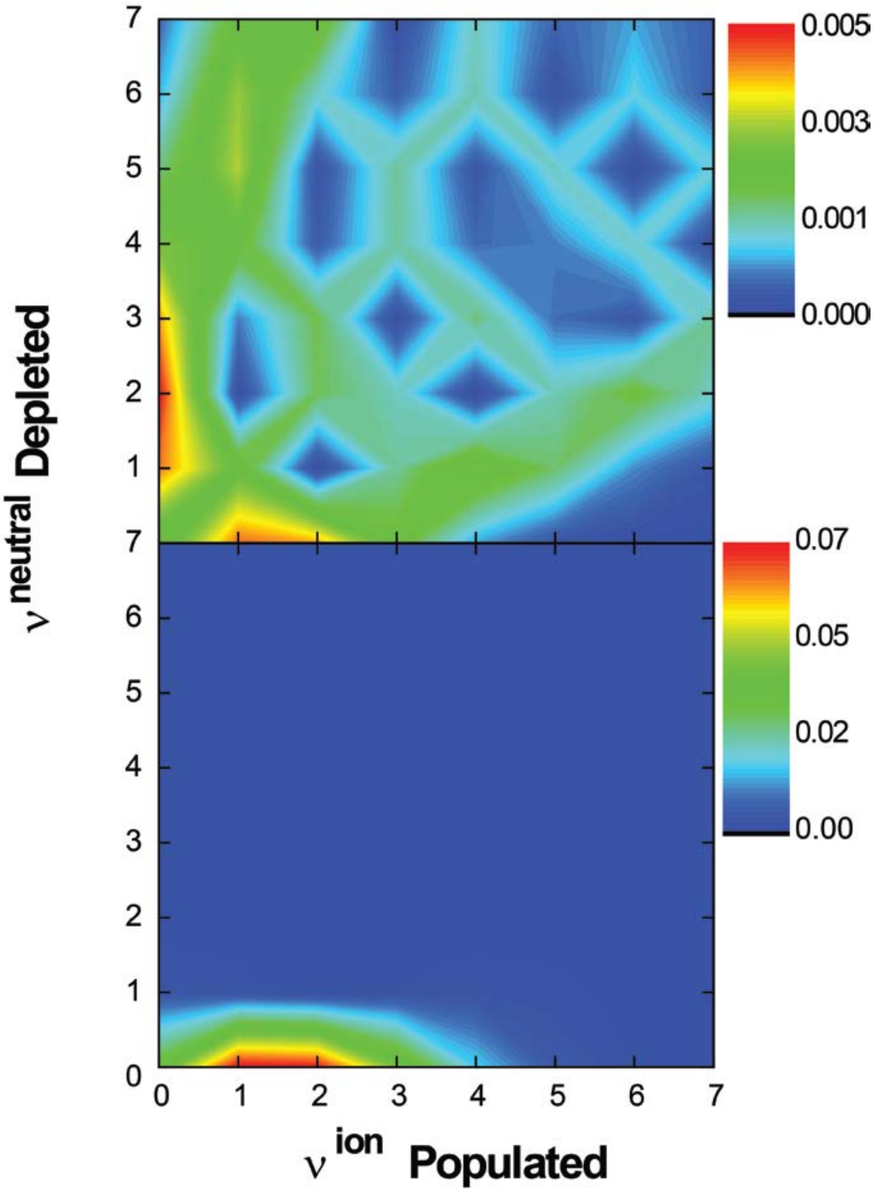

Figure 2.3: False Color plot of the R_{ν}-ADK tunnel ionization calculations at 5 x 10^{14} W/cm^2 for molecular bromine determining the vibrational state population of the ion utilizing the Franck-Condon factors coupling the vibrational states of the neutral and ion. The false color scaling represents a relative value for the population in each state. The plot should be read as the ionization from the ground state on the y-axis populates the vibrational state of the ion on the x-axis. (Top) Vibrational state population transfer assuming that each ground state vibrational level is populated equally. (Bottom) Vibrational state population transfer given a Boltzmann distribution at 300 K for the ground state vibrational levels. Clearly, $\nu = 0$ is the predominant source for populating a broad vibrational manifold of the ion.

2.3 Restricted Excitation Window Time-Dependent Density Functional Theory

Time-dependent density functional theory (TD-DFT) calculations are conducted employing the NWCHEM 6.1 program package[161] to obtain the dependence of the XUV transition energy on internuclear separation. TD-DFT allows calculation of excited states of a molecular system based within the Runge-Gross theorem,[179] the time-dependent version of the Hohnberg-Kohn theorem.[180] For the calculation of the XUV transition energies for a particular core-level, the ground state geometry is first optimized employing the Becke (B3) hybrid exchange functional[181] and the correlational function of Lee, Yang, and Parr (LYP)[182] with the polarized split-valence triple zeta basis set 6-311g*. Calculation of the transition energy to the desired core-hole excited state is accomplished by Restricted Excitation Window (REW) calculations, which isolate a certain set of core orbitals based on the binding energy.[161,162] Isolation of particular core level transitions eliminates irrelevant roots of the valence electron solutions, calculating the transition energy as well as the oscillator strengths at varying internuclear separations via solutions of the von Neumann equation. The results for the $3d \longrightarrow \sigma^*$ core-hole excitation of Br_2 as a function of internuclear separation are presented in figure 2.4.

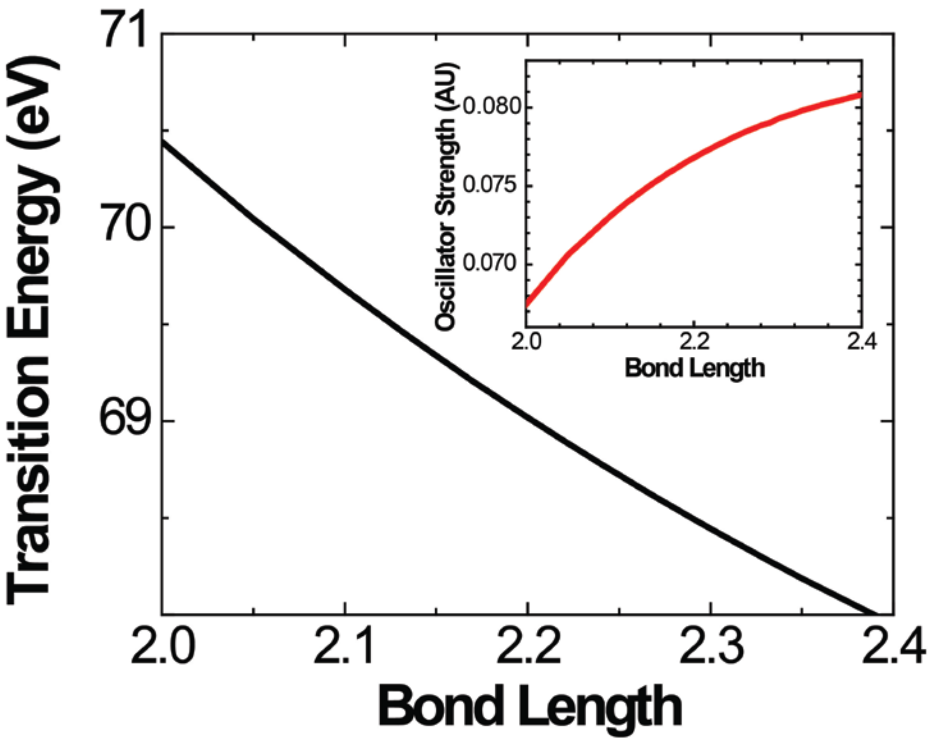

Figure 2.4: REW-TD-DFT calculation results for the transition energy for the formation of a $3d^{-1}$ core-hole in Br_2 as a function of internuclear separation. As the bond elongates, the transition energy decreases, indicating the core-hole excited state is repulsive around the equilibrium geometry of Br_2. The inset shows the increase in oscillator strength with R for the promotion of a 3d electron.

2.4 Determination of XUV Transient Absorption Spectrum

Just as the simulation of the time-dependent attosecond transient XUV absorption spectrum of Kr^+ may be calculated from the formulation of the XUV absorption cross section's evolution as a function of time delay during and after strong-field ionization, so may the time dependent XUV absorption spectrum be calculated for molecular vibrational wave packets through the calculation of the R_v-ADK strong-field response in combination with REW-TD-DFT modeling of core-hole excitations. For a given phase of the vibrational wave packet, the time evolving transition probability may be calculated employing the time-dependent vibrational probability density from equation 2.27 in combination with equation 2.26 and the results of the REW-TD-DFT calculations. Essentially, the transition probability to the core-hole excited state is evaluated at all times *t* for a given instantaneous vibrational probability density distribution, effectively calculating the time evolving dynamic XUV absorption spectrum as seen in figure 2.5 for the strong-field generated wave packet in bromine.

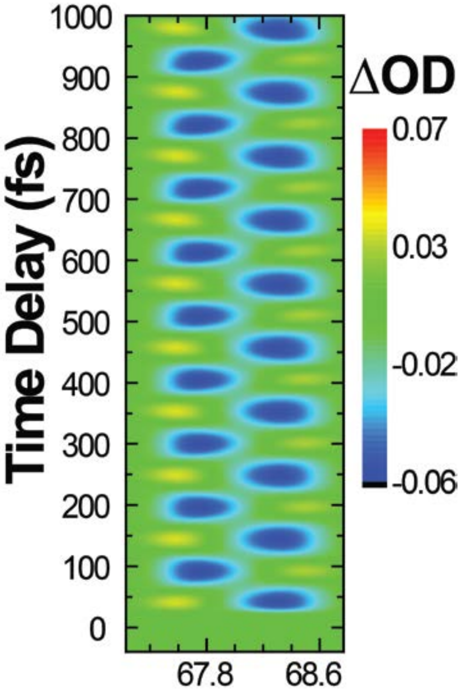

Figure 2.5: REW-TD-DFT calculation for the core-hole excitation, $\sigma^* \rightarrow 3d^{-1}$, of neutral bromine following strong-field ionization. The R-dependence of the XUV excitation and the generated ground state vibrational wave packet by R-selective ionization yields a transient XUV absorption signal, which oscillates in time in accordance with the period of the superimposed states.

Chapter 3

Methods for Femtosecond Extreme-Ultraviolet Transient Absorption of Vibrational Wave Packets

The experimental apparatus discussed here was largely designed, tested, and qualified by Zhi-Heng Loh during the course of his PhD studies.[19] Several key innovations of the apparatus have allowed for the investigation of time-dependent strong-field chemical dynamics with a resolution of ~1 cm^{-1} over the course of several days. The innovations facilitate a greater stability to the instrument as well as an increase in the photon flux and capabilities. These improvements as well as the day-to-day operational details and pitfalls are described here.

3.1. Experimental Improvements

To conduct successful multi-day transient absorption experiments, several system upgrades were instituted covering various aspects of the apparatus. Without these improvements it would not have been possible to examine the complex strong-field induced molecular dynamics discussed later. Even so, there are still advances that can increase the robustness of the apparatus, allowing continuous operation with unprecedented stability and minimal user interaction. The development of the apparatus as well as suggestions for further improvements is described herein.

The femtosecond XUV transient absorption instrument is based on a high-harmonic source, which originally consisted of a capillary waveguide and was eventually converted to a semi-infinite gas cell due to considerable instrumental downtime and lack of repeatability in the harmonic flux from the original source. The system can be divided into several key sections, each of which must be optimized independently to yield stable operation: femtosecond laser, strong-field dynamics pump (power and polarization control), high-harmonic source, vacuum apparatus and gas isolation, XUV optics and spectrometer.

3.1.1. Femtosecond Laser System

The experimental apparatus is based around a Newport Corporation, Spectra-Physics Spitfire Pro femtosecond laser system yielding, by the book, sub-40 fs, 2.5 mJ, 800 nm center pulses at a 1 kHz repetition rate with turn-key operation. In actuality, the system at the beginning of my PhD studies originally produced pulses of approximately 47-50 fs duration (FWHM), 2.7 mJ energy, and centered at 800 nm with significant spectral-spatial chirp and unreliable operation beyond several days. These parameters show the immediate issues to be axial-spatial chirp (spectral chirp across the horizontal or vertical beam axis) and the pulse-duration, but throughout the course of attempting to optimize the harmonic flux and stability of the capillary waveguide source additional problems relating to the pointing stability as well as the M^2 (beam product parameter) of the system were unearthed.

The Spitfire Pro is a regenerative chirped pulse amplification (CPA) system. CPA is accomplished by amplifying the output of a titanium: sapphire oscillator, in this case a Spectra-Physics Tsunami, by first temporally and spectrally chirping the pulse in a four pass grating stretcher. The Tsunami operates at an 80 MHz repetition rate, the pulse train of which is reduced to 1 kHz and amplified in a regenerative amplifier. The temporal and spectral chirp is then reversed by a four pass grating compressor to yield a compressed, ultrafast pulse close to the original pulse duration of the oscillator. The system is therefore subdivided into three parts; stretcher, regenerative cavity, and compressor.

The Tsunami yields approximately 200 mW of 800 nm centered light at an 80 MHz repetition rate with anywhere between 45-70 nm of bandwidth (55 nm is optimal), depending on the weather. In humid or cold conditions the oscillator does not maintain optimal bandwidth or mode-locking, but with dry, warm conditions in the lab (30% humidity and 24ºC) the oscillator bandwidth approaches 70 nm of bandwidth and the mode-locking is steadfast. The oscillator is run 24/7 and is constantly purged with dry nitrogen to reduce the humidity in the cavity for stability. This operational mode is particularly favorable for the output of the Millennia continuous-wave 532 nm pump laser. Constant start-up and shut-down of the system reduces the lifetime of the diodes and alters the operational mode of the system due to the stress induced by ramp-up and cool down.[183]

The first issue to be resolved was the axial-spatial chirp, i.e. the pulse is unequally chirped from one end to the other in space. The axial-spatial chirp was identified to occur in two different places of the amplifier, before the regenerative cavity and after the compressor. This originated from two different misalignments, one in the stretcher and one in the compressor. The first was a transverse spatial chirp in the stretcher before the amplification cavity across the axis of the stretcher. In the stretcher, the pulse is meant to be stretched along the axis of propagation, not the (horizontal) transverse axis of the beam relative to the propagation vector (spectral dispersion plane). This horizontal transverse chirp resulted from the misalignment of the roof end mirrors after the stretcher grating. By adjusting the distance between the roof end mirror and the stretcher fold mirror, the over or under spatial chirping of the pulse may be corrected by monitoring it with a fiber optic cable connected to an Ocean Optics HR2000 spectrometer and scanning along the transverse axis of the beam relative to the beam propagation along the spectral plane of the stretcher, i.e. vertical axis of the beam's mode after the periscope, before the regenerative cavity.

The translation stage of the roof mirror may then be locked into position to maintain the chirp of the stretched pulse.

The second misalignment resulted in an axial-spatial chirp in the output pulse of the regenerative amplifier. This occurred in the compressor after the regenerative cavity due to a misalignment of the interferometically aligned vertical retroreflector mirrors, yielding a horizontal chirp (along the spectral dispersion plane of the compressor) again in the output beam. The angle of the retroreflector to the incoming beam was not at normal incidence, resulting in an uneven compression of the beam and the observed axial-spatial chirp along the axis of the compressor. By aligning the beam back along itself as well as employing the same procedure with a spectrometer as was done for the misalignment in the stretcher, the axial-chirp was able to be minimized.

Correction of the two misalignments in the stretcher and the compressor yielded an output pulse duration that is consistent with the factory obtained values. Through years of maximizing the output power in this misaligned state (constantly walking the beam away from the optimal alignment), the regenerative cavity also needed to be aligned to efficiently amplify the non-axially chirped pulse. It was during this process that the M^2 of the system became quite large. The factory specification is <1.4, but values of 2.0 and greater were obtained. The M^2, or Beam Product Parameter, is a figure of merit for the quality of a laser beam relating to its focusability as introduced by A.E. Siegman.[184] M^2 is incorporated to equations relating to a laser beam's divergence angle (θ):

$$\theta = M^2 \frac{\lambda_0}{\pi w_0^{4\sigma}} \tag{3.1}$$

Therefore,

$$w = M^2 \frac{\lambda_0 f}{\pi w_0} \tag{3.2}$$

where λ_0 is the wavelength of the laser light, f is the focal length of the lens, and w, $w_0^{4\sigma}$, and w_0 are the initial beam waist before the lens, the focal beam radius at the beam waist as measured by the D4σ, second moment width, and $1/e^2$ techniques, respectively.[102,184] The D4σ width corresponds to the beam diameter that is four times the standard deviation of the axial marginal distribution, and the $1/e^2$ width is the beam diameter at 13.63% of the peak intensity. The value of the M^2 of the laser relates directly to the coupling efficiency into a capillary waveguide as was discussed in chapter 1. At the time that this issue arose, the capillary was the only harmonic source in use and thus it was necessary to improve the M^2 of the system to yield higher harmonic flux with greater pulse-to-pulse stability. As was presented in Chapter 1, an increase in the M^2 of the driving laser leads to a decrease in coupling efficiency as the numerical aperture of the beam deviates from that of the fiber.

The M^2 of the laser system is affected by every optic. As a result, it is a daunting task to determine which optic or alignment point leads to an enlarged M^2. The only method to troubleshoot this is to incrementally and systematically adjust the system or replace optics, constantly measuring the overall M^2 of the system. The M^2 was measured by determining the D4σ width of the beam over a distance of several centimeters around the focal spot of the beam focused by a lens. The M^2 can then fit directly given:

$$w(z)_{\text{actual}} = \sqrt{\left(w_0^2 + M^2 \left(\frac{\lambda_0 (z - z_0)}{\pi w_0} \right)^2 \right)} \tag{3.3}$$

Where z_0 is the $1/e^2$ focal position, $w(z)_{\text{actual}}$ is the actual D4σ beam waist at all points along the measured propagation direction z, and ω_0 is the theoretical beam radius at z_0. Each M^2 measurement requires approximately 45 minutes to yield an accurate measurement since the camera must be manually scanned and the horizontal and vertical beam waist independently recorded and fit. Eventually, it was determined that the defect lied in the fold mirrors of the regenerative cavity which guide the beam into the Ti:sapphire crystal, and these were subsequently replaced and are now constantly monitored. These mirrors become damaged after approximately one year of routine operation and must be rotated to a new spot to maintain the M^2 quality. This issue is not uncommon with this particular commercial system, but it is usually the cavity end mirrors after the Pockels cells that become damaged after extended use.

The damage induced on the cavity fold mirrors in the regenerative amplifier also leads to a constantly evolving set of collimation parameters for the expansion telescope before the compressor. It is therefore necessary to verify the collimation of the Spitfire Pro output beam every few months to guarantee the parameters of the expansion telescope are correct. The drift in collimation is due to damage induced on the coating layer of the regenerative cavity fold mirrors over time, which eventually leads to the poor M^2 of the system. As such, the quality of the output beam of the Spitfire is a moving target at all times. This is one of the primary reasons that the switch was made to a semi-infinite gas cell harmonic source since it is less sensitive to beam quality and alignment.

The last issue to be addressed involved the pointing stability of the system. There are two main causes for beam pointing drift: thermal drift and mechanical drift, each of which may occur within the amplifier and the external optics. The main reason for mechanical drift is the perturbation of the table by the turbomolecular and mechanical pumps, both of which were isolated as much as possible using sand buckets to isolate the mechanical pumps and water cooling for the turbomolecular pumps to eliminate forced air currents. Previous experiments published from this apparatus involved data collection times of several hours at most, requiring a short window of optimal laser coupling into the gas filled capillary to complete an experiment. Operation beyond this timeframe required constant adjustment of the capillary to maintain proper coupling conditions and with each adjustment lead to a shift in the spectral calibration as well as a change in the overlap of the pump and probe beams. Therefore it was necessary after each optimization of the capillary to re-align the pump beam and calibrate the system. This was resolved by installing a beam stabilization system from Newport Corporation, the GuideStar II, shown in figure 3.1. This system employs a pair of picomotor actuated mirrors which actively lock the beam position to two separate CCD cameras via a feed-back loop. The locking routine fits the imaged beam to a Gaussian profile and locks the Gaussian center to a predetermined set point. This beam stabilization system actively locks the pointing of the system to within ± 10 µm at the interaction region, an improvement of five times over the previous performance measured over 30 minutes, now extended to an unlimited amount of time.

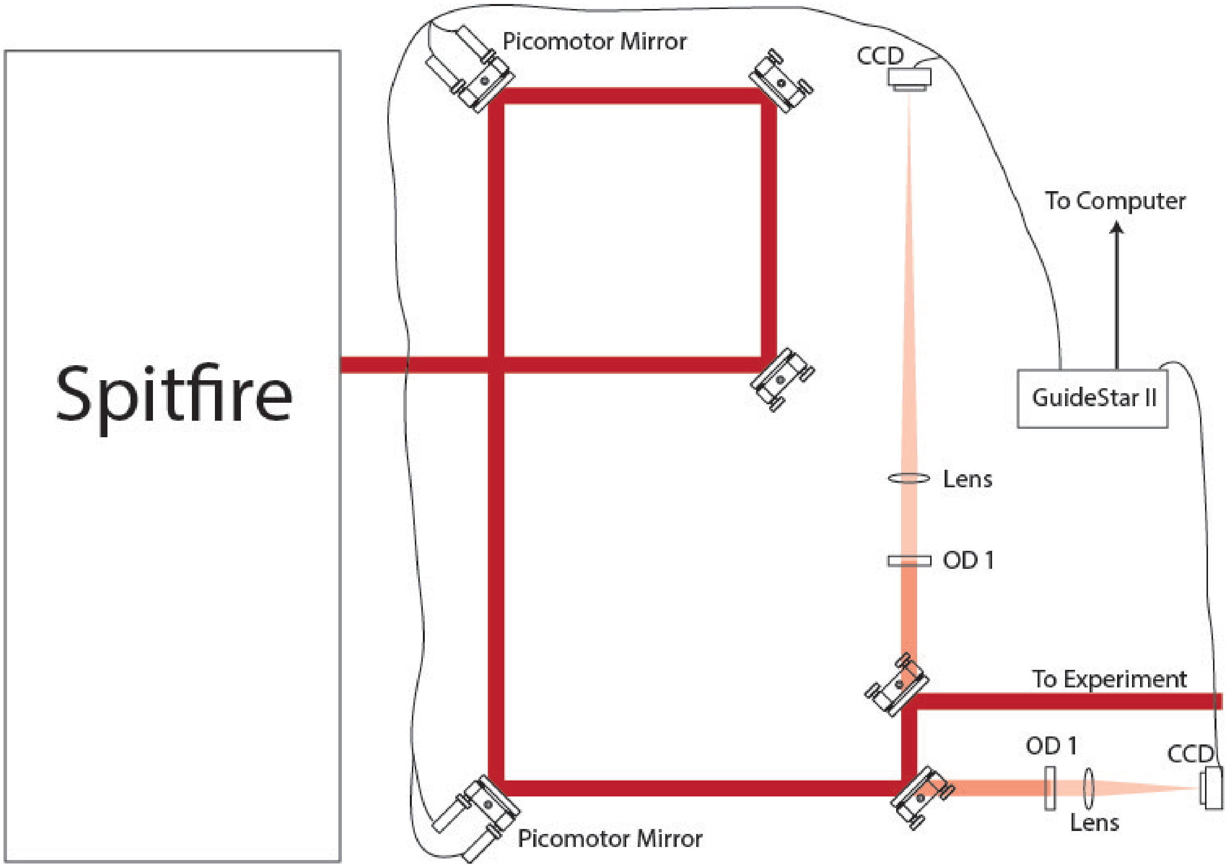

Figure 3.1: Beam pointing stability system illustration. In order to achieve the most precise locking, insensitive to minor beam deviations, the separation of the motorized mirrors should be as large as possible. Both CCD cameras must be after the second motorized mirror to provide a unique locking solution, but they should also be as far from the motorized mirrors as possible. The camera paired with the last motorized mirror should be as far from the optic and as close to the same distance as the application as possible.

After instituting all of the changes described above, the system can routinely deliver pulses between 37-40 fs duration (FWHM), 2.9 mJ output energy, centered at 800 nm at a 1 kHz repetition rate. All pointing drift in the system as a result of thermal fluctuations in the lab has been eliminated by instituting the GuideStar II, but there still remains significant pulse-to-pulse jitter which is within 10 microns at the interaction region and therefore has a negligible impact on the experimental results.

3.1.2. Strong-Field Dynamics Pump

A portion of the 800 nm output of the Spitfire Pro is picked off by an 80/20 beamsplitter (CVI, BS1-800-80-2012-45P) and used to drive the high-field ionization dynamics (pump) of the analyte molecule in the interaction region. Control of the polarization and intensity of the pump is necessary in order to control the ionization dynamics observed in the sample, i.e. high field intensity leads to the formation of multiply charged ions and subsequent Coulomb explosion, while lower field intensity may yield only singly charged species with interesting wave packet dynamics. Polarization control is necessary in order to determine whether the ionization dynamics result in any alignment of the sample relative to the polarization of the pump. Previous experiments had employed a ½ waveplate (CVI, QWPM-800-10-2) and linear Polarcor polarizer (Newport, 10P109AR.16) pair to control the polarization, while the field intensity was manipulated by an iris.

Control of the polarization as previously employed was not effective, and as such the results obtained in the prior configuration may not be as accurate as originally thought. This is due to the waveplate and polarizer being placed in the optical line before a mirror which was not used at 45º incidence. The mirror in question was actually at approximately 60º incidence, yielding a beam no longer at the specified polarization and thus angular dependent measurements of the strong-field induced hole quantum state distribution may not be completely accurate. This supposition was confirmed experimentally by measuring the polarization purity before and after the 60º incidence mirror, where it was determined that significant polarization impurities were introduced by the mirror. In order to rectify this, the Polarcor polarizer was moved after the 60º incidence mirror, allowing the polarization to be more properly controlled at the interaction region. The polarization of the beam at the interaction region was subsequently confirmed by employing a second Polarcor and measuring the power through rotation.

Manipulation of the field intensity by an iris led to the additional issue that as the iris is closed to reduce the power at the interaction region, the pump beam focal waist and focal position would also change. This required that the experimentalist constantly adjust the focal position (coarsely) before experiments to the power to be employed, and then optimize the system at that power (overlap of pump and probe as well as the focal position (finely)). To counter this, a thin-film polarizer (CVI, TFPK-800-PW-1025-C) and ½ wave plate (CVI, QWPO-800-08-2-R10) pair were added to the pump optical line to enable a finer control of the field intensity as well as to not affect the focusing parameters at the interaction region.

By instituting a new set of power variation optics and by relocating the Polarcor polarizer to after the 60º mirror, it is possible to finely control the field intensity in strong-field experiments as well as obtain an accurate polarization in the interaction region. This allows reliable experiments to be conducted based on field intensity and polarization variation.

3.1.3. High-Harmonic Source

High-harmonic generation may be accomplished by several means including a free focusing geometry (gas jet or gas cell), hollow-core waveguide (capillary), or self-guiding geometry (semi-infinite gas cell) as discussed earlier. The original experimental set-up employed a capillary waveguide source since it provided a high degree of coherence and minimal XUV beam divergence. Due to experimental difficulties of fabricating the waveguides as well as the downtime required to optimize each new capillary, it was decided to switch to a semi-infinite gas cell source. A brief description of the difficulties incurred with the hollow-core waveguide and a description of the results obtained with the semi-infinite gas cell illustrate why the change in source was made.

3.1.3.1. Capillary Waveguide

The advantages of the capillary waveguide have been described above and in the literature,[111] but the procedural implementation for robust day-to-day operation is quite different, especially with the laser system employed in this experiment. One advantage is the highly coherent nature of the light produced by the waveguide and small XUV divergence angle, which is excellent for spectroscopy. The mode of the output XUV beam from the capillary waveguide is directly coupled to the spectrometer resolution, i.e. if the mode is poor (non-Gaussian, poor focusability, etc…) and thus occupies more pixels per harmonic then the resolution is also less than optimal. Moreover, since the capillary is a fixed source and the coupling lens is moved relative to the entrance of the waveguide, the XUV optics' parameters remain constant (object-mirror and mirror-image plane distances). Lastly, there is a great tunability of the capillary source with respect to the photon energy of the generated XUV light. Each harmonic may be blue or red shifted by approximately 1.5 eV,[32] although as the harmonic is red/blue-shifted, the efficiency of harmonic generation decreases exponentially. Frequency shifting of the harmonics is accomplished by tuning the compression of the incoming 800 nm driving pulse, the gas pressure in the waveguide, and/or by aperaturing the driving beam.[19]

In spite of the advantages of a capillary waveguide, there are several downfalls. The first of which is the introduction of the gas into the hollow-core. This proved to be the pivotal point for experiments with a capillary waveguide source in this apparatus. Several techniques for introducing gas to the capillary were explored by the group of Margaret Murnane and Henry Kapteyn by Ariel Paul, and it was finally determined that employing a CO_2 laser to ablate two gas inlets was the most successful solution.[104] The issue with this solution is that great care must be taken in calibrating and aligning the CO_2 laser drilling platform to make sure that the ablated hole is the correct shape, depth, and location. Over drilling of the hollow-core waveguide and subsequent deformation of the internal cavity led to a slew of capillaries that were ineffective in high harmonic production. Once the CO_2 beam punches into the center cavity, ablated material begins to accumulate in the waveguide core. When the capillary is then coupled to the 800 nm driver for high harmonic generation, this material ablates (clearly visible around gas inlets) and significantly decreases the coupling efficiency, which results in an order of magnitude less harmonic flux. This renders the instrument unusable for extended spectroscopic scans since the usable instrument time is approximately five hours, not including the time required to optimize the high harmonic generation process (8+ hours).

Separate from the detrimental ablation effects, there was also an inherent difficulty in the utilization of a hollow-core capillary waveguide for high harmonic generation. For ease, the capillary is aligned to the laser for optimal coupling, but even this is quite difficult and requires constant adjustment of the capillary before scientific investigations can be conducted. Aligning the laser to the fiber results in changing the optimal pointing for the fiber, creating substantial difficulty in aligning the XUV to the experimental application. Initially, the waveguide is aligned at ambient pressure to an attenuated 800 nm driver that has been aligned to the XUV optics. Once an intense EH_{11} mode is obtained in the far-field with the weak 800 nm light, the capillary is pumped down to vacuum and the full power 800 nm driver is aligned in the same fashion. At this point, high harmonics may be generated, but the initial flux is quite low. The initial low flux is due to bending losses in the capillary as well improper mode coupling into the fiber. Bending losses occur due to the nonlinearity of the waveguide resulting from the manufacturing process (radius of curvature of > 6 meters). To reduce bending losses, the waveguide must be physically bent by the alignment actuators to achieve the cleanest EH_{11} mode and highest coupling efficiency, optimizing the high harmonic flux. As the high harmonic flux is optimized, the entrance to the hollow core waveguide is ablated slightly, creating a conical entrance for the driving laser beam. Once the entrance is ablated, harmonic flux is substantial and robust on short timescales (2-3 hours). Unfortunately, the process of ablating the capillary to achieve continuous operation may take upwards of a week of daily, 8-hr operation, but once this is completed the apparatus takes approximately an hour to “warm-up.” The large M^2 of the Spitfire Pro makes it inherently difficult to couple the 800 nm driving laser into the waveguide due to the mismatch in the numerical apertures as discussed earlier. This process must be repeated for each new capillary, and each capillary has a lifetime of approximately one to two months. This means that about one week in four is required just to optimize the waveguide for operation.

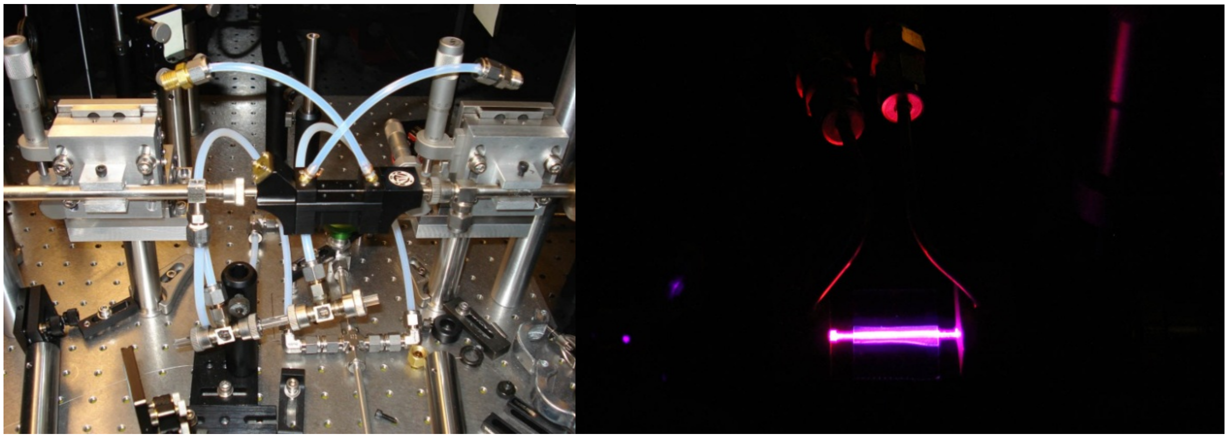

Figure 3.2: Image of the capillary waveguide assembly on the apparatus. A third generation capillary waveguide is mounted into the alignment actuators, and a second generation capillary is attached to the gas inlet lines in the foreground (Left). (Right) Capillary waveguide in operation producing neon harmonics. The v-groove 3rd generation capillary is meant to reduce bending losses and reduces alignment and “warm-up” time, which it does quite well, but due to the ablation damage discussed the semi-infinite gas cell was still preferable.

One the waveguide has been optimized and the experimental apparatus calibrated, chemical dynamics investigations can be conducted. During the course of these investigations, the capillary requires constant realignment as the driving laser beam pointing will drift slightly, changing the coupling efficiency and thus the harmonic flux. Since the hollow-core capillary is a waveguide, once the harmonic flux is re-optimized the instrument must be recalibrated from scratch again since the pointing to the XUV camera will have changed as well as the pump-probe overlap. This means that every 2-3 hours of experimental time, the system will need to be recalibrated.

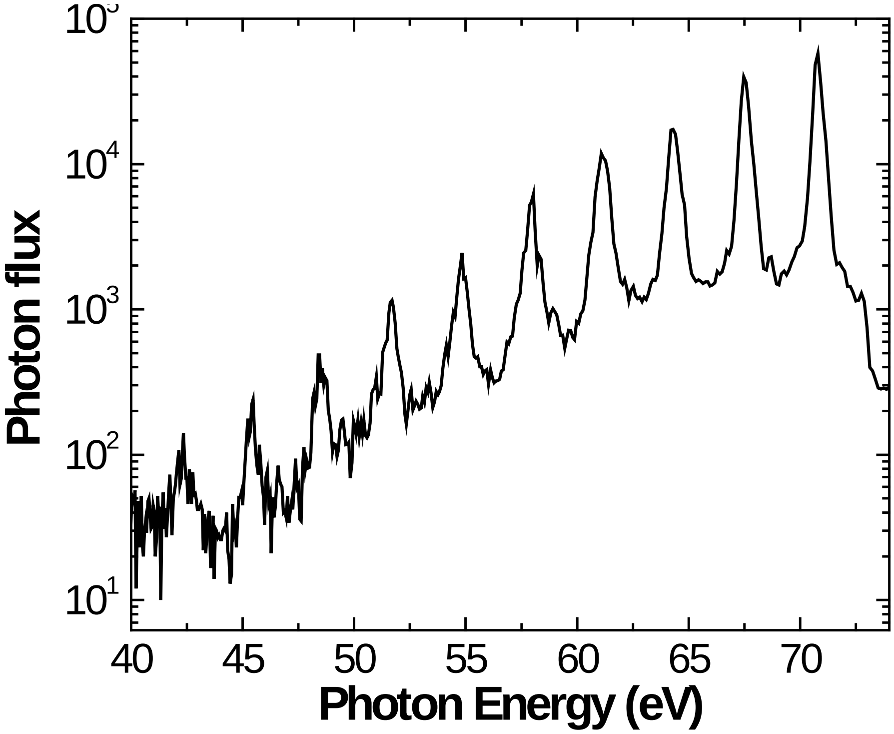

Figure 3.3: Typical neon high harmonics generated with 1.6 mJ of 800 nm, 40 fs pulses at a 1 kHz repetition rate in a capillary waveguide (2 s integration, 1 μm of Al foils). The photon flux is given on a Log_{10} scale for clarity. The significant continuum between harmonics 50 and 72 eV is what facilitates effective, quantitative transient absorption investigations by ensuring detection of optical transitions not overlapped with the harmonics. The continuum allows observation of optical transitions that fall within the 3 eV gap between adjacent harmonics, each of ~1 eV bandwidth.

Development of capillary waveguides for high harmonic generation has led to a generation of sources involving an aluminum v-groove to reduce bending losses and decrease alignment time. This had the effect of increasing harmonic flux by a factor of two since shorter waveguides could be used and still provide the same XUV beam mode as their longer counterparts. The difference between these two generations is illustrated between figures 3.3 and 3.4. The third generation capillary delivers increased photon flux with higher definition harmonics (increased mode quality), which is expanded upon in the generation of the even harmonics. Even with this advancement, the issue of ablation damage of the waveguide was still prevalent, preventing steadfast daily operation, which was not helped by the large M^2 of the Spitfire Pro. It was at this time that it was decided to change the harmonic source to a semi-infinite gas cell.

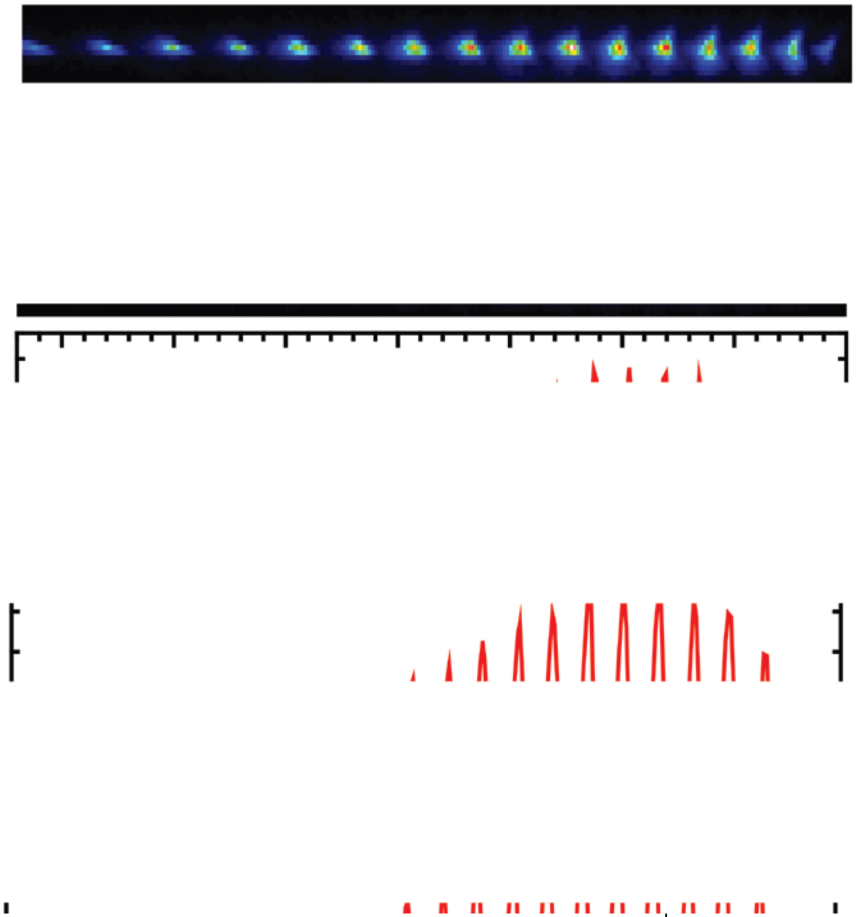

Figure 3.4: (Top) Image of even and odd harmonics generated in a 3rd generation v-groove 5 cm capillary waveguide in Neon. The image was collected in a single exposure with an integration time of 0.2 s with 80 Torr of Neon. (Bottom) Lineout spectrum of the high harmonic image collected.

3.1.3.2. *Semi-Infinite Gas Cell*

The semi-infinite gas cell allows the production of high harmonics over an extended interaction length due to the loose focusing geometry, combining the easy alignment of a gas cell with the interaction length of a hollow-core waveguide. The semi-infinite gas cell was introduced in several phases to test its compatibility with the existing experimental apparatus, and at each design phase, improvements were made to increase the robustness and easy of the high harmonic generation optimization process.

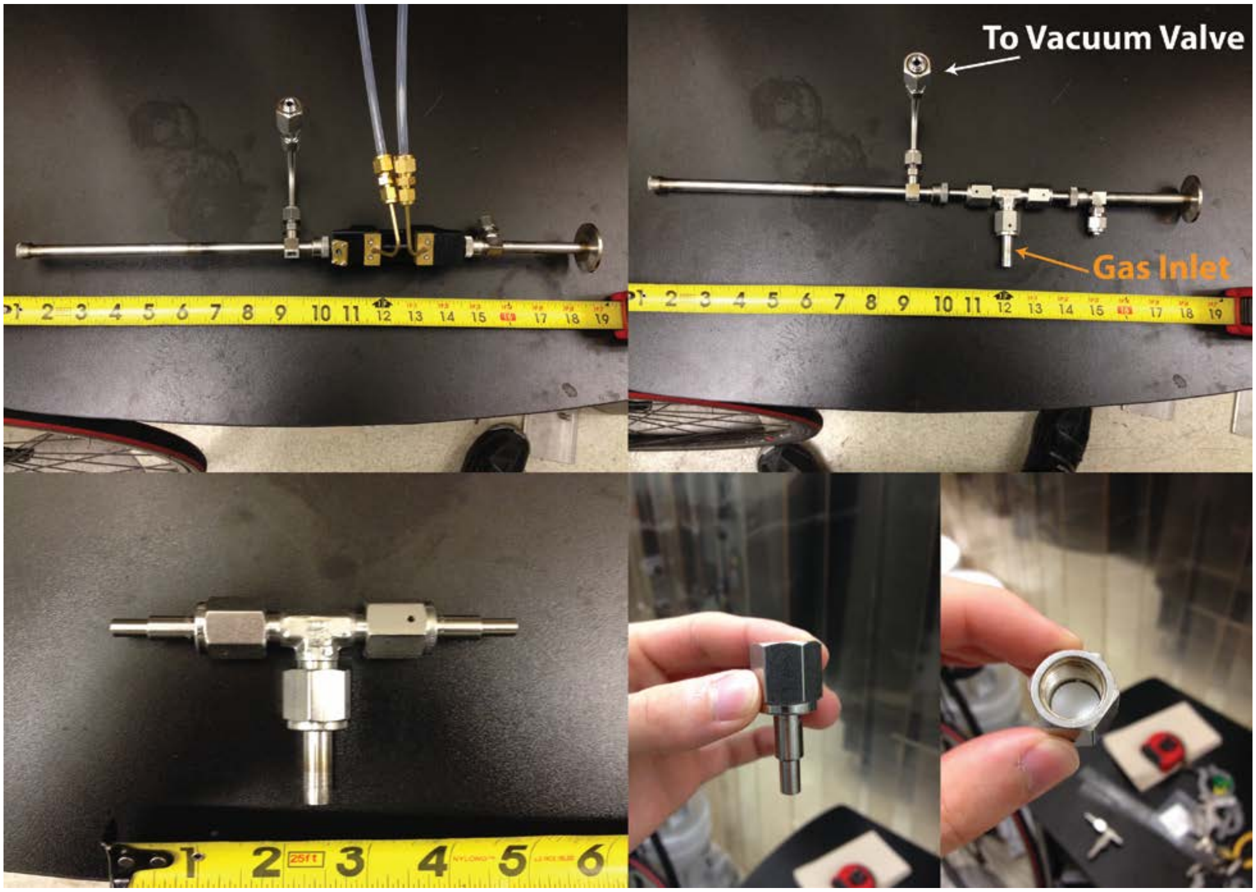

Figure 3.5: First generation semi-infinite gas cell as proof of concept for transient absorption spectroscopy. (Top Left) Front end of transient absorption apparatus for high harmonic generation in a capillary waveguide. The front of the assembly (left) is connected to a roughing pump via the VCR fitting to differentially pump the high harmonic gas away from the front of the fiber. The 3rd generation capillary wave guide is in the middle with gas connections leading to the fiber, and the back of the assembly (right) connects to the vacuum chambers of the rest of the experiment with an NW 25 connection. (Bottom Left) VCR assembly for a makeshift semi-infinite gas cell consisting of a VCR tee, 2x ¼" weldable butts, and a ½" weldable butt. The weldable butts allow a vacuum tight connection to ultraTorr fittings. (Top right) VCR semi-infinite gas cell attached to the same construction as the capillary wave guide but now the front assembly VCR does not connect to the vacuum line and the high harmonic gas is fed into the ½" weldable butt of the VCR tee. (Bottom right, pair) VCR tee and placement of the Teflon foil for the semi-infinite gas cell. The Teflon foil acts as a gasket on the downstream end of the VCR tee assembly in this configuration to both seal the cell and act as the exit foil for the semi-infinite gas cell. For all of these setups, the 800 nm driving laser enters the assembly from the left.

The first generation of the semi-infinite gas cell (figure 3.5) was constructed in approximately ten minutes and consisted of the front and rear mounts for the capillary waveguide and a VCR tee. Weldable ¼" butts were used on the parallel ends of the VCR tee to mount it into the capillary's position and the third connection introduced the inert high harmonic medium (argon or neon gas). At the exit connection of the VCR tee closest to the toroidal mirror chamber, a thin

0.03” Teflon foil was placed between the weldable butt and the tee as opposed to a copper or stainless steel gasket. This foil acted as the semi-infinite gas cell exit foil to be laser ablated and provide the XUV exit aperture. After ablating the Teflon foil, high harmonics were observed at the Princeton Instruments PIXIS:XO 100B x-ray camera for both argon and neon mediums with flux rivaling the 3rd generation capillary waveguides. The main limitation of this design was the limited pumping speed at the exit foil of the semi-infinite gas cell. The small dimensions of the capillary and the long interaction length yielded typically gas densities at the waveguide exit and entrance on the order of a few tenths of a milliTorr, but for the semi-infinite gas cell several Torr were observed initially due to the constricted vacuum system construction (low conductance) and limited pumping speed at the aperture. The large gas pressure after the high harmonic generation region and the mismatch between the object and image plane distance of the refocusing toroidal mirror after the semi-infinite gas cell substantially deformed the XUV beam profile as seen in figure 3.6. This affects the XUV resolution in strong-field investigations as a larger beam profile samples a larger range of field intensities in the interaction region. The next generation semi-infinite gas cell required the incorporation of a higher pumping speed and conductance around the exit aperture.

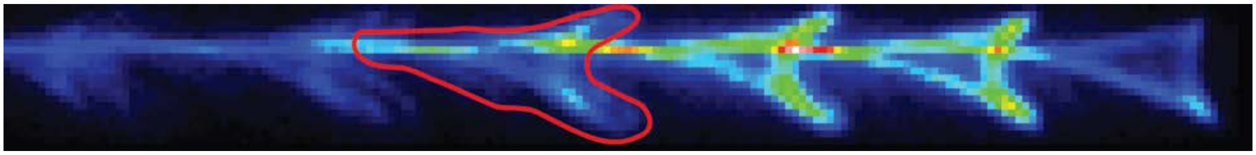

Figure 3.6: Poor XUV mode obtained after spectral dispersion employing the VCR semi-infinite gas cell. The poor mode is obtained due to a mismatch in the optimal object plane distance from XUV refocusing mirror and the exit foil of the semi-infinite gas cell. Energy of the high harmonics increases from left to right while the vertical is energy independent. The dim harmonic at the far-right is at the Al $L_{2,3}$ edge at ~72.5 eV. The mode of a single harmonic has been outlined in red.

The second generation semi-infinite gas cell (figure 3.7) utilized a dedicated mechanical pump evacuating a large chamber with the exit foil of the semi-infinite gas cell in the center. The Teflon exit foil was then mounted in an ultraTorr fitting (figure 3.8), between the set nut and the O-ring, at the end of a 14” x ¼” tube. The use of the ultraTorr fitting created a better gas seal for the cell. This version also maintained effective pumping speed during high harmonic generation, limiting deformation of the XUV beam profile due to plasma and dispersion effects. In this configuration, it was found that the positioning of the semi-infinite gas cell exit foil and the focus of the 800 nm driver were critical for the spectral resolution of the instrument as well as the beam waist of the XUV beam in the interaction region. This is the major constraint of the semi-infinite gas cell. Great care had to be taken in order to find the optimal position for the exit foil and the 800 nm beam focus, utilizing the XUV focal spot size, spectrometer resolution, and harmonic flux intensity as figures of merit. Only by iteration could the optimal conditions be determined, but unfortunately this version did not afford the flexibility to easily iterate through the possible configurations.

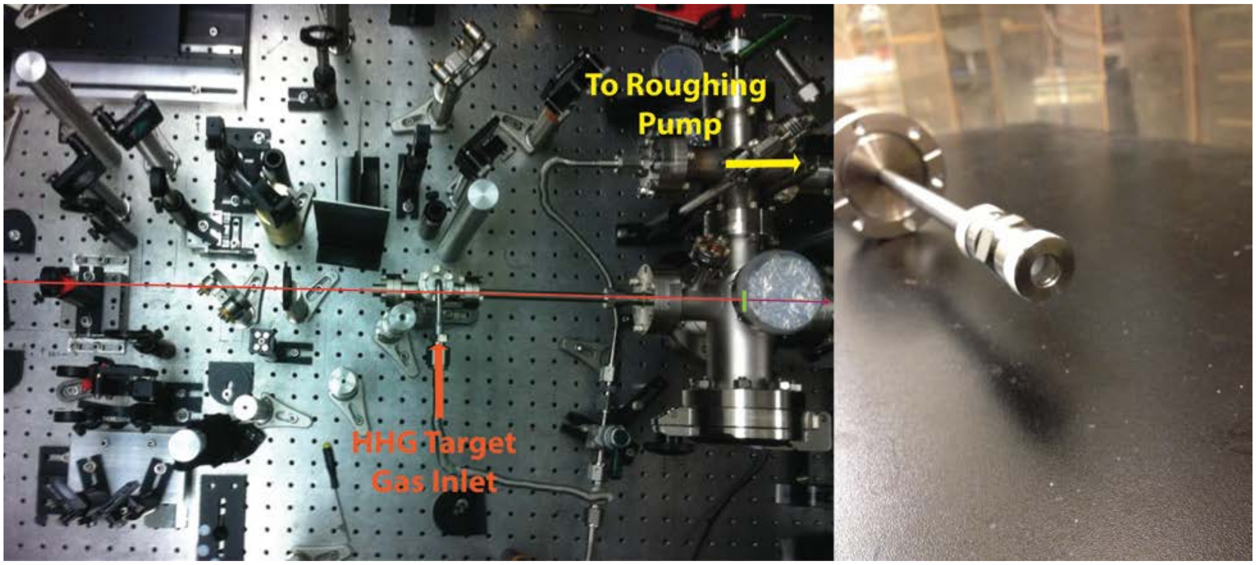

Figure 3.7: Second version of the semi-infinite gas cell. (Left) Chamber assembly for the semi-infinite gas cell. This version boasted an increased pumping speed at the exit foil (located at green hash mark) of the semi-infinite gas cell due to the improved conductance to the roughing pump. The exit foil in this version was mounted utilizing an ultraTorr fitting, preventing the possibility of puncturing the foil when tightening the VCR fitting in the first version. The O-ring of the ultraTorr fitting, shown in figure 3.8, provided an excellent vacuum seal. The 800 nm driver and XUV beam are shown in red and purple, respectively. (Right) Exit foil of the semi-infinite gas cell detached from the chamber assembly. The exit foil of the semi-infinite gas cell was positioned at the center of the makeshift chamber.

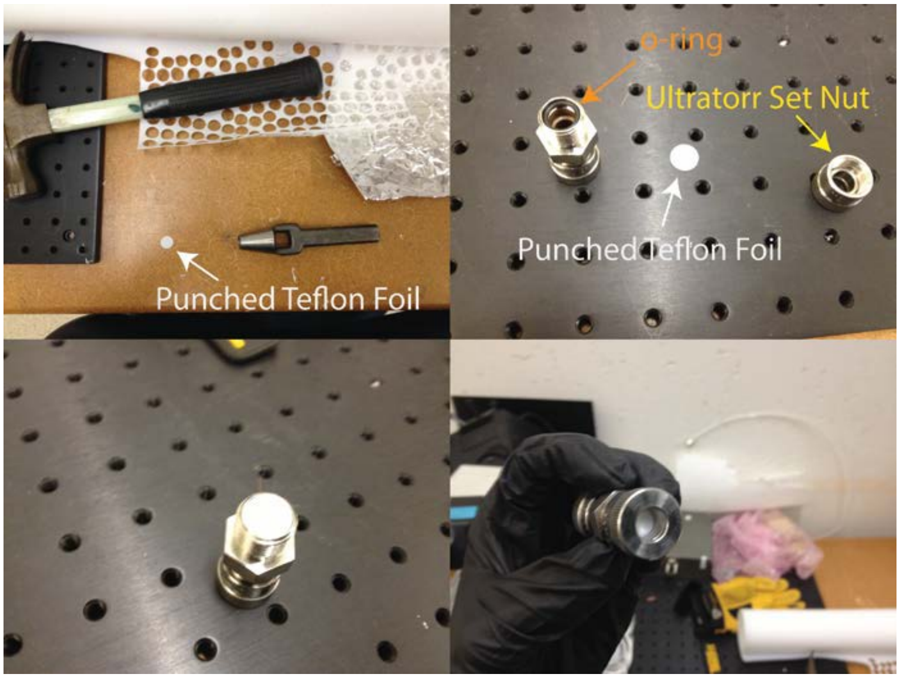

Figure 3.8: Procedure for creating a semi-infinite gas cell out of an ultraTorr union. (Top Left) a 12 mm Semi-infinite gas cell foil is punched from a sheet of 0.03” thick Teflon, and the foil is then wiped cleaned with methanol. (Top Right) The Teflon foil (center) is then placed between the ultraTorr fitting O-ring (left) and the retainer nut (right) as seen in the bottom right and left pictures.

The final version (figure 3.9) of the semi-infinite has cell utilized a specially fabricated exit foil mount of 0.5” diameter (for easy alignment, limiting the risk of ablating the stainless steel tube) and a 14” x 1” semi-infinite gas cell tube. The semi-infinite gas cell tube itself is mounted on a 1” travel translation stage, and in this configuration the parameters of the source could easily be iterated to determine the optimal position for the exit foil and 800 nm focus for maximum spectral resolution, minimum XUV beam waist, and highest harmonic flux. This configuration also allowed easy changing of the semi-infinite gas cell foil without venting the toroidal mirror chamber. The chamber where the semi-infinite gas cell terminates was changed to an 8” diameter by 12” tall chamber with a 1000 L/s Varian turbomolecular pump. This reduced the gas density after the exit foil of the semi-infinite gas cell to a few tenths of a milliTorr. It is paramount that the differential pressure across the semi-infinite gas cell be as large as possible to prevent plasma distortion of the high harmonic beam as well as reabsorption. This third version of semi-infinite gas cell is robust. Once optimized, the only maintenance required is the daily replacement of the semi-infinite gas cell foil and the usual alignment of the 800 nm beam to the XUV optics.

In comparison to the hollow-core capillary waveguide source, the semi-infinite gas cell is substantially more user friendly and reliable. The parameters of both sources are compared in table 3.1:

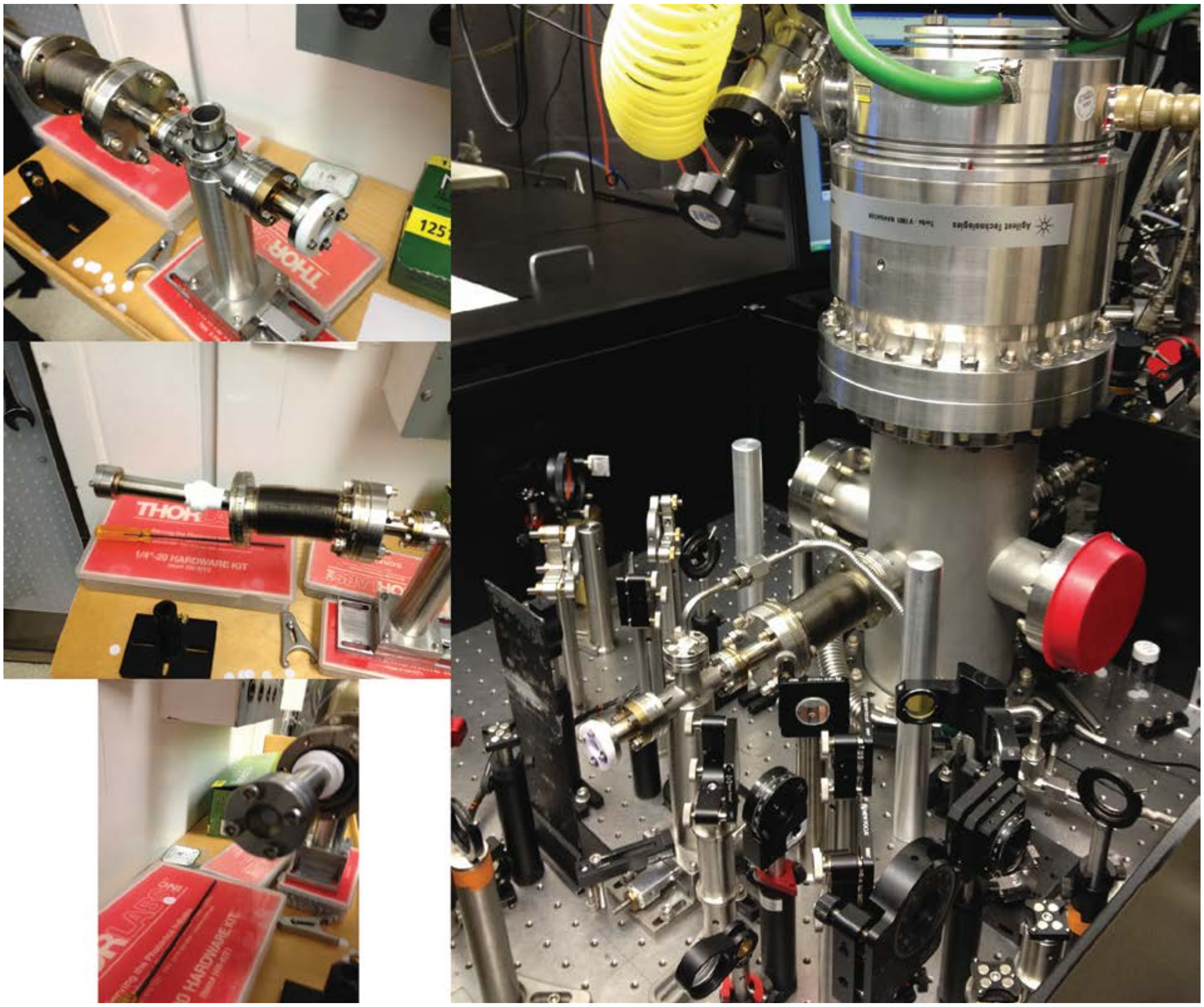

Figure 3.9: Third and final version of the semi-infinite gas cell for XUV transient absorption and high harmonic chamber. (Left set of three) Semi-infinite gas cell from three different perspectives. (Left-Top) Semi-infinite gas cell as viewed from the front, showing the fused-silica laser window affixed to the cell with a Teflon retainer ring and O-ring. The entrance window is attached to a mini-CF tee welded to a post. The vertical part of the tee is the gas inlet for the high harmonic target gas, far from the exit aperture to minimize pressure variation in the harmonic generation region. A translation stage is visible at the bottom and controls the exit foil distance to the refocusing toroidal mirror, TM1. (Left-Center) Middle of the semi-infinite gas cell. An edge-welded bellows is utilized to allow ease of translation of the cell when optimizing the spectral resolution of the instrument. Also, Teflon tape is wrapped around the girth of the cell to prevent sagging of the beam pipe in vacuum due to its own weight; the cell then fits snuggly in the 1.5” diameter vacuum tube of the high harmonic chamber. (Left-Bottom) Teflon exit foil of the semi-infinite gas cell secured with stainless-steel mounting bracket and an O-ring. (Right) Semi-infinite gas cell assembly connected to the high harmonic generation chamber with Varian TV-1001 turbomolecular pump mounted on top.

Table 3.1: Parameters and specifications of high harmonic generation with a semi-infinite gas cell and hollow-core capillary waveguide sources.

Source	**HHG Medium**	**Inlet Pressure (Torr)**	**HHG driver pulse energy (mJ)**	**Output Photons per Pulse at 65 eV**	**Shot-to-Shot Stability**	**Time between alignment**
Hollow-core Capillary Waveguide[19]	Neon	80	1.8	6×10^4	± 15 %	3 hrs
Semi-infinite Gas cell	Neon	140	1.5	1×10^6	± 5 %	> 4 days

One possible explanation for the substantial increase in harmonic flux of the semi-infinite gas cell relative to the capillary is that the decreased interaction length has led to the peak of the harmonic flux being centered at a lower energy (below the Al $L_{2,3}$ edges at ~65 eV). Examining the photon flux per harmonic between the capillary and semi-infinite gas cell in figures 3.4 and 3.10 does not show any significant difference in the peak of the photon flux, therefore it is believed that the semi-infinite gas cell actually generates more harmonic flux than the capillary. Also, it is important to note that the overall increase in total photon flux indicates that not only does the semi-infinite gas cell generate 100x more flux, but also 100x more continuum, which is extremely important for transient absorption. Previous experiments with odd harmonics from a capillary waveguide either required tuning of the harmonic spectrum to the atomic/molecular transitions to be investigated or detuning of the spectrum to generate continuum while sacrificing overall photon flux and resolution. The increase in the continuum flux for the semi-infinite gas cell provides a truly continuous XUV spectrum from ~40-73 eV, a key component for quantitative transient core-level absorption spectroscopy, i.e. resonances falling between harmonics have extremely poor detection efficiency and signal-to-noise.

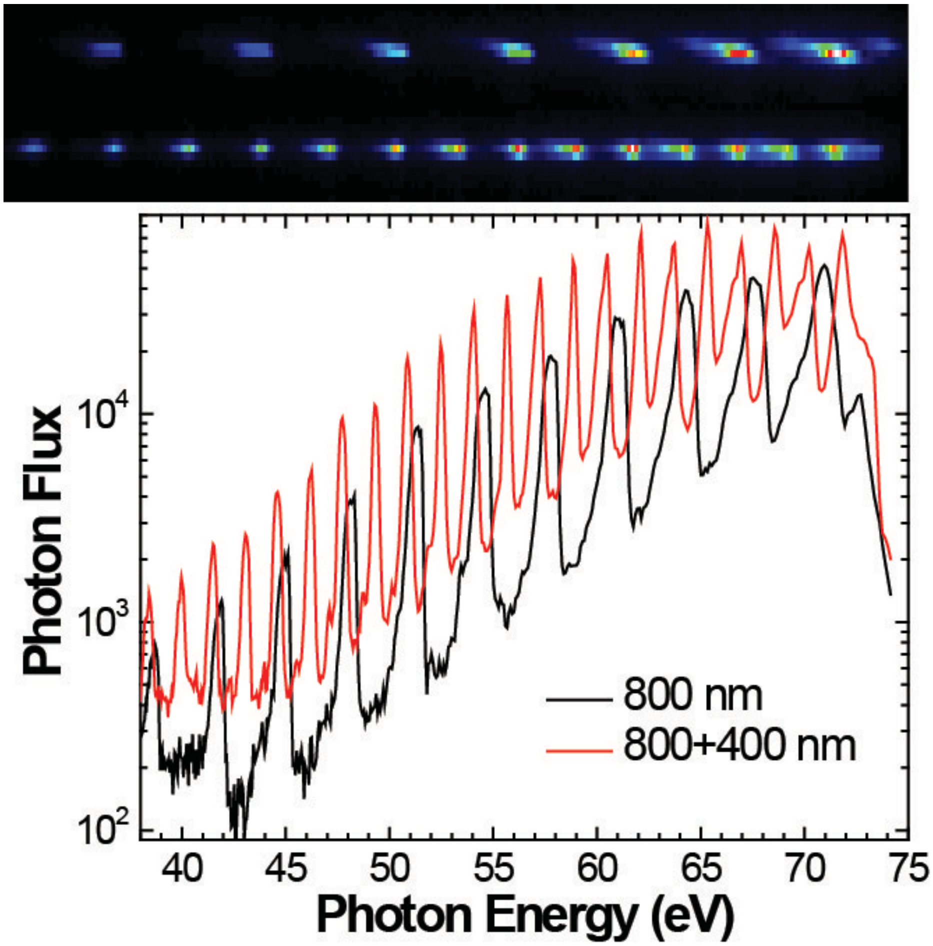

Figure 3.10: Comparison of odd and even high harmonic generation in a semi-infinite gas cell. (Top) Images of the high harmonic spectra measured by the PIXIS:XO 100B CCD camera after spectral dispersion in the homebuilt spectrometer. The upper image is 800 nm driver only high harmonics (odd) and the bottom image is 800 + 400 nm high harmonics (even + odd). (Bottom) Plot of the lineout spectra of even (red) and odd (black) high harmonic generation. It is apparent that generation of even harmonics has a tendency to reduce the spectral width of each harmonic and substantially increase the continuum between adjacent harmonics and the overall photon flux.

3.1.4. Even High-Harmonic Generation

To increase the spectral coverage of the high harmonic transient absorption probe, both odd and even harmonics must be generated, reducing the harmonic spacing from 3 eV to 1.5 eV and also increasing the continuum flux due to the decrease in XUV pulse production by the driving laser. This is seen in figure 3.10. For a 40 fs pulse, there are approximately 15 sub-cycles, and each sub-cycle may generate two bursts of XUV radiation. The interference of 30 XUV pulses leads to a very discrete odd harmonic spectrum with little continuum (10^4 photons per pulse), but by reducing the number of XUV bursts per sub-cycle to one, only 15 XUV pulses are produced. The limited number of XUV pulses leads to an increase in the continuum between harmonics, yielding a more efficient broadband probe.

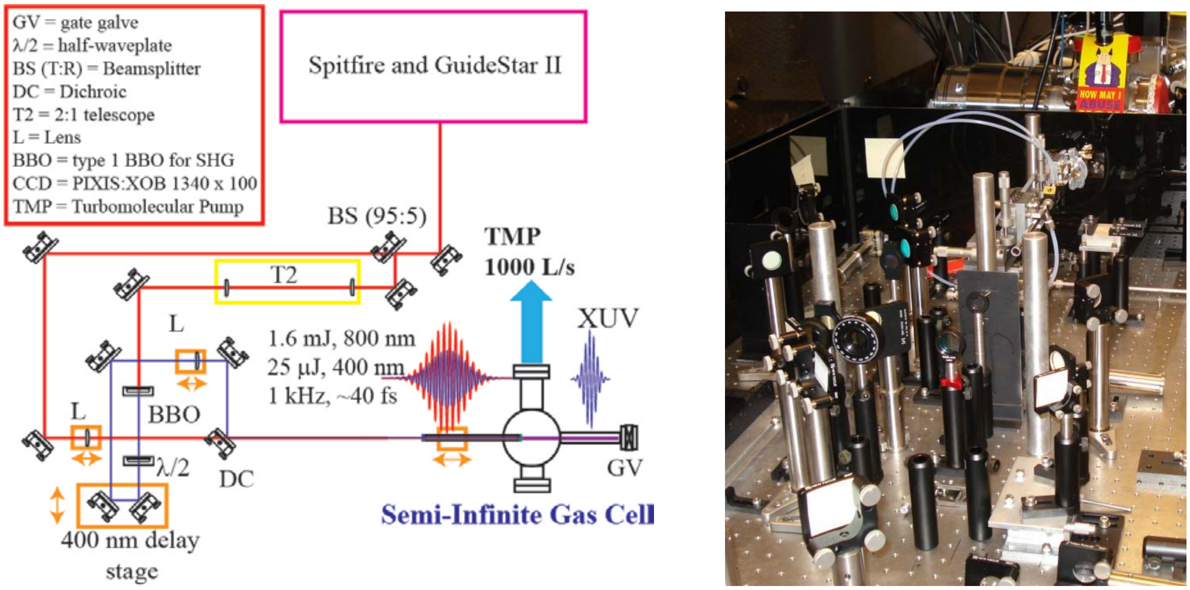

Figure 3.11: (Left) Optical line diagram of the 400 nm SHG line for even harmonic generation. Translation stages are shown as orange boxes. (Right, foreground) Actual optical assembly for even harmonic generation. Legend boxed in red describes all of the abbreviations in the diagram.

An optical layout (figure 3.11) for generating a small amount (20-50 μJ) of the second harmonic of 800 nm (400 nm) was installed prior to the semi-infinite gas cell. Previously, this SHG optical line was installed with the capillary waveguide, but the principle is the same as was discussed in section 1.2.5. The 800 nm high harmonic driver is first split with an 95:5 (Transmitted %:Reflected %) beamsplitter (CVI, BS1-800-90-1012-45P, P = p-polarization) and telescoped to half the original beam waist with a -20 cm (CVI, PLCC-25.4-103.0-UV-800) and 40 cm (CVI, PLCX-25.4-180.3-UV-800) focal length lenses. The beam is telescoped down to increase the doubling efficiency. The 800 nm beam (90 μJ, 40 fs) is then frequency doubled in a 0.2 mm thick Type 1 ß-barium-borate crystal coated P/P for 400-800, $\theta = 29.2^\circ$, $\varphi = 0^\circ$ yielding 30 μJ of 400 nm light (30% efficiency). The polarization of the 400 nm is then controlled by a half-waveplate (CVI, QWPO-400-08-2-R10), and rotates the second harmonic polarization to match the 800 nm driver. A manually actuated translation stage with Vernier micrometer (1 μm precision) acts as a delay line between the 800 nm and 400 nm beams (400 nm is translated so as not to change time zero of the XUV probe relative to the pump beam). The retroreflector is composed of two 400R/800T (R: reflect, T: transmit) dichroic mirrors to remove the residual 800 nm beam from the even harmonic line. All subsequent mirrors are 400 nm HR mirrors (CVI, TLM1-400-45-1025). Finally a 65 cm focal length lens (CVI, PLCX-25.4-309.1-UV-400) focuses the 400 nm beam to the same focal plane as the 800 nm driver, which is recombined with a high energy harmonic beam separator (CVI, BSR-48-1025). Alignment of the SHG optical line for optimal even harmonic generation is described in section 3.3.1.

Generation of even harmonics easily doubles the photon flux observed at the detector. This can be seen in figure 3.12. The fundamental only and 800+400 nm mixed harmonic flux of the odd harmonics remains constant, but in the 800+400 nm mixed case the even harmonics reach the same intensity as the odds. Harmonic generation by the 400 nm beam alone is not capable of generating high harmonics, indicating that the overall driving electric field is altered by frequency mixing and there are not two harmonic generation regions (800 nm and 400 nm). The ratio of even to odd order harmonic as well as overall harmonic flux is dependent on the degree of spatial and temporal overlap of the 800 and 400 nm beams, i.e. if the second harmonic beam waist is smaller than the fundamental or time-delayed the even to odd harmonic ratio will be less than unity. An even and odd order harmonic spectrum with optimal overlap is shown in figure 3.12.

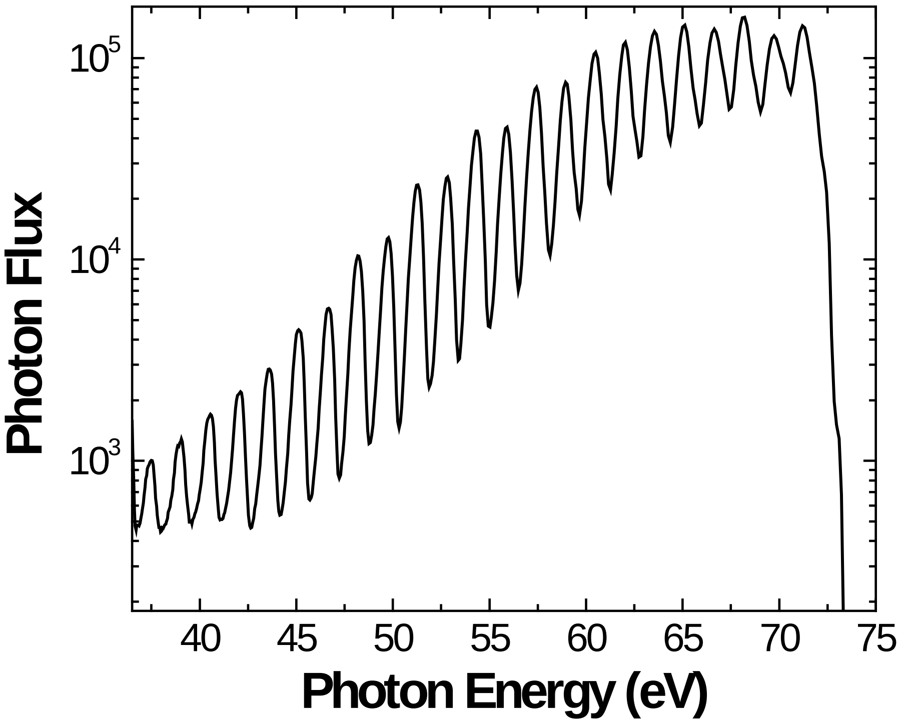

Figure 3.12: Typical neon even + odd high harmonics generated with 1.6 mJ of 800 nm + 25 μJ of 400 nm, 40 fs pulses at a 1 kHz repetition rate in a semi-infinite gas cell (0.1 s integration, 1.8 μm of Al foil). The photon flux is given on a Log_{10} scale for clarity. The significant continuum improvement between harmonics and the general increase in photon flux greatly improves the instrument's detection efficiency and effectiveness.

3.1.5. Vacuum Apparatus and Gas Isolation

Experiments involving corrosive and toxic gases led to deterioration of the optics and optomechanical assemblies in the vacuum chambers. Corrosion occurred predominantly along the XUV beam path as the sample gas cell essentially acts as a molecular beam skimmer, creating a directional source of corrosive materials. The most devastating effect of this was deposition of bromine and iodide on the refocusing toroidal mirror (TM1) after the semi-infinite gas cell. The spectrometer chamber is largely protected due to the Al foil employed to remove the remnant and scattered 800 nm pump light. This Al foil creates a gas barrier between the corrosive material, spectrometer optics, and TE-cooled x-ray CCD camera. In the initial experimental setup, there was no physical barrier to prevent back streaming of chemicals to TM1, which led (in combination with an unfortunate incident involving XeF_2) to the coating of TM1 and the corrosion of all optomechanical components in the chamber as seen in figure 3.13. The chamber needed to be completely replaced due to the persistent contamination and the toroidal mirror was stripped, re-polished, and re-coated by Horiba, Jobin Yvon.

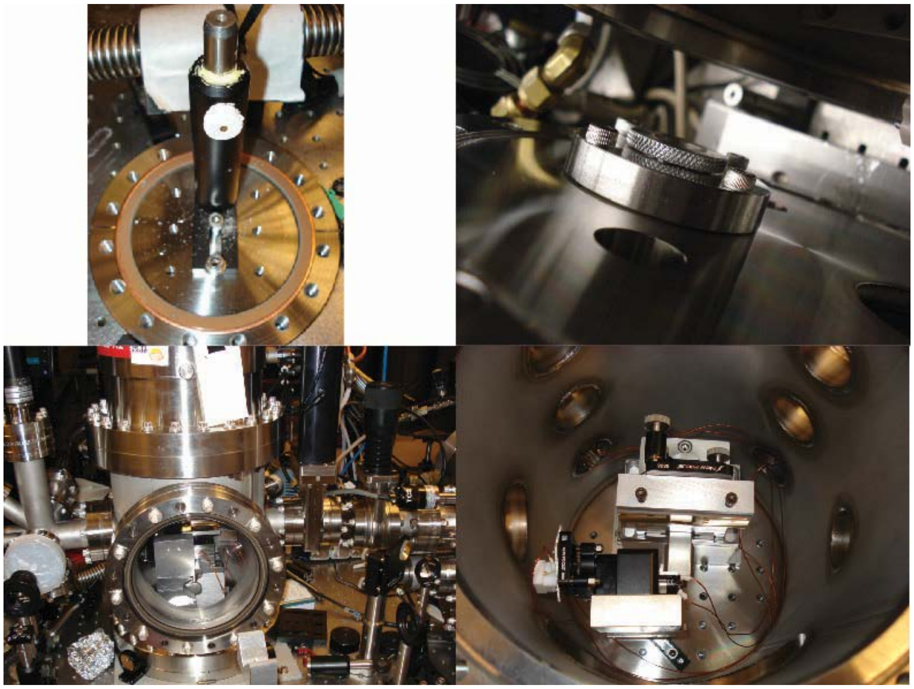

Figure 3.13: (Top Left) Corrosion of post-pedestal assembly originally made from anodized aluminum. The contamination of the toroidal mirror chamber required a complete rebuilding of the mounting assembly and chamber. (Bottom Left) New toroidal mirror chamber exterior and interior (Bottom right) with XUV photodiode on remote controlled flipper mount and toroidal mirror on a translation stage (New Focus, 9067-V). (Top Right) Gas tight Al foil assembly in spectrometer chamber mounted on top of the entrance port for the XUV beam into the chamber.

The replacement of the toroidal mirror chamber afforded the opportunity to incorporate several improvements to the experimental apparatus. First, the turbomolecular pump for the chamber was upgraded to a 1000 L/s Shimadzu Mag-Lev pump to decrease reabsorption of the XUV light as well as reduce vibrational perturbations to the XUV and IR optics, reducing fluctuations in the high harmonic signal. Secondly, the size of the chamber was increased to allow a XUV photodiode to be placed before TM1 as an active monitor of the high harmonic flux independent of the rest of the apparatus. Thirdly, the toroidal mirror was mounted on a translation stage oriented at the optimal angle of reflection (5^o), which allowed the mirror to be aligned easily to the XUV beam yielding the minimum Gaussian beam waist at the focus. Lastly, a VAT (01032-UE01-AAV2) UHV manual Mini-gate valve with 21 mm clear aperture window and 2 ¾ “ UNF flanges was added between the sample and toroidal mirror chambers. Inserting a 200 nm Al foil (Lebow, 0.2Al-0-V1.5) in the VAT gate valve allows gas insolation of the sample chamber during experiments when the valve is closed. This effectively prevents any corrosive material from leaving the sample chamber except via the turbomolecular pump, which was upgraded to a Shimadzu 1000 L/s with nickel coated components to prevent corrosion. Additionally, the Al foil in the spectrometer chamber was reconfigured so that an O-ring is used to seal the foil to the chamber to prevent gas flow (a gas bypass was also installed for pumping across the foil when evacuating or venting the chamber) instead of electrical tape as was previously done. These improvements in conjunction with an argon gas jet purging the pump beam mirror before the sample cell (D-mirror) allows continuous, safe operation with corrosive materials.

3.1.6. XUV Spectrometer

There is a current, chronic issue with the experimental apparatus that requires either a redesign of the spectrometer chamber or a change in how the chamber should be mounted to the table. Currently, the spectrometer chamber is an 8” diameter pipe with a 6” diameter tube extending on center to create a tee-shaped chamber. The tee is oriented such that the 6” tube faces away from the table, forcing the chamber to be mounted into two v-groove stands at either end of the 8” tube as illustrated in figure 3.14.

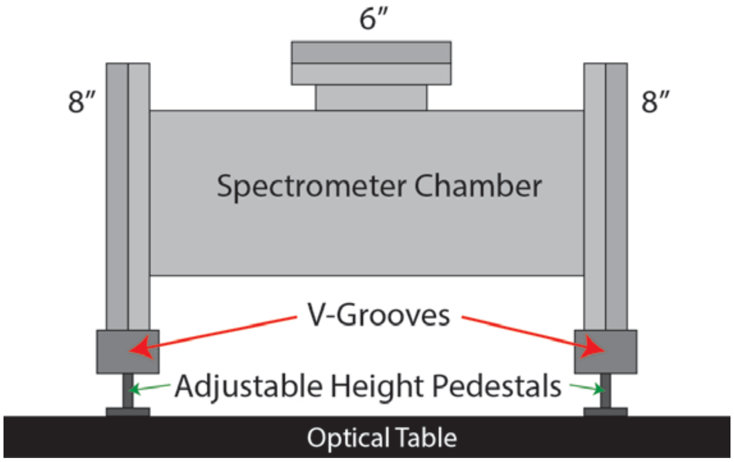

Figure 3.14: Illustration of the current mounting of the spectrometer chamber with indicators for the v-groove mounts and adjustable pedestals.

The issue with the current mounting method of the spectrometer chamber is the adjustable pedestals. These pedestals provide flexibility for orienting the chamber relative to the incoming XUV beam with regard to angle and height, but the weight of the chamber is constantly driving these pedestals to shorter heights. This is due primarily to the constant vibration of the chamber by the turbo pump and the lack of strength in the threads of the adjustable height screws. As a result, the entire chamber is sagging very slowly and manifests itself as a constantly degrading spectrometer resolution due to the changing angle of the XUV beam to the toroidal mirror (TM2), which focuses onto the x-ray CCD camera as seen in figure 3.15. The spectrometer resolution at one point in time was at 400-600 meV due to this sagging process. By iterating adjustments to the pitch, roll, yaw, and height of the chamber over a month, constantly checking the spectral resolution at the xenon $4d^{10}5s^{2}5p^{6} \rightarrow 4d^{9}5s^{2}5p^{6}np$ Rydberg transitions, the spectrometer resolution was restored to 250 meV or better.

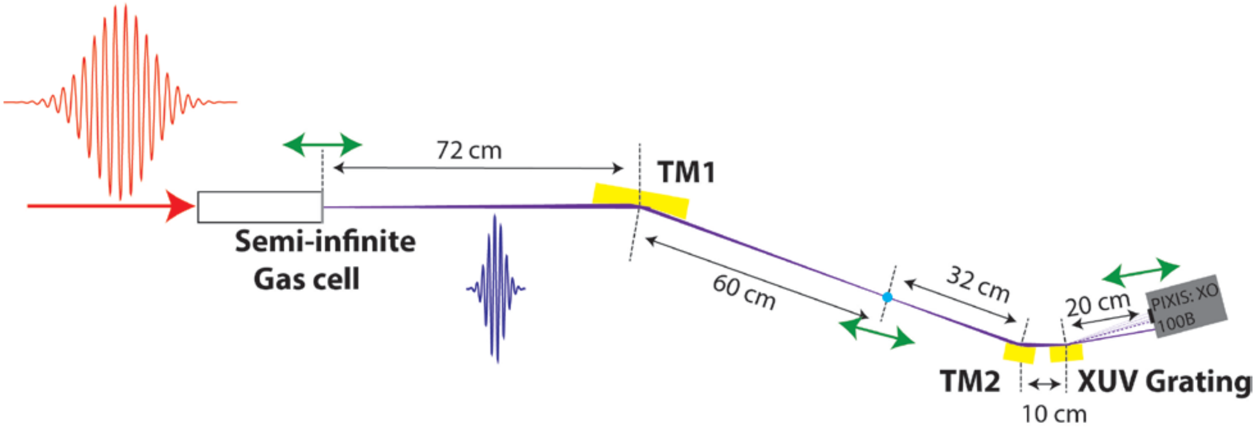

Figure 3.15: XUV optical layout for a semi-infinite gas cell source with all relevant distance parameters provided.[19] The focusing toroidal mirrors for the interaction region gas cell (blue dot) and the toroidal mirror for focusing onto the PIXIS:XO 100B XUV camera are labeled TM1 and TM2, respectively. As the focal plane of the 800 nm driver in the semi-infinite gas cell is adjusted to tune the energy of the harmonics, the additionally coupled XUV imaging distances of TM1 and TM2 change as well and are labeled with green arrows.

3.1.7. Al Foils in Experimental Set-up

The additional photon flux generated by the semi-infinite gas cell requires that additional foils be placed in the beam path, increasing the total foil thickness experienced by the XUV beam from 1 μm to 1.8 μm. The increased number of foils is necessary to prevent over-saturation of the CCD camera at the minimum integration time, corresponding to the read-out time of the array. Moreover, if the peak-to-valley ratio of the harmonics is too large, quantitative resolution is lost in the valley of the harmonics due to the contrast range limitations of the camera. The camera gain could be lowered by switching from “low-noise” to “high-throughput” mode, but this would increase the shot noise of the system as the amplifier used in the signal read-out is changed. The camera is currently on the lowest gain setting for “low-noise” mode. As a result, increasing the Al foil thickness in the beam path attenuates the beam instead, and the extent of attenuation may be determined from the CXRO database of materials transmission.[185,186] In addition, each aluminum foil upon exposure to air oxidizes to Al_2O_3 within 100 ps, yielding an approximate 4-5 nm passivation layer of Al_2O_3 on each surface of a foil.[187] Several plots are presented in figure 3.16 demonstrating the effect of the Al_2O_3 passivation layer, and figure 3.17 shows the total XUV transmission after considering all foils in the XUV beam path and how it compares to the observed high harmonic spectrum. It can clearly be seen that the observed harmonic flux intensity follows the shape of the transmission curve in energy.

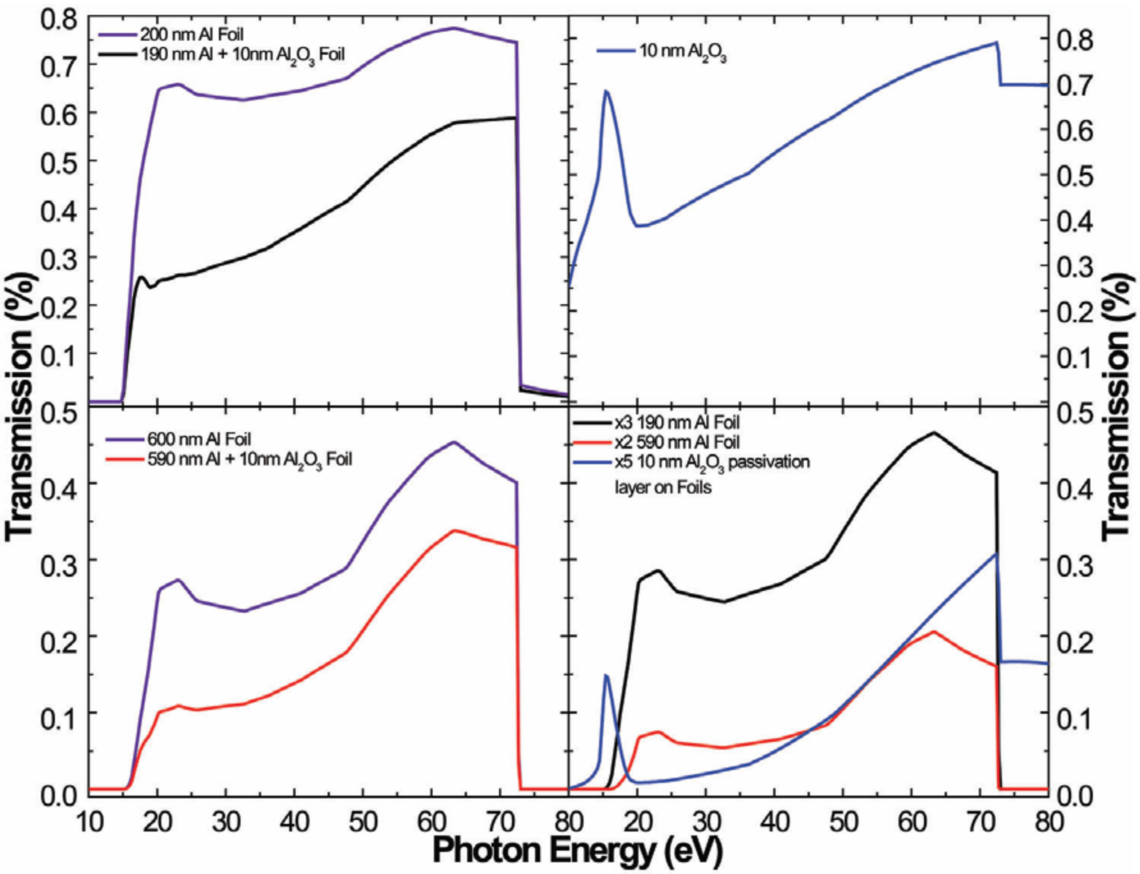

Figure 3.16: Plots of the transmission efficiency for Al foils and their Al_2O_3 passivation layer of approximately 4-5 nm at each surface. (Top Left) Transmission of a single 200 nm Al oxide free foil in red and a 190 nm Al, 10 nm Al_2O_3 foil in black. (Bottom Left) Transmission of a single 600 nm Al oxide free foil in red and a 590 nm Al, 10 nm Al_2O_3 foil in black. (Top Right) Transmission of a 10 nm Al_2O_3 passivation layer in blue. (Bottom Right) Overlay of Al foils total thickness (200 nm and 600 nm foils) and the total Al_2O_3 passivation layer thickness.

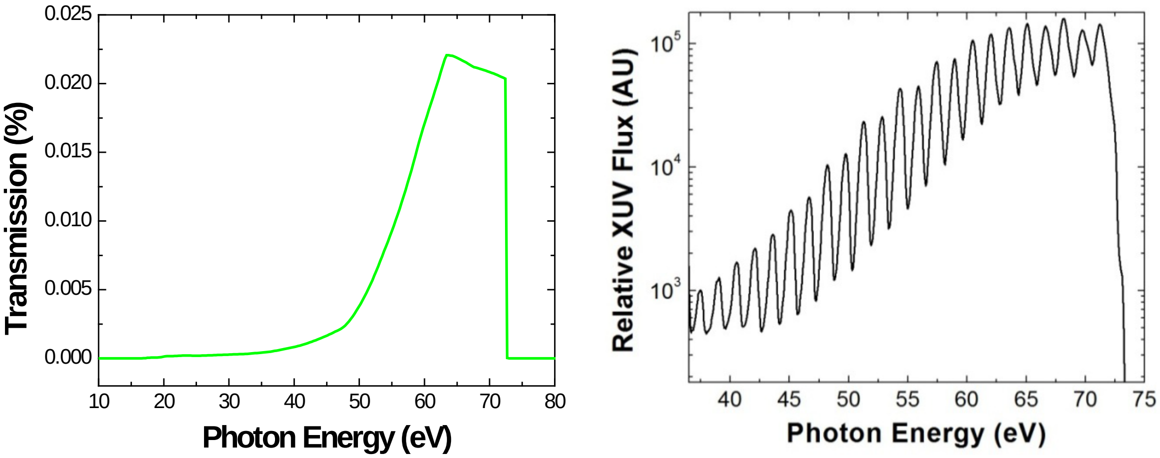

Figure 3.17: (Left) Total transmission of the Al foils taking into consideration the Al_2O_3 passivation layer as compared to the measured XUV spectrum (Right).

3.2. Current Experimental Apparatus

Taking into account all of the experimental changes, figure 3.18 accumulates these adaptions and illustrates the layout of the current experimental apparatus:

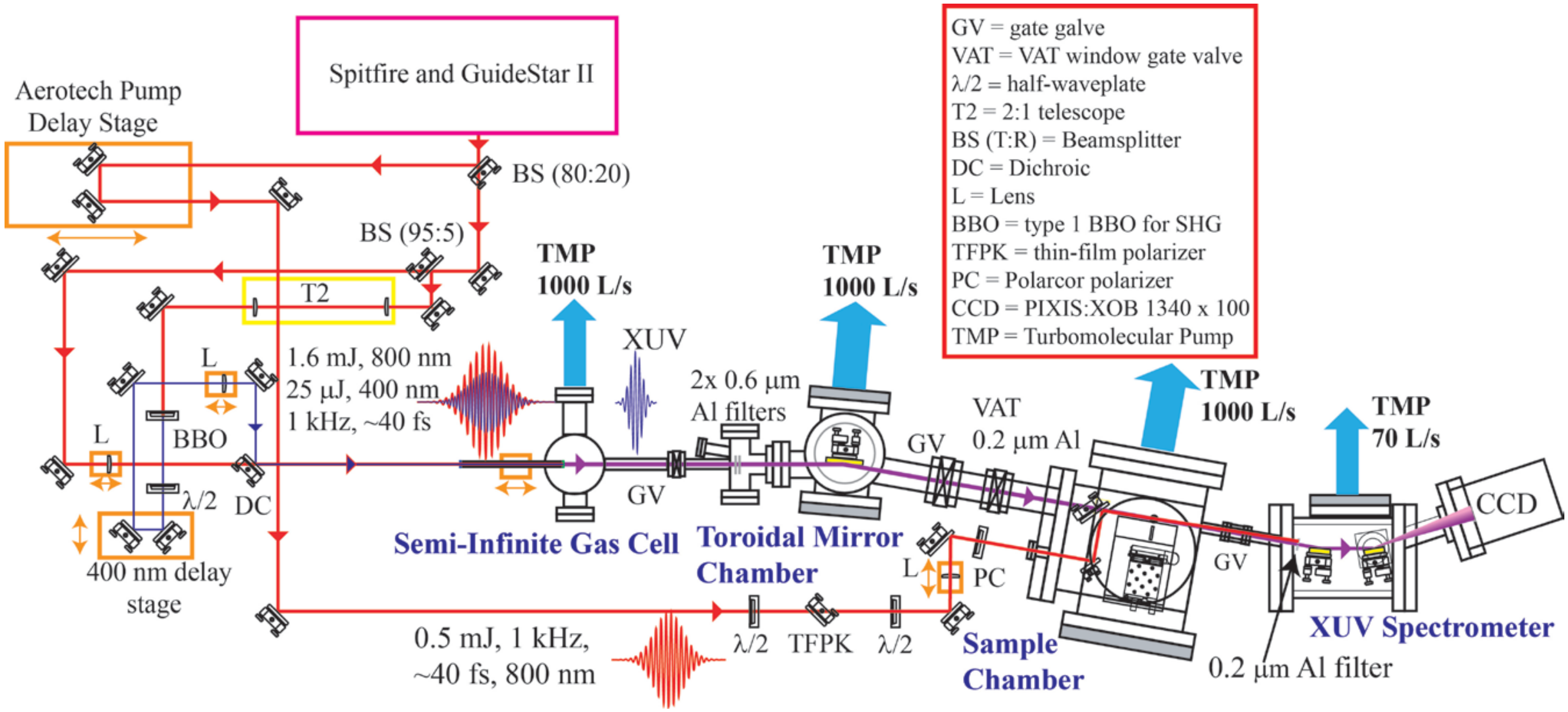

Figure 3.18: Diagram of the revamped femtosecond XUV transient absorption apparatus. The legend boxed in red describes all of the abbreviations in the diagram. Each chamber is labeled in bold blue type, translation stages are boxed in orange, and the location of all turbomolecular pumps is indicated by a blue arrow.

3.3. Experimental Operation for Sustained Data Collection

Typical preparation for a multi-day experiment is in itself a several day procedure as it requires the utmost stability of the laboratory environment, femtosecond laser system, and vacuum apparatus. Single day operation may be accomplished within only a few hours if the femtosecond laser has been successfully aligned and maintained the previous day. Both operation methods are described here, first the single day operation is described in detail, and then multi-day operation is described as an adaptation of the single day procedure given the various changes and important stability factor guidelines.

3.3.1. Single Day Operation

For single day operation, the Spitfire Pro is typically started first thing in the morning by initializing the Empower pump laser. The Tsunami and Millennia are typically already in operation as warm-up time for these systems are several days to several weeks depending on the environmental conditions. The Spitfire regenerative cavity is allowed to thermalize for at least thirty minutes before the high-speed drivers of the Pockels cells are engaged. This allows the cavity to obtain close to normal operation conditions before ejecting the amplified beam to the compressor cavity. This prevents abnormal thermal drift in the compressor and decreases the need to realign optics therein. Spectra-Physics states that the laser is stable within 30 minutes of operation, but typically the regenerative amplifier requires 2 hours for the intra-cavity pulse train to reach a steady-state build-up time. Alignment of the optical system may be conducted during this period given that the GuideStar II system is active and the alignment occurs beyond the position locking system. If the GuideStar II is to be aligned, the Spitfire should be allowed to stabilize first to prevent erroneous alignment. Alignment of the GuideStar should be conducted as outlined in the Newport manual in conjunction with typical iris alignment procedures. Alignment of the second motorized mirror and the following mirror should be done by removing the successive mirror and aligning with irises at a distance, respectively.

Once the Spitfire Pro has reached optimal operation or the GuideStar II has been engaged, the Teflon foil of the semi-infinite gas cell must be replaced with a new foil. Each successive day of operation requires a new semi-infinite gas cell 0.03” thick by 0.5” diameter Teflon foil as the alignment of the system will have changed slightly. Replacement of the foil reduces unnecessary gas flow across the aperture due to an oversized exit hole as discussed above. Replacement of the foil and alignment of the semi-infinite gas cell requires venting of the first (SIGC chamber) and second (toroidal mirror and Al foil chamber) vacuum chambers. The SIGC chamber is vented directly to atmosphere, after the turbomolecular pump has spun completely down, as there are no critical components that will suffer from exposure to humid air. The toroidal mirror chamber, and all the other chambers for that matter, is vented with dry nitrogen. Each chamber has an overpressure flange that prevents the chamber from being pressurized with nitrogen to a dangerous level. It is crucial that the overpressure flange be put in the venting configuration before purging with nitrogen. The pressure on the nitrogen tank is also set so as not to pressurize beyond 15 psia as an additional safety precaution. For the SIGC chamber, a 1 1/3” CF tee is on the backside of the chamber with a Viton gasket seal, which must be loosened prior to venting to prevent overpressurization. For the interaction chamber and the spectrometer chamber, the top access flanges are Viton gasket sealed so the retainer bolts should be removed before purging.

Once the first two chambers have been vented, the two 7.000” (height table to iris center), keyed (tight-fit ¼”-20 dowel pin matched to the optical table) optical post irises may be used to align the beam employing a beam profiling CCD camera and a turn-out mirror (in the same chamber as the Al foils) for removing the 800 nm driver from the high harmonic beam. Once the driving laser beam has been aligned to the first two chambers, the rest of the apparatus will be aligned as well to the XUV, which follows closely the 800 nm driver path. The semi-infinite gas cell is then reinstalled and the system returned to vacuum.

It is important to note here that the two 7.000”, keyed irises are crucial to the experimental apparatus as the entire system is aligned to them. During the upgrade of the system described above, each chamber and XUV optic was aligned using these irises. Aligning the system to a different iris set will result in a change of the properties of the XUV beam at the interaction region focus and the spectral dispersion in the spectrometer, even if they differ by a few tenths of an inch (which is insignificant if using post-pedestal irises). The change from post-pedestal irises to pure post, keyed irises greatly improved the consistency of alignment day-to-day and person-to-person.

Upon reaching the optimal base pressure of at least 10^{-5} Torr, high harmonics may be generated. With all gate valves closed, the 1.5 – 1.7 mJ 800 nm driver may be let into the semi-infinite gas cell chamber with the cell pressurized with neon gas to approximately 120 Torr. This laser-ablates an exit aperture for the semi-infinite gas cell. The presence of the neon gas limits the amount of Teflon ablated debris that deposit on the entrance window (CVI: W2-PW1-0704-UV-670-1064-0: UV-grade fused-silica window, 670-1064 nm AR coated, 1/8” thick x 0.75” diameter). The neon gas in the cell is then purged to remove any remaining material from the laser ablation process and the cell is refreshed with neon to a pressure of approximately 120 Torr. The pressure is measured via a Baratron gauge (MKS Baratron: 890B13TCB2GT1S, type 890 single-ended, absolute, 1000 Torr pressure range, 4 VCR male rotatable, +13 to +32 VDC input, 1% accuracy reading, integrated LED display, standard enclosure, side exit electrical connector) attached to the semi-infinite gas cell itself. After allowing several minutes for the stabilization of the neon gas pressure as well as any additional laser ablation resulting from pointing corrections of the GuideStar II system, the x2 0.6 μm Al foils for removing the 800 nm pulse from the XUV beam are put into the beam path in the toroidal mirror chamber (gate valve between SIGC and foils is still closed at this point). The gate valves for the system may then be opened, and the VAT gate valve with the additional 0.2-0.3 μm Al foil is closed, gas sealing the interaction region (there is an additional Al 0.2 μm Al foil at the entrance to the spectrometer chamber which is pumped across by a bypass VCR valve). With all the foils in place, there is 1.8 μm of Al foil in the beam path, attenuating the beam as noted and discussed previously.

The 800 nm driver may then again be sent into the interaction region. The PIXIS:XO 100B 1340x100 pixel x-ray CCD camera should have previously been activated and cooled to at least -70 ºC, assuming the spectrometer chamber has attained at least a vacuum base pressure of high

10^{-7} Torr. If the base pressure of the spectrometer is higher, the risk is run that water or oil will condense onto the CCD array. If water condenses on the array, the chip may short out. With the camera at temperature, the driving laser will generate harmonics and should be visualized on the output of the camera. Typical optimization routines are conducted with the PIXIS camera gain at 1 (this means 4 electrons generated by XUV hits on camera per pixel are required for one digital count), “low-noise” mode with an integration time of 0.05-0.2 seconds, depending on the harmonic flux and read-out time. If the system is running effectively, harmonics from 40 to 72.5 eV should easily be observed with a count rate of 60k per image, per pixel with a 0.2 s integration time. The semi-infinite gas cell does proceed through a “warming-up” period of approximately 1 hour before the most stable, highest XUV flux is obtained. If the harmonics do not reach this throughput, it may be necessary to optimize the high harmonic process. Typically, the compression of the 800 nm pulse from the Spitfire Pro requires adjustment as it drifts from the minimum pulse duration on a 30 minute to an hour timeframe, which is discussed later. The pressure in the semi-infinite gas cell may also need to be adjusted, but the optimal pressure is typically found between 100 and 140 Torr, while efficiency drops dramatically outside of this range. Lastly, if the collimation or beam size of the Spitfire has changed, it may be necessary to translate the focusing lens of the driver for the semi-infinite gas cell. This may attenuate the photon flux and/or the peak energy obtained by the high harmonic generation process. These two parameters are coupled to the distance between the focal plane of the driving laser beam and the exit foil of the semi-infinite gas cell. Adjustment of these parameters is essentially optimizing the filament produced near the semi-infinite gas cell foil to obtain the longest interaction length (high harmonic flux and high energy photon generation) and proper phase matching conditions for the photon energies being produced. This is analogous to the procedures employed to optimize high harmonic generation in a capillary waveguide, except in a semi-infinite gas cell the filament length and position are additional parameters. Typically, if the semi-infinite gas cell has been optimized recently, very little of the variables have changed beyond the compression of the Spitfire. This drastically reduces day-to-day operational optimization time.

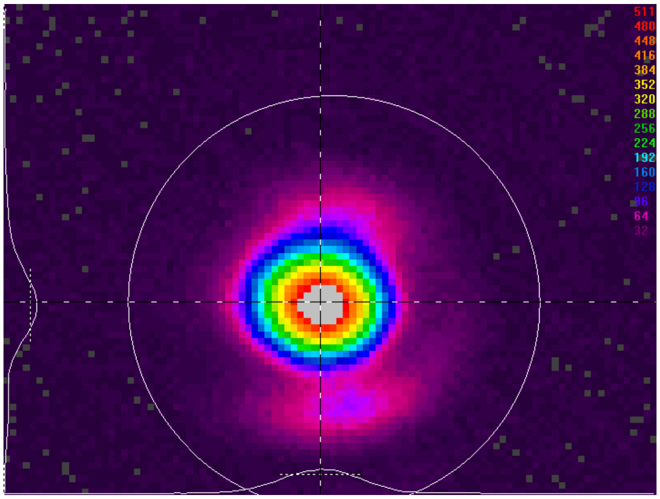

Figure 3.19: Spiricon beam profile of the focus of a 78 cm focal length lens (CVI, PLCX-25.4-360.6-UV-800) at the exit foil of the semi-infinite gas cell. The beam waist is Gaussian with ω_0 = 100 μm.

Until this point, only the odd harmonics have been generated due to the symmetry of the driving 800 nm field. To increase the ability of the instrument to detect all possible transient chemical species via their optical signatures, it is desirable to increase the spectral coverage of the high harmonic probe. This is accomplished by introducing approximately 25 μJ of the second harmonic (400 nm) to the 800 nm driving beam for high harmonic production as was outlined above. Once constructed, the day-to-day alignment is quite simple, except for the overlap in time and space with the main 800 nm driver of the high harmonics. To overlap the beams in space, the 400 nm beam is aligned to the same 7.000”, keyed irises that the 800 nm beam is aligned, which is sufficient at this point. Spatial overlap can further be adjusted once temporal overlap has been achieved and the 800 nm driver has laser ablated the exit aperture of the semi-infinite gas cell by using the hole as a positional reference. When the 400 nm beam is centered on the laser ablated hole, symmetric diffraction patterns of the beam is observed in the far field (employing the turn-out mirror in the toroidal mirror chamber). The temporal overlap is established by inserting a Type 1 ß-barium-borate crystal coated P/P for 400-800/267 nm, $\theta = 55.5^\circ$, $\varphi = 0^\circ$ in the shared beam path of the 400 and 800 nm light after the recombining harmonic separator and rotating the polarization of the 400 nm light perpendicular to the polarization of the 800 nm light. By monitoring the output spectrum on an Ocean Optics HR2000 spectrometer after four 267 nm high reflection mirrors, the time delay of the 400 nm beam relative to the 800 nm beam can be adjusted to generate 267 nm light, indicating temporal overlap of the fundamental and second harmonic pulses. Final adjustment of the temporal and spatial overlap is accomplished by observing the ratio of even and odd harmonics on the PIXIS CCD camera. Optimal even harmonic generation is achieved when the even and odd harmonic flux is equal (by maxima) and the maximum matches or exceeds the flux of just the odd harmonic alone.

Once harmonic generation has been optimized, the interaction gas cell may be moved into the beam path. The center of the gas cell may be found by scanning the cell horizontally, perpendicular to the XUV beam path to an edge of the entrance/exit slit and then scanning the vertical direction. By iterating horizontal and vertical movements while monitoring the XUV photon flux, the edge of the entrance/exit slit may be outlined until a tangential point is found (any vertical movement decreases photon flux). The cell may then be scanned to the opposite edge of the entrance/exit slit and the center can be calculated since the stage is encoded. The gas cells have an entrance/exit slit width of 200 μm, or 2000 counts on the stage since 1 count = 0.1 μm. At this point it may also be necessary to obtain the high harmonic beam waist.

The high harmonic beam waist may be determined by scanning the horizontally perpendicular translation stage (Physik Instrumente: M-665-K003) to 60k counts, where a knife-edge is located. Scanning the stage positively in 100 count (10 μm) steps and monitoring the integrated photon flux of a single harmonic provides an estimate for the XUV beam waist. Monitoring at multiple harmonics shows that the beam waist is independent of energy, but for ease an intense harmonic is chosen for the measurement. Figure 3.20 shows a typical knife-edge measurement of the harmonic at 65 eV, yielding a beam waist of 22 ± 2 μm. This beam waist is similar to those obtained for a capillary waveguide on this experiment.

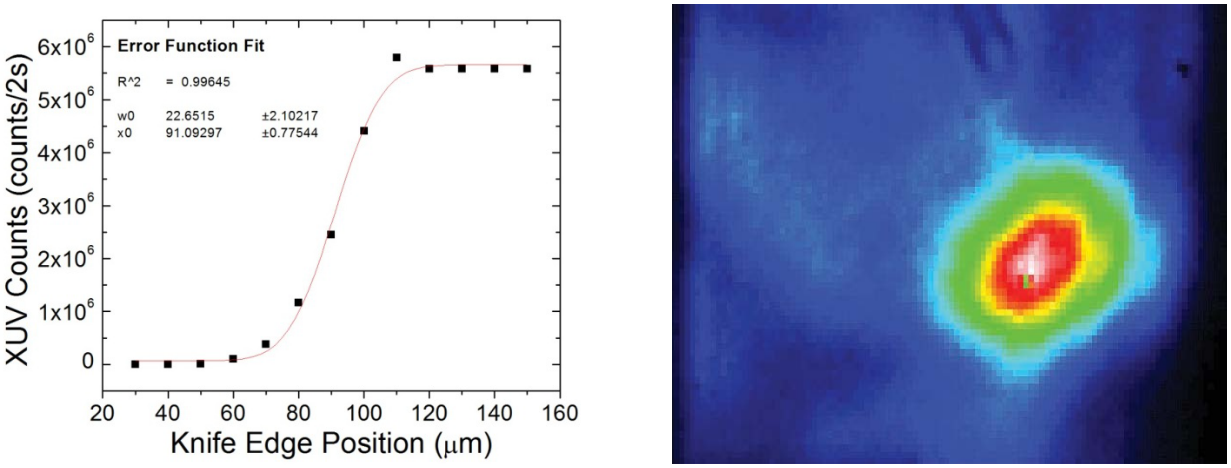

Figure 3.20: (Left) Knife-edge measurement of XUV beam waist at the interaction region for harmonic at 65 eV with Error function fit yielding a beam waist of 22 ± 2 μm. (Right) Typical XUV beam profile from a semi-infinite gas cell showing the excellent beam mode quality as measured by the PIXIS:XO 100B CCD camera mounted to the exit 1 1/3” flange of the gate valve between the sample and spectrometer chambers. The incoherent scattering of the beam illuminates the near-edge shape of TM1 as seen in blue. The beam is centered on the mirror.

An XUV beam waist larger than ~20 - 25 μm indicates that either the focal plane at the interaction region has shifted to before or after the sample gas cell, or the beam waist itself has increased. If the beam waist is larger, two things must be checked:

1) The knife-edge must be scanned parallel to the XUV beam path and the beam waist re-checked after each position iteration to verify that the knife-edge (and subsequently the center of the interaction gas cell) is at the focal plane. The knife-edge should be positioned at the focal plane following this procedure. Given the long confocal parameter of the XUV beam (~5 cm), the position of the knife-edge is a course adjustment. New Focus picomotor movements of 50k counts (arbitrary motor runtime during actuation by Newport proprietary software) in either direction relative to the beam propagation are sufficient for finding the XUV beam waist.

2) If the knife-edge iterative scan for finding the focal plane determines that the beam waist itself is abnormally large implies that the distance between the semi-infinite gas cell exit foil and the toroidal mirror is not correct. This error in the object plane distance (TM1 to semi-infinite gas cell) affects both the XUV focus and the resolution of the spectrometer. The distance between the semi-infinite gas cell exit foil and toroidal mirror must then be iterated and checked by the spectrometer resolution, monitoring the static absorption of xenon. Once the maximum spectral resolution is obtained, the focal plane of the XUV light at the interaction region may be found and the beam waist determined via step 1. At maximum spectral resolution, the minimum beam waist should be obtained.

After the minimum beam waist is obtained, the $4d \rightarrow 5p$ static absorption spectrum for atomic xenon may be collected to establish the spectral resolution of the instrument. First, since the high harmonics only illuminate 3-5 rows (60-100 μm) of the PIXIS CCD camera, a "region of interest" (ROI) is specified so that only ~10 rows of data are collected, minimizing the readout time of the camera and decreasing overall data collection time. Then, a rough energy calibration may be determined for the high harmonic spectrum employing the four orders of diffraction observed of the Al $L_{2,3}$ absorption edge at 72.7 and 73.1 eV, respectively.[19] This provides a very rough energy calibration of the instrument (±0.2 eV). Finally, two measurements are needed to acquire a static spectrum and these measurements should be taken as quickly as possible relative to each other to minimize the noise induced by the fluctuation in the harmonic flux. Ideally, to minimize this noise, data should be collected in the manner of gas in, gas out, gas in, gas out, etc…, but this takes an excessive amount of time. Instead, a collection of spectra (64 images, 0.2 s integration, ROI) are taken in the presence and absence of xenon gas in the interaction cell. Employing a Valin 4A-H1L-V-SS-TC metering valve (HR Series inline metering valve with $C_v = 0.007$, ¼" double compression ferrules both inlet and outlet, stainless steel, fluorocarbon rubber gasket seals, with turns counter), four turns yields approximately 20-25 Torr of xenon (non-resonant OD ~64 eV of >0.1) gas in the interaction region, which is sufficient for static measurements. Four spectral features are observed with the following final states and transition energies: 65.1 eV $4d^9 5s^2 5p^6 (^2D_{5/2})6p$, 66.4 eV $4d^9 5s^2 5p^6 (^2D_{5/2})7p$, 67.03 $4d^9 5s^2 5p^6 (^2D_{3/2})6p$, and 68.3 $4d^9 5s^2 5p^6 (^2D_{3/2})7p$.[153] Analysis of the various $4d^{10} 5s^2 5p^6 \rightarrow 4d^9 5s^2 5p^6 np$ Rydberg states yields the instrument resolution by fitting the resonances to a Voigt profile, which is a convolution of a Gaussian and Lorentzian peak function. The equation for a Lorentzian peak function is:

$$Lorentzian(E) = OD_0 + \frac{2A_L}{\pi} \frac{\Gamma_L}{4(E - E_c)^2 + \Gamma_L^2} \tag{3.4}$$

where OD_0 is the baseline non-resonant absorption around the fit resonance, A_L is the area of the Lorentzian peak, Γ_L is the Lorentzian peak width, and E_c is the peak center. The equation for a Gaussian peak function is:

$$Gaussian(E) = OD_0 + \frac{A_G}{\Gamma_G \sqrt{\pi/2}} e^{-2\frac{(E - E_c)^2}{\Gamma_G^2}} \tag{3.5}$$

where A_G and Γ_G are the area and width of the Gaussian peak, respectively. By convolving the Gaussian and Lorentzian peak functions, the equation for a Voigt peak function is:

$$Voigt\left(E\right) = OD_0 + A_V \frac{2\ln\left(2\right)}{\pi^{3/2}} \frac{\Gamma_L}{\Gamma_G^2} \bullet \int_{-\infty}^{\infty} \frac{e^{-E'^2}}{\left(\sqrt{\ln\left(2\right)}\frac{\Gamma_L}{\Gamma_G}\right)^2 + \left(\sqrt{4\ln\left(2\right)}\frac{\left(E-E_c\right)}{\Gamma_G} - E'\right)^2} dE' \tag{3.6}$$

where A_V is the area of the Voigt peak and E' is the energy difference from E_c. The width of the Lorentzian is fixed to the corresponding natural lifetime of the transition ($\Gamma_L = 114$ meV for the $4d^9 5s^2 5p^6 (^2D_{5/2}) 6p$ state at 65.1 eV)[153] as shown in figures 3.21 and 3.22. The spectrometer resolution is then determined by the Gaussian width of the Voigt fit, which typically ranges between $\Gamma_G = 170 - 250$ meV.

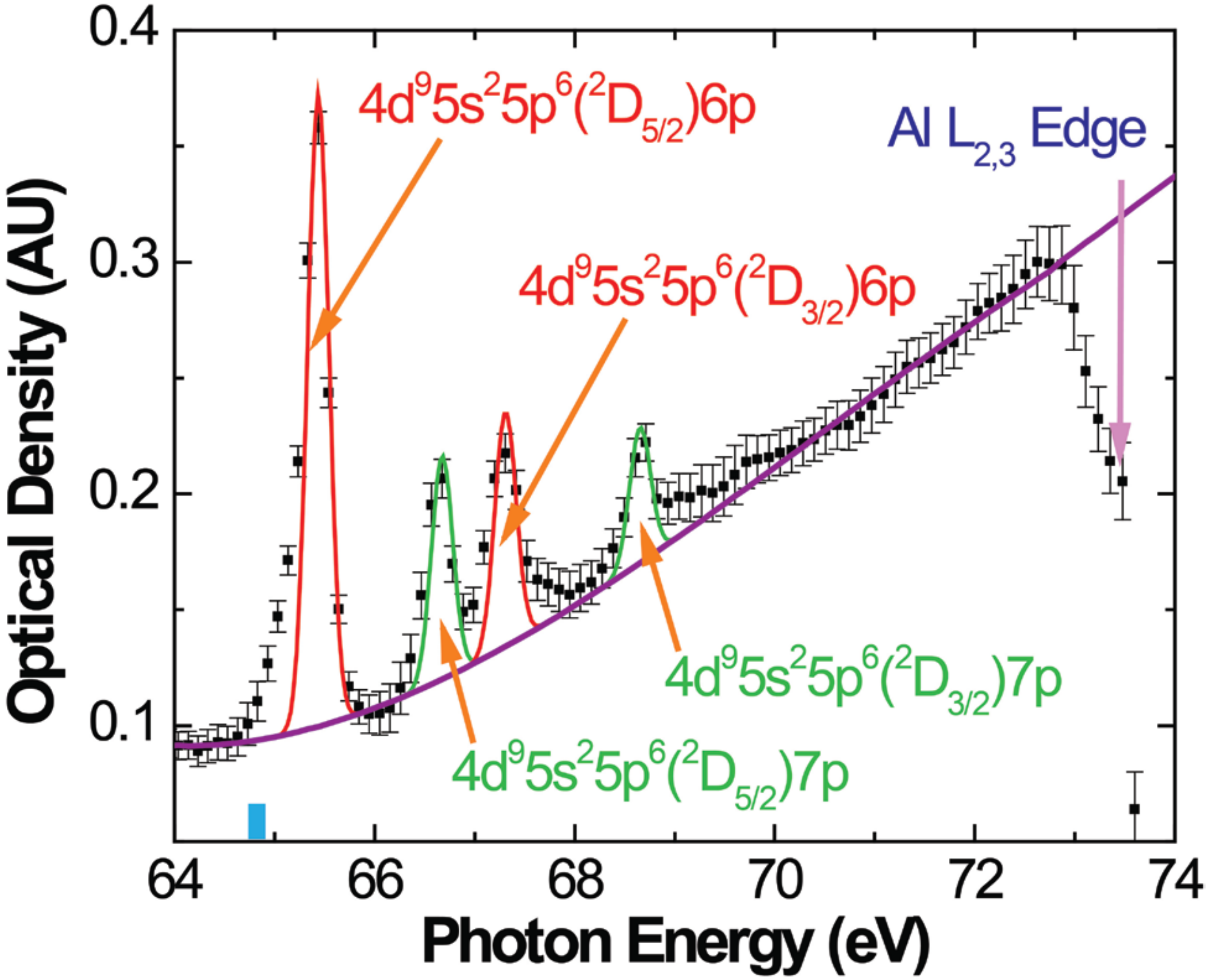

Figure 3.21: Xenon static absorption spectrum from 64 to 74 eV showing the four predominant Rydberg $4d \rightarrow 5p$ transitions: 65.1 eV 4d^{9}5s^{2}5p^6(^{2}D$_{5/2}$)6p, 66.4 eV 4d^{9}5s^{2}5p^6(^{2}D$_{5/2}$)7p, 67.03 4d^{9}5s^{2}5p^6(^{2}D$_{3/2}$)6p, and 68.3 4d^{9}5s^{2}5p^6(^{2}D$_{3/2}$)7p. The ^{2}D$_{5/2}$ series is highlighted in red while the ^{2}D$_{3/2}$ series is highlighted in green. Each transition is fit with a Voigt profile with the Lorentzian width fixed to the lifetime of the transition, and the Gaussian function determines the instrumental spectral resolution, which is found here to be 174 ± 20 meV as seen in figure 3.22 for the 65.1 eV transition. The Al L$_{2,3}$ absorption edge is observed above 72.5 eV by the steep decline in optical density. The non-resonant background is accounted for by a B-spline fit function (violet) and the determined spectral resolution of the instrument is represented by the blue block near 65 eV on the x-axis.

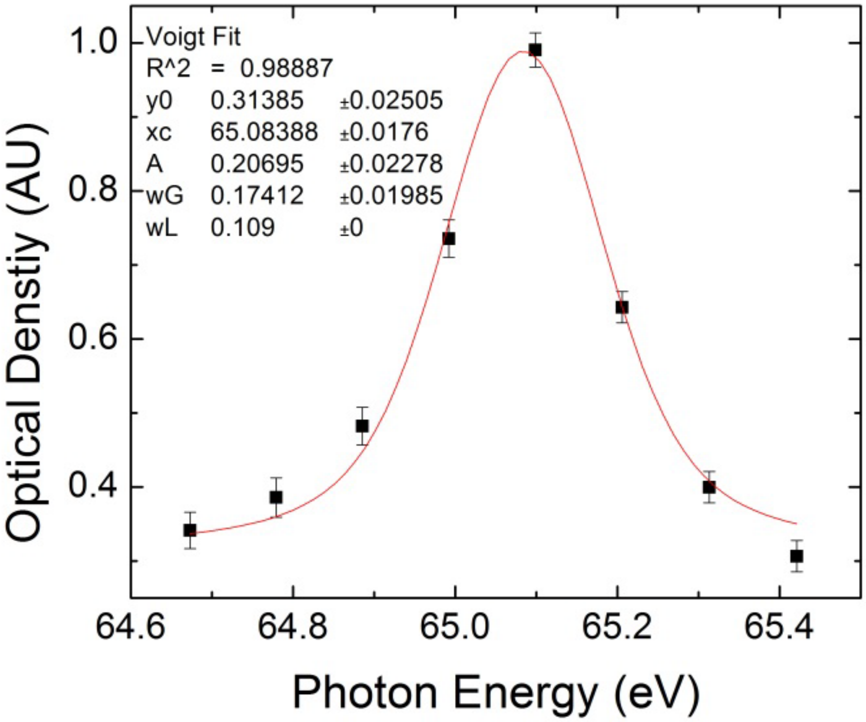

Figure 3.22: Example fit of a Voigt profile to the Xe $4d^{10}5s^25p^6 \rightarrow 4d^95s^25p^6(^2D_{5/2})6p$ transition at 65.1 eV. The Lorentzian linewidth is fit to the lifetime of the final state and the Gaussian fit is determined to be 174 ± 20 meV, the spectrometer resolution on this particular day. The peak is centered at 65.08 ± 18 meV, very close to the literature value of 65.11 eV.[153]

Once the xenon static calibration is completed, time zero and the optimal pump-probe overlap may be determined. This implies that the pump arm of the optical assembly is aligned. The alignment of the pump arm is trivial, except that the delay stage is mounted to the table at an angle due to a slope in the aluminum baseplate. The slope of the stage is perpendicular to the incoming beam, out of the plane of the table. This may be compensated for by angling the incoming and outgoing beams from the stage and aligning the two successive mirrors to remove the out-of-plane tilt in the beam path. To determine the degree of offset in the alignment, the stage is scanned over the full range while the incoming beam alignment to the stage is adjusted until the outgoing beam is stationary. Typical pump-probe scans from time zero to 100 ps only requires a translation of 1.5 cm, so the variation in beam position with changing time delay is minimum. This was confirmed by comparing xenon pump probe data at various, well-separated time delays.

After the delay stage is aligned, the pump beam may be aligned to the interaction region gas cell (figure 3.23). The pump beam should be aligned with the last mirror prior to the AR coated fused-silica window to the sample chamber, reflected off the very edge of the D-mirror in the chamber, and passed cleanly through the gas cell as observed on the in-vacuum flipper mount. If the beam does not pass through the gas cell cleanly, it will be necessary to re-align the in-vacuum mirrors as the overlap between pump and probe may not be optimal, leading to poor temporal resolution.

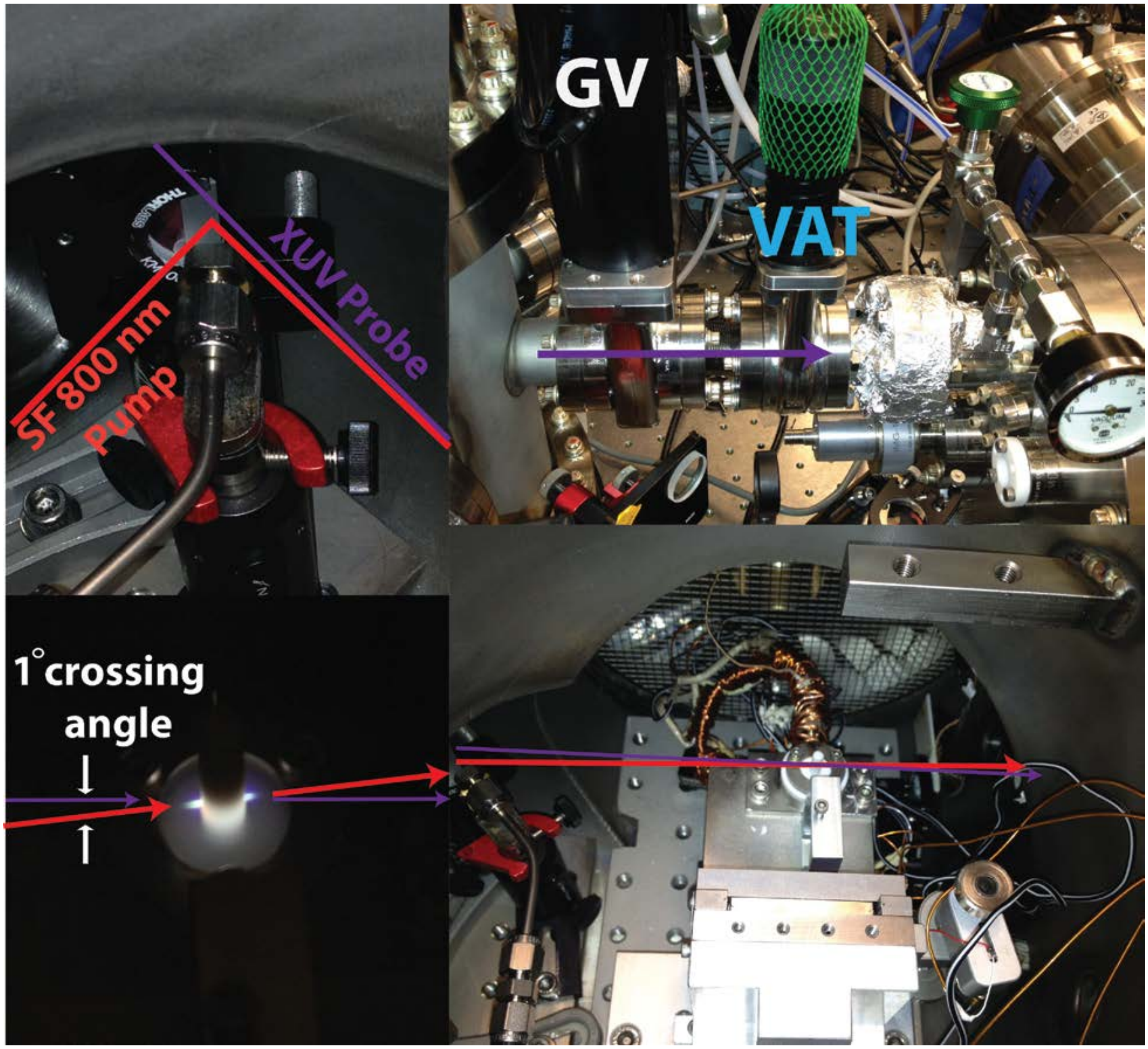

Figure 3.23: Sample chamber construction. (Top-Right) D-mirror of the pump beam. The 800 nm pump pulse (red) reflects off the very edge of the D-mirror closest to the 45° vertical cut face while still preserving mode quality, i.e. the edge of optics is typically not as flat as the center of the optic, nor does the coating later extend completely to the edge. The XUV beam (purple) passes along the 45° vertical cut face of the mirror. The argon gas jet for purging the overlap mirror can be seen in the foreground. This D-mirror can easily be exchanged for multiple wavelength high-reflectance mirrors. (Top-Left) Gate valve configuration between the refocusing toroidal mirror (left) and sample (right) chambers. It can also be seen that the last mirror the pump beam enters the sample chamber is motorized. This is to increase the accuracy and consistency of pump-probe overlap in the sample gas cell. (Bottom-Left) Sample gas cell pressurized with 50 Torr of xenon gas that has been strong-field ionized to produce visible plasma. (Bottom-Right) Top-down view of the sample chamber showing the translation stage configuration (XY New Focus 9067 picomotor translation stages, Z (beam propagation axis)

Physik Instrumente M665-K003), beam path, and heated sample gas line to maintain constant sample gas pressure and prevent condensation.

A rough determination of time zero between the XUV probe and 800 nm pump may be found by employing a Type 1 ß-barium-borate crystal $\theta = 29.2^{\circ}$, $\varphi = 0^{\circ}$ at the position of the interaction gas cell. Instead of using the XUV beam, the attenuated (by an OD 2 filter) 800 nm driver is utilized. Since the pump and probe beam intersect at a 2º crossing angle, when the two 800 nm pulses are overlapped in time, a third beam will be visible after the crystal (on the flipper mount plate installed) between the two incoming beams (at 1º crossing angle). This provides a rough estimate of the location of time zero to within a few picoseconds.

Pump-probe spectroscopy of the strong-field ionization of xenon (three turns of metering valve, ~10 Torr of Xe) provides an excellent calibration of the temporal resolution of the instrument for strong-field studies as well as the exact determination of time zero. In previous experiments, the formation time for Xe^{2+} (measured via the combination of the $^3P_2$ $(5p^{-2}) \rightarrow {}^1D_2(4d^{-1}5p^{-1})$ and $^3P_2$ $(5p^{-2}) \rightarrow {}^3D_3(4d^{-1}5p^{-1})$ transitions at 56.94 and 57.11 eV, respectively) was observed as fast as 13 ± 3 fs employing a capillary waveguide high harmonic source.[19] This provides a measure of the Gaussian instrument response function for the experimental apparatus. Typical instrument response functions with the semi-infinite gas cell source, measuring the Xe^+ (observed via the $^2P_{3/2} \rightarrow {}^2D_{5/2}$ transition at 55.4 eV as seen in figure 3.24) formation time, tend to be between 20 and 30 fs as seen in figure 3.25. The transient absorption signal is fit to a convolution of a Gaussian and Heaviside function (yielding an error function). A Heaviside function is simply the integral of the Dirac delta function and accounts for the strong-field ionization response to the assumed Gaussian laser pulse shape, i.e ionization may occur approximately instantaneously at any point during the strong-field pulse. By setting the delay stage to +5 ps pump-probe time delay and monitoring the XUV flux at 55.4 eV, the overlap of the pump and probe beams can be optimized via the last turning mirror before the interaction chamber. The lens (PLCX-25.4-206.0-UV-800, 45 cm focal length lens at 800nm) position for focusing the pump beam may also be optimized under these conditions. By maximizing the change in optical density signal for the 55.4 eV transition of Xe^+, the pump-probe overlap is optimized. Finally, by scanning through pump-probe time delays, time zero may be determined to within a few femtoseconds.

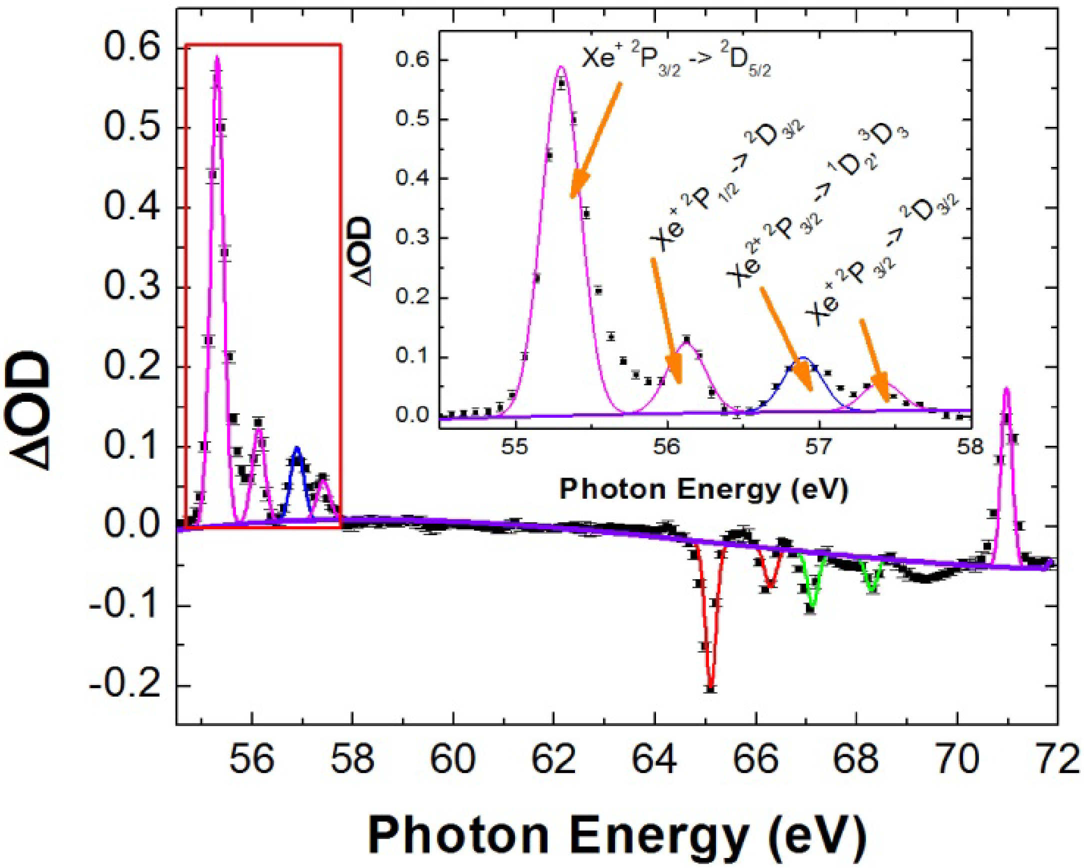

Figure 3.24: Typical transient absorption of the strong-field ionization $\left(1.0\times10^{14}\ \mathrm{W}/\mathrm{cm}^2\right)$ of xenon. The Xe^{+} transitions are represented in pink, the Xe^{2+} peaks in blue, and the static neutral depletion transitions are represented in the same color style as in figure 3.21. The Xe^{+} and Xe^{2+} transitions are labeled in the inset. An additional Xe^{+} transition is observed at 71.0 eV and corresponds to a 4d → 4f transition.[188-190] The spectral resolution in this measurement is determined to be approximately 250 meV for all transitions, demonstrating the constant spectral resolution over the entire XUV photon energy range detected. At higher field intensities, the area ratio of the Xe^{+}/Xe^{2+} transitions at 55.4 and 57.1 eV decreases from greater than 1 to less than 1 at approximately $\left(6.0\times10^{14}\ \mathrm{W}/\mathrm{cm}^2\right)$. Due to the increased plasma effects in the interaction region, an erroneous pump-probe overlap and time zero can be obtained.

It is important to note that while determining time zero and the optimal pump-probe overlap it is possible to obtain erroneous values if the field intensity is too high. At field intensities above the saturation intensity, $\left(\sim1.0\times10^{14}\ \mathrm{W}/\mathrm{cm}^2\right)$, and above 10 Torr of xenon in the interaction region, plasma effects become apparent, shifting the optimal overlap position outside the gas cell and yielding a time zero greater than the actual value. This occurs as a result of the pump pulse arriving first, ionizing the medium, and causing plasma defocusing as well as diffraction of the XUV beam.[191] As a result, the determined experimental calibration becomes a function of plasma density in the interaction region. High field intensity also introduces the option of multiple ionization pathways due to the formation of Xe^{2+}, further complicating the calibration. To avoid this issue, it is necessary to reduce the sample gas pressure to a minimum, still yielding sufficient signal-to-noise to execute the planned experiment. This regime is typically obtained at <10 Torr of sample density for high field intensity, $\left(>4.0\times10^{14}\ {}^{W}\!/_{cm^2}\right)$, but the sample density may be increased at low field intensities, $\left(<2.0\times10^{14}\ {}^{W}\!/_{cm^2}\right)$, to compensate for the reduced populations of transient species. The best method to avoid this issue is to optimize the pump-probe overlap and determine time zero at the minimal field intensity required to observe the Xe^+ $^2P_{3/2} \rightarrow {}^2D_{5/2}$ transition at 55.4 eV. The gas pressure and field intensity may then be increased as long as the overlap and time zero values remain consistent with the low power measure. When introducing the analyte gas (Br_2, CH_3I, etc…) the calibration parameters should remain unchanged, i.e. if optimal pump-probe overlap is observed at a different location than Xe^+ then the gas pressure is too high in the interaction region relative to the field intensity.

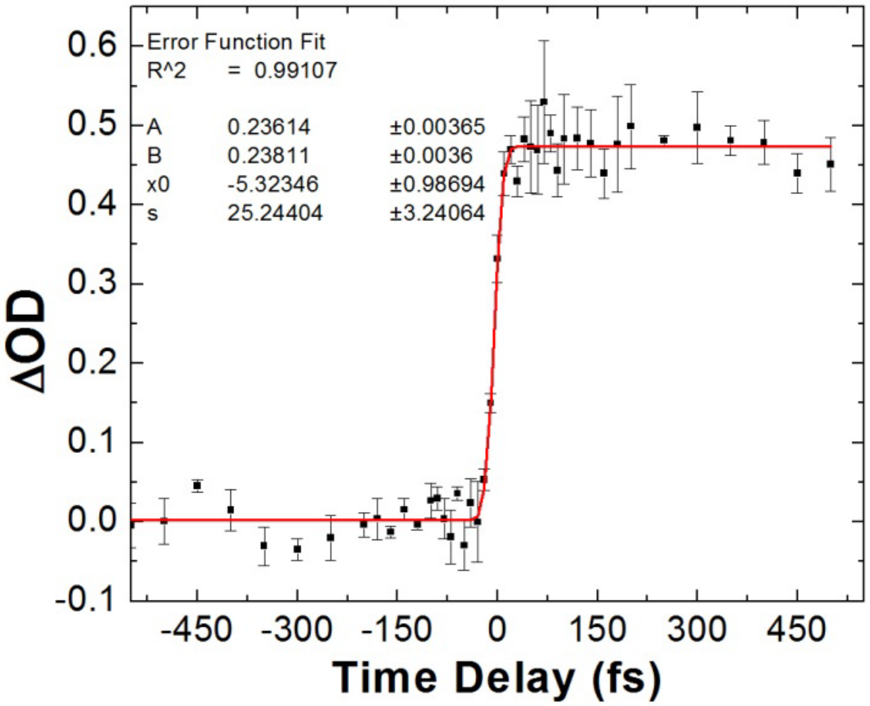

Figure 3.25: Cross-correlation of pump (800 nm, 40 fs, $1.0\times10^{14}\ {}^{W}\!/_{cm^2}$) and probe (broadband XUV) measured at the Xe^+ $^2P_{3/2} \rightarrow {}^2D_{5/2}$ transition at 55.4 eV. A range of time points with decreasing separation around zero (Δt = 50 fs $\{-550\rightarrow-200\}$, Δt = 20 fs $\{-200\rightarrow-100\}$, Δt = 50 fs $\{-100\rightarrow+100\}$, etc…) is chosen to accurately determine time zero. Here, a typical the instrument response function is determined to be 25 ± 3 fs at $t_0 = -5 \pm 1$ fs, obtained by an Error function fit of the transient signal. The delay stage after this scan would be reinitialized with a 5 fs offset so that 0 fs would be the actual time zero, which would be confirmed by a successive scan.

Since the values of the Xe, Xe^{+}, and Xe^{2+} transitions are known in the literature,[153,188-190] a new calibration may be made employing these values. This is a more robust calibration method as opposed to just using the Al $L_{2,3}$ edge,[192] due to the inaccuracy of assessing the exact pixel corresponding to the onset of the aluminum edges as seen in figure 3.17. The accuracy of calibrating the spectrometer with the lines from the strong-field ionization of xenon is typically within 100 meV. The spectrometer calibration equation (Eq 3.8) is adapted from the traditional grating equation (Eq 3.7):

$$m\lambda\sigma = \sin[\gamma]\left(\sin[\alpha] + \sin[\beta]\right) \tag{3.7}$$

$$\frac{0.73905n}{E(\text{transition})} = D\arcsin\left[\sin[\beta] - Pixel\right] - C \tag{3.8}$$

where the imaging distance of the grating (D), dispersion in the spectral plan (C), and azimuthal angle of the dispersed light (ß/p) are the parameters of the spectrometer. The grating equation includes the order of diffraction (*m*), the half-angle of the cone into which the light is diffracted (γ), and the grating groove density (600 lines/mm, σ). The calibration curve determining the parameters of the spectrometer is seen in figure 3.26.

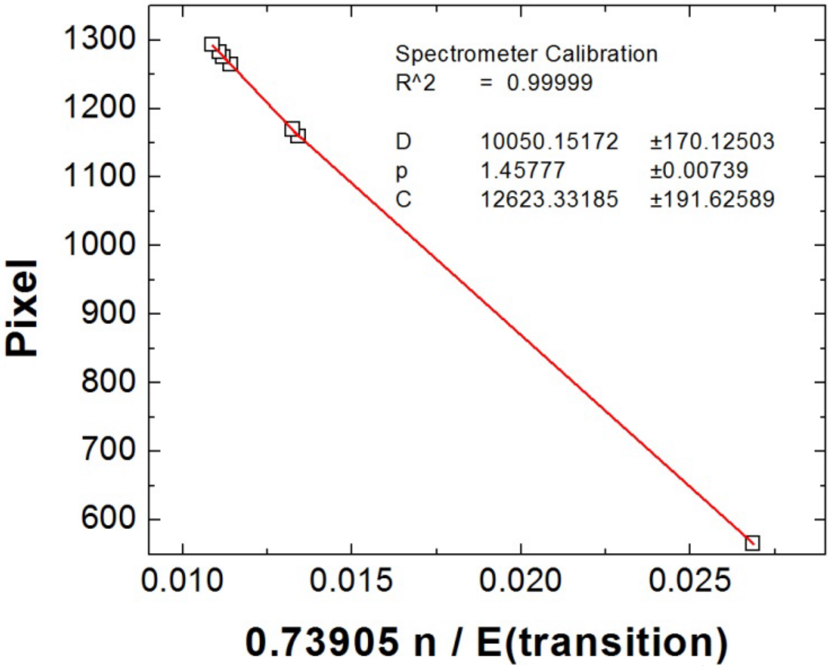

Figure 3.26: Plot of the pixel number where several Xe, Xe^{+}, and Xe^{2+} resonances are observed versus the conversion factor between pixel and photon energy given by the grating equation. The fit yields the imaging distance of grating (D), dispersion in the spectral plan (C), and azimuthal angle of the dispersed light (ß/ p), which may then be used to determine the photon energy at each pixel as seen in figure 3.27.

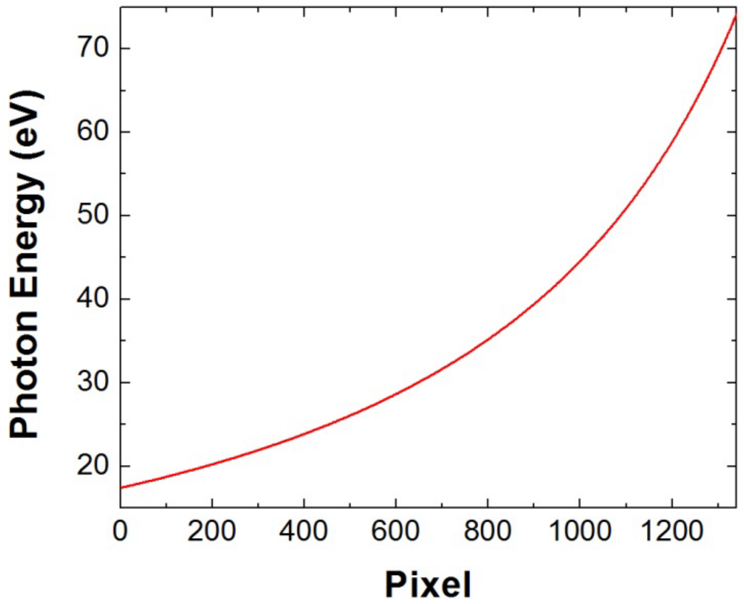

Figure 3.27: Plot of photon energy vs. pixel as determined by the XUV spectrometer calibration and fit to the grating equation.

At this point, the system is calibrated both spectrally and temporally. Introduction of the analyte gas may begin. If the analyte is expected to fragment, it is crucial that the D-mirror in vacuum be purged with argon. This prevents the buildup of material on the optic, which would lead to a constantly changing field intensity in the interaction region. A small gas blower made from a Swagelok cap may be positioned within several millimeters of the D-mirror, effectively preventing material buildup over any period of time. The D-mirror is a half plate mirror (look like a D) that has the straight edge cut at a 45° angle to allow placement of the optic extremely close to another beam running parallel to the cut face. This optic therefore allows the overlap of two beams at a 1° or less crossing angle.

Secondly, if the analyte gas is corrosive the bearings of the turbomolecular pump must be purged with dry nitrogen. Between these two considerations, and the two Al foils at the XUV entrance and exit of the sample chamber, experiments on corrosive molecules may be conducted for any amount of time. The usable experimental time with molecules is typically governed by the deposition rate on the entrance and exit aperture of the sample gas cell, which to this point has not been resolved. This is specifically detrimental in experiments involving the strong-field ionization of carbon containing species, which degrade to graphite and deposit on the entrance/exit slits of the gas cell, blocking gas flow and the pump/probe pulses. Lastly, for use of any corrosive material in the sample chamber, LN_2 traps must be employed between the turbomolecular pump and the mechanical pump to prevent damage to the mechanical pump and venting of corrosive and toxic gases to the atmosphere. Once the sample is condensed in the LN_2 trap and the experiment over, it may be safely neutralized/disposed of in a fume hood.

Strong-field experiments require knowledge of the field intensities utilized, which may be determined by measuring the spot size at the interaction region and the pulse duration. A Spiricon beam profiler is employed to measure the pump beam waist ($^1/_{e^2}$) at the interaction gas cell, and a single-shot autocorrelator measures the pulse duration. The peak field intensity (I_0) is then given as:

$$I_0 = 2\frac{E_{pulse}/1000}{(area)\ \tau} \tag{3.9}$$

where τ is the pulse duration in seconds, E_{pulse} is the pulse energy in millijoules, and the area of the focus is given as $area = \pi * \omega_{0,x} * \omega_{0,y}$, with $\omega_{0,x}$ and $\omega_{0,y}$ being the horizontal and vertical beam waists, respectively. The spatial/temporal distribution of the field intensity is given as:

$$I(r,t) = I_0 e^{-\frac{2r^2}{\omega_0^2}} e^{-4\ln[2]\frac{t^2}{\tau^2}} \tag{3.10}$$

For effective measurement of strong-field dynamics at a particular peak intensity, it is necessary that only a small volume of the pump focus be sampled. This is fulfilled if $\omega_{0,pump} > \omega_{0,XUV}$, which is satisfied in the presented experiments since $\omega_{0,\ pump}$ is ~32-42 μm and $\omega_{0,\ XUV}$ is ~20 μm. Integrating the areas of the pump and probe beams it is found that the peak field intensity of the pump only varies by 5% in the majority of the volume sampled by the probe as illustrated in figure 3.29.

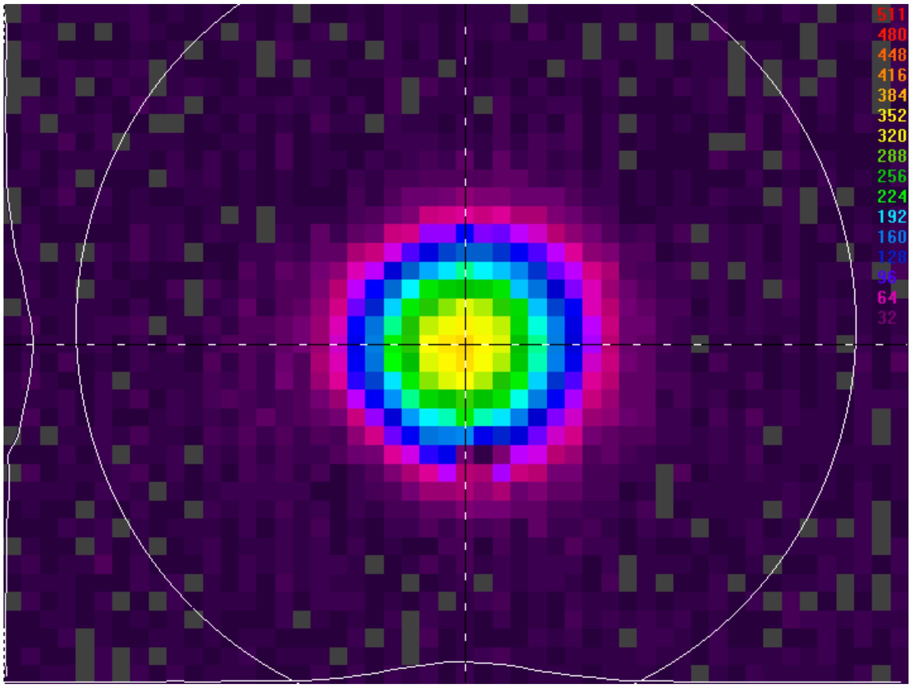

Figure 3.28: Beam profile from Spiricon CCD of the pump beam focus at the sample gas cell. The Gaussian fit $1/e^2$ beam waist is 32 μm x 33 μm.

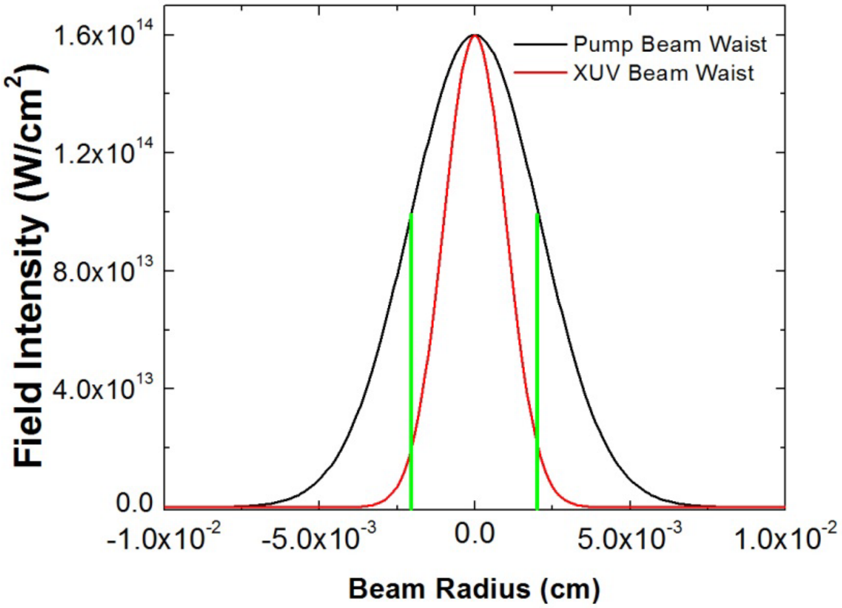

Figure 3.29: Plot of the sampled pump intensity by the XUV probe given the experimentally determined beam waists of $\omega_{0,\ \text{pump}}$ = 42 µm and $\omega_{0,\ \text{XUV}}$ = 20 µm. The green bars represent the $1/e^2$ beam waist of the probe.

At this point, the majority of the operational procedure for the femtosecond XUV transient absorption apparatus and its calibration has been described. During operation, it is necessary to constantly verify the pulse duration between data collection runs, at least every hour if not every half-hour. Otherwise, the apparatus is extremely robust and will operate effectively for an extended period of time.

3.3.2. Multi-Day Operation

There are only slight modifications to the experimental operating procedure for single-day operation to run the experimental apparatus for extended periods of time to obtain high signal-to-noise or conduct low noise extended scans (>500 time points). These modifications are intended to increase the stability of the apparatus over several days and minimize any variation in the harmonic signal due to temperature and humidity variations in the lab. The stability of the lab environmental conditions directly affects the fluctuations in the high harmonic signal.

One particular condition that greatly affects the operation of the transient absorption apparatus is when additional laser systems are run in the lab, in particular either the argon-ion or V-18 Verdi laser system on the confocal microscopy experiment in the same room. When the argon-ion laser is started in the lab, the temperature in the lab increases by 3 ºC over the course of the day, and then drops by 5 ºC during the evening. Luckily, this laser was replaced by the V-18 Verdi. The

V-18 laser system has less of a thermal effect on the lab, but the temperature still rises by 2 ºC during the day and drops by 3 ºC during the evening. If neither laser is run during the course of a day, the temperature fluctuates by approximately 1 ºC overall around 24 ºC.

Thermal drift may also occur while the Spitfire Pro and Empower laser system are warming up. This may be avoided by starting the femtosecond amplifier the previous day and allowing it to thermalize overnight. This prevents thermal drift in the amplifier, but also ensures that the system's operation is stable (pointing, power, pulse duration). Thermal drift also occurs as the temperature fluctuates due to flexion in the optical table and optomechanical components. By warming the laser system up the previous day, overall thermal drift on data collection days is minimized.

While the femtosecond laser system is warming up the previous day, high harmonics are also generated if the experiment is expected to continue for several days. Drift of the beam is unavoidable, but the drift is almost cyclic so almost the entire beam pointing space is explored in a 24-hr period if there are no additional perturbations to the lab environment. By generating high harmonics during the day prior to an experimental collection and overnight (with the GuideStar II actively stabilizing the pointing), the large majority of the beam pointing space is explored, and as a result the semi-infinite gas cell exit foil is drilled out to its maximum size. As the exit foil is continually laser ablated, it will become larger, changing the gas conductance across the aperture. To maintain the consistency of the gas pressure and the pressure gradient across the exit aperture, a low pressure regulator (0 to 0.68 bar, Swagelok regulator: KLF1CFH412A20000, C_v = 0.06, max inlet pressure of 16 psi) is employed. This greatly minimizes any fluctuation in the harmonic flux during data collection. Essentially, the system reaches a steady state after 24-hrs of operation and will continue to operate likewise for several days (save the pulse duration drift, which is correctable). During the course of extended operation, temporal and spectral resolutions are preserved. This allows for operation for days at a time, while previous conditions only allowed operation for a few hours at the very most. Currently, no identifiable limit for experimental operation has been observed.

3.4. Future Improvements

The apparatus changes discussed here have expanded the repertoire of experiments possible for femtosecond XUV transient absorption spectroscopy, allowing for continuous, multi-day operation. Even so, there are several areas in which the instrument could be improved with little cost and high pay-off. This includes stabilization of the Spitfire Pro pulse duration, further beam pointing stabilization, and replacement of the sagging spectrometer chamber.

The drift in the pulse compression results from a communication error in the timing-delay generator hardware for the Spitfire, to which there is no ready solution without introducing a home-built feedback system. The feedback system would require replacing the translation stage in the Spitfire Pro's compressor with a homebuilt stage/retro-reflector assembly coupled to the output of a two-photon photodiode. By translating the stage to optimize the signal on the photodiode in a feedback loop, the pulse compression could be maintained indefinitely.

The institution of further beam stabilization is most likely not necessary and any remaining beam drift is due to vibrational perturbation of the optical table. By further isolating the mechanical roughing pumps and water chillers, these perturbations could be significantly reduced. Also, with all the mechanical pumps and chillers under the optical table, there is a temperature difference of 5ºC between the bottom and top plate of the table. This causes flexion of the optical table, perturbing the optical alignment, especially since the spectrometer is directly over all of the mechanical pumps. Either by moving the mechanical pumps or installing a ventilation system, the uneven heating of the table could be avoided. If further beam stabilization is necessary, actively locking the last mirror of the driving 800 nm beam for high harmonic generation to the exit foil of the semi-infinite gas cell and the last mirror for the pump beam before the interaction region to the sample gas cell would completely stabilize the system.

The last systematic improvement would involve replacing the spectrometer chamber with one that is directly mounted to the table, leaving the degrees of freedom for aligning the toroidal mirror and grating in the spectrometer to the optical mounts they are positioned on. A similar translation stage system that was instituted for TM1 could also be employed in the spectrometer optics to simplify alignment. Also, the spectrometer could be replaced with a concave variable-line-spaced grating, which would increase the spectral resolution from better than 250 meV to better than 50 meV. Already, a resolution of better than 10 meV has been realized on a similar experimental apparatus, opening additional avenues of possible experiments for XUV transient absorption spectroscopy.

Chapter 4

Characterization of Vibrational Wave Packets by Core-Level High-Harmonic Transient Absorption Spectroscopy

The ground-state vibrational wave packet produced by strong-field ionization of Br_2 is characterized by femtosecond high-harmonic transient absorption spectroscopy. Vibrational motion is observed in time by a change in the 3d core-level transition energy with bond length, 0.14 eV per picometer to higher energies at shorter bond lengths. The wave packet has the expected period of 104 fs for the predominant $\nu_0\nu_1$ vibrational quantum beat, which is prepared toward the outer turning point with a phase of $0.21\pi \pm 0.05\pi$ due to the increased ionization rate at short bond lengths. Simultaneous observation of a wave packet on the $Br_2^+\ {}^2\Pi_{g,3/2}$ electronic state prepared at the ion's equilibrium bond distance confirms increased ionization on the inner turning point of the neutral. The Br_2 ground state wave packet has a degree of coherence ranging between 0.19 and 0.24, due to scrambling of the vibrational level phases. The results demonstrate the sensitivity of core-level transient absorption spectroscopy to bond length and oxidation state, providing a means to analyze the formation and evolution of vibrational wave packets.

4.1 Introduction

Strong-field ionization is a fertile ground for the exploration of electron and nuclear dynamics, providing insight into electron recollision phenomena[54,193] and tunnel ionization processes.[51,79,194,195] In atoms and molecules, the abrupt ionization process also forms electronic[24] and vibrational[139] superposition states in the resulting ion and depleted neutral species, leading to electronic and vibrational wave packet motions.[70,155,159] Unraveling the precise composition and phase of the wave packet motion can be challenging,[135] due to the difficulty to obtain specific information about the wave packet localization in the time-resolved probe step. Extreme ultraviolet (XUV) core level spectroscopic probing can provide a previously unrecognized bond-length-specific detection of vibrational wave packets. Coupled with the element-selective, oxidation-state sensitive nature of core level spectroscopic transitions, ultrafast high-harmonic transient absorption spectroscopy is a powerful means to investigate strong-field ionization dynamics.[23]

The tunneling rate of molecules is dependent upon the nuclear coordinate's ionization energy. For diatomic molecules this amounts to a dependence on the bond length, R, the degree to which the laser field perturbs the nuclear potential energy curves, and the orientation of the molecular axis with the polarization of the laser electric field.[64,82,86] This can be visualized in a semi-classical picture, in which increased ionization of molecules with bond lengths shorter (longer) than the equilibrium bond length shifts the remaining ground state vibrational amplitude toward the outer (inner) turning point. A coherent superposition of vibrational states in the resultant ion populations simultaneously forms with ionization of the ground state. This non-uniform ionization scheme with bond length yielding vibrational wave packets on the ground state is known as the Lochfraß mechanism.[70,134,139] Depending on the degree of distortion of the molecular potentials by the intense laser field, the bond length corresponding to the maximum ionization rate may change. Preparation of vibrational superpositions on both the neutral and ion potentials is therefore also dependent on R and the degree of molecular potential field-dressing.

Initial studies of strong-field ionization that produce vibrational wave packets were limited to those generated on ion states. Non-Franck Condon ionization of $H_2 \longrightarrow H_2^+$ shows the excited ion vibrational population is prepared in the lower energy vibrational states due to the variation in ionization energy with bond length.[61] The R dependence of the ionization rate in H_2/D_2 has been explored in terms of both the Born-Oppenheimer and strong-field perturbed potential curves. In both cases, the ionization energy decreases (ionization rate increases) with increasing bond lengths. Lochfraß vibrational wave packets in H_2/D_2, primarily composed of the ground vibrational state, are observed due to the resulting localized ionization.

Perturbation of the diatomic molecular potentials by the strong laser electric field increases ionization at elongated bond lengths. As the bond stretches, the probability of tunnel ionization at one atomic center, through the internal Coulomb barrier and directly into the continuum increases dramatically and peaks at a critical-internuclear separation, R_c. Intense laser ionization of room temperature I_2 shows enhanced ionization at elongated bond lengths, preparing a ground state vibrational wave packet on the inner turning point of the molecular potential. Furthermore, the overall vibrational energy on the ground state is reduced, creating a superposition primarily composed of the ν_0 and ν_1 vibrational states.[136] The wave packet is detected by a second strong-field ionization step to the $I_2^{2+} \longrightarrow I^{2+} + I$ asymmetric dissociation channel.[56,68] The exact position of the vibrational wave packet may then be retrieved by projection of the kinetic energy and/or ion yield onto a time-dependent positional subspace determined by a weighting of the standard molecular hydrogen potential surfaces.

Preparation of ground state vibrational wave packets in both H_2/D_2 and I_2 represent a Lochfraß ionization scheme, but it is unclear as to the importance of the field-free R dependent ionization energy on the tunneling rate. The field ionization of I_2 clearly demonstrates the importance of ionization at R_c, while it is difficult to distinguish the precise ionization mechanism for H_2/D_2. Furthermore, experiments investigating Lochfraß wave packets to date have utilized a second strong-field pulse as a probe of the vibrational dynamics.[136,139] The comparable intensity of the pump and probe pulses suggests additional perturbation of the nuclear potential may affect the retrieved dynamics. Utilizing a weak-field XUV probe allows direct interrogation of the ground state vibrational dynamics without distorting the nuclear potentials.

Here, we present the experimental evidence for the formation of a ground state vibrational wave packet in Br_2 initially prepared at the outer turning point by strong-field ionization, and the first estimate for the degree of coherence for a Lochfraß wave packet. The wave packet is detected by bond-length-specific XUV transient absorption as schematically outlined in Fig 4.1. The ground state ionization energy of Br_2 increases with R according to the Born-Oppenheimer Br_2 $^1\Sigma_g^+$ and Br_2^+ $^2\Pi_{g,3/2}$ potential curves. The dependence of ionization energy on R for Br_2 results in selective ionization of the vibrational population at short bond lengths, creating a hole in the ground state vibrational amplitude. This non-uniform depletion of the thermally populated ground state vibrational levels at 300 K forms the vibrational wave packet on the outer turning point. According to electronic structure calculations, the core-hole excited state at bond lengths around the Br_2 equilibrium length, $R_e^{Br_2}$, decreases at stretched bond lengths. Therefore, as the mean bond length of the vibrational wave packet oscillates, the Br_2 $3d \rightarrow \sigma_{LUMO}^*$ core-level transition energy correspondingly evolves, monitoring the vibrational wave packet in time.

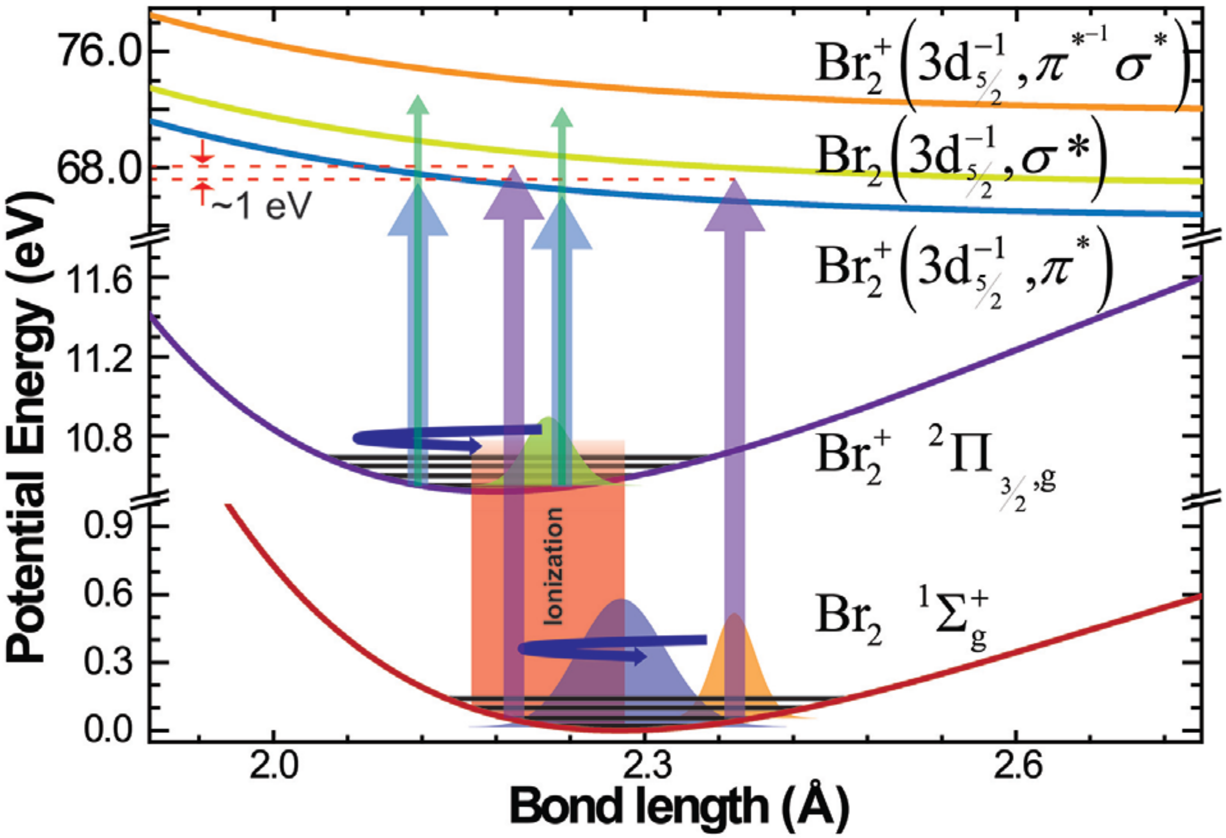

Figure 4.1: Schematic potential energy diagram of the strong-field ionization of Br_2 showing R-dependent ionization (preferred ionization region shaded in red) and the sensitivity of core level absorption to the motion of the generated vibrational wave packet on the ${}^1\Sigma_g^+$ surface. Colored Gaussians illustrate relevant probability densities: (blue) incoherent Br_2 ${}^1\Sigma_g^+$ Boltzmann population before ionization, (orange) exaggerated $\nu_0\nu_1$ vibrational superposition localized on the outer turning point resulting from the strong-field ionization, which also generates the (green) Br_2^+ ${}^2\Pi_{3/2,g}$ vibrational wave packet. The Br_2 ${}^1\Sigma_g^+$ and Br_2^+ ${}^2\Pi_{3/2,g}$ potentials are taken from literature Morse potential values and the core-hole excited states are calculated via REW-TD-DFT.

Femtosecond dynamic white light absorption spectroscopy has demonstrated itself as a versatile tool for investigating chemical dynamics since its introduction by Pollard and Mathies.[18,142,143] A broadband probe spectrally dispersed after the sample allows monitoring of multiple optical transitions simultaneously as well as direct detection of vibrational dynamics in real-time. The time-dependent nature of a wave packet is therefore observed by its position sensitive transition energy to a probe state, dictated by the potential energy surfaces. Here, we show that like dynamic white light absorption, high harmonic generation supplies an ultrafast, broadband probe for investigating vibrational dynamics, but also offers elemental and oxidative state specificity by virtue of exciting the core-level transitions of the target. XUV transient absorption spectroscopy thus provides a localized, elemental probe of chemical processes.

The Br_2 ground to core-hole excited state transition energy is measured here to be extremely sensitive to internuclear separation with a resolution of approximately $0.14\ ^{\mathrm{eV}}\!\!/_{\mathrm{pm}}$. The sensitivity of the XUV absorption allows for direct detection of vibrational wave packet dynamics and preparation. For the strong-field ionization of Br_2, a partially coherent wave packet primarily composed of the $\nu_0\nu_1$ vibrational beat is observed to originate at the outer turning point, consistent with the calculated increase in tunneling rates as the molecular bond length approaches the region of minimum ionization energy. For this investigation, the peak ionizing laser intensity of $1.6 \text{ x } 10^{14}\ ^{\mathrm{W}}\!\!/_{\mathrm{cm}^2}$ was chosen to achieve threshold strong-field ionization for a high contrast change in optical density of the neutral core-level transitions with vibrational motion. This experiment demonstrates, for the first time, the utility of XUV transient absorption as a bond-length-specific probe of vibrational wave packet dynamics, allowing determination of the superposition's characteristics even when a small range of bond lengths is explored.

4.2 Computational Methods

The goal of this work is to understand the strong-field ionization dynamics of Br_2 as probed by bond-length-specific XUV transient absorption. Toward this end, the experiment may be divided into the pump and probe step, where the pump is used to strong-field ionize Br_2 and the XUV probe interrogates the dynamics. Tunnel ionization rate determinations are employed to model the pump, while electronic structure calculations model the energetics of the XUV probe accessed core-hole excited state. By combining the results of both calculations with standard propagation operator techniques, a theoretical XUV transient absorption signal for the ground state vibrational wave packet may be obtained.

4.2.1 Restricted Excitation Window Time-Dependent Density Functional Theory (REW-TD-DFT)

REW-TD-DFT[162] calculations are performed employing the NWCHEM 6.1[161] program package to model the $3d_J^{-1},\sigma^*$ core-hole excitation of Br_2 at all experimentally accessed bond lengths, where $3d_J^{-1},\sigma^*$ is the final state electronic structure (nl_j^{-1} symbolizes a hole in the atomic nl orbital with angular momentum j, λ symbolizes an electron the molecular orbital $\lambda = \left\{\sigma, \pi, \pi^*, \sigma^*\right\}$). The calculations do not take into account the spin-orbit state of the core-level, but rather determine spin-orbit averaged results, which is generally applicable to both the $3d_{5/2}^{-1},\sigma^*$ and $3d_{3/2}^{-1},\sigma^*$ states. The results of the calculation are seen in Fig. 4.2. The Br_2 ${}^1\Sigma_g^+ \longrightarrow 3d_{5/2}^{-1},\sigma^*$ XUV transition energy is observed to decrease with R, indicating the core-hole excited state is repulsive around $R_e^{Br_2}$. The slope of the core-hole excited state is shown in Fig. 4.1 relative to the relevant neutral and ion potential energy surfaces for this experiment (please note the change in scaling for the core-hole excited state). The shape of the core-hole excited state is consistent with the expectation for an electronic configuration with 3d core-hole and an additional electron in a σ^* orbital within a molecular system with several lone pair electrons.[196] The additional electron in the σ^* orbital weakens the bond by ½, according to the bond-order, but the core-hole creates an attraction due to the ion-induced polarizability between the localized atomic-like vacancy and the electron cloud of the molecule. These two new forces dictate the curvature of the core-hole excited state. According to the bond-order, the potential minimum should be found at $R > R_e^{Br_2}$, which concurs with the REW-TD-DFT calculations. The strong dependence of the XUV transition energy with R therefore allows highly accurate bond-length-specific probing, which is characterized in Sec. IV.

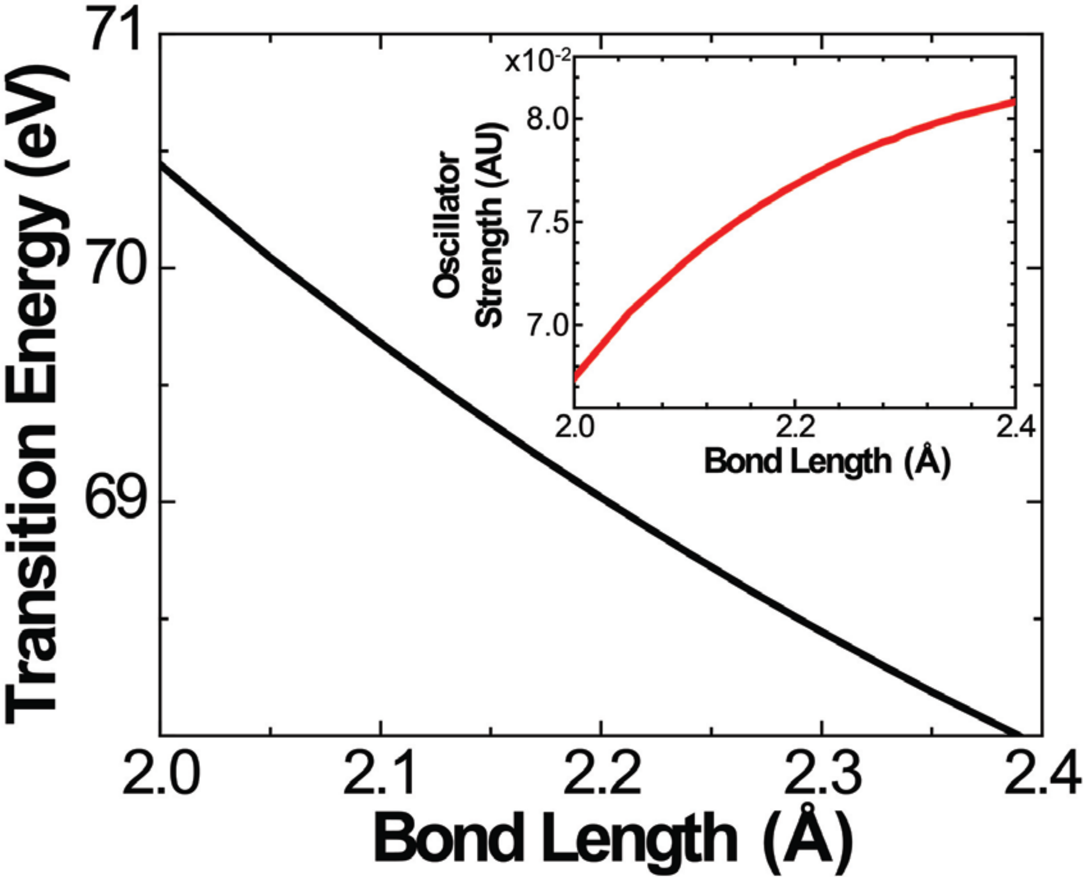

Figure 4.2: Variation of XUV transition energy with internuclear separation as calculated by REW-TD-DFT calculations employing B3LYP model chemistry with a 6-311g* basis set. Inset shows the change in the calculated oscillator strength with internuclear separation.

4.2.2 Vibrational/Bond Length Dependent Ammosov-Delone-Krainov Tunnel Ionization Rate (R_v-ADK)

Tunnel ionization calculations utilizing a variation of Ammosov-Delone-Krainov theory that incorporates the molecule's ionization energy as a function of bond length and vibrational level (R_v-ADK) are performed to predict the Br_2 $^1\Sigma_g^+$ vibrational level population distribution.[166] Standard ADK theory has been demonstrated to be effective in modeling the ionization of small molecules, while the incorporation of molecular symmetry with respect to the electric field vector of the ionizing laser field and the asymptotic nature of the electronic wave function have been required for larger molecules.[175] The basic structure of the R_v-ADK calculation is outlined by Brichta et al., where the tunnel ionization rate is determined as a function of bond length and subsequently averaged over each vibrational level probability density distribution.[166] Here, we remove the vibrational averaging in favor of a fully bond length dependent result. Accounting for the shape of the vibrational amplitude with R grants insight into the selective depletion of each ground state vibrational level following bond-length dependent strong-field ionization. For the calculations, the ionization energy as a function of bond-length and the solutions for the vibrational energy levels are determined from the spectroscopic parameters for Morse potential fits of the Br_2 $^1\Sigma_g^+$ and Br_2^+ $^2\Pi_{g,3/2}$.[169,171] The tunnel ionization rate, $W_{ADK}^{v}(R,I)$, for each vibrational level $\psi_{v_n}(R)$ as a function of field intensity, *I*, over an incremental section of R, ΔR, is then:

$$W_{ADK}^{v}(R,I) = \int_{R}^{R+\Delta R} \left|\psi_{v_n}(R)\right|^2 dR \; W_{ADK}(R,I) \qquad (4.1)$$

where $W_{ADK}(R,I)$ is the ADK tunnel ionization rate where the variation in ionization with R of the ground state potential has been incorporated. The tunnel ionization probability is then given as $P_{ADK}^{v}(R,I) = 1 - e^{-\int W_{ADK}^{v}(R,I)dt}$ and is seen in Fig. 4.3. Clearly, the ionization probability is maximum for higher vibrational states at $R = R_e^{Br_2^+}$, and the tunneling probability decreases as the molecule is stretched or compressed. Accounting for the initial vibrational amplitude distribution, the vibrational levels are preferentially depleted at $R < R_e^{Br_2}$ as seen in Fig. 4.3.

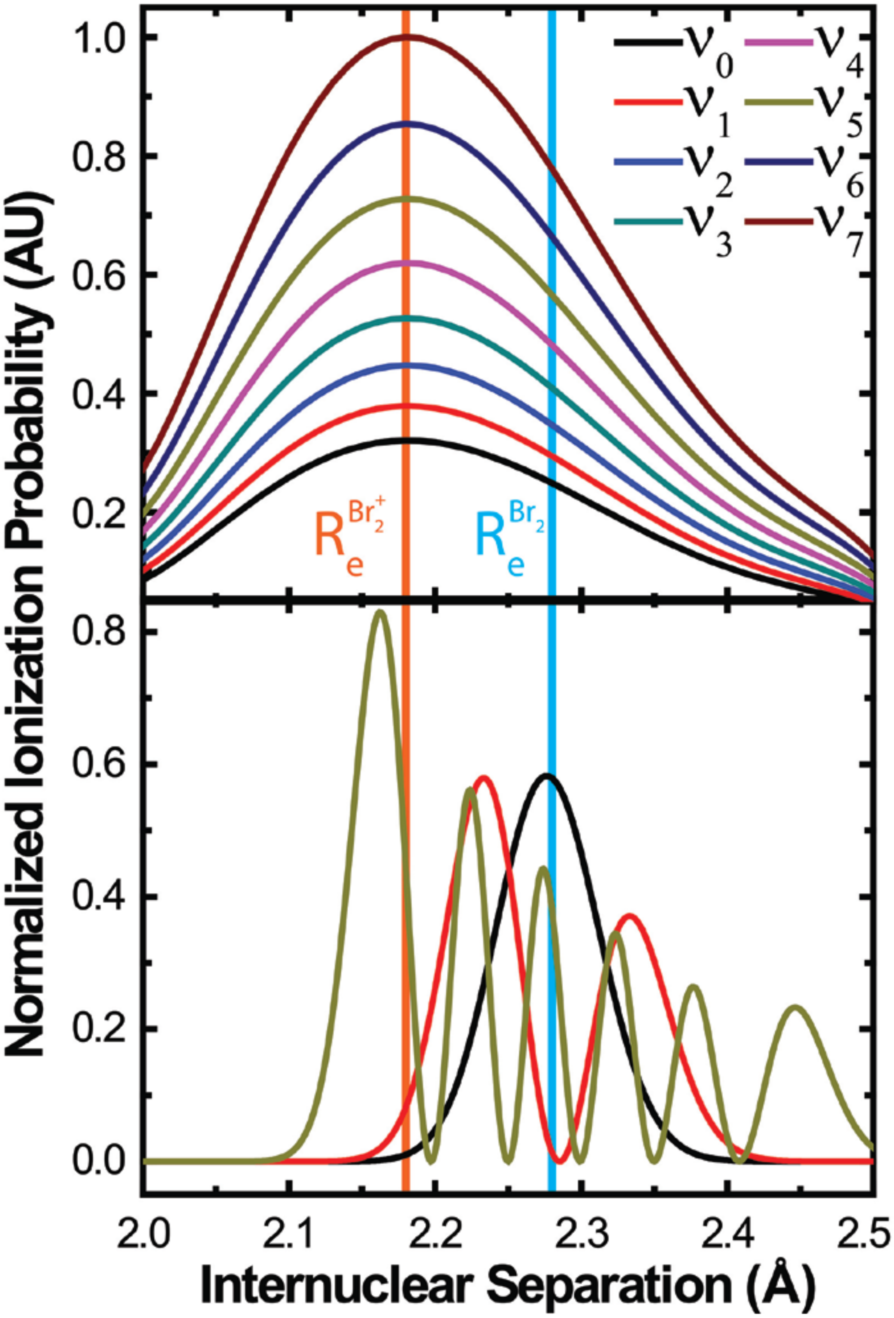

Figure 4.3: (Top) ADK tunnel ionization probability dependence on vibrational energy level and internuclear separation. The equilibrium bond lengths for Br_2 (2.28 Å) and Br_2^+ (2.18 Å) are marked in blue and orange, respectively. The ionization rate clearly increases with vibrational level and peaks around the internuclear geometry of the ion state at $R < R_e^{Br_2}$. (Bottom) Plot of the vibrational level probability density for $\nu_n : n = \{0,1,5\}$ depleted by ADK tunnel ionization. The asymmetry of the ionization rate around $R_e^{Br_2}$ may clearly be seen, even for ν_0.

Examination of the quantitative effect of R_v-ADK ionization is accomplished by selectively integrating the ionization probability with respect to bond length. Integrating over all internuclear separations indicates that ionization from ν_1 is 5% more likely than ν_0, whereas integration from zero to $R_e^{Br_2}$ doubles the preference for tunneling from ν_1. Therefore, if ν_0 and ν_1 are equally populated, then 10% of ν_0 (11% of ν_1) is ionized, a trend which is consistent with higher vibration levels. This sample calculation of R_v-ADK matches the intuitive prediction above, demonstrating increased ionization of higher vibrational states at $R < R_e^{Br_2}$. Ionization with a bond length and vibrational level dependence thereby shifts the initially incoherent $\mathrm{Br}_2\ {}^1\Sigma_g^+$ vibrational amplitude toward the outer turning point of the potential in Br_2 as seen in the bottom portion of Fig. 4.3, creating a partially coherent superposition of the remaining populated vibrational levels. For all subsequent calculations of R_v-ADK probabilities, an initial Boltzmann distribution of vibrational state populations is employed. At 300 K (the conditions of the experiment), the following square vibrational level wave function cofactors up to ν_3 are taken from the Boltzmann distribution: $\left|a_0\right|^2 : \left|b_0\right|^2 : \left|c_0\right|^2 : \left|d_0\right|^2$ = 79%:17%:3%:<1%, given the incoherent probability density of the vibrational states is $\left|\mathrm{a}_0\psi_{\upsilon=0}\right|^2 + \left|\mathrm{b}_0\psi_{\upsilon=1}\right|^2 + \cdots + \left|\mathrm{n}_0\psi_{\upsilon=\mathrm{n}}\right|^2 = 1$.

It is necessary to determine the degree to which the intense laser electric field perturbs the nuclear potentials and thereby the impact on ionization rates. Tunnel ionization is by definition facilitated by suppression of the electron binding potential by the interacting laser electric field, and while the impact on the nuclear potential curves is similar, perturbation of the Born-Oppenheimer curves at low ionizing field intensities is minimum.[139] Here, we have calculated the R_v-ADK tunnel ionization rates according to the ionization energy with R of the field-free Born-Oppenheimer potential curves, which is an accurate approximation within the experimentally chosen ionizing pump field intensity set to achieve threshold ionization of Br_2.

4.3 Experimental Set-up

The experimental apparatus is presented in Fig. 4.4 and has been described in detail previously.[19] The high harmonic source was changed from a capillary waveguide to a semi-infinite gas cell[36] for increased pulse-to-pulse XUV stability and a 10^3 increase in photon flux. The high harmonic generation process is driven by 800 nm (1.6 mJ) + 400 nm (25 μJ) 40 fs, 1 kHz linearly polarized light, producing both even and odd order harmonics of the fundamental for increased spectral coverage. Removing the inversion symmetry of the driving laser electric field limits XUV pulse generation to once every full optical cycle of the driving laser, generating both the even and odd order harmonics.[120] The decrease in XUV pulse production increases the continuum observed between adjacent harmonics resulting from the reduced interference between pulses in the XUV pulse train. The increased spectral coverage of the even and odd harmonics improves the effectiveness of the XUV probe, improving the signal-to-noise of absorption features between adjacent odd harmonics. The XUV light is focused (beam waist = w_0 = 20 μm) into the sample gas cell filled with 3.4 kPa of Br_2 and overlapped at a 1° crossing angle with a 180 μJ, 800 nm pump pulse (w_0 = 42 μm) for strong-field ionization; the polarization is parallel to the XUV probe. The XUV transient absorption signal is obtained by measuring the optical density (OD) of the transient species relative to the static absorption in absence of the pump pulse to yield the ΔOD. Transient absorption spectra are collected from -0.3 to 40 ps in 20 fs steps averaging 16 scans with an integration time of 0.2 s at each time delay. Each data point is referenced to a unique “pump-off” spectrum utilizing an electronic shutter to block the pump beam and allow for correction of the fluctuation in XUV flux. The temporal resolution of the instrument is 25 ± 5 fs, as determined by the rise-time of the strong-field ionization of Xe → Xe^+ measured by the $5p_{3/2}^{-1}\left({}^2P_{3/2}\right) \longrightarrow 4d_{5/2}^{-1}\left({}^2D_{5/2}\right)$ transition at 55.4 eV.[20,22]

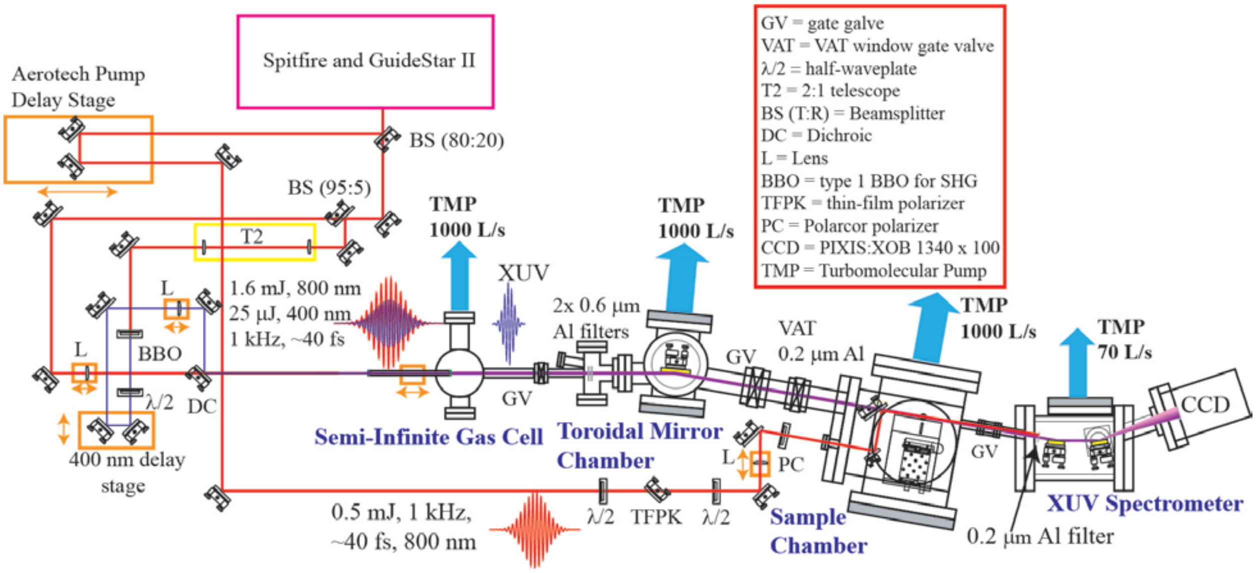

Figure 4.4: Schematic of the experimental apparatus for 800 nm strong-field pump and XUV probe, utilizing a semi-infinite gas cell for high-harmonic generation of the XUV probe. The pointing of the Spitifire Pro beam has been actively stabilized utilizing a Newport GuideStar II.

4.4 Results and Discussion

In Fig. 4.5, a portion of the observed XUV transient absorption signal is displayed as a function of pump-probe delay between the ionizing 800 nm pump and XUV high-harmonic probe pulse. The formation of atomic bromine from dissociative ionization is observed through the ${}^2P_{3/2} \longrightarrow {}^2D_{5/2}$ (64.4 eV), ${}^2P_{1/2} \longrightarrow {}^2D_{3/2}$ (65.1 eV), and ${}^2P_{3/2} \longrightarrow {}^2D_{3/2}$ (65.4 eV) optical transitions. Clear oscillations in transition energy and optical density (OD) are observed in the Br_2 ${}^1\Sigma_g^+$ ground state transitions at 68.3 eV $\left({}^1\Sigma_g^+, \sigma^{*-1} \rightarrow 3d_{5/2}^{-1}\right)$ and 69.4 eV $\left({}^1\Sigma_g^+, \sigma^{*-1} \rightarrow 3d_{3/2}^{-1}\right)$, where λ^{-1} represents a hole in a molecular orbital. Furthermore, the two 3d spin-orbit state transitions of the neutral beat against each other in the energy range around 68.8 eV, leading to reduced contrast of the $3d_{3/2}^{-1}$ transition.

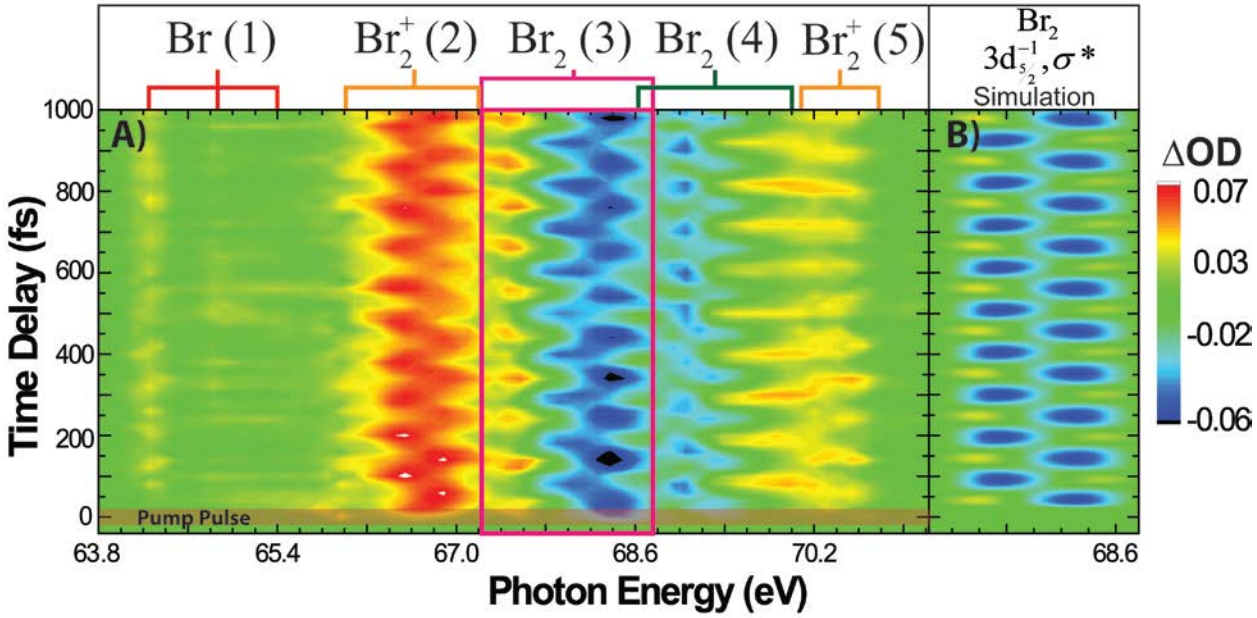

Figure 4.5: Comparison of experimental data and simulation of the core-level transient absorption signal of strong-field ionized Br₂. A) False color map of the experimental absorption signal in time using an ionizing 800 nm pump field of $1.6\,\mathrm{x}\,10^{14}\ \mathrm{W}/\mathrm{cm}^2$ (shown at t = 0 in transparent red). The ${}^1\Sigma_g^+$ ground state wave packet is observed to launch on the outer turning point of the potential with a period of 104 fs by the transitions bracketed (3) and (4), corresponding to the Br₂ ${}^1\Sigma_g^+$ $\sigma^{*-1} \rightarrow 3d^{-1}_{5/2}$ and $\sigma^{*-1} \rightarrow 3d^{-1}_{3/2}$ transitions, respectively. The ${}^2\Pi_{3/2,g}$ ion wave packet is observed through transitions (2, $\pi^{*-1} \rightarrow 3d^{-1}_{5/2}$) and (5, $\sigma^{*-1} \rightarrow 3d^{-1}_{5/2}$), with a 94 fs period. Atomic Br transitions are labeled (1), corresponding to the ${}^2P_{3/2} \longrightarrow {}^2D_{5/2}$ (64.4 eV), ${}^2P_{1/2} \longrightarrow {}^2D_{3/2}$ (65.1 eV), and ${}^2P_{3/2} \longrightarrow {}^2D_{3/2}$ (65.4 eV) transitions. B) Simulation of the core-level absorption of the ${}^1\Sigma_g^+$ wave packet probed to the $3d^{-1}_{5/2}$ core-hole state (cf. experimental data (3) boxed in pink) employing R-dependent ADK theory and REW-TD-DFT calculations for the strong-field ionization response and core-hole excitation, respectively.

The ${}^1\Sigma_g^+$ wave packet optical signatures, in particular the $\sigma^{*-1} \rightarrow 3d^{-1}_{5/2}$ resonance boxed in red in Fig. 4.5, present both positive and negative features oscillating in amplitude and transition energy periodically. The neutral transitions appear predominantly as -ΔOD due to depletion of the ${}^1\Sigma_g^+$ population through ionization. As the vibrational wave packet coalesces at the ${}^1\Sigma_g^+$ outer (inner) turning point, the core-excitation energy is lower (higher) than for the static population as determined by the REW-TD-DFT calculations in Sec. II. Examining the outer turning point, the dynamic-static spectral overlap yields a positive and negative ΔOD feature observed at 67.8 eV and 68.4 eV, respectively, whereas localization at the inner turning point shifts the positive feature to a higher energy relative to the depletion. This periodic oscillation of the static absorption features is shown in Fig. 4.6. Evolution of the wave packet relative to the static absorption provides a direct measure of the vibrational amplitude position and shape at all pump-probe delay times.

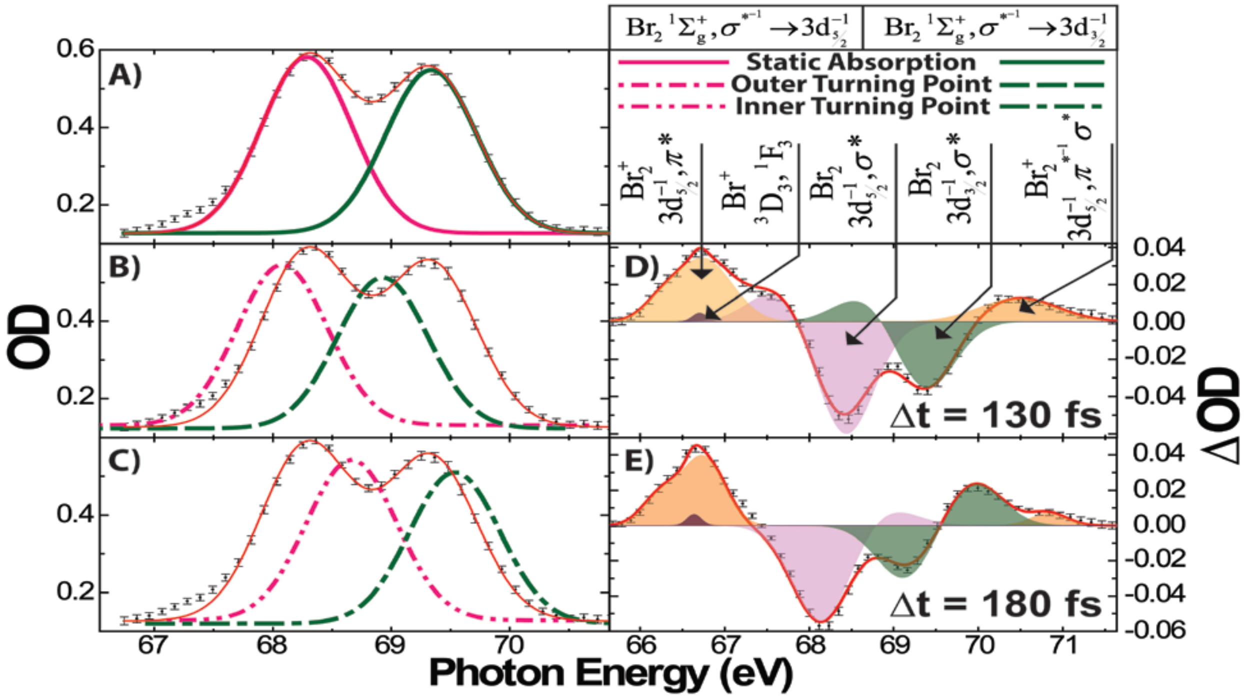

Figure 4.6: Core-level ($3d_{5/2, 3/2}$) absorption spectra of Br₂. A) The static absorption ("pump-off") signal of Br_2 (black dots with standard error of the mean) fit to two Gaussians, each of 0.8 eV width, resulting in the red trace. B) (outer turning point) and C) (inner turning point) correspond to the time evolving absorption of the $\widetilde{X}\,^1\Sigma_g^+$ simulated vibrational wave packet signal at the turning points of the potential relative to the static absorption signal. D) The observed transient absorption signal at 130 fs pump-probe delay (outer turning point), and E) the transient absorption signal at 180 fs delay (inner turning point). The transitions are labeled according to the electronic structure of the final state.

To confirm the interpretation of the XUV transient absorption signal with respect to the strong-field generated ground state vibrational dynamics, the results of the REW-TD-DFT and R_v-ADK calculations are combined to simulate the pump-probe $Br_2\ ^1\Sigma_g^+$ spectrum. The remaining ground state vibrational level populations after interaction with the ionizing pump are calculated by R_v-ADK and propagated by the time evolution operator. The resulting time-dependent vibrational amplitude is utilized to calculate the XUV transient absorption signal for the wave packet by incorporating the REW-TD-DFT results. The simulated XUV transient absorption signal for the $Br_2\ ^1\Sigma_g^+\ \sigma^{*-1} \rightarrow 3d_{5/2}^{-1}$ transition presented in Fig. 4.5 is found to agree well with the experimental result.

Fast-Fourier Transform (FFT) of the Br_2 $^1\Sigma_g^+$ XUV transient absorption signal resolves the composition of the vibrational wave packet with unprecedented spectral resolution (~1 cm^{-1}) for femtosecond core-level transient spectroscopy as shown in Fig. 4.7. The three natural isotopic Br_2 $\nu_0\nu_1$ vibrational beats are observed with the correct ratio of 1:[1.8± 0.2]:1 $\left({}^{79-79}Br_2 : {}^{79-81}Br_2 : {}^{81-81}Br_2\right)$, and the ${}^{79-81}Br_2$ $\nu_0\nu_1$ beat has the expected frequency of 321 cm^{-1}, i.e. period $\left(\tau_{\nu_0\nu_1}\right)$ of 104 fs.[171] Fitting the transient absorption signal at 68.3 eV, seen in the inset of Fig. 4.7, with a convolution of Heaviside (strong-field depletion), Gaussian (instrumental response function), and cosinusoidal (wave packet) functions confirms the wave packet period, 104 ± 1 fs, and determines a $\nu_0\nu_1$ beat amplitude of 0.008 ± 0.001 OD. The phase is measured relative to the center of the Br_2 depletion and describes the relative bond length where the wave packet is prepared. A phase of π indicates a wave packet is prepared at short R, while zero corresponds to a wave packet prepared at long R.[136] Correlating the measured phase of $0.21\pi \pm 0.05\pi$ with the progression of the $^1\Sigma_g^+$ transient absorption signal in Fig. 4.5 confirms the wave packet is prepared near the outer turning point, indicative of increased ionization at the inner turning point.

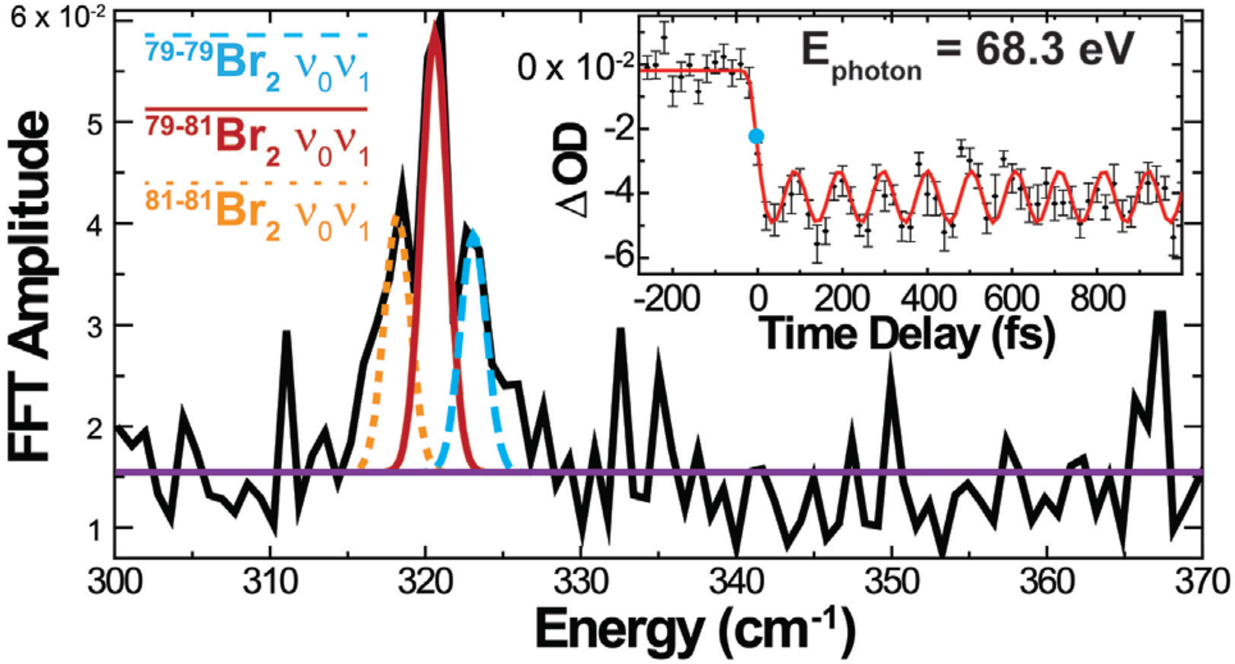

Figure 4.7: FFT of the transient absorption signal from 67.4 to 70.5 eV. The inset shows the fit of the Br_2 $^1\Sigma_g^+, \sigma^{*-1} \rightarrow 3d_{5/2}^{-1}$ transient absorption signal at 68.3 eV. The wave packet is measured to have a 104 ± 1 fs period with a phase of 0.21 ± 0.05π relative to the Br_2 strong-field response (blue dot, -5 ± 2 fs) and an oscillatory amplitude of 0.008 ± 0.001 ΔOD. Error bars correspond to one standard error of the mean.

The change in the $3d^{-1}_{5/2}$ core-hole transition energy with bond length may be estimated knowing the beat composition of the Br_2 ${}^1\Sigma_g^+$ wave packet and the transition energy at the molecular potential inner and outer turning point. The maximum shift in transition energy is experimentally found to be 0.5 eV from the static resonance. Representing the ${}^1\Sigma_g^+$ state by the spectroscopically determined Morse potential,[171] the change in R is 7 pm from the inner to outer turning points of a $\nu_0\nu_1$ wave packet, calculated relative to the mean of the vibrational amplitude. The $3d \rightarrow \sigma^*_{LUMO}$ change in transition energy with bond length is determined to be approximately $0.14\ {}^{\mathrm{eV}}\!/_{\mathrm{pm}}$, indicating the $3d^{-1}_{5/2},\ \sigma^*$ state is repulsive around $R_e^{Br_2}$. Therefore, a high degree of sensitivity for the XUV absorption energy with bond length is realized, facilitating direct probing of a vibrational wave packet exploring a small oscillatory range.

Inspecting the cation core-level transition energies in Fig. 4.5, the average bond length where the ion vibrational wave packet is prepared may be determined. The oscillating transitions centered at 66.7 eV $\left({}^2\Pi_{g,3/2}, \pi^{*^{-1}} \rightarrow 3d^{-1}_{5/2}\right)$ and 70.4 eV $\left({}^2\Pi_{g,3/2}, \sigma^{*^{-1}} \rightarrow 3d^{-1}_{5/2}\right)$ excite the Br_2^+ ion wave packet to separate core-hole states, filling either the strong-field generated π^* hole or the unoccupied σ^* molecular orbital. As with the neutral wave packet, evolution of the internuclear separation of the ion leads to a change in the XUV transition energy to the corresponding core-hole excited states. The lack of a static reference feature for the ion means that the transient absorption signal is always positive and dependent only on the transition energy and oscillator strength with R. The lineshape of the resonance at each time delay is a direct measure of the vibrational wave packet amplitude. Examining the ion vibrational wave packet at the molecular potential turning points shows the vibrational amplitude piling up, spectrally manifesting as an increase in optical density and a narrowing of the lineshape as seen in Fig. 4.5. Though this result could be expected from similar investigations in the visible regime, it illustrates the effectiveness of bond-length-specific XUV probing for directly visualizing vibrational dynamics.

Intuitively, Franck-Condon ionization of $Br_2\left({}^1\Sigma_g^+\right) \rightarrow Br_2^+\left({}^2\Pi_{g,3/2}\right)$ predicts the ion vibrational wave packet to be initially localized at $R_e^{Br_2}$, toward the ${}^2\Pi_{g,3/2}$ outer turning point as $R_e^{Br_2^+} < R_e^{Br_2}$, exciting a broad manifold of vibrational states centered on ν_2.[197] Contrariwise, Lochfraß predicts preferential depletion of the ${}^1\Sigma_g^+$ vibrational population at the inner turning point, preparing the Br_2^+ ${}^2\Pi_{g,3/2}$ wave packet close to $R_e^{Br_2^+}$. Examining the Br_2^+ $3d^{-1}_{5/2},\ \pi^*$ transition energy in Fig. 4.5 at ~20 fs pump-probe delay shows the ion superposition is birthed at $R \approx R_e^{Br_2^+}$, indicative of Lochfraß. Fitting the measured ion vibration signal at 66.7 eV in the same manner as the neutral reveals the vibrational period is 93 ± 1 fs $\left(\tau_{\nu_0\nu_1}^{Br_2^+} = 92\text{ fs}\right)$. FFT of the ion wave packet reveals only a broad feature centered at 360 cm^{-1}. Although the exact composition of the vibrational wave packet cannot be retrieved, it can be inferred by the width of the FFT feature that several vibrational levels are substantially populated. Comparable results are observed for the strong-field ionization of H_2, where $\nu_0 \longrightarrow \nu_2$ are populated almost equally. Furthermore, by utilizing the spectroscopically measured parameters[169] for the $\mathrm{Br}_2^+\ {}^2\Pi_{\mathrm{g},3/2}$ state modeled by a Morse potential, the slope of the ion $3d_{5/2}^{-1},\ \pi^*$ potential curve may be determined in a similar fashion as was conducted for the neutral $3d_{5/2}^{-1}$ core-hole state. The probing of the $\mathrm{Br}_2^+\ {}^2\Pi_{\mathrm{g},3/2}$ vibrational wave packet to $3d_{5/2}^{-1},\ \pi^*$ state is determined to have a change in XUV transition energy with bond length of approximately $0.09\ \mathrm{eV}/\mathrm{pm}$. The increased bond strength of the ion reduces the bond-length-specificity of the XUV probe due to the softened curvature of the $3d_{5/2}^{-1},\ \pi^*$ core-hole excited state as observed experimentally.

Tunnel ionization's effectiveness to prepare a ground state vibrational wave packet is gauged by the degree of coherence of the vibration within the sampled ensemble, measured by the magnitude of the off-diagonal terms of the density matrix $\rho_{\nu_0\nu_n}$. The probability of finding a molecule in vibrational states $\{\nu_0,\cdots,\nu_n\}$, with $\nu_\mathrm{n} = \mathrm{n}\psi_{\mathrm{v=n}}\mathrm{e}^{-\mathrm{i}\omega_\mathrm{n}\mathrm{t}}$, is given by:

$$\rho_{\nu_0\nu_\mathrm{n}} = \begin{bmatrix} |\mathrm{a}^2| & \cdots & \mathrm{n}^*\mathrm{a}\mathrm{g}_{\upsilon_0\upsilon_\mathrm{n}} \cos\left[\omega_{\upsilon_0\upsilon_\mathrm{n}}\mathrm{t} + \varphi_{\upsilon_0\upsilon_\mathrm{n}}\right] \\ \vdots & \ddots & \vdots \\ \mathrm{a}^*\mathrm{n}\mathrm{g}_{\upsilon_0\upsilon_\mathrm{n}} \cos\left[\omega_{\upsilon_0\upsilon_\mathrm{n}}\mathrm{t} + \varphi_{\upsilon_0\upsilon_\mathrm{n}}\right] & \cdots & |\mathrm{n}^2| \end{bmatrix} \tag{4.2}$$

where $\omega_{\upsilon_\mathrm{m}\upsilon_\mathrm{n}}$, $\varphi_{\upsilon_\mathrm{m}\upsilon_\mathrm{n}}$, and $g_{\nu_m\nu_n}$ are the frequency, phase, and degree of coherence of the $\nu_\mathrm{m}\nu_\mathrm{n}$ vibrational beat, respectively. Diagonal elements of $\rho_{\nu_0\nu_n}$ account for the neutral depletion ΔOD, and the off-diagonal elements describe the oscillation in the ΔOD amplitude due to the wave packet motion. Comparing the Br_2 transient depletion optical density at positive time delays and the $3d_{5/2} \rightarrow \sigma_{LUMO}^*$ static absorption, ~5% of the Br_2 population in the XUV focal volume is determined to be ionized by the pump, i.e. $\mathrm{Tr}\left[\rho_{\nu_0\nu_\mathrm{n}}\right] = 0.95$.

In typical formulations of the density matrix, $g_{\nu_m\nu_n}$ is absent and the coherences are determined directly from the off-diagonal elements. Introduction of $g_{\nu_m\nu_n}$ provides a means to quantify the degree of coherence between the vibrational beats composing the strong-field generated wave packet. Before the interaction with the strong-field pump, the phases between the vibrational levels are randomly distributed over 2π. After ionization, a distinct $\varphi_{\upsilon_\mathrm{m}\upsilon_\mathrm{n}}$ exists for part of the measured molecular ensemble, while some of the population still has a randomly distributed phase over 2π. The ratio of ensemble's population with a phase of $\varphi_{\upsilon_\mathrm{m}\upsilon_\mathrm{n}}$ verses a random phase is gauged by $g_{\nu_m\nu_n}$. Here, a $g_{\nu_m\nu_n}$ of unity indicates only one value of the phase exists between ν_m

and ν_{n} in the measured molecular ensemble, while zero specifies a random phase distribution over 2π.

The FFT in Fig. 4.7 shows $\nu_0\nu_1$ is the dominant quantum beat, and coherence terms involving ν_2 and greater are found to be quite small. For determination of the degree of coherence of the ground state vibrational wave function, contributions of ν_2 and greater are neglected, but a static population in ν_2 is retained to account for the $\mathrm{Tr}\left[\rho_{\nu_0\nu_{\mathrm{n}}}\right]$. Furthermore, convolution of the instrument response function with the $\nu_0\nu_2$ overtone frequency indicates the beat is beyond the temporal resolution of the instrument and therefore not resolved and may also be discounted in determination of the wave packet's degree of coherence.

The degree of coherence is evaluated at the center of the ${}^1\Sigma_g^+, \sigma^{*-1} \rightarrow 3d^{-1}_{5/2}$ static absorption Gaussian fit at 68.3 eV shown in the inset of Fig. 4.7. The change in optical density with time is:

$$\Delta OD(E) = \left(OD_{incoherent}(E) + OD_{coherent}(E,t)\right) - OD_{static}(E) \qquad (4.3)$$

$$\left[|a|^2\left|\psi_{v=0}(E)\right|^2 + |b|^2\left|\psi_{v=1}(E)\right|^2 + |c|^2\left|\psi_{v=2}(E)\right|^2\right] p_{XUV} = OD_{incoherent}(E) \qquad (4.4)$$

$$2 * \mathrm{Re}\left[a^* b g_{\nu_0\nu_1} p_{XUV} \psi^*_{v=0}(E)\psi_{v=1}(E)\cos\left[\omega_{\upsilon_0\upsilon_1} t + \varphi_{\upsilon_0\upsilon_1}\right]\right] = OD_{coherent}(E,t) \qquad (4.5)$$

where $OD_{incoherent}(E)$ and $OD_{coherent}(E,t)$ relate to the transient absorption amplitude of the incoherent and coherent components of the population, respectively. $OD_{coherent}(E,t)$ is given by the time-dependent amplitude associated with $\cos\left[\omega_{\upsilon_0\upsilon_1} t + \varphi_{\upsilon_0\upsilon_1}\right]$, and p_{XUV} is an experimentally estimated ${}^1\Sigma_g^+, \sigma^{*-1} \rightarrow 3d^{-1}_{5/2}$ core-hole transition probability. The transition probability cofactor is obtained by fitting the static OD to the probability density multiplied by a constant relating to the experimental conditions (transition strength, gas density, interaction length) at 68.3 eV. An estimate for $g_{\nu_0\nu_1}$ can be determined by considering the extreme case where 5% of the initial ${}^1\Sigma_g^+$ population is removed entirely from only one vibrational level. The range of $g_{\nu_0\nu_1}$ satisfying the experimental data as interpreted by Eq. (4.3-4.5) is 0.19 → 0.24. A previous experiment also demonstrated a lack of perfect coherence resulting from strong-field ionization, which was attributed to scrambled vibrational level phases.[136] Ionization of the ground state occurs during the entirety of the pump pulse, constantly varying $\varphi_{\upsilon_0\upsilon_1}$ of the generated coherence. Therefore, phase scrambling is dependent on the ratio of the experimental pump pulse duration to the vibrational beat. Here, we present the first estimate of the Lochfraß wave packet degree of coherence, and subsequently the qualitative degree to which $\varphi_{\upsilon_0\upsilon_1}$ remains scrambled after ionization for an ensemble of molecules, given the experimental conditions $\left(\tau_{pump} \approx \tau_{\nu_0\nu_1}/2\right)$.

The estimation of $g_{\nu_0\nu_1}$ could be inaccurate due to compounding factors, two of which are considered here. Firstly, the possibility exists that population is transferred coherently/incoherently by Raman excitation to higher vibrational states.[131,198] Recalculating $g_{\nu_0\nu_1}$ with a 50% increase of the ν_2 incoherent population from ν_0 or ν_1 still yields a $g_{\nu_0\nu_1}$ less than 0.5 as predicted utilizing equations (4.3-4.5), i.e. at least 50% of the ensemble vibrational phases are randomly distributed. Absence of high-order vibrational beats in the FFT presented in Fig. 4.7 discounts excitation of coherent vibrational population to higher lying levels. Therefore, the impact of neglecting Raman processes is minor. Moreover, impulsive stimulated Raman scattering could account for the origin of the ground state vibrational superposition, as Raman is phase coherent, but full coherence is lost due to the time required to pump from one state to another. Raman does not however account for the correlation between the Br_2 $^1\Sigma_g^+$ and Br_2^+ $^2\Pi_{3/2,g}$ vibrational wave packets as Raman is not an ionizing process. Secondly, loss of XUV absorption signal due to rotation of the coherently vibrating Br_2 molecular ensemble relative to the XUV probe polarization could also lead to an inaccurate estimation of $g_{\nu_0\nu_1}$. No inaccuracy is expected due to the rotational dynamics of the molecule as the current estimate of $g_{\nu_0\nu_1}$ is obtained from the transient absorption signal within the first picosecond of pump-probe delay and the rotational period of Br_2 is 205 ps.[170] Considering an initially isotropic distribution of diatomic molecules, perfect phase matching of all molecular oscillators is most likely impossible to obtain as a long pulse would favor alignment of the molecular ensemble with the field, while a comparatively short pulse to the vibrational period will maximize phase coherence.

As mentioned previously, Lochfraß in diatomics is dependent upon the ionization energy at various bond lengths and the degree to which the laser field distorts the potential energy surfaces. Investigations of ground state wave packet formation in I_2 serves as a model system for ionization that is dependent on field-dressed molecular potentials,[136,140,164] whereas results for H_2/D_2 are independent of the degree of field perturbation. Strong-field studies of room-temperature I_2 demonstrate increased ionization at elongated bond lengths, despite the increase in ionization energy with R under field-free conditions.[135] Field-dressing of the molecular potentials inverts the slope of the ionization energy with R, resulting in a wave packet at the inner turning point.[136,140] However, Lochfraß of few-Kelvin H_2/D_2 is explained by R dependent ADK calculations employing the field-free molecular potentials.[70,134,139] Field perturbation of the H_2/D_2 potential pushes the region of preferred ionization to longer bond lengths, but still selectively ionizes the ground state at the outer turning point of the potential curve.[58,164] Therefore, the ground state vibrational wave packet is prepared at the inner turning point as with I_2. These model experiments have left an open question as to whether preferential ionization can occur without field-dressing the molecular potentials, allowing increased ionization at a vibrational potential curve's inner turning point. This experiment provides a missing link between studies in I_2 and H_2/D_2, demonstrating clear, bond-length dependent ionization of Br_2 under conditions in which significant field-dressing of the nuclear potentials does not occur.

Lastly, a narrow absorption feature with a 0.2 eV Gaussian width is observed at 66.6 eV in Figs. 4.5 and 4.6, assigned to the Br^+ transitions of ${}^2P_3 \longrightarrow {}^3D_3$ and ${}^1D_2 \longrightarrow {}^1F_2$. The feature is too narrow to be a molecular transition and is constant in time as observed at both 130 fs and 210 fs, indicating it does not stem from the molecular wave packet dynamics (localization at a turning point). Current work at the Advanced Light Source has shown that both atomic transitions have similar cross-sections near the observed transition energy with linewidths less than the spectral resolution of the instrument.[199] Therefore, the two transitions are indistinguishable with the current experimental configuration.

4.5 Conclusions and Outlook

In conclusion, we observe the formation of a ground state vibrational wave packet in room-temperature bromine without consequential field perturbation of the molecular potentials by utilizing the expanded capabilities of XUV transient absorption spectroscopy.[188,200,201] The present work demonstrates this technique to be an effective method for bond-length-specific probing and real-time determination of vibrational wave packet properties. These results indicate that the ground state wave packet is prepared on the outer turning point of the potential by bond-length sensitive XUV absorption of the neutral and ion states, and substantiated by ADK and REW-TD-DFT calculations. Furthermore, the degree of coherence for a Lochfraß wave packet is directly measured for the first time. At the experimental field intensity, there is no indication of sizable vibrational population redistribution to higher levels as a result of Raman pumping or ionization at long bond lengths.

Finally, we would like to emphasize the far-reaching consequences of bond-length-sensitive XUV transient absorption: Here, we have demonstrated core-level, bond-length specific probing on the femtosecond timescale for a homonuclear diatomic. The natural extension is to investigate heteronuclear systems, fully utilizing the element specific capabilities of the XUV probe and allowing detection of vibrational motion with bond-length-specificity at multiple reporter atoms. Expansion of this technique to the attosecond regime may facilitate detection of correlated electronic and nuclear coherences in real-time. This has implications for studying phenomena such as charge-transfer/localization and non-Born-Oppenheimer dynamics with unprecedented resolution and clarity.[202,203]

Chapter 5

Field Intensity Dependence of Vibrational Wave Packets in Br_2 as Probed by High-Harmonic Extreme Ultraviolet Transient Absorption Spectroscopy

Dependence of ground state vibrational wave packets on the ionizing field intensity is investigated in molecular bromine by bond-length-specific extreme ultraviolet (XUV) transient absorption. A change in the ionization mechanism and preparation of the vibrational superposition as a function of field intensity is observed. At low peak intensities, a ground state wave packet is prepared on the ${}^1\Sigma_g^+$ outer turning point by preferential ionization at the minimum energy between the field-free Br_2 ${}^1\Sigma_g^+$ and Br_2^+ ${}^2\Pi_{g,3/2}$ states. The wave packet is primarily composed of the v_0v_1 beat, as determined by Fast-Fourier transform (FFT) analysis of the transient absorption signal, indicating a dissipation of vibrational energy by ionization. As the field intensity increases, the involvement of a Raman pumping mechanism, which drives the ground state population to higher vibrational levels becomes evident as beats are observed in the FFT up to $\nu_3\nu_4$. Also, field-dressing of the molecular potentials facilitates tunneling over a larger range of bond lengths, which is directly observed by a shift in the ion core-hole transition energy within the ionizing pulse envelope. This experiment demonstrates a correlation between the ionizing laser field intensity and the dynamics of the generated ground and ion state vibrational wave packets.

5.1 Introduction

The molecular electron and nuclear dynamics coupled to the intensity of a strong-laser field provide a unique environment to explore the optical manipulation of chemical reactions.[29,48] Interaction of molecules with an intense laser pulse, comparable in magnitude to the binding potential experienced by valence electrons, facilitates a reduction of the ionization continuum threshold, allowing removal of one or multiple electrons.[52,94] Therefore, depending on the ionizing field intensity, the charge of the created photoion may be selected to some extent, dictating the subsequent dissociation pathways.[46,51,75,83] Even in the absence of ionization, field-dressing of the molecular potential energy surfaces by AC-Stark shifting enables direct control of photochemical processes by strong-field pulses.[73,204] Finally, formation of vibrational superpositions by tunnel ionization is also intrinsically tied to the field intensity of the driving laser, providing a nonresonant ionizing pathway for wave packet preparation on both ground and ion potentials.[70,71,164]

Detection of nuclear motion in real-time provides insight into the potential energy landscape driving chemical reactions and molecular dynamics.[15,205] Few-femtosecond visible pump-probe experiments are particularly successful at allowing a direct monitoring of vibrational wave packets in real-time by virtue of spectrally dispersing the bond-length-specific probe after the interaction region.[18,142,143] Even-so, traditional single-photon pump-probe experiments are limited to investigating vibrational wave packets driven by the bandwidth of femtosecond pulses on an excited state, or consist of complex pump-dump-probe schemes to access the ground state.[206-208] Beyond single photon absorption for the creation of a vibrational superposition, the involvement of multiple photons may also induce coherent vibrational motion. By increasing the field intensity of the pump pulse, Impulsive Stimulated Raman Scattering (ISRS) can nonresonantly excite vibrational superpositions on the ground state due to the force exerted on the molecular vibrational modes by the electric field of the laser.[131] Increasing the laser intensity further prepares correlated vibrational wave packets on the ground and ion states by a localized ionization pathway.

The two mechanisms for ground state vibrational wave packet formation by Raman scattering generate two quite different vibrational population distributions. For Resonant ISRS, the wavelength difference and temporal separation between the excitation pulse and the Stokes pulse determine the composition of the ground state vibrational superposition. Red shifting of the Stokes pulse with respect to the excitation pulse leads to a vibrational level (ν) population distribution in the ground state centered at $\nu > \nu_0$. Time delaying the Stokes pulse relative to the excitation pulse allows the propagation of the wave packet on the excited state surface, altering the ν distribution on the ground state after the Stokes pulse. Nonresonant ISRS may generate a ground state vibrational superposition through an impulsive driving force to the molecule via the pump pulse. The magnitude of the force applied to the molecule is proportional to the intensity of the electric field of the pump pulse and the polarizability of the vibrational mode, given that the excited mode is Raman active and the pulse duration is short compared to the vibrational mode oscillatory period. In the weak-field limit, contributions above $\Delta\nu=1$ are often small.[131,209] In the strong-field regime it is possible to directly generate ground state vibrational coherences as a result of selective depletion of the vibrational amplitude via an ionization mechanism.

The interaction of an intense ionizing laser with diatomic molecules provides a model system for investigating ground state vibrational dynamics by internuclear separation, R, dependent ionization.[71] By selectively depleting the ground state vibrational amplitude, the remaining population is coherently formed into a superposition of states. Increased ionization is observed around the minimum ionization energy, which is dictated by the nuclear coordinates and the degree to which the intense laser field has perturbed the potential energy surfaces. This process of localized preferential ionization has become known as the Lochfraß mechanism.[70] Calculating the ionization rate according to the static molecular potentials is straightforward, but incorporating the degree of distortion by the intense field is computationally intensive for H_2 and prohibitively so for heavier diatomics. Even so, the distortion of the molecular potentials is pinnacle in understanding the ground state ionization dynamics and the formation of vibrational coherence populations in the molecular ion. Experimental investigation of Lochfraß vibrational wave packets has been explored for several systems including H_2, I_2, and most recently Br_2, each of which demonstrates preparation of the superposition differently in terms of the initial localization and vibrational beat composition.

The strong-field ionization of H_2/D_2 has been investigated extensively both experimentally and theoretically in terms of the field-free and distorted potential energy surfaces.[69] For H_2/D_2 initially in the ν_0 state, preferential ionization, Lochfraß, is consistently observed at the molecular potential outer turning point.[134,139] Population transfer from ν_0 to ν_1 is also observed in these studies, indicating the activity of a Raman pumping mechanism, a necessity for wave packet formation in H_2/D_2 at 3 K. Under field-free conditions, the minimum ionization energy is located near the outer turning point as calculated by the potential energy surfaces.[70] The position of the minimum ionization energy also corresponds to the maximum ionization rate according to Ammosov-Delone-Krainov (ADK) theory.[50] As a perturbative strong-field is applied to the potentials, the ionization rate at long internuclear separations increases due to Enhanced Ionization and peaks at a critical bond length, R_c.[164,210] Vibrational wave packet preparation in H_2/D_2 is therefore difficult to interpret as preparation occurs on the inner turning point regardless of the perturbation of the potential curves. Enhanced ionization at R_c is not an exclusive effect for H_2, but rather it is a broadly applicable phenomena involving the perturbation of the molecular potentials that has also been observed for the strong-field ionization of I_2. For Br_2 R_c is determined to be 3.86 Å according to the formulation presented by Seideman et al.[164]

One of the hallmarks of Lochfraß wave packets is the small subset of superimposed vibrational states, typically only ν_0 and ν_1 for cold H_2/D_2. Preparation of a superposition in room temperature I_2, where ν_0 contains only ~59% of the ground state population, by enhanced ionization at R_c also leads to a predominantly $\nu_0\nu_1$ wave packet formed on the inner turning point.[136] Preferentially depletion of the higher lying vibrational states forms the $\nu_0\nu_1$ wave packet due to the dependence of the ionization energy with R and the vibrational amplitude distribution with ν.[135] As the field intensity is increased, the ground state vibrational population is found to decrease in energy, concentrating the population in ν_0. I_2 has also been exploited as a platform for examining the R dependence of strong-field ionization by increasing the bond length range explored by the generated wave packet. Experiments involving a pump-dump scheme to create a vibrational wave packet in $\nu = 33$ of I_2 confirm the trending of increasing ionization rates with R over a larger range of internuclear separations. The preferential ionization is attributed to tunnel ionization from the HOMO-2$\left(\sigma_g\right)$, which is aligned with the electric field of the ionizing laser yielding an increased ionization rate.[66,140] The increased ionization from the HOMO-2 indicates a preference for tunneling from an aligned state over the smaller ionization energy of the HOMO.

Most recently, selective depletion of Br_2 was observed at the inner turning point, and no field dressing of the molecular potentials was required to interpret the observed vibrational wave packet preparation.[211] While both I_2 and Br_2 have a minimum in ionization energy at R shorter than their respective equilibrium bond lengths (R_e), wave packet are observed to be prepared on the opposite ends of the molecular potentials. The difference in the preparation mechanism for the superposition is the degree to which the potential curves are distorted by the strong-field. For Br_2, only the Born-Oppenheimer curves are necessary in the analysis, while in I_2, the observed enhanced ionization at R_c is facilitated by the distortion of the potential energy curves. This suggests a link between wave packet preparation and field intensity. Varying the ionizing field in I_2 reveals a reduction in neutral molecule vibrational energy with increasing field intensity, leaving the vibrational population mainly in the ground vibrational state, but no trend between the tunneling mechanism and wave packet preparation was established.[68,135,136] Due to the difference in the ionization energy of I_2 and Br_2, it is expected that the same field intensity distorts the I_2 potential curves but does not affect the Br_2 curves.

Here, we investigate the intensity dependent strong-field ionization dynamics of vibrational wave packet formation in Br_2 with the objective of qualitatively establishing the mechanism for preparing the superposition in terms of the field perturbation of the nuclear potential energy surfaces. Four separate intensities are measured including, $1.0 \text{ x } 10^{14}\, {}^{W}\!/\!{}_{cm^2}$, $1.6 \text{ x } 10^{14}\, {}^{W}\!/\!{}_{cm^2}$, $2.0 \text{ x } 10^{14}\, {}^{W}\!/\!{}_{cm^2}$, and $4.0 \text{ x } 10^{14}\, {}^{W}\!/\!{}_{cm^2}$. By monitoring the *3d* core level transitions of neutral bromine, the preparation of the ground state wave packet is directly retrieved. Examination of the XUV absorption of the bromine molecular cation formed by strong-field ionization elucidates the effect of increasing the laser intensity on the potential energy curves as schematically illustrated in Fig. 5.1. Furthermore, the experiments presented here unveil a direct correlation between field intensity and the composition of the vibrational wave packets. The remainder of this chapter is organized as follows. The tunnel ionization rates for the initial Br_2 room temperature molecular ensemble at multiple field intensities are calculated in Sec. 5.2. An overview of the experimental methods utilized in this study is given in Sec. 5.3. The experimental results for the XUV absorption of Br_2 before and after the strong-field ionization are presented in Sec. 5.4.1 and 5.4.2, respectively. The dissociation timescale of Br_2 and Br_2^+ for the formation of Br, Br*, and Br^+ are presented in Sec. 5.4.3. The vibrational wave packet dynamics in Br_2 and Br_2^+ are presented in and Sec. 5.4.4 and 5.4.5, respectively. The temporal dynamics and phase of the Br_2 and Br_2^+ vibrational wave packets are determined in Sec. 5.4.6. A discussion of the experimental results relating to field intensity and wave packet preparation follow in Sec. 5.5. Finally, the chapter concludes with a summary of the key results in Sec. 5.6.

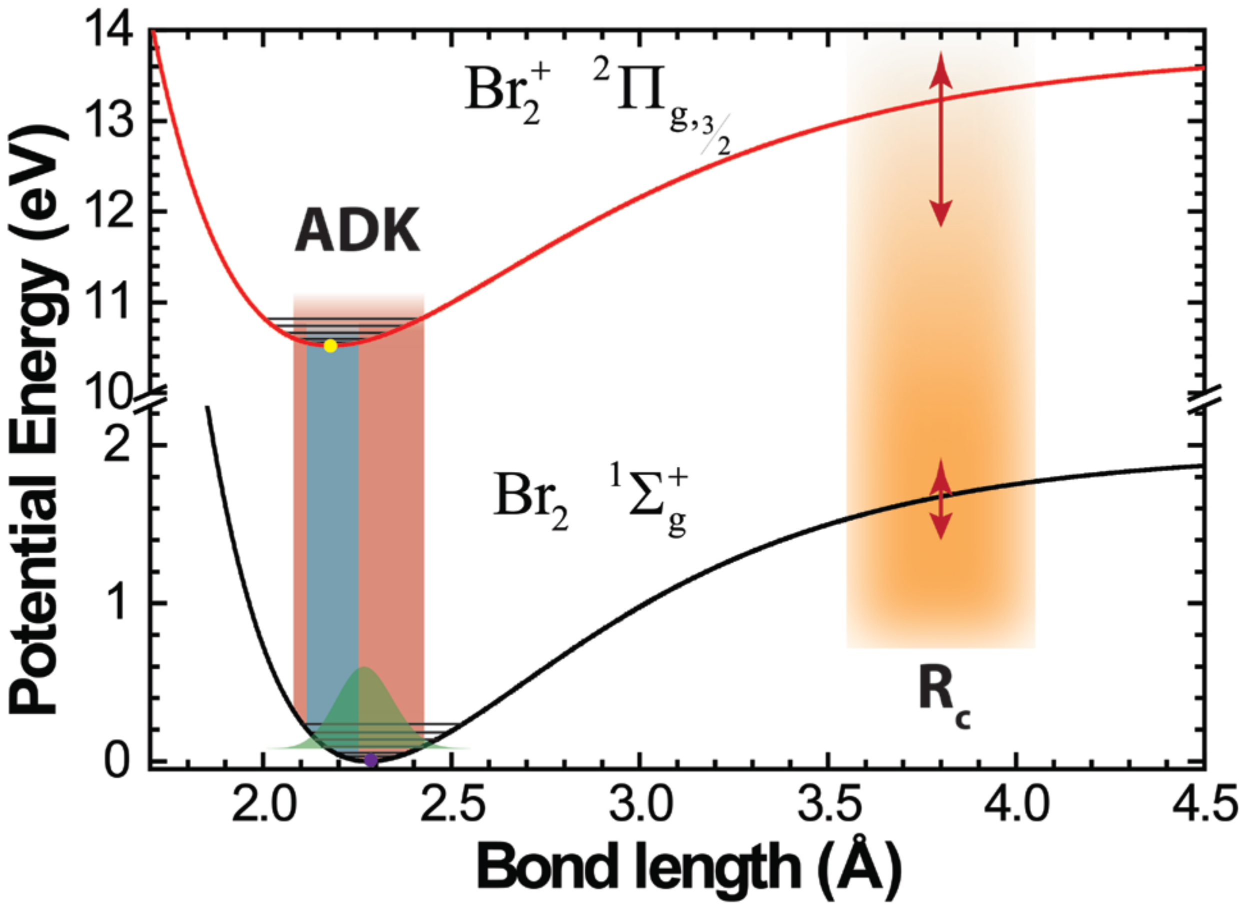

Figure 5.1: Schematic potential energy diagram for the strong-field of ionization of Br_2, depicting the bond length of preferential ionization for the field-free and distorted potentials by the strong field. At the minimum field intensity required for ionization, preferential depletion of the ground state wave function occurs at the equilibrium bond length of the ion, 2.18 Å, as indicated by the yellow marker and the blue "window" of ionization. As the field intensity increases, without considering the distortion of the potentials, the likelihood of ionization at longer bond lengths increases beyond the ground state equilibrium bond length, indicated by the purple marker and the red "window" of ionization. Both the blue and red "windows" of ionization can be interpreted in terms of the ADK ionization rates. Distortion of the potentials within the AC laser field, as illustrated by the red arrows, decreases the ionization energy at elongated bond lengths and leads to increased ionization at a critical internuclear separation, $R_c = 3.86$ Å,[164] as marked by the orange ionization "window," assuming one potential is more distorted over the other.

5.2 Theory

The XUV transient absorption spectrum is calculated utilizing a variant of ADK theory and Restricted Excitation Window Time-Dependent Density Functional[162] calculations (REW-TD-DFT), where ADK models the pump strong-field ionization and REW-TD-DFT calculates the XUV probe *3d* core-level transition energy. Each calculation accounts for the various internuclear separations of Br_2 encountered in the experiment.[166] The ADK calculations also account for the variation in ionization rate between vibrational states, determining the individual vibrational level populations after strong-field ionization and therefore the vibrational wave packet composition. Propagating the resulting ground state vibrational wave packet with the time evolution operator and examining the change in transition energy with R utilizing the REW-TD-DFT results allows a direct prediction of the XUV transient absorption signal. The details of this calculation have been discussed previously.[211] Here, only a brief description of the results is presented.

Application of a strong laser field, which facilitates tunnel ionization, intrinsically distorts the binding potential of the valence electrons. Here, we are concerned with the dynamics of the nuclei, and therefore only consider the strong-field's effect on the nuclear potential curves. Tunnel ionization may still occur without distorting the nuclear potentials to a degree that would change the ionization energy between the neutral and ion potential curves, altering the bond length of preferential ionization according to Lochfraß. This regime is referred to from now on as occurring according to the "field-free" nuclear potentials. The ADK calculations preformed are conducted in this regime.

Vibrational level sensitive ADK calculations are conducted as a function of the ionization energy with internuclear separation (R_v-ADK). These R_v-ADK calculations take into consideration the shape of the vibrational probability density as well as the ionization energy as a function of R. The ionization probabilities are calculated for the first seven vibrational levels of Br_2 independent of the population of each level at field intensities of $1.0 \text{ x } 10^{13} \, {}^{\text{W}}\!/_{\text{cm}^2}$, $4.0 \text{ x } 10^{13} \, {}^{\text{W}}\!/_{\text{cm}^2}$, $5.0 \text{ x } 10^{13} \, {}^{\text{W}}\!/_{\text{cm}^2}$, and $8.0 \text{ x } 10^{13} \, {}^{\text{W}}\!/_{\text{cm}^2}$. The results are presented in Fig. 5.2. Preferential ionization is observed to occur at $R < R_e^{Br_2}$, peaking at $R_e^{Br_2^+}$, with an inclination to deplete higher vibrational levels. Preferential ionization of particular vibrational levels stems from the level's probability density distribution with R, as higher lying vibrational levels have more population toward the turning points than lower lying levels. Increased ionization at the molecular potential turning points selectively depletes the upper states first, decreasing the molecule's overall vibrational energy.

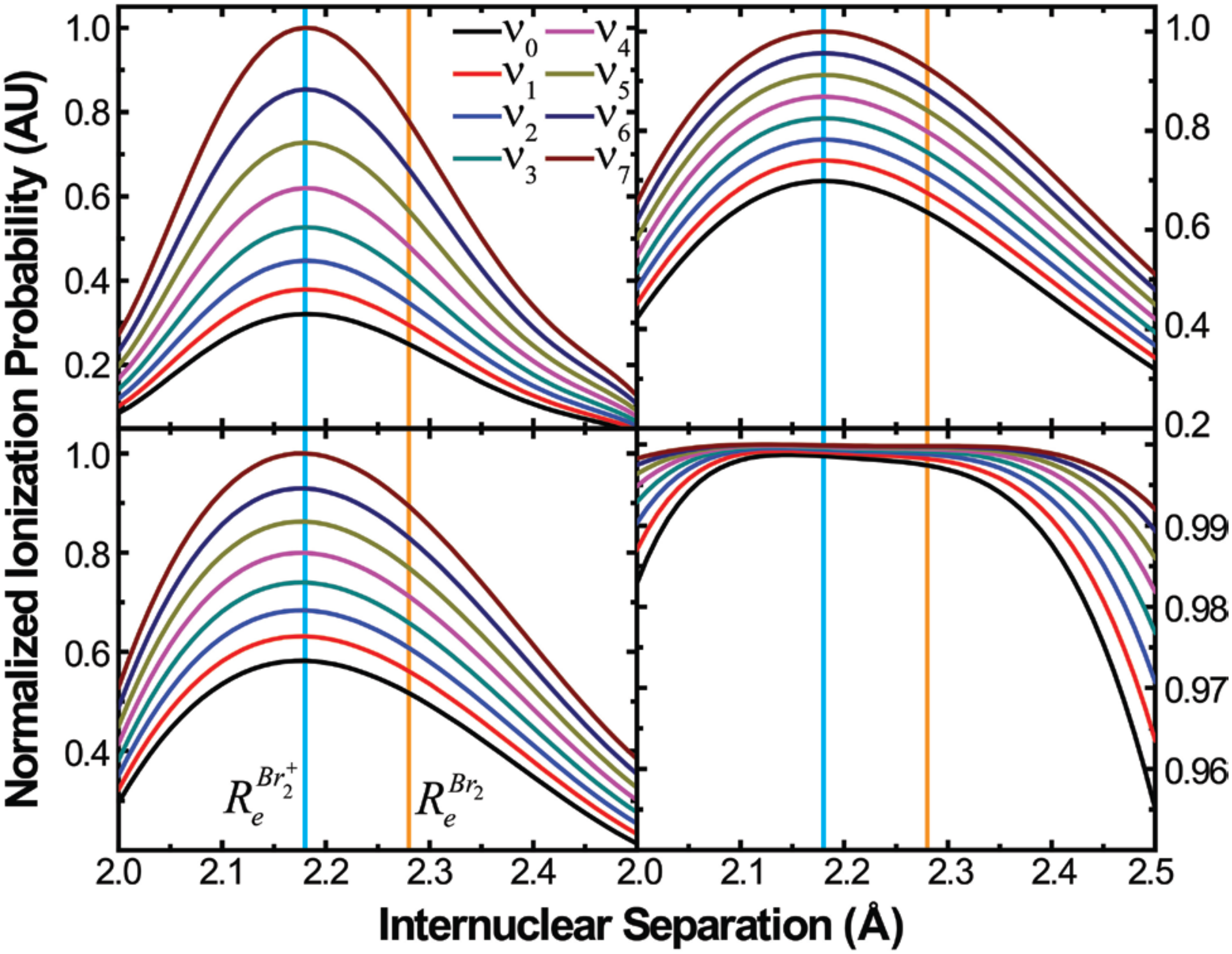

Figure 5.2: Calculated ADK ionization rates for Br_2 over a range of internuclear separations and vibrational energy levels for: $1.0 \times 10^{13}\, {}^{W}\!/_{cm^2}$ (Top Left), $4.0 \times 10^{13}\, {}^{W}\!/_{cm^2}$ (Bottom Left), $5.0 \times 10^{13}\, {}^{W}\!/_{cm^2}$ (Top Right), and $8.0 \times 10^{13}\, {}^{W}\!/_{cm^2}$ (Bottom Right). The internuclear and vibrational level selectivity is lost as the field intensity increases. The equilibrium internuclear separation for Br_2 $\left(R_e^{Br_2}\right)$ and Br_2^+ $\left(R_e^{Br_2^+}\right)$ are labeled in orange and light blue, respectively.

The NWCHEM 6.1[161] program package was employed for the REW-TD-DFT calculations. The B3LYP/6-31g* model chemistry was utilized for all calculations of the *3d* core level XUV transition energies as a function of internuclear separation. The bond length interval around $R_e^{Br_2}$ is kept small, but then increased at long and short internuclear separations to trace the core-hole excited state potential energy curve from 1.8 Å to 8 Å. The core-hole transition energy is found to decrease with elongating bond length.

Finally, it is necessary to consider the extent to which the strong-field perturbs the molecular ground and ion state nuclear potentials. Starting with a Morse representation of the neutral ${}^1\Sigma_g^+$ and ion ${}^2\Pi_{g,3/2}$ potentials, the ionization energy is calculated as a function of bond length. The

Franck-Condon ionization energy of 10.54 eV is obtained at $R_e^{Br_2}$, but the energy required to access the $^2\Pi_{g,3/2}$ state is seen to decrease as the bond is compressed. The dependence of the ADK tunnel rate on ionization energy indicates preferential ionization should occur at $R < R_e^{Br_2}$. As a higher field is applied, the potential energy curves can become distorted. Simulating the degree of distortion relative to the field-free potentials, the impact on the ionization energy with bond length is shown in Fig. 5.3. A decrease in the ionization energy is observed to occur beyond the outer turning point, which eventually decreases below the value seen at $R < R_e^{Br_2}$. Preferential ionization therefore occurs at the outer turning point at high field intensities. As the field intensifies, the location of increased ionization should visibly shift from the inner to outer turning point in Br_2. This will manifest as a clear change in the phase of the ground state vibrational wave packet. Examining the ionization curve at a time averaged electric field strength of 0.01 a.u. shows the ionization energy actually plateaus, indicating a particular field intensity exists such that preferential ionization versus internuclear separation should be lost.

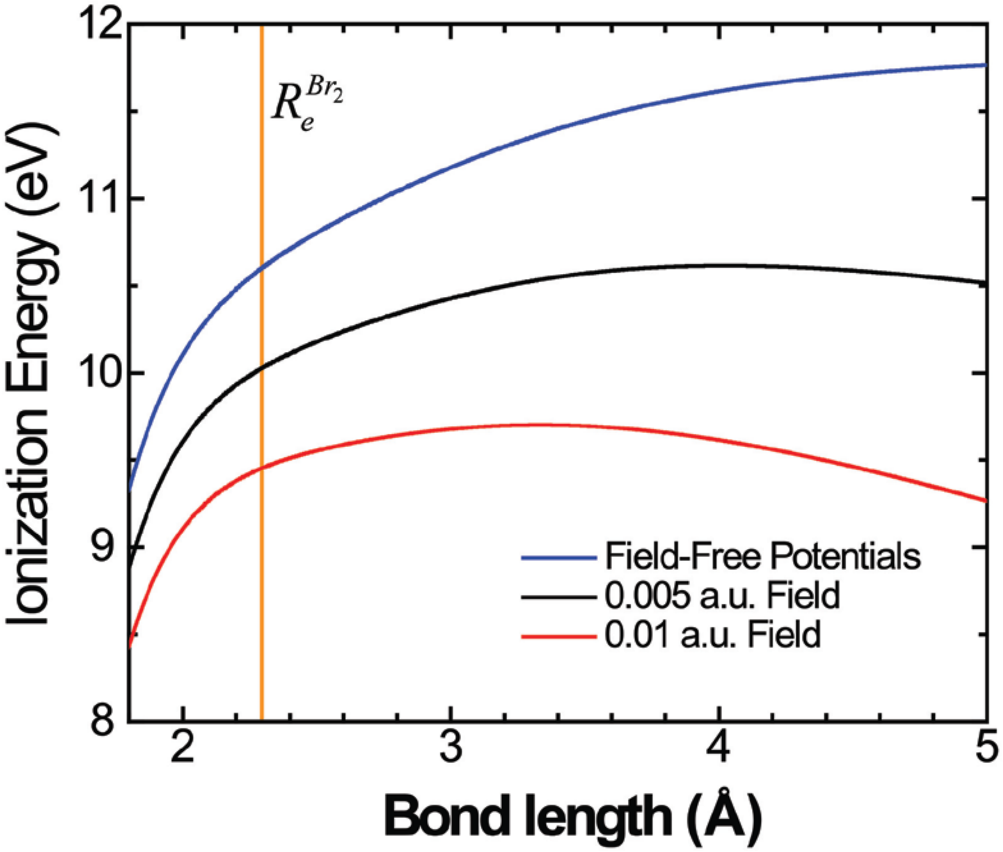

Figure 5.3: Simple calculation of the ionization energy for $Br_2\ ^1\Sigma_g^+ \xrightarrow{\text{strong-field}} Br_2^+\ ^2\Pi_{g,3/2}$ determined by the field-free potentials and the strong-field perturbed potentials at two time-averaged electric field strengths, 0.005 and 0.01 a.u., where one atomic unit of field strength is $5.1422 \times 10^{11}\ \mathrm{V/m}$. For the field-free potentials, the minimum ionization energy is at $R < R_e^{Br_2}$, but as the intense laser field intensity increases, the minimum ionization energy moves to longer bond lengths.

The ionization rate is also dependent on the vibrational probability density. Although increased ionization is expected at $R < R_e^{Br_2}$ when the laser intensity is not sufficient to distort the potential energy curves, the majority of the probability density is located at $R_e^{Br_2}$ for a Boltzmann distribution of vibrational level populations at room temperature. The resulting strong-field "hole" in the ground state probability density is therefore little more than an induced asymmetry of the vibrational amplitude, although still sufficient to form a superposition of the remaining population. It is important to note that preferential ionization prepares the coherent vibrational amplitude away from the region of depletion, i.e. if the minimum ionization energy occurs on the inner turning point; the ground state coherent vibrational amplitude is prepared at longer bond lengths. For the calculation of the XUV transient absorption spectra, each vibrational level's initial population is given according to a Boltzmann distribution at 300 K.

5.3 Experimental Methods

The majority of the XUV experimental apparatus has been described previously[19], so only the modifications to the system are described. The XUV high-harmonic source has been converted from a capillary waveguide to a semi-infinite gas cell.[35,36] The cell itself is 14" x ½" diameter, employing a 0.031" thick Teflon foil to create the high-harmonic exit aperture by laser ablation. A static neon pressure of 14.7 kPa is maintained in the cell using a regulator to minimize pressure fluctuations. The source conversion results in a 200-fold increase in high harmonic flux at 35-72.5 eV over the previous configuration. The current estimated photon flux is 10^7 photons per pulse per harmonic.

To increase the spectral coverage of the system, an optical line for producing both the even and odd harmonics is employed.[118] An 85/15, transmit/reflect, beamsplitter is inserted into the probe arm, and the reflected beam is used to generate 50 μJ of 400 nm light, which has a polarization parallel to the 800 nm driver for the high harmonics. The 400 nm + 800 nm light are recombined by a dichroic mirror and overlapped in both space and time at the exit Teflon foil of the semi-infinite gas cell. This technique doubles the overall high harmonic photon flux, and can provide a peak to valley continuum ratio of 5:1 between each harmonic, now only separated by 1.55 eV.

The spectral and temporal resolution of the instrument was established previously employing a capillary source, and the implementation of the semi-infinite gas cell does not affect either. The temporal resolution of the instrument is 25 ± 5 fs centered at 0 ± 2 fs, determined by the rise-time of the strong-field ionization of Xe → Xe^+ as monitored by the $5p^{-1}_{3/2}\left({}^2P_{3/2}\right)\longrightarrow 4d^{-1}_{5/2}\left({}^2D_{5/2}\right)$ transition at 55.4 eV (nl^{-1}_{j} symbolizes a hole in the atomic nl orbital with angular momentum j; the corresponding term symbol is in parentheses).[20] The time trace of the strong-field response is fit by a convolution of a Heaviside and Gaussian function. A spectral fit of the Xe^+ peak at 55.4 eV to a Voigt function yields a Gaussian resolution of better than 250 meV, given the Lorentzian lineshape of the transition's natural lifetime.[47,189]

For high harmonic generation utilizing a semi-infinite gas cell, the positioning of the plasma filament, supported by the 800 nm high harmonic driver, relative to the XUV optics of the apparatus dictates the spectral and temporal resolution of the instrument. Optimization of the high harmonic flux by adjustment of the aperaturing, chirp, and focal positioning of the driving pulse as well as the neon pressure in the cell affect the location of the plasma filament and the high-harmonic phase matching. Therefore, by iterating the pulse parameters and the position of the semi-infinite gas cell, the optimal spectral and temporal resolutions are obtained as stated above. Furthermore, an XUV beam waist of 20 μm is obtained at the interaction region, which is a small-aperture (200 μm) macor gas cell pressurized with 3.4 kPa of Br_2.

The pump intensities quoted for these experiments are a reflection of the maximum peak intensity at the interaction region within the spatial and temporal envelope of the pulse. For a field intensity of $2.0 \text{ x } 10^{14} \text{W}/_{\text{cm}^2}$, a 200 μJ, 40 fs, 1 kHz pulse is focused to a 40 μm beam waist. For a pulse that is Gaussian in both space (r) and time (t), the field intensity variation is $I(r,t)=I_0 e^{-\frac{2r^2}{\omega_0^2}} e^{-4\ln 2\frac{t^2}{\tau^2}}$, where I_0 is the maximum field intensity, w_0 is the $^1/_{e^2}$ beam waist, and τ is the FWHM of the pulse. The pulse energy is attenuated via a quarter waveplate and thin-film polarizer pair, thereby preserving the temporal and spatial characteristics of the pump across different field intensities. The polarization of the pump beam is also controlled through the use of a second quarter waveplate and a PolarCor linear polarizer pair. Significant chirp is not introduced into the pump pulse due to these additions.

Focal volume averaging of the pump pulse intensity sampled by the XUV probe must be considered. The ratio of the pump focal waist to the probe waist is approximately 2 to 1, leading to a variation in the sampled field intensity by the probe of <15 %. As a result, intensity spatial averaging effects are neglected in this experiment.

Pump-probe transient absorption spectra are obtained from an average of 16 scans, with the x-ray CCD integration time set to 0.2 s. Each transient absorption spectrum is collected utilizing an electronic shutter for the “pump-off” spectrum. Each time delay is referenced to an individual “pump-off” spectrum to account for any fluctuation in the XUV flux. The change in the optical density is then given by: $\Delta OD = -\log\frac{I(E,\Delta t)}{I(E,\text{"}pump-off\text{"})}$. The pump-probe time delay is varied in 20 fs steps from -300 fs to 40 ps for the three highest measured power intensities. Here, negative time denotes that the XUV probe arrives at the sample first, while positive time denotes that the ionizing 800 nm pump has arrived first. The time scan length permits a Fast-Fourier transform (FFT) energy resolution of ~1.5 cm^{-1}, capable of resolving individual vibrational states in Br_2. All reported error bars correspond to one standard error of the mean. For the lowest measured power intensity, only the time delays from -100 fs to 400 fs are collected and averaged for 32 scans due to the low signal to noise. No FFT analysis is conducted at $1.0 \text{ x } 10^{14} \text{W}/_{\text{cm}^2}$.

The length of the pump-probe time trace scans necessitated that the entire apparatus is stable over the course of several days. This implies the XUV source must be robust. Switching the source to a semi-infinite gas cell configuration and stabilizing the beam pointing of the laser system yielded a high-harmonic fluctuation of less than 5 % RMS. Pressure fluctuations of the

Br_2 sample in the sample gas cell also need to be stabilized, and therefore the regulating needle valve is heated slightly to prevent sample condensation. Stability of bromine pressure is monitored by the amplitude of the neutral depletion at 68.3 eV and is not observed to change significantly over the course of the entire experiment.

5.4 Results

The goal of the experiment is to elucidate the intensity dependent effects of the strong-field ionization of Br_2. In particular, the field dependence of ground state vibrational wave packet preparation and the degree to which the potential energy curves are distorted by the ionizing laser pulse are determined. Toward this end, experiments are carried out at three separate pump field intensities: $1.6 \text{ x } 10^{14}\, {}^{\mathrm{W}}\!/_{\mathrm{cm}^2}$, $2.0 \text{ x } 10^{14}\, {}^{\mathrm{W}}\!/_{\mathrm{cm}^2}$, and $4.0 \text{ x } 10^{14}\, {}^{\mathrm{W}}\!/_{\mathrm{cm}^2}$. Transient absorption spectra are collected from -0.3 to 40 ps. It is important to consider that over the measured timescale the rotational dephasing of the molecule will detract from the XUV detection of the vibrational wave packets, with a rotational full revival time of 205 ps.[170] After 10 ps the initial coherence has reduced in strength by a factor of five, but there remains sufficient modulation depth for information about the vibrational beat contributions to be retrieved.

The initial phase of the vibrational wave packet and time zero for the dynamics are determined by cross correlation of the XUV probe and strong-field pump by monitoring the strong-field depletion of Br_2. Neglecting the vibrational dynamics, fitting the neutral depletion with a convolution of a Gaussian and Heaviside function determines time zero (t_0) for the wave packet preparation. Convoluting a cosinusoidal function to the strong-field depletion, the change in optical density due to the vibrational wave packet motion may be recovered as well as the phase. Considering the transient absorption spectra are collected over several days, t_0 and the instrument response function varies slightly between data sets, but are each within ± 5 fs of the average value and are incorporated into the analysis. Therefore, the measured phase of the vibrational wave packets is unaffected.

5.4.1 Static XUV Absorption Spectrum of Br_2

A static absorption spectrum of Br_2 is presented in Fig. 5.4 from 66.7 to 70.8 eV. There are two dominant spectral features at 68.3 and 69.3 corresponding to the Br_2 ${}^{1}\Sigma_{g}^{+}$ ground to core-hole excited state transitions of $\sigma^{*^{-1}} \rightarrow 3d^{-1}_{5/2}$ (pink) and $\sigma^{*^{-1}} \rightarrow 3d^{-1}_{3/2}$ (purple), respectively. The observed transition energies match well with those obtained by Johnson et al.[212] The use of aluminum foils in the experiment to prevent the driver and pump light from reaching the detector preclude observation of the Rydberg series of transitions for the core levels above 72.5 eV due to the Al $L_{2,3}$ absorption edge. As the ground state wave packet evolves, the XUV *3d* core-level absorption signal also changes in energy according to the vibrational amplitude distribution with R. This produces both positive and negative spectral features for both spin-orbit transitions, which has been discussed previously and is illustrated in Fig. 5.4.[211]

Each intensity dependent experiment was conducted on a separate day and thereby has a separate static absorption spectrum. The optical density (OD) of the static absorption experiment is utilized to estimate the ionization percentage from the change in optical density (ΔOD) spectrum, and this factor is used to compare the results, i.e. if the $OD_{Br_2\ \sigma^{*-1} \rightarrow 3d^{-1}_{5/2}} = 0.6$ and $\Delta OD_{Br_2\ \sigma^{*-1} \rightarrow 3d^{-1}_{5/2}} = 0.03$, then ~5% of the sample is ionized. For each power intensity, the ionization percentages are: 1.0 x $10^{14}\ \text{W}/\text{cm}^2$ <5 %, 1.6 x $10^{14}\ \text{W}/\text{cm}^2$ = 5 %, 2.0 x $10^{14}\ \text{W}/\text{cm}^2$ = 15 %, and 4.0 x $10^{14}\ \text{W}/\text{cm}^2$ = 50 %.

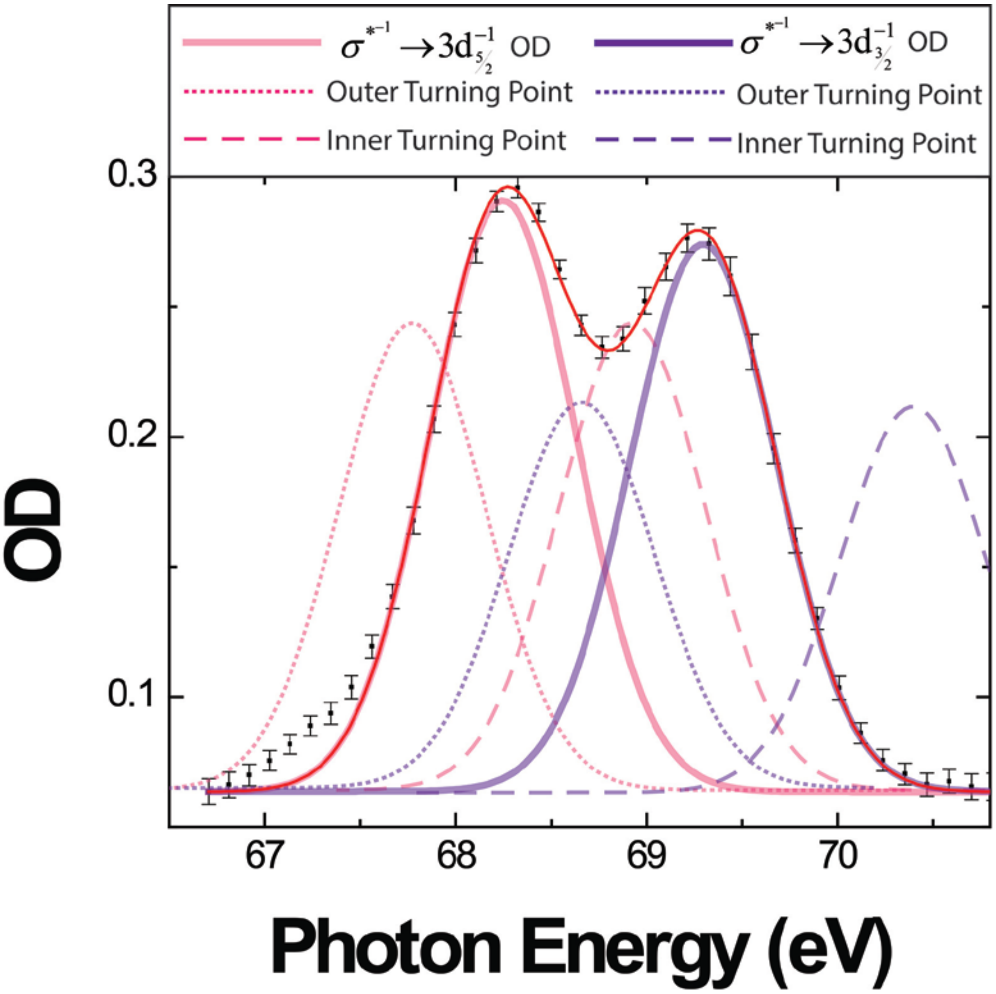

Figure 5.4: XUV static absorption spectrum of Br_2. The peaks at 68.3 eV (pink) and 69.3 eV (purple) correspond to the $Br_2\ {}^1\Sigma_g^+\ \sigma^{*-1} \rightarrow 3d^{-1}_{5/2}$ and $\sigma^{*-1} \rightarrow 3d^{-1}_{3/2}$ transitions, respectively. The corresponding color-coded dashed and dotted feature of each transition corresponds to the wave packet XUV absorbance at the inner and outer turning points, respectively.

5.4.2 Transient Absorption Spectrum at $1.6 \text{ x } 10^{14}\, {}^{\text{W}}\!/\!_{\text{cm}^2}$

The transient absorption spectrum measured at a field intensity of $1.6 \text{ x } 10^{14}\, {}^{\text{W}}\!/\!_{\text{cm}^2}$ and pump-probe time delays of 160 fs and 210 fs is presented in Fig. 5.5. The spectral assignments are typical of those at all power intensities, with the exception of the relative amplitudes of the features. The entire spectrum is fit to a spline baseline to account for the changes in the non-resonant contribution to the absorption and is subsequently subtracted. The spectral features are fit using a series of Gaussians to model the core-level transitions of each transient. The center of each peak is initially fixed to the maximum of the observed spectral feature. The width and peak location of each feature is then iteratively fit by a Levenberg-Marquardt algorithm.[213] The positive features for the neutral depletions are allowed to float to the best fit of the unassigned XUV absorption. After iterating to the best possible fit, it is found that the positive component of the $\sigma^{*^{-1}} \rightarrow 3d^{-1}_{5/2,3/2}$ transitions relax to the same separation from the center of their corresponding depletions. This indicates the probing of the ${}^{1}\Sigma_{g}^{+}$ wave packet is insensitive to the spin-orbit state of the core-hole created via the XUV transition.

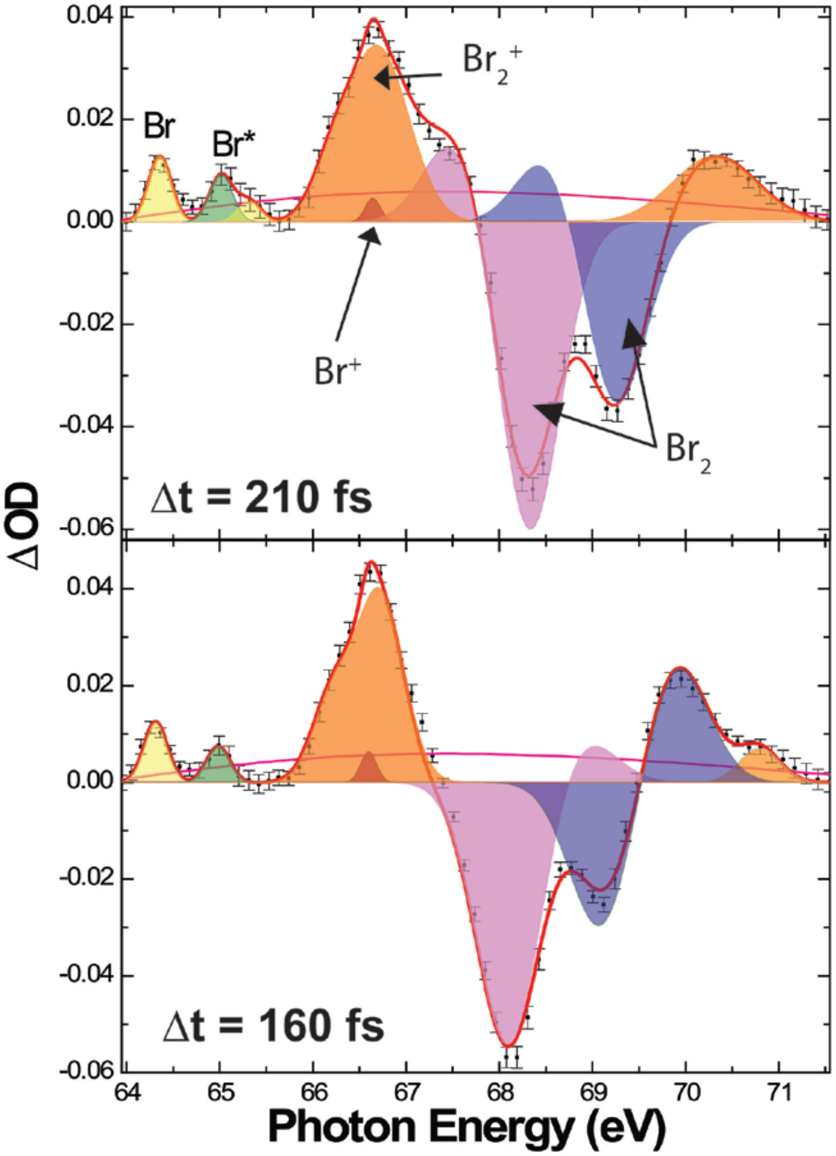

Figure 5.5: XUV transient absorption spectrum at $1.6 \text{ x } 10^{14}\, {}^{W}\!/_{cm^2}$ and pump-probe time delays of 210 fs and 160 fs, when the Br_2 ${}^1\Sigma_g^+$ wave packet is localized at the inner and outer turning points, respectively. The magenta line corresponds to the subtracted cubic spline baseline, and the red trace corresponds to the sum of the peak fit for spectral window. The transitions at 64.4, 65.1, 65.4 eV correspond to the atomic Br ${}^2P_{3/2} \rightarrow {}^2D_{5/2}$, ${}^2P_{1/2} \rightarrow {}^2D_{3/2}$, ${}^2P_{3/2} \rightarrow {}^2D_{3/2}$ transitions, respectively. The Br_2 transitions contain both positive and negative features depending on the phase of the ground state wave packet relative to the static absorption. The pink and purple features correspond to the Br_2 ${}^1\Sigma_g^+$ $\sigma^{*-1} \rightarrow 3d_{5/2}^{-1}$ and $\sigma^{*-1} \rightarrow 3d_{3/2}^{-1}$ transitions, respectively. The Br_2^+ molecular ion has two resonances at 66.8 and 70.7 eV corresponding to the ${}^2\Pi_{g,3/2}$ $\pi^{*-1} \rightarrow 3d_{5/2}^{-1}$ and $\sigma^{*-1} \rightarrow 3d_{5/2}^{-1}$ transitions, respectively. The spectral peak at 66.5 is identified as a combination of the Br^+ ${}^2P_3 \rightarrow {}^3D_3$ and ${}^1D_2 \rightarrow {}^1F_2$ resonances.

The atomic bromine resonances are seen at 64.3, 64.9, and 65.3 eV corresponding to the ${}^2\mathrm{P}_{3/2} \rightarrow {}^2\mathrm{D}_{5/2}$, ${}^2\mathrm{P}_{1/2} \rightarrow {}^2\mathrm{D}_{3/2}$, and ${}^2\mathrm{P}_{3/2} \rightarrow {}^2\mathrm{D}_{3/2}$ transitions, respectively. The widths of the Br atomic transitions are fixed to the Gaussian spectral resolution (250 meV) of the instrument as the natural linewidths of the $3d^{-1}_{5/2}$ (100 meV) and $3d^{-1}_{3/2}$ (90 meV) states are smaller.[214] The optical density signal of these features is quite low, which leads to difficulty in extracting the ${}^2\mathrm{P}_{3/2} \rightarrow {}^2\mathrm{D}_{3/2}$ transition in the global fitting at 160 fs pump-probe delay.

Evolution of the ground state wave packet from the inner to the outer turning point results in a blue shifting of the positive component of the $\sigma^{*-1} \rightarrow 3\mathrm{d}^{-1}_{5/2}$ (pink) and $\sigma^{*-1} \rightarrow 3\mathrm{d}^{-1}_{3/2}$ (purple) spectral features as described above and illustrated in Fig. 5.4. This may clearly be observed between the transient absorption spectra at pump probe time delays corresponding to the wave packet localizing at the inner (160 fs) and outer (210 fs) turning points of the ${}^1\Sigma^+_g$ potential energy surface of Br_2. The transient absorption spectra at the inner and outer turning point are repeatedly observed after successive time delays corresponding to one vibrational period.

The Br_2^+ *3d* core-level to singly occupied valence molecular orbital transition energies are estimated from the difference in Br_2 *3d* electron binding energy and the valence ionization potential, which is adequate within the single-particle picture.[215] The vertical ionization potential for a *3d* electron in Br_2 is 77.8 eV, and the valence ionization potential is 10.54 eV, yielding a spin-orbit averaged $\pi^{*^{-1}} \rightarrow 3d^{-1}$ transition energy of 67.3 eV. Considering a spin-orbit splitting of 1.05 eV the two $\pi^{*^{-1}} \rightarrow 3d^{-1}_{5/2}$ and $\pi^{*^{-1}} \rightarrow 3d^{-1}_{3/2}$ ion transitions are predicted to occur at 66.8 and 67.8 eV, respectively.[214] The spectral feature at 66.8 is thus assigned to the Br_2^+ $\pi^{*^{-1}} \rightarrow 3d^{-1}_{5/2}$ transition. Retrieving the $\pi^{*^{-1}} \rightarrow 3d^{-1}_{3/2}$ transition is complicated by the neutral depletion occupying the same spectral region. Fitting the time trace of the transient absorption signal at 67.8 eV provides no evidence for the ion spin-orbit transition, and therefore it is concluded the transition is quite weak. The $\pi^{*^{-1}} \rightarrow 3d^{-1}_{5/2}$ ion spectral feature is necessarily fit with an asymmetric lineshape, which is a direct representation of the vibrational amplitude shape at the inner and outer turning point. The ion vibrational amplitude is observed to peak at each turning point but still maintain an approximate 1 eV linewidth. An additional Br_2^+ transition is predicted to occur at higher energy, corresponding to a $\sigma^{*^{-1}} \rightarrow 3d^{-1}$ transition. A feature is observed at 71.1 and found to have an oscillatory period of 93 ± 1 fs, indicating that it corresponds to the ${}^2\Pi_{g,3/2}$ ion state, and is assigned to the ${}^2\Pi_{g,3/2}, \sigma^{*^{-1}} \rightarrow 3d^{-1}_{5/2}$ transition.

It is necessary to consider alternatives to the peak assignments made herein, namely the formation of atomic charged states. Recent experiments at the Advanced Light Source (ALS) at

Lawrence Berkeley National Lab have yielded absolute photoabsorption cross sections for the series of atomic bromine ion species from Br^+ to Br^{3+}.[199] These experiments allow for direct assignment of atomic bromine ion features in the transient absorption spectrum. For Br^+, the ground state is $3d^{10}4s^24p^4\ {}^3P_2$ with excited states (${}^3P_1$, ${}^3P_0$, ${}^1D_2$, and ${}^1S_0$).[214] One transition for Br^+ is observed at 66.5 eV, and this feature cannot be explained by the vibrational dynamics of the molecular ion as the peak is observed to be constant in intensity with pump-probe delay and therefore cannot be due to localization of the wave packet at a turning point. Two possible Br^+ transitions at 66.39, and 66.55 eV are detected in high resolution studies, and are observed here as a single resonance at 66.5 eV, corresponding to the ${}^2P_3 \to {}^3D_3$ and ${}^1D_2 \to {}^1F_2$ transitions. For the current experimental configuration, the spectral resolution of the instrument is not sufficient to resolve the individual Br^+ transitions. Similar spectral features could arise for additional states of Br^+ or higher atomic charged species, but no evidence for these is observed in the temporal or spectral measurements.

5.4.3 Dissociation Timescale for Br_2 and Br_2^+ at Several Field Intensities

The timescales for the strong-field ionization are retrieved by fitting the energy line-out spectra as a function of pump-probe time delay. Each transition is fit to a convolution of a Gaussian and a Heaviside function. The Gaussian function models the envelope of the intense pump pulse and the Heaviside function accounts for the instantaneous strong-field ionization response. An additional exponential function is further convolved to the fitting routine when determining the timescale for the dissociation of the molecular species. From the results of the fitting routine, the temporal dynamics of the strong-field dissociation of Br_2 and Br_2^+ at various field intensities may be retrieved.

The formation of atomic bromine in its ground and spin-orbit excited state at $4.0\text{x}10^{14}\ {}^{\text{W}}\!/\!_{\text{cm}^2}$ occurs by dissociative ionization, and the timescale of dissociation is determined by fitting the transient absorption signal at 64.3 eV and 64.9 eV, respectively. Dissociative ionization of Br_2 occurs at the other measured field intensities, but the signal to noise is too poor to extract reliable timescales. Fig. 5.6 shows the time trace for the dissociation of Br_2 to the Br ${}^2P_{3/2}$ state, and the rise time is determined to be 44 ± 12 fs. The Br ${}^2P_{1/2}$ state displays a similar timescale as seen in the top portion of Fig. 5.7. An additional timescale is observed for the ${}^2P_{3/2}$ state at long timescales, with a rise time of at least 10's of picoseconds. The actual timescale could not be determined due to an insufficient length of the time scan. No change is observed in the Br ${}^2P_{1/2}$ state, indicating the change in ${}^2P_{3/2}$ population is not due to the pump-probe overlap changing with time-delay or instability in the sample gas pressure. Simultaneously, a decrease in the Br_2^+ ion signal at 66.7 eV is seen to occur at the same rate as the formation of Br ${}^2P_{3/2}$ as presented in the bottom portion of Fig. 5.7. Due to the correlated Br $^{2}P_{3/2}$ rise and Br_2^+ $^{2}\Pi_{g,3/2}$ decay times it is determined that dissociation of the molecular ion occurs slowly across a predissociative state to form the spin-orbit atomic ground state and Br^+ $\left(^{2}P_{3},{}^{1}D_{2}\right)$. Furthermore, inspection of the neutral Br_2 core-level absorbance at long time delay presents no evidence for long timescale dissociation.

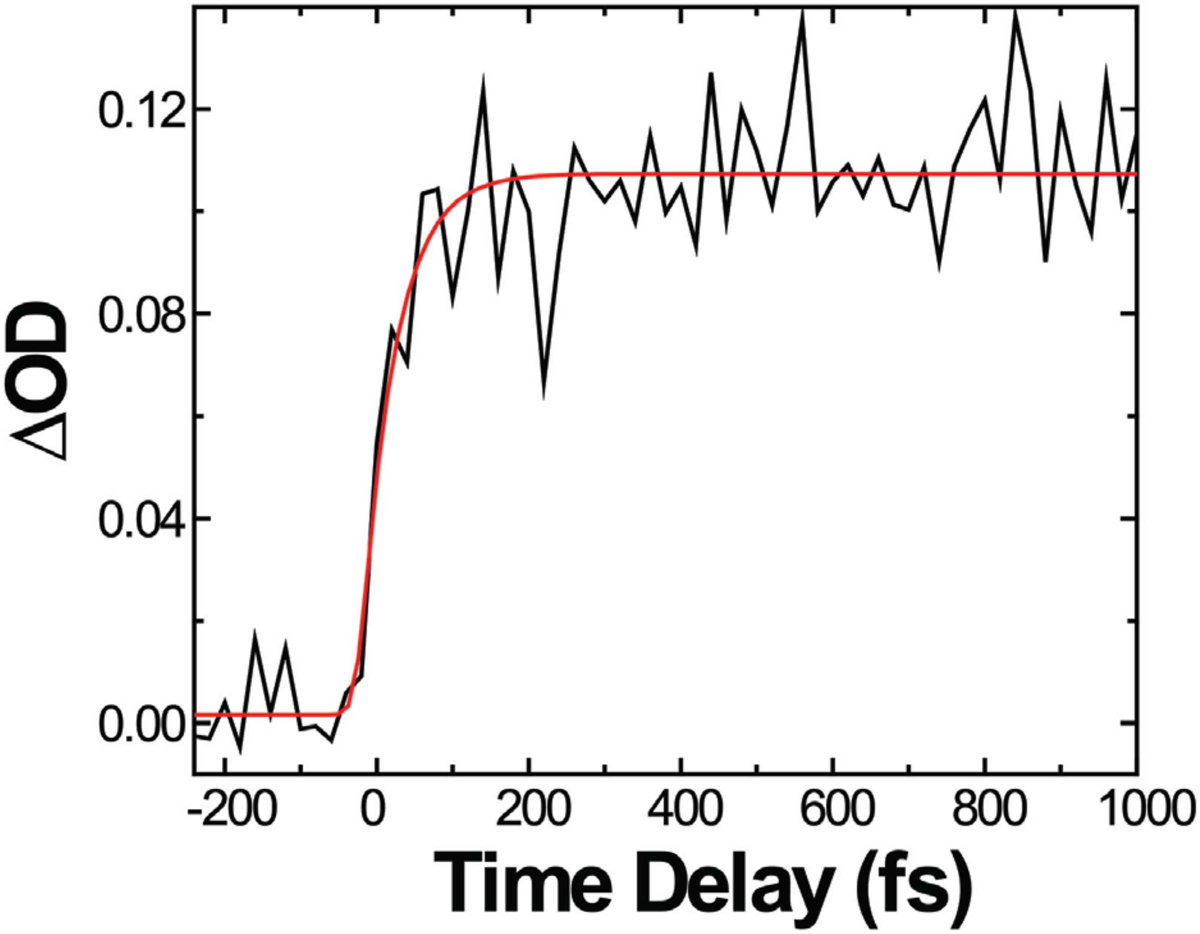

Figure 5.6: Pump-probe time trace for the appearance of the atomic Br^* photofragment at 65.1 eV at a field intensity of $4.0 \text{ x } 10^{14}\ \mathrm{W}/\mathrm{cm}^2$. A rise time of 44 ± 12 fs is observed for the fragment.

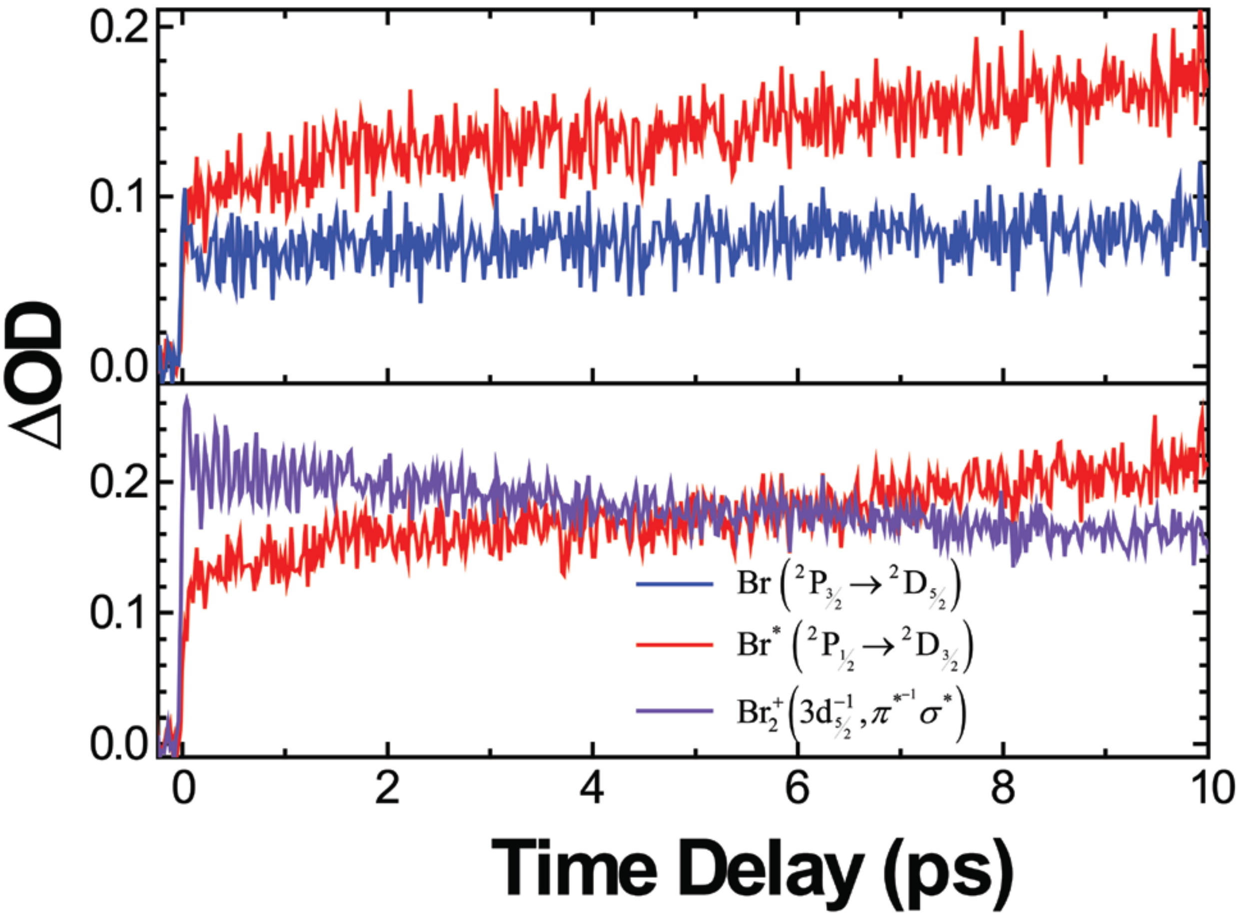

Figure 5.7: Pump-probe time traces for the atomic bromine photofragments and the strong-field generated Br_2^+ ion at a field intensity of $4.0 \text{ x } 10^{14}\,{}^{W}\!/_{cm^2}$. (Top) Comparison of the formation of ground state (red) atomic bromine and the spin-orbit excited state, Br^*, (blue). The ${}^2P_{1/2}$ Br^* photofragment is constant in time, while the ${}^2P_{3/2}$ Br is constantly increasing with a rise time of at least 10’s of picoseconds. The exact rise time was not retrievable by the current measurement. (Bottom) Comparison of the formation of Br in the ${}^2P_{3/2}$ state in relation to the long-time depletion of the Br_2^+ molecular ion. The timescale for the loss of Br_2^+ is the same as the rise time of Br in the ${}^2P_{3/2}$.

5.4.4 Br$_2$ Wave Packet Dynamics at Several Field Intensities

In order to understand the strong-field wave packets dynamics induced in Br$_2$, it is necessary to observe the process at multiple field intensities. In particular, we have simulated and experimentally observed the Br$_2$ $^1\Sigma_g^+$ Lochfraß wave packet at $1.0 \text{ x } 10^{14}\,{}^{\mathrm{W}}\!/_{\mathrm{cm}^2}$, $1.6 \text{ x } 10^{14}\,{}^{\mathrm{W}}\!/_{\mathrm{cm}^2}$, $2.0 \text{ x } 10^{14}\,{}^{\mathrm{W}}\!/_{\mathrm{cm}^2}$, and $4.0 \text{ x } 10^{14}\,{}^{\mathrm{W}}\!/_{\mathrm{cm}^2}$. Fig. 5.8 presents XUV transient absorption spectra at the four intensities over time delays of -60 to 400 fs. For each intensity, the R$_v$-ADK simulation for the corresponding peak intensity is shown on the right side, and the left side shows the experimental data.

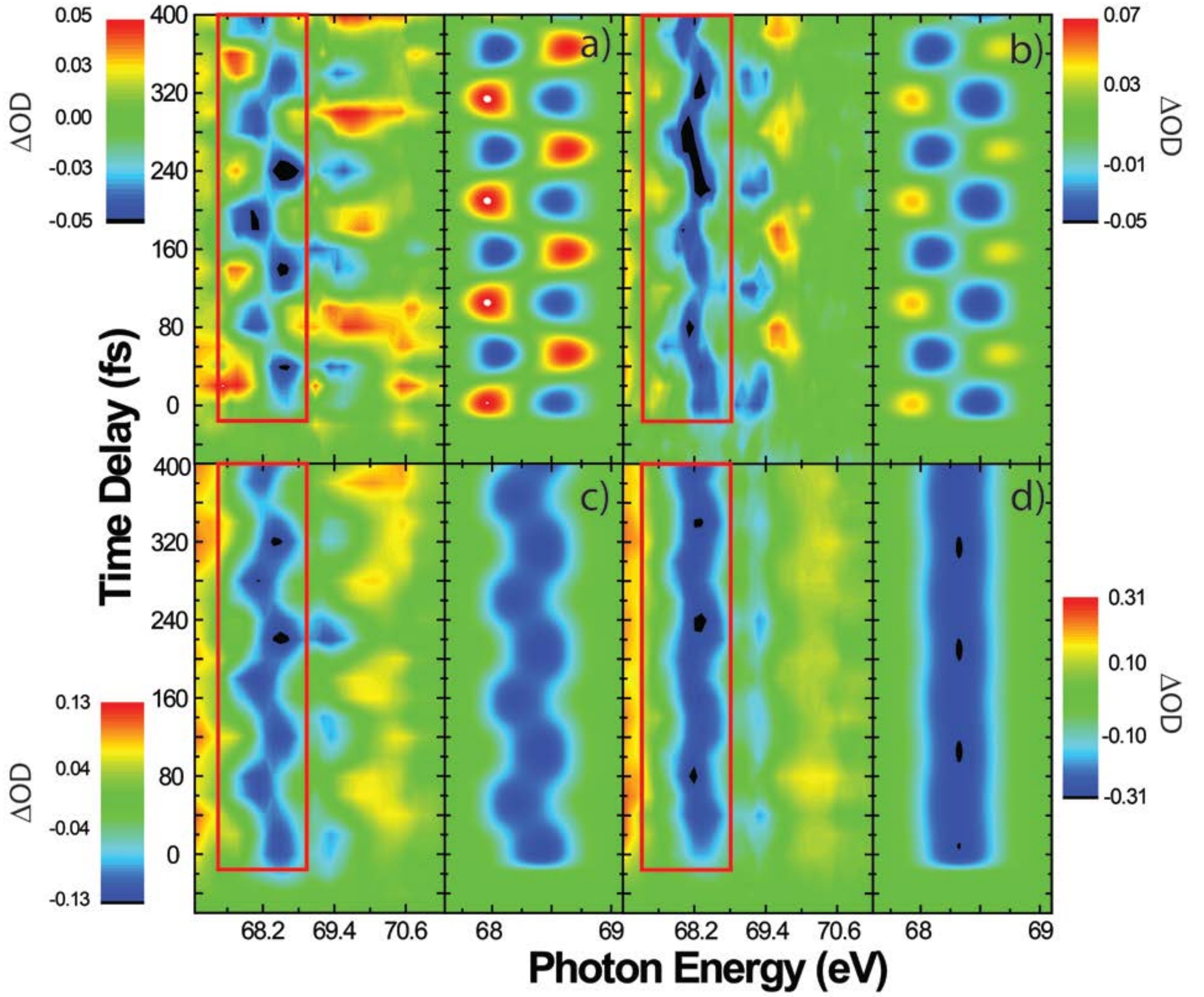

Figure 5.8: Contour plots of the experimental XUV transient absorption signal (left) and their predicted XUV absorption spectra from R$_v$-ADK and REW-TD-DFT calculations (right) at varying power intensities: a) $1.0 \text{ x } 10^{14}\,{}^{\mathrm{W}}\!/_{\mathrm{cm}^2}$, b) $1.6 \text{ x } 10^{14}\,{}^{\mathrm{W}}\!/_{\mathrm{cm}^2}$, c) $2.0 \text{ x } 10^{14}\,{}^{\mathrm{W}}\!/_{\mathrm{cm}^2}$, d) $4.0 \text{ x } 10^{14}\,{}^{\mathrm{W}}\!/_{\mathrm{cm}^2}$. The experimental XUV absorption signal to be modeled is boxed in red.

The R_v-ADK/REW-TD-DFT calculation is only conducted for the neutral Br_2 $^1\Sigma_g^+\ \sigma^{*-1} \rightarrow 3\text{d}^{-1}_{5/2}$ transition, which is experimentally found to be centered at 68.3 eV, oscillating by up to 0.5 eV. Two Br_2^+ ion transitions may also be observed at 67 eV and 71 eV and are discussed in the next section. For each laser intensity, the neutral depletions at 68.3 eV and 69.3 eV are observed to oscillate in energy and amplitude as well as lineshape, which results from the evolution of the wave packet with R and is well described by Fig. 5.4. Results from the REW-TD-DFT calculations indicate the *3d* core-level transition energy of the $^1\Sigma_g^+$ state decreases as the bond is elongated. The calculation results are consistently shifted by a constant energy at each field intensity to match the experimentally observed transition energy. Applying the REW-TD-DFT results to the intensity dependent R_v-ADK calculations it is seen that each of the vibrational wave packets are prepared close to the outer turning point, consistent with the minimum ionization energy. As the field intensity is increased, the contrast between the static absorption reference and the remaining ground state population decreases. Therefore, the lowest field intensity measured appears to present the largest range of vibrational motion, but this is really a result of the change in contrast between each measurement dependent on the percentage of ionized Br_2. Each wave packet of similar beat composition explores the same R, regardless of field intensity.

Strong-field ionization at $1.0\ \text{x}\ 10^{14}\ \text{W}/\text{cm}^2$ is quite noisy due to the small ionization percentage of Br_2, but even so, a clear ground state vibrational beat is observed for the $\sigma^{*-1} \rightarrow 3\text{d}^{-1}_{5/2}$ core-hole transition. The oscillation of positive and negative features for the ground state wave packet matches well with the corresponding R_v-ADK theory, while the spin-orbit transition is only partially resolved. At $1.6\ \text{x}\ 10^{14}\ \text{W}/\text{cm}^2$ and higher intensities, the $\sigma^{*-1} \rightarrow 3\text{d}^{-1}_{3/2}$ detection of the vibrational beat is more clear. Due to the overlap of the spin-orbit features, observation of the positive OD feature in each transition is best realized on the outer turning point for the $\sigma^{*-1} \rightarrow 3\text{d}^{-1}_{5/2}$ (positive feature at lower energy relative to the negative depletion) and the inner turning point for the $\sigma^{*-1} \rightarrow 3\text{d}^{-1}_{3/2}$ (positive feature at higher energy relative to the negative depletion). At $1.0\ \text{x}\ 10^{14}\ \text{W}/\text{cm}^2$ and $1.6\ \text{x}\ 10^{14}\ \text{W}/\text{cm}^2$ in Fig. 5.8, the vibrational superposition is observed to be prepared on the outer turning point, while at $2.0\ \text{x}\ 10^{14}\ \text{W}/\text{cm}^2$ and $4.0\ \text{x}\ 10^{14}\ \text{W}/\text{cm}^2$ the wave packet is prepared at $R \approx R_e^{Br_2}$.

An FFT analysis was conducted at each field intensity, except $1.0\ \text{x}\ 10^{14}\ \text{W/cm}^2$, in order to determine intensity dependence of the vibrational beat components following strong-field ionization. Each energy bin (≈ 0.1 eV) corresponding to the $\sigma^{*-1} \rightarrow 3\text{d}^{-1}_{5/2,3/2}$ transitions is FFT-ed individually and the results summed. By FFTing each energy bin individually, the amplitudes of the oscillations are allowed to add constructive by disentangling the relative FFT phase of each bin. Each energy bin is zero-padded to increase the number of bins employed by the FFT routine. Due to the natural isotopic abundance of ^{79}Br:^{81}Br (1:1), all three possible species of Br_2 must be considered in the vibrational beat reconstruction, namely $^{81\text{-}81}\text{Br}_2$:$^{79\text{-}81}\text{Br}_2$:$^{79\text{-}79}\text{Br}_2$ (1:2:1). The fundamental frequency for each species is: $^{81\text{-}81}Br_2$ = 321 cm^{-1}, $^{79\text{-}81}Br_2$ = 323 cm^{-1} ,$^{79\text{-}79}Br_2$ = 325 cm^{-1}.[171]

At $1.6 \times 10^{14}\ {}^{W}\!/_{cm^2}$, three main beats are observed in Fig. 5.9 after conducting an FFT analysis around the energies corresponding to the $\sigma^{*-1} \rightarrow 3d^{-1}_{5/2,3/2}$ transitions. The three peaks are each fit to a Gaussian peak function and it is found that the relative area of each fits the expected isotopic abundance, 1:[1.8± 0.2]:1 $\left({}^{79-79}Br_2 : {}^{79-81}Br_2 : {}^{81-81}Br_2\right)$. The largest peak at 321 cm^{-1} corresponds to the $^{79\text{-}81}Br_2$ $\nu_0\nu_1$ beat, and the two adjacent peaks at 323 and 319 cm^{-1} match the $^{79\text{-}79}Br_2$ $\nu_0\nu_1$ and $^{81\text{-}81}Br_2$ $\nu_0\nu_1$ beats, respectively.

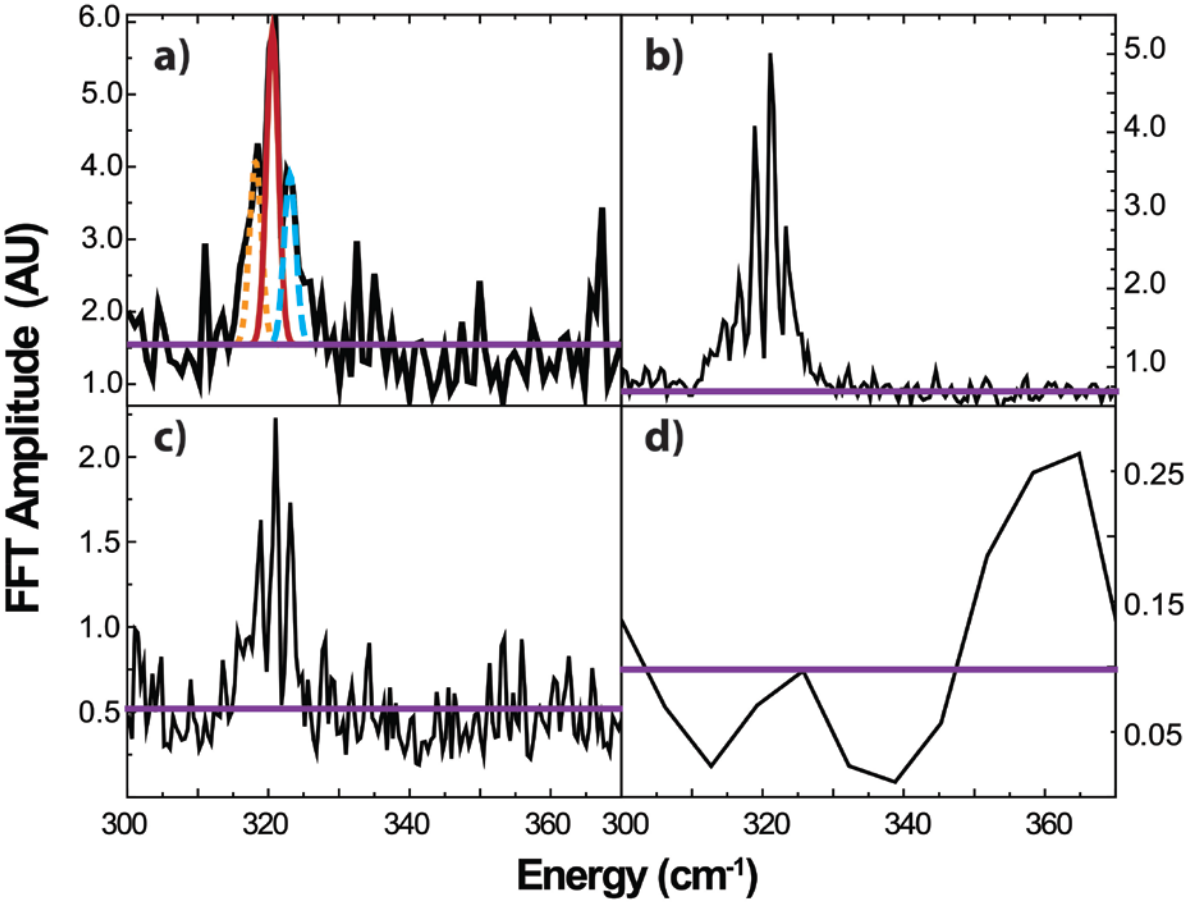

Figure 5.9: Fast-Fourier transform of the transient absorption signal at various field intensities from 67.4 to 70.5 eV, corresponding to the Br_2 $^1\Sigma_g^+, \sigma*^{-1} \rightarrow 3d^{-1}_{5/2}$ absorptions. (a) $1.6 \times 10^{14}\ {}^{W}\!/_{cm^2}$, (b) $2.0 \times 10^{14}\ {}^{W}\!/_{cm^2}$, and (c) $4.0 \times 10^{14}\ {}^{W}\!/_{cm^2}$. The FFT is fit at $1.6 \times 10^{14}\ {}^{W}\!/_{cm^2}$ to three Gaussians of 1.5 cm^{-1} width, indicating the resolution of the measurement and showing the correct isotopic abundance is retrieved. (d) FFT of the Br_2^+ $^2\Pi_{g,3/2}, \pi^{*-1} \rightarrow 3d^{-1}_{5/2}$ transition over the range of 66.5-67.0 eV at $1.6 \times 10^{14}\ {}^{W}\!/_{cm^2}$ for the first 10 ps of pump-probe time delay. A broad peak is observed at 360 cm^{-1}.

At $2.0\ \mathrm{x}\ 10^{14}\ {}^{\mathrm{W}}\!/_{\mathrm{cm}^2}$, Fig. 5.10 shows several new peaks at 317, 315, 313, and 311 cm^{-1} corresponding to a combination of higher vibrational state beats, namely $\nu_1\nu_2$., $\nu_2\nu_3$, and $\nu_3\nu_4$ Immediately, the peak at 319 cm^{-1} is observed to no longer be in proper isotopic ratio, indicating that it now contains the higher vibrational beats $\nu_1\nu_2$ of $^{79\text{-}81}\mathrm{Br}_2$ and the $\nu_2\nu_3$ beat of $^{79\text{-}79}\mathrm{Br}_2$ as well as the $^{81\text{-}81}\mathrm{Br}_2$ $\nu_0\nu_1$ beat. The observed vibrational beats are overlapping due to the isotopic and matching beat spacing of 2 cm^{-1}. The FFT is therefore decomposed into the individual isotopic components and their respective vibrational beats.

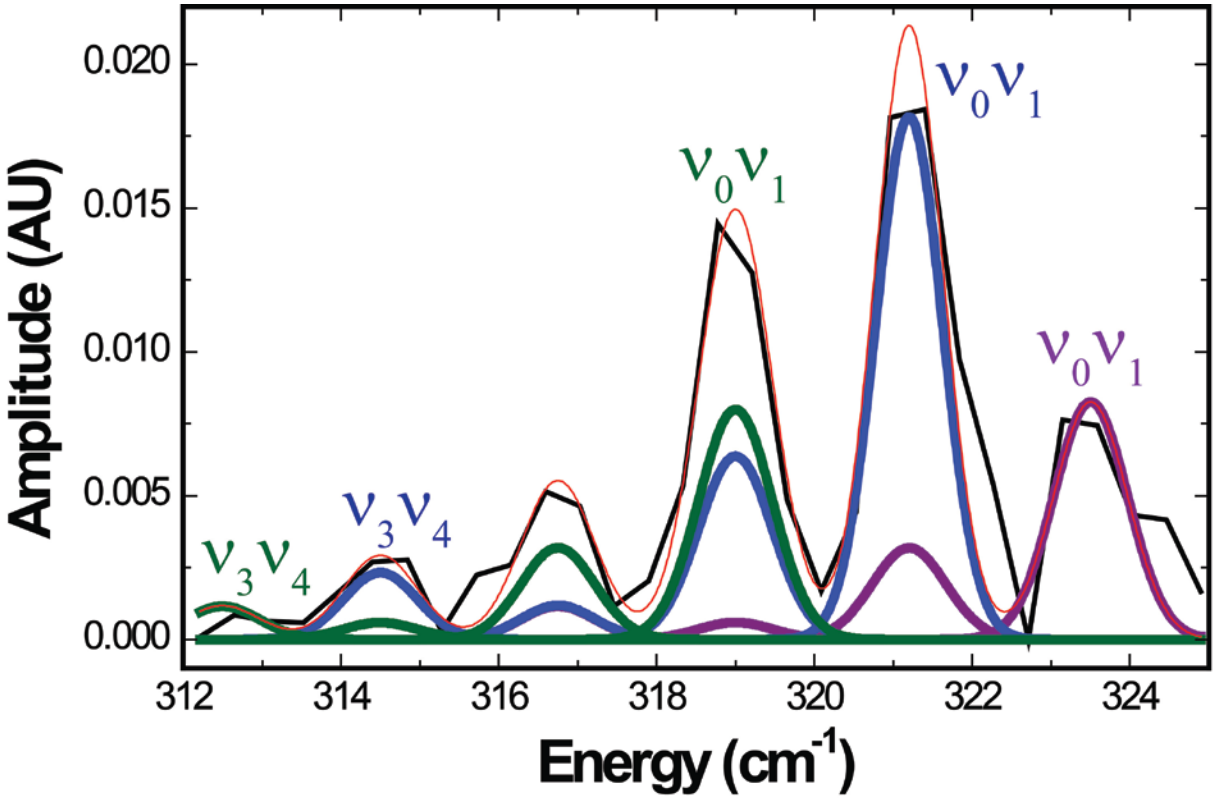

Figure 5.10: Vibrational beat reconstruction for the FFT of the $^1\Sigma_g^+, \sigma^{*-1} \rightarrow 3d^{-1}_{5/2}$ transition of Br_2 at a field intensity of $2.0\ \mathrm{x}\ 10^{14}\ {}^{\mathrm{W}}\!/_{\mathrm{cm}^2}$ (black). Each Br_2 isotope is fit to a Gaussian which is color coded according to the isotope: $^{79-79}\mathrm{Br}_2$ (purple) $^{79-81}\mathrm{Br}_2$ (blue) $^{81-81}\mathrm{Br}_2$ (green). The natural isotopic abundance is conserved in the fit of each peak to yield the overall fit in red.

The vibrational beats in the $2.0\ \mathrm{x}\ 10^{14}\ {}^{\mathrm{W}}\!/_{\mathrm{cm}^2}$ FFT are decomposed based on the natural isotopic abundance, a fixed ratio, and fit in a sequential manner, starting with the $^{79\text{-}79}\mathrm{Br}_2$ $\nu_0\nu_1$ at 323 cm^{-1}. The amplitude of the $^{79\text{-}79}\mathrm{Br}_2$ $\nu_0\nu_1$ beat is used to predict the amplitude of the $^{79\text{-}81}\mathrm{Br}_2$ $\nu_0\nu_1$ beat at 321 cm^{-1}, which is overlapped only with the $^{79\text{-}79}\mathrm{Br}_2$ $\nu_1\nu_2$ beat at the same energy, knowing the natural abundance is 2:1 for $^{79\text{-}81}Br_2$: $^{79\text{-}79}Br_2$. The remaining beat amplitude at 321 cm^{-1} after fitting the $^{79\text{-}81}Br_2$ $\nu_0\nu_1$ beat must then correspond to the $^{79\text{-}79}Br_2$ $\nu_1\nu_2$ beat. Fitting the peak at 319 cm^{-1} may then be accomplished utilizing the natural isotopic abundance and the ratio of the $^{79\text{-}79}Br_2$ $\nu_1\nu_2$ and $\nu_0\nu_1$, which must also remain fixed. In this manner, the entire FFT spectrum at $2.0 \text{ x } 10^{14}\,{}^{\text{W}}\!/_{\text{cm}^2}$ may be decomposed into the separate isotopic species of bromine and their respective vibrational beats. After decomposition, the overall fit is found to agree quite well with the experimental data as seen in Fig. 5.10. The beat composition of the $^1\Sigma_g^+$ ground state Br_2 wave packet prepared at a field intensity of $2.0 \text{ x } 10^{14}\,{}^{\text{W}}\!/_{\text{cm}^2}$ is reconstructed to be: $\{\nu_0\nu_1 : \nu_1\nu_2 : \nu_2\nu_3 : \nu_3\nu_4 : \nu_4\nu_5\} : \{62.5\%: 24.1\%: 4.5\%: 8.8\%: 0.1\%\}$.

After decomposition, a higher manifold of vibrational states is seen to be populated well above the baseline of the FFT spectrum. Furthermore, examining each 0.1 eV energy slice of that FFT data shows that the peak of the transition at 68.3 eV yields little high vibrational beat structure, but examining the FFTs away from resonance displays a higher contribution of $\nu_1\nu_2$ and $\nu_2\nu_3$ states as seen in Fig. 5.11. Through summing all of the FFTs together, it is found that the majority of the amplitude for the higher vibrational beats is obtained off of the actual static resonance energy. This agrees well with intuition about a vibrational superposition. As the vibrational wave packet moves toward the inner or outer turning point, the contribution of $\nu_0\nu_1$ decreases, while the higher vibrational level contributions increases. This provides a direct measure of vibrational beat contribution to the wave packet signal as a function of internuclear separation.

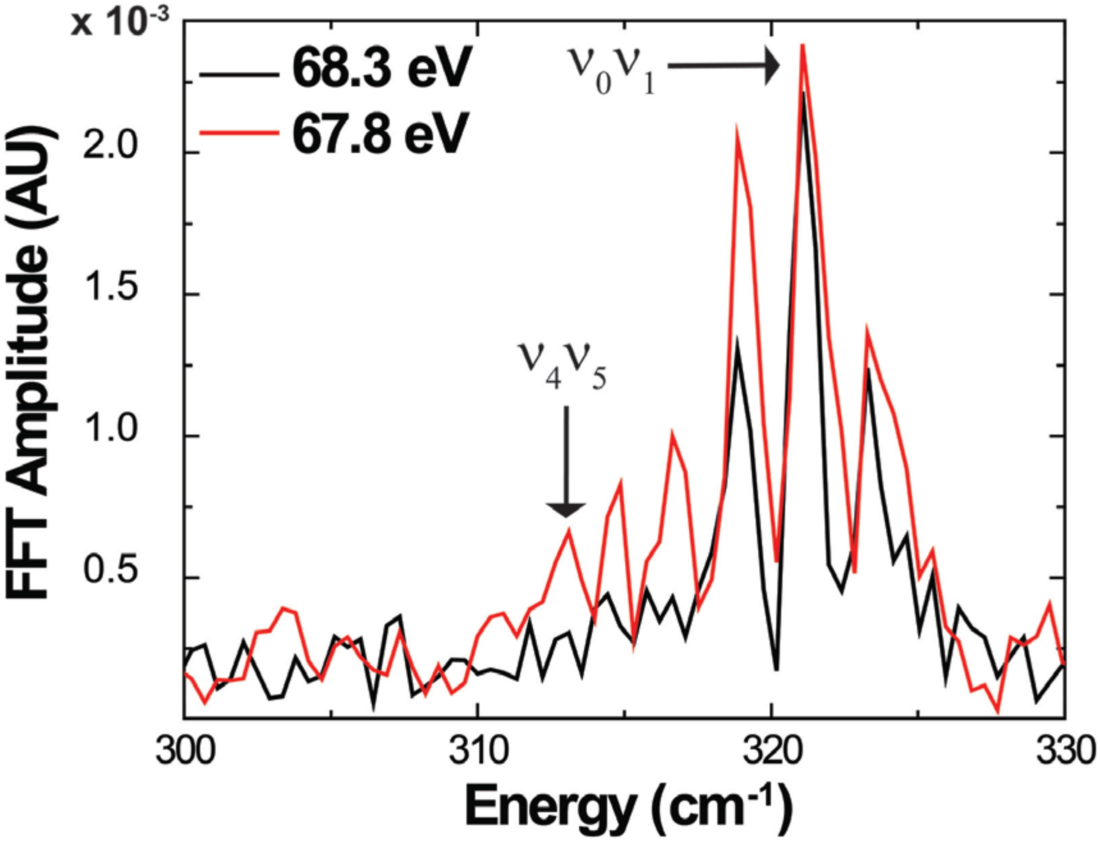

Figure 5.11: FFT results at 67.8 eV and 68.3 eV for the ground state wave packet observed via the ${}^{1}\Sigma_{g}^{+}, \sigma*^{-1} \rightarrow 3d_{5/2}^{-1}$ transition of Br_2 at a field intensity of $2.0 \times 10^{14}\, W/cm^2$. The peak of the static transition occurs at 68.3 eV, while the outer turning point is located near 67.8 eV. The higher frequency components of the vibrational wave packet are only retrieved away from R_e, while the $\nu_0\nu_1$ beat is predominantly seen near R_e.

At the maximum experimental field intensity of $4.0 \times 10^{14}\, W/cm^2$, the FFT of the transient absorption signal yields similar higher vibrational beat structure as observed at $2.0 \times 10^{14}\, W/cm^2$, but the signal to noise is significantly lower as seen in Fig. 5.9. This is due to the decrease in contrast between the remaining ground state wave packet population and the static absorbance reference. As a result, the positive spectral feature of the wave packet XUV absorption at the inner and outer turning point is considerably diminished due to the large relative change in optical density. Even so, vibrational beat structure is observed up to $\nu_2\nu_3$, but the exact peak ratios could not be decomposed in confidence.

5.4.5 Br_2^+ Wave Packet Dynamics at Various Field Intensities

In addition to the Br_2 ground state vibrational wave packet, there is also a correlated superposition of vibrational states on the Br_2^+ $^2\Pi_{g,3/2}$ state. False color plots are presented in Fig. 5.12 for all four measured field intensities, showing the ion vibrational wave packet dynamics outlined in purple. At $1.0 \text{ x } 10^{14}\,W/cm^2$ and $1.6 \text{ x } 10^{14}\,W/cm^2$, the vibrational motion is well-defined and is observed to be launched at approximately the center of the transition energy explored. The extremes of the observed ion core-hole transition energy define the inner and outer turning points of the Br_2^+ vibrational wave packet on the $^2\Pi_{g,3/2}$ state, and therefore the wave packet is determined to be prepared near $R_e^{Br_2^+}$. As the field intensity increases, the definition of the vibrational wave packet motion normally observed by a change of the transition energy is lost, and at $4.0 \text{ x } 10^{14}\,W/cm^2$ only a change in the transition intensity is observed at pump-probe time delays greater than 50 fs. At times shorter than 50 fs, a discrete change in transition energy is detected from high to low energy. According to the results of REW-TD-DFT calculations, the observed change in transition energy indicates a vibrational wave packet is formed at the ion inner turning point and moves toward longer bond lengths after preparation. This does not agree with the positioning of the neutral and ion potential energy curves with R, which even under field perturbed conditions would not lead to the formation of an ion vibrational wave packet at very short bond lengths. Instead, the ion $^2\Pi_{g,3/2}$ state is lowered in energy by the strong-field, increasing the XUV core-level transition energy as seen by the tail in the transient energy in Fig. 5.12 for the ion molecular resonance at 67.0 eV. After the pump interaction, the $^2\Pi_{g,3/2}$ state returns to its field-free shape and energy, yielding the same core-hole transition energy as at lower-field intensities. Similar barrier suppression for tunnel ionization occurs at $2.0 \text{ x } 10^{14}\,W/cm^2$, but not to the same degree as at $4.0 \text{ x } 10^{14}\,W/cm^2$.

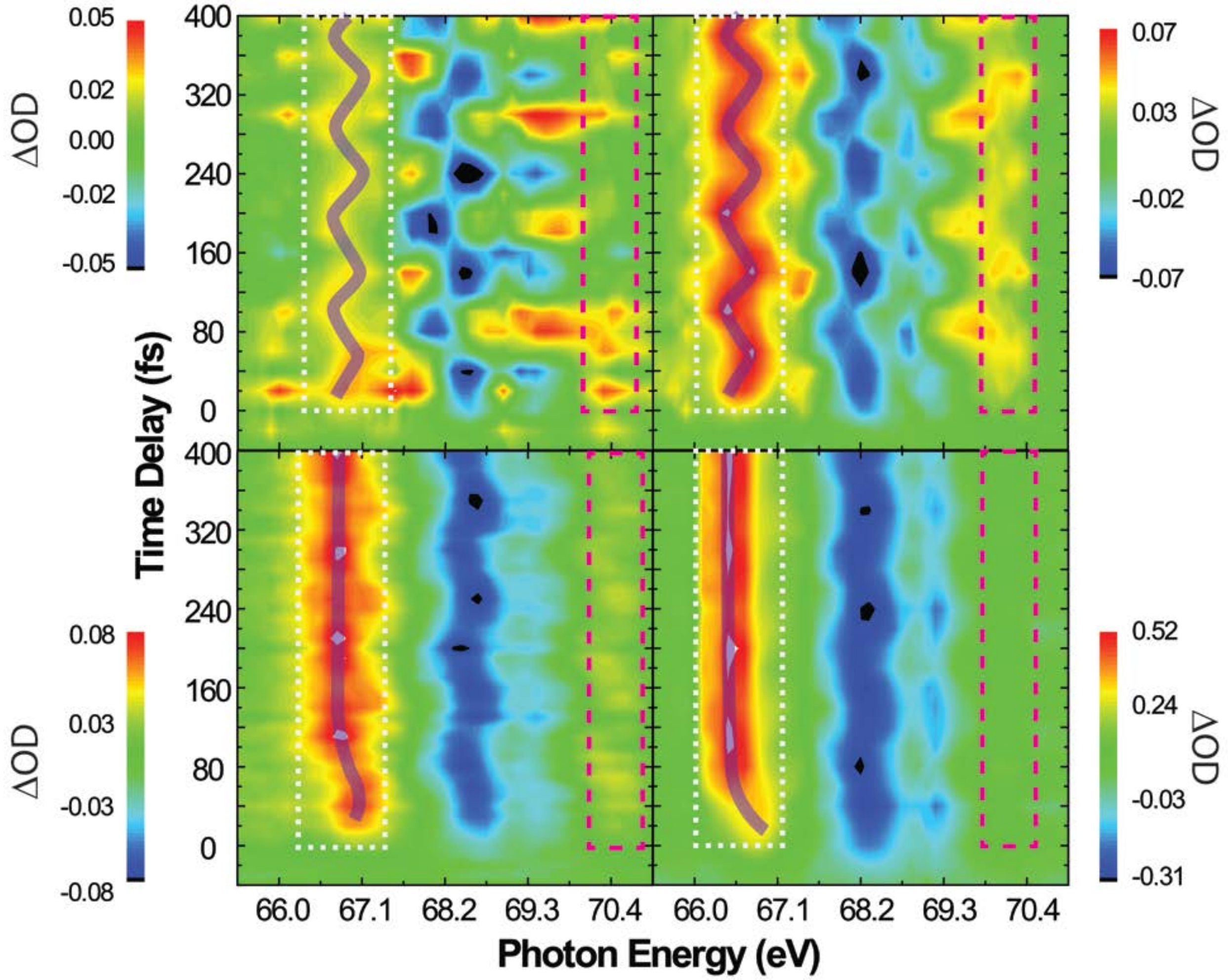

Figure 5.12: Intensity dependent data for the $^{2}\Pi_{g,3/2},\pi^{*^{-1}} \rightarrow 3d^{-1}_{5/2}$ (boxed in dotted white) and $^{2}\Pi_{g,3/2},\sigma^{*^{-1}} \rightarrow 3d^{-1}_{5/2}$ (boxed red) at 66.8 eV and 71.1 eV, respectively. The ion vibration wave packet is traced in purple, showing the dependence of the superposition preparation on the field intensity. The field intensities are: (Top Left) $1.0 \text{ x } 10^{14}\ \mathrm{W/cm^2}$, (Top Right) $1.6 \text{ x } 10^{14}\ \mathrm{W/cm^2}$, (Bottom Left) $2.0 \text{ x } 10^{14}\ \mathrm{W/cm^2}$, (Bottom Right) $4.0 \text{ x } 10^{14}\ \mathrm{W/cm^2}$.

Fast-Fourier transforms of the Br_2^+ transitions at 66.8 eV and 71.1 eV do not yield sharp spectral features as with the analysis of the Br_2 vibrational beats. Instead, a broad vibrational beat is observed at 360 cm^{-1} for a field intensity of $1.6 \text{ x } 10^{14}\ \mathrm{W/cm^2}$ as seen in Fig. 5.9, corresponding to the vibrational frequency of the $^{2}\Pi_{g,3/2}$ state. A vibrational energy of 360 cm^{-1} is equivalent to a vibrational period (τ) of 92 fs, matching, within error, the results retrieved in the time trace fitting of the $^{2}\Pi_{g,3/2}$ transient absorption signal. The broad FFT feature implies a broad manifold of vibrational levels are superimposed. As noted earlier, the vibrational period measured by the transient absorption time traces indicates that vibrational beats up to and including $\nu_2\nu_3$ may be excited.

5.4.6 Br$_2$ Wave Packet Time Dynamics at Several Field Intensities

The timescales for the strong-field ionization and vibrational dynamics are retrieved by fitting the energy line-out spectra as a function of pump-probe time delay. Each transition is fit to a convolution of a Gaussian, Heaviside, and cosinusoidal function to obtain the dominant wave packet period for each molecular species at the various field intensities. The Gaussian function models the envelope of the intense pump pulse, the Heaviside function accounts for the instantaneous strong-field ionization response, and the cosinusoidal function evaluates the vibrational wave packet dynamics (phase and frequency/period). From the results of the fitting routine, the temporal dynamics of the strong-field ionization of Br$_2$ at various field intensities may be retrieved.

The depletion timescale for Br$_2$ is measured at the $\sigma^{*^{-1}} \rightarrow 3\mathrm{d}^{-1}_{5/2}$ for all four peak intensities, yielding a strong-field response of 15 ± 5 fs, centered over the pump pulse. As the intensity is increased, the phase and amplitude of the ground state vibrational wave packet changes, and is qualitatively presented in Fig. 5.13. Each time trace is taken at 68.3 eV, corresponding to the center of the static $\sigma^{*^{-1}} \rightarrow 3\mathrm{d}^{-1}_{5/2}$ XUV absorbance.

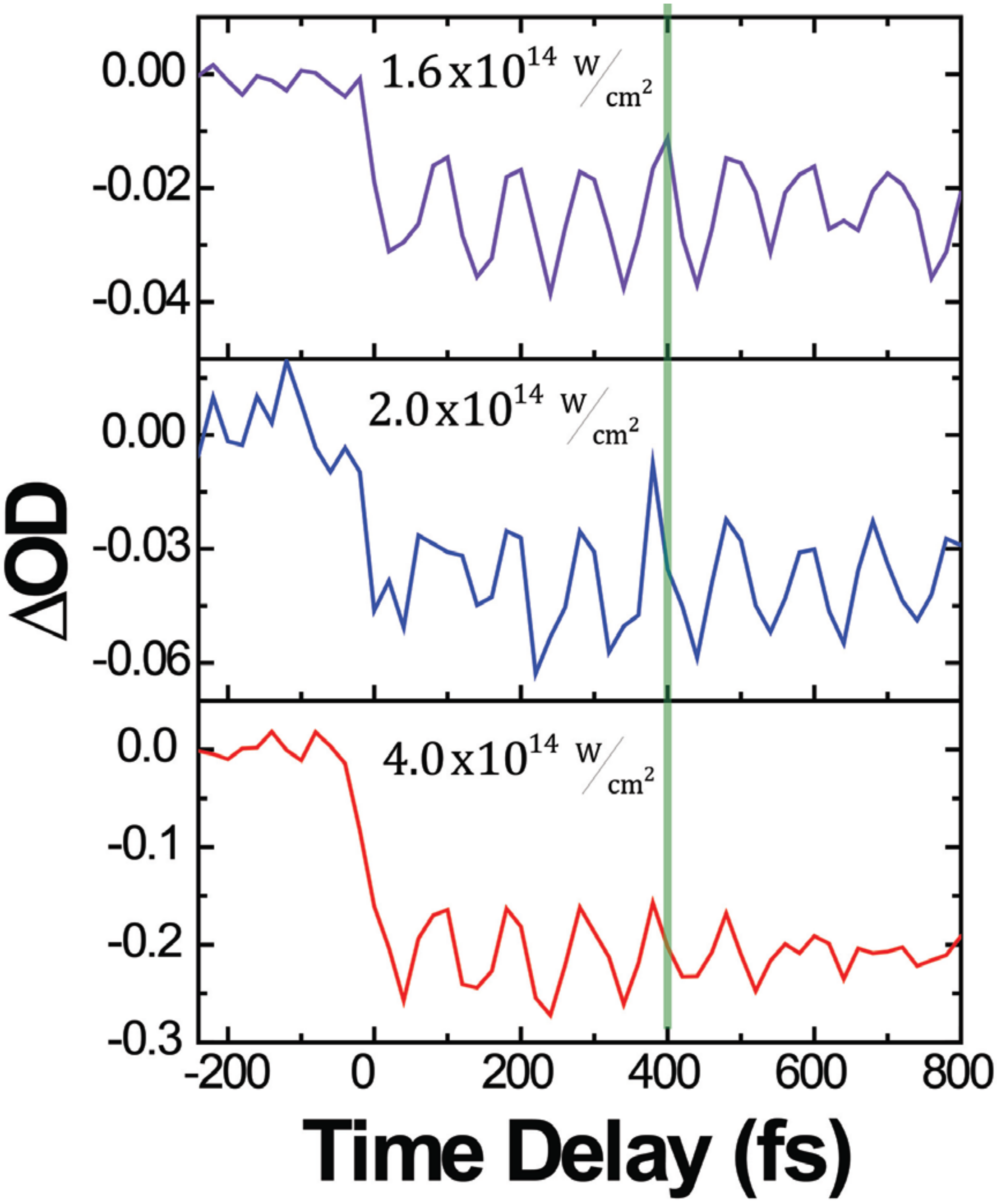

Figure 5.13: Pump-probe time traces for the $\mathrm{Br_2}\ {}^1\Sigma_g^+, \sigma^{*-1} \rightarrow 3d_{5/2}^{-1}$ depletion at 68.3 eV for the various investigated field intensities. The green mark is meant to provide a guide for the reader's eye, showing the phase variation in the vibrational wave packet with field intensity. The phase is better extracted through the fitting of the time traces due to the need to set the preparation time of the vibrational wave packet to the peak of the strong-field depletion. A smaller time step interval would also reveal a more qualitative depiction of the phase.

Overlap of the Br_2 *3d* core-level transitions prevents an extraction of the $\sigma^{*-1} \rightarrow 3\mathrm{d}^{-1}_{3/2}$ depletion timescale. Instead, the wave packet oscillation amplitude dwarfs the strong-field depletion as seen in Fig. 5.14 at 69.4 eV. The $\sigma^{*-1} \rightarrow 3\mathrm{d}^{-1}_{5/2,3/2}$ spectral overlap prevents direct observation of the vibrational beat at both the inner and outer turning point analyzing a single resonance, but by correlating the spin-orbit transitions this issue is overcome. The $\sigma^{*-1} \rightarrow 3\mathrm{d}^{-1}_{5/2}$ absorption provides an excellent indicator for wave packet localization at the outer turning point (lower transition energy), while the $\sigma^{*-1} \rightarrow 3\mathrm{d}^{-1}_{3/2}$ best indicates localization at the inner turning point (higher transition energy). This effect is presented in Fig. 5.14, where the neutral depletion of the $\sigma^{*-1} \rightarrow 3\mathrm{d}^{-1}_{5/2,3/2}$ transitions (68.3 eV, $3d^{-1}_{5/2}$:69.4 eV, $3d^{-1}_{3/2}$) are presented with their corresponding low (67.8 eV, $3d^{-1}_{5/2}$) and high energy (69.9 eV, $3d^{-1}_{3/2}$) positive ΔOD features for Br_2, respectively. The oscillations are exactly $\pi/2$ out of phase, which is to be expected from the vibrational motion of the wave packet from $R_e^{Br_2}$ to a turning point and back again. In conjunction, these two measures provide a real-time indicator of the ground state wave packet position, but they also provide an excellent measure of the superposition preparation by the intense pump pulse.

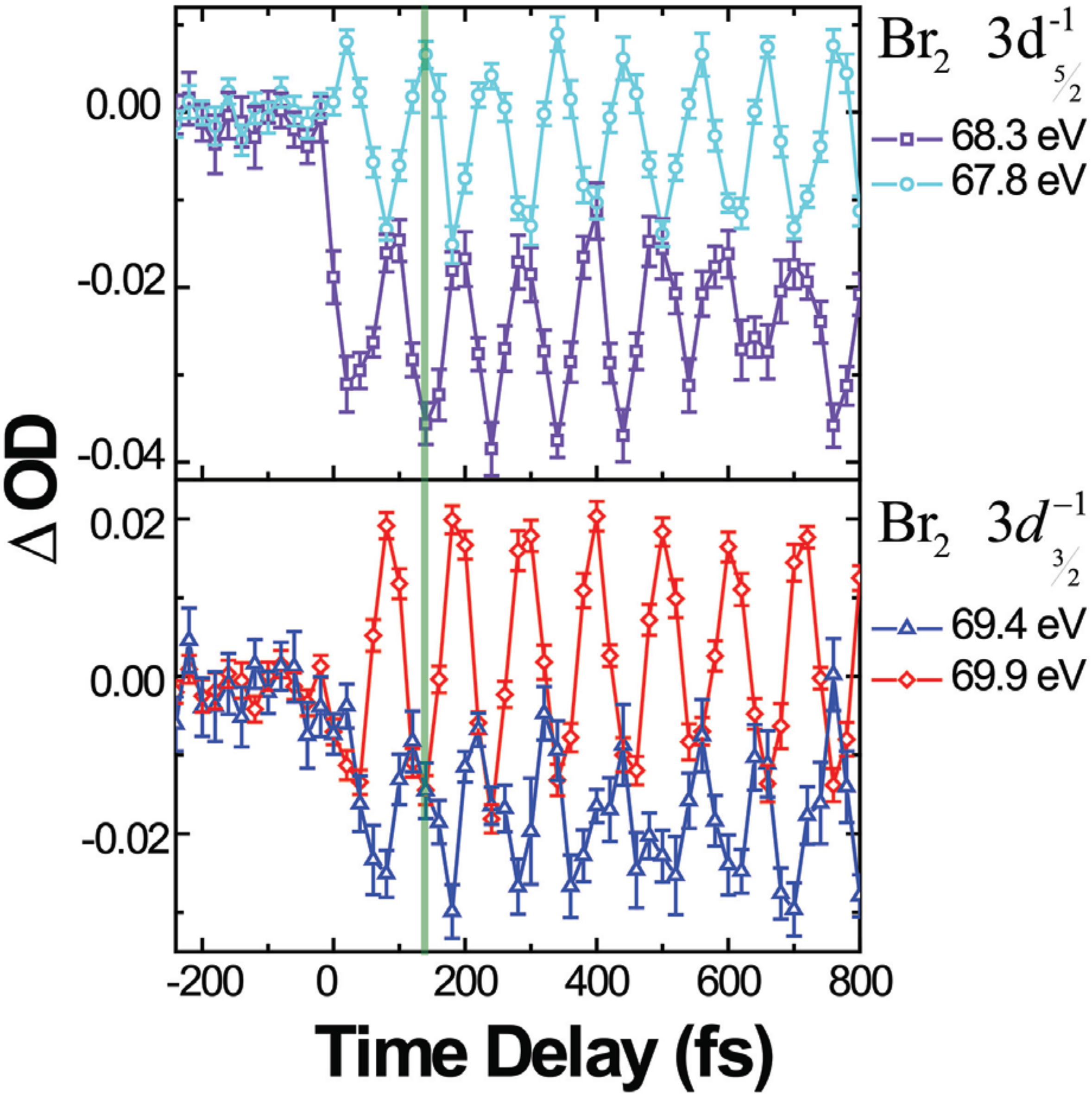

Figure 5.14: Pump-probe time traces for the $Br_2\ {}^1\Sigma_g^+, \sigma^{*^{-1}} \rightarrow 3d^{-1}_{5/2}$ and $\sigma^{*^{-1}} \rightarrow 3d^{-1}_{3/2}$ depletions at various energies measured at a field intensity of $1.6 \times 10^{14}\ W/cm^2$. (Top) The purple trace with square data points is measured at 68.3 eV, the center of the $\sigma^{*^{-1}} \rightarrow 3d^{-1}_{5/2}$ static absorption, while the turquoise trace with circle data points is at slightly lower energies, the outer turning point. (Bottom) The blue trace with triangle data points is measured at 69.4 eV, the center of the $\sigma^{*^{-1}} \rightarrow 3d^{-1}_{3/2}$ static absorption, while the red trace with diamond data points is at slightly higher energies, the inner turning point. The combination of all of these time traces follows the vibrational wave packet from the outer turning point to the inner turning point and back again. The green mark is meant to provide a guide for the reader's eye showing the consistent phase of the wave packet between the measures at various energies.

The formation time for Br_2^+ is measured by the rise of the ${}^2\Pi_{g,3/2}, \pi^{*^{-1}} \rightarrow 3d_{5/2}^{-1}$ transition for all four peak intensities and is found to be 40 ± 20 fs, centered over the pump pulse. An insufficient number of time delays were sampled around time zero to more accurately measure the ionization timescale. As the intensity is increased, the amplitude of the ion vibrational wave packet remains constant as is qualitatively shown in Fig. 5.15, taking into consideration the scale of each plot. The phase of the wave packet is seen to change between $1.6 \text{ x } 10^{14}\,\mathrm{W/cm^2}$ and $2.0 \text{ x } 10^{14}\,\mathrm{W/cm^2}$. Each time trace is taken at 66.7 eV, corresponding to the center of the oscillating ${}^2\Pi_{g,3/2}, \pi^{*^{-1}} \rightarrow 3d_{5/2}^{-1}$ transition.

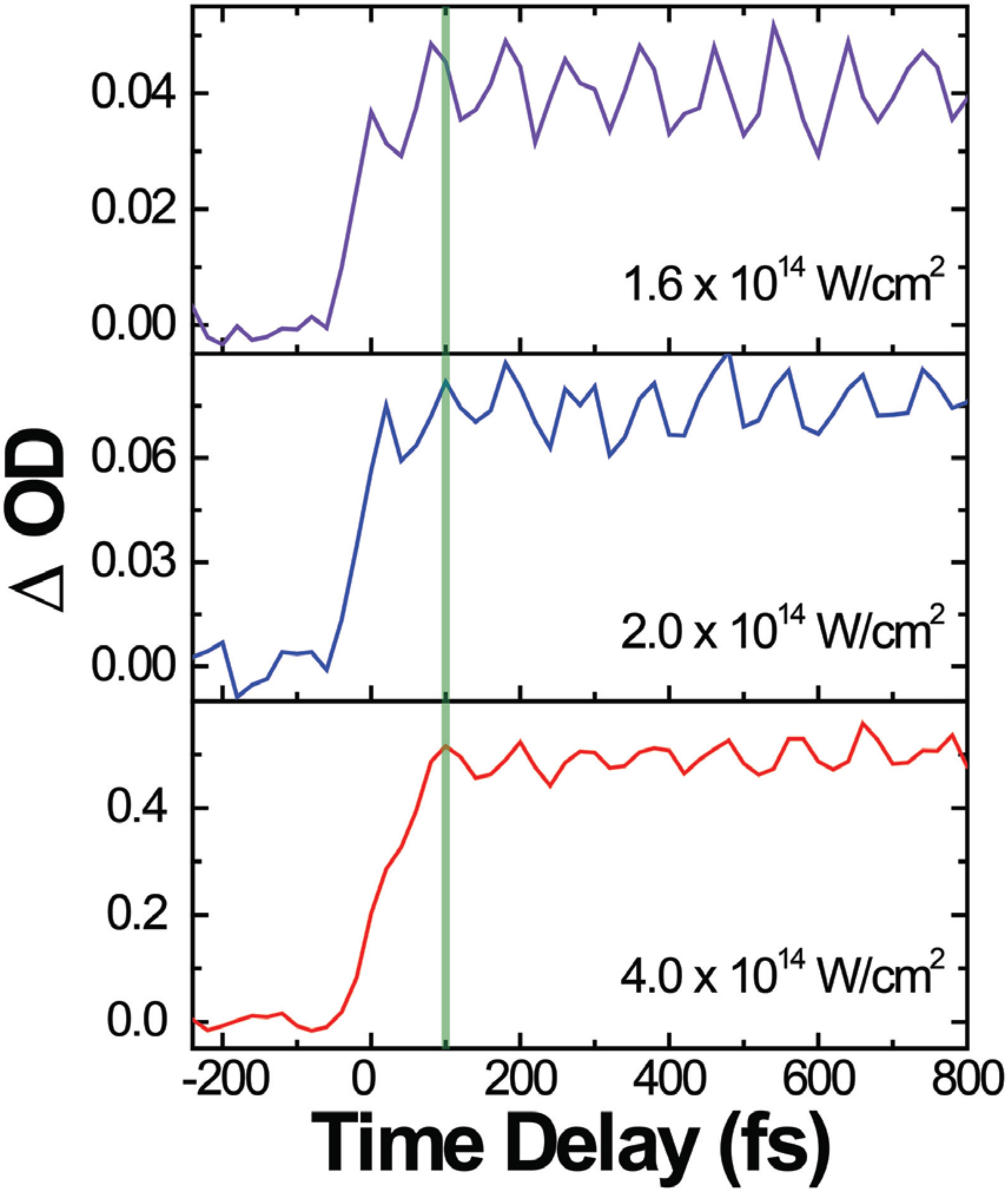

Figure 5.15: Pump-probe time traces for the $^{2}\Pi_{g,3/2}, \pi^{*-1} \rightarrow 3d^{-1}_{5/2}$ absorption at 66.7 eV for the various investigated field intensities. The green mark is meant to provide a guide for the reader's eye to identify the phase of the vibrational wave packet on the Br_2^+ $^{2}\Pi_{g,3/2}$ state. A phase shift similar to the ground state wave packet with field intensity is observed here.

The results for the energy line-out fits (vibrational amplitude and phase) of the Br_2 $\sigma^{*-1} \rightarrow 3d^{-1}_{5/2}$ and $\sigma^{*-1} \rightarrow 3d^{-1}_{3/2}$ transitions as well as the Br_2^+ $^2\Pi_{g,3/2}$ $\pi^{*-1} \rightarrow 3d^{-1}_{5/2}$ excitation are presented in Table 1. Both the Br_2 spin-orbit state depletions are found to have a dominant vibrational period of 104 ± 1 fs, while the Br_2^+ period is determined to be 93 ± 2 at all field intensities. The lack of variation in the periods of the vibrational wave packets indicates they are each composed predominantly of one beat. For Br_2, a vibrational period of 104 ± 1 fs corresponds to the $\nu_0\nu_1$ vibrational beat, and a period of 93 ± 2 fs in the ion matches the Br_2^+ $\nu_1\nu_2$ and $\nu_2\nu_3$ beats. The measured phases refer to the relative localization of the vibrational wave packet on the inner and outer turning point of the molecular potential. A phase of 0π indicates the wave packet is prepared on the outer turning point, while a phase of π signifies the wave packet has been prepared on the inner turning point. Phases between 0π and π indicate the wave packet has been prepared between the inner and outer turning point, where a phase of 0.5π would suggest the wave packet is prepared at R_e.

Table 5.1: Retrieved XUV transient absorption information at varying field intensities.

	Br_2 $3d^{-1}_{5/2} \leftarrow \sigma^*$		Br_2 $3d^{-1}_{3/2} \leftarrow \sigma^*$		Br_2^+ $3d^{-1}_{5/2} \leftarrow \pi^*$	
Peak Laser Intensity (W/cm^2)	Phase (π)	Amplitude (Δ^2 OD)	Phase (π)	Amplitude (Δ^2 OD)	Phase (π)	Amplitude (Δ^2 OD)
$1.0\text{x}10^{14}$	0.03 ± 0.09	0.012 ± 0.002	0.12 ± 0.04	0.03 ± 0.004	1.40 ± 0.05	0.005 ± 0.001
$1.6\text{x}10^{14}$	0.21 ± 0.05	0.008 ± 0.001	0.20 ± 0.02	0.012 ± 0.004	1.54 ± 0.04	0.007 ± 0.003
$2.0\text{x}10^{14}$	0.38 ± 0.01	0.015 ± 0.001	0.45 ± 0.02	0.025 ± 0.001	1.64 ± 0.10	0.008 ± 0.001
$4.0\text{x}10^{14}$	0.51 ± 0.04	0.020 ± 0.003	0.44 ± 0.05	0.042 ± 0.003	1.88 ± 0.06	0.024 ± 0.002

5.5 Discussion

The detection of both the Br and Br* spin-orbit components indicates that multiple potentials are involved in the dissociation of Br_2. A similar dynamic was also observed by our group with the strong-field dissociation of CH_2Br_2 and was attributed to dissociation across multiple field-dressed states.[22] The similar timescales for the formation of Br and Br* indicates a similar shape to the excited state potentials accessed, and the same appearance time implies that both states are populated simultaneously. Likewise to the CH_2Br_2 analysis of atomic bromine formation, other pathways resulting in dissociation of Br_2 are discounted, such as multiphoton ionization to a Rydberg state followed by dissociation. Due to the low ionization barrier of the Rydberg states the strong-field pulse will prefer to directly access ion states and therefore dissociation of Br_2 via a Rydberg state is discounted.

The rise time of the Br $^2P_{3/2}$ spin-orbit ground state observed at long pump-probe delays at $4.0 \text{ x } 10^{14}\ W/cm^2$ is attributed to predissociation of the Br_2^+ $^2\Pi_{g,3/2}$ state due to the correlation in the ion's decay time. The dissociation energy of the Br_2^+ $^2\Pi_{g,3/2}$ state is 3.26 eV, greater than the neutral binding energy of 1.97 eV. From the Fourier and time trace analysis of the ion vibrational wave packet, it is not obvious that a significant amount of vibrational energy is imparted to the ion by strong-field ionization. The fitting of the time traces indicate the dominant vibrational beat is either $\nu_1\nu_2$ or $\nu_2\nu_3$, ~1,000 cm^{-1} of vibrational energy. The detected vibrational excitation of the ion is insufficient to overcome the dissociation barrier. The $\tilde{A}^2\Pi_{u,3/2}$ state is the closest lying potential curve to the $\tilde{X}\,^2\Pi_{g,3/2}$ and is ~16,600 cm^{-1} higher in energy, but is also bound.[170] No spectral evidence for population of the $\tilde{A}^2\Pi_{u,3/2}$ state either by vibrational motion or strong-field ionization is observed in the XUV transient absorption spectra. It is possible that some population is present in the higher lying vibrational levels of the $\tilde{X}\,^2\Pi_{g,3/2}$ state which undergo a curve crossing to the $^2\Sigma_g^+$ dissociative state (~30,600 cm^{-1}).[170] Predissociation of the $\tilde{X}\,^2\Pi_{g,3/2}$ has been observed in REMPI 2+1 experiments where Br_2^+ is excited with >20,000 cm^{-1} of vibrational energy access higher lying electronic curves containing curve crossings to dissociation channels yielding Br $^2P_{3/2}$ and Br$^+$ in various ^3P states.[216] Nevertheless, the temporal dynamics of atomic bromine and Br_2^+, as well as the detection of Br$^+$ indicates dissociation occurs for Br_2^+ at long time delays.

Also, it may be suspected that ionization of Br$_2$ to the ion $\tilde{B}^2\Sigma_g^+$ state would be preferable due to the alignment of the HOMO-2 σ_g orbital to the polarization of the ionizing 800 nm pump pulse.[66] The $\tilde{B}^2\Sigma_g^+$ state is 3.80 eV higher in energy than the ion $\tilde{X}\,^2\Pi_{g,3/2}$ ground state. Any ionization to the $\tilde{B}^2\Sigma_g^+$ state would result in an additional feature in the XUV transient absorption signal, which would be 3.80 eV lower in energy than the $\tilde{X}\,^2\Pi_{g,3/2}$ feature at 66.7 eV. No absorption signal is observed at 62.9 eV at any of the measured field intensities, therefore ionization of room temperature bromine is concluded to occur predominantly from the HOMO π_g^* orbital.

The remainder of this section is divided into three parts. Section 5.5.1 discusses the impact of field intensity on the Br$_2$ $^1\Sigma_g^+$ ground state vibrational wave packet preparation, while section 5.5.2 examines the field's impact on the ion $^2\Pi_{g,3/2}$ vibrational wave packet. Section 5.5.3 then discusses the ionization mechanism for vibrational wave packet preparation as a function of field intensity.

5.5.1 Field Intensity Dependent Br_2 Vibrational Wave Packet Dynamics

Determination of the vibrational beat contributions to the ground state wave packet at various field intensities provides insight into vibrational superposition preparation in the strong-field regime. Assuming non-specific ionization of an initial Boltzmann distribution of vibrational states at 300 K, the integrated peak area ratios of the resulting vibrational beats are: $\frac{\nu_1\nu_2}{\nu_0\nu_1}=0.044$, $\frac{\nu_2\nu_3}{\nu_0\nu_1}=0.002$, $\frac{\nu_3\nu_4}{\nu_0\nu_1}=0.00008$, etc... Here, we have discounted the overtone beats, which are beyond the resolution of the instrument. At $1.6 \text{ x } 10^{14}\, \text{W}/\text{cm}^2$, the experiment agrees well with the predicted vibrational beat distribution as no $\nu_1\nu_2$ beat is evident. Evidence for preferential ionization is found in terms of the corresponding bond length for correlated preparation of the ion and neutral vibrational wave packets around $R_e^{Br_2^+}$ and $R > R_e^{Br_2}$, respectively. Franck-Condon ionization of Br_2 would result in preparation of the ion wave packet at $R > R_e^{Br_2^+}$ due to the overlap of the neutral and ion potential curves. The isotopic abundance of Br_2 is seen to be conserved at this field intensity, allowing it to be used in further analysis of the vibrational beats at higher intensities.

At $2.0 \text{ x } 10^{14}\, \text{W}/\text{cm}^2$ a progression of vibrational beats up to $\nu_3\nu_4$ are observed well above the baseline of the FFT for all three natural occurring isotopes of Br_2. It has been predicted that the vibrational energy of highly excited molecules is dissipated by strong-field ionization as has been observed in I_2 and calculated here by R_v-ADK theory.[135,136] Selective ionization of the higher lying vibrational levels reduces the target molecule to lower vibrational states, leading to a predominantly $\nu_0\nu_1$ wave packet as seen at $1.6 \text{ x } 10^{14}\, \text{W}/\text{cm}^2$. Moreover, the Boltzmann distribution of vibrational level populations does not account for the higher beats observed in the FFT at $2.0 \text{ x } 10^{14}\, \text{W}/\text{cm}^2$, therefore an additional mechanism must coherently populate the higher-lying vibrational states. At field intensities below the strong-field regime, Raman excitation of vibrational modes may induce ladder climbing if a sequence of pulses or a chirped pulse is employed. In this experiment, Raman pumping is suspected as the mechanism for populating the higher lying states as the higher field intensity is akin to employing multiple successive pulses. Preferential ionization and depletion of the vibrational energy of the molecule is overcome by strong-field distortion of the ion and neutral potentials accessing a regime where preferential ionization is not as selective in R as under field-free conditions. The calculations of the perturbation of the nuclear potentials presented in Fig. 5.3 demonstrate this regime at a field intensity of 0.01 a.u.. Constant ionization energy with R allows Raman pumping to dominate on the ground state of Br_2 due to equal ionization of all vibrational level. At higher or lower field intensities, preferential ionization results in the depletion of high vibrational levels either at long or short bond lengths, i.e. as Raman pumping populates higher levels they are selectively depleted. The negligible difference in ionization energy with vibrational level is insignificant compared to the slope of the ionization energy and vibrational amplitude distribution with R. At the highest measured field intensity for this experiment, $4.0 \text{ x } 10^{14}\, \text{W}/\text{cm}^2$, preferential ionization is observed to be once again asserting itself, but now slightly toward the outer turning point according to the phase measurement and the observed Br_2 neutral depletion transition energy. Therefore, Raman pumping is hypothesized to occur at all field intensities, but may only dominate when preferential ionization is lost due to distortion of the potential energy curves, which further dictate the bond length corresponding to selective ionization. Raman preparation of the vibrational wave packet may not be invoked to rationalize the entirety of the results as it would be expected that the trend of higher vibrational beats at increasing field intensity would follow from $2.0 \text{ x } 10^{14} \text{W}/_{\text{cm}^2}$ to $4.0 \text{ x } 10^{14} \text{W}/_{\text{cm}^2}$. Also, relatively similar beat distribution would be expected for all investigated field intensities as even the lowest field intensity should act as a series of Raman pump pulses leading to population of high vibrational levels. This analysis conforms to the results found here as well as previous experiments where selective ionization occurs at R-critical.

5.5.2 Field Intensity Dependent Br_2^+ Vibrational Wave Packet Dynamics

Preparation of the ion vibrational wave packet on the ${}^2\Pi_{g,3/2}$ shows a strong dependence on the distortion of the molecular potentials. In the presence of a strong-field, the molecular potentials may be shifted as illustrated in Fig. 5.1, hardening and softening the molecular bond with the oscillating laser field. The perturbed potentials facilitate increased ionization at internuclear separations not accessible along the field-free curves, i.e. enhanced ionization at R_c, which is typically 50% longer than the equilibrium bond length.[164] At $1.0 \text{ x } 10^{14} \text{W}/_{\text{cm}^2}$ and $1.6 \text{ x } 10^{14} \text{W}/_{\text{cm}^2}$, depletion of the neutral ground state population occurs as predicted by R_v-ADK for the field free potentials, preparing the ion vibrational wave packet at $R \geq R_e^{Br_2^+}$. As the field intensity is increased to $2.0 \text{ x } 10^{14} \text{W}/_{\text{cm}^2}$, the ion vibrational wave packet is no longer prepared near $R_e^{Br_2^+}$, but rather the transition energy at the time of the superposition launch has shifted to higher energies. Either the wave packet has formed at $R < R_e^{Br_2^+}$ or the potentials have been distorted by the strong field. With little non-coherent vibrational amplitude at $R < R_e^{Br_2^+}$ initially, it is determined that the strong-field suppresses the ion ${}^2\Pi_{g,3/2}$ potential, raising the XUV transition energy to the $3d^{-1}_{5/2},\pi^*$ core-hole excited state. Increasing the field intensity to $4.0 \text{ x } 10^{14} \text{W}/_{\text{cm}^2}$, the launch vector of the ion vibrational wave packet has changed completely. The wave packet transition energy is shifted higher than observed at any other power intensity or time delay. This is a clear indication of distortion of the ${}^2\Pi_{g,3/2}$ potential, which relaxes to the field-free potential once the strong-field is no longer present. Maximum change in the energy of the potential is achieved at the peak of the pump pulse, and then the potential proceeds to relax over the trailing edge of the pulse. Utilizing this explanation, a maximum change in the energy of the $^2\Pi_{g,3/2}$ potential of ~0.5 eV is observed at $4.0 \text{ x } 10^{14}\, \mathrm{W/cm^2}$.

It is possible the strong-field increases the potential of the core-hole excited state as well, which would yield the same result. Considerable experimental work has been conducted on the strong-field response of molecular potentials relating to ground and singly charged ion states where the vacancy is created in the valence orbitals, while minimal effort has been invested into understanding the strong-field response of core-hole states.[59,63,64,82] It is expected that the core-hole will not interact with the strong-field to a detectable degree. This deduction is confirmed by attosecond core-hole streaking experiments, where only the interaction of the ionized electron with the intense few-cycle pulse is considered in the resulting kinetic energy spectrum and not the AC-stark shifting of the core-levels.[78]

XUV transient absorption retrieves the vibrational amplitude shape of the prepared superpositions projected onto the core-hole excited state. The ground state amplitude is difficult to realize as the spin-orbit transition are spectrally overlapped, while the ion vibrational wave packet shape is obtained easily from the transient absorption signal. At $1.0 \text{ x } 10^{14}\, \mathrm{W/cm^2}$ and $1.6 \text{ x } 10^{14}\, \mathrm{W/cm^2}$, the resulting wave packet propagates along the $^2\Pi_{g,3/2}$ state as a small distribution of vibrational levels, yielding a well resolved coherence that is seen to localize at the inner and outer turning points. Localization of the vibrational amplitude (probability density) at the turning points manifests as an increase in the XUV absorption intensity as well as a narrowing of the spectral feature as seen in Fig. 5.12. At $2.0 \text{ x } 10^{14}\, \mathrm{W/cm^2}$ and $4.0 \text{ x } 10^{14}\, \mathrm{W/cm^2}$, the excited vibrational manifold is larger, allowing the superposition to be better treated as a bound 1-D Gaussian wave packet. Utilizing Discrete-Variable-Representation[217] (DVR) techniques to solve the time-dependent Schrödinger equation, calculations of a Gaussian wave packet launched on the $^2\Pi_{g,3/2}$ potential at $R > R_e^{Br_2^+}$ show the superposition initially spreads toward both turning points and then coalesce at $R_e^{Br_2^+}$. The wave packet continues to oscillate between being delocalized toward both turning points followed by coalescence at $R_e^{Br_2^+}$ a full vibrational period later. This dynamic is observed in the false-color plots in Fig. 5.12, where the $^2\Pi_{g,3/2}, \pi^{*-1} \rightarrow 3d_{5/2}^{-1}$ resonance spreads in energy (delocalization of the wave packet) and then peak at 66.7 eV (coalescence at $R_e^{Br_2^+}$) every 93 fs, measuring the dynamics of the vibrational amplitude in real-time.

5.5.3 Strong-Field Ionization Mechanism Dependence on Field Intensity

Extensive experimental and theoretical efforts have been expended to determine the ionization mechanism for diatomics as a model system for larger molecules. The distinguishing feature between the proposed mechanisms has been the phase of the vibrational wave packet and the internuclear separation corresponding to the preferential ionization. For the strong-field ionization of Br_2 investigated here, the ground state vibrational wave packet is observed to be prepared at the outer turning point for the field intensities of $1.0 \text{ x } 10^{14} \,{}^{\text{W}}\!/\!_{\text{cm}^2}$ and $1.6 \text{ x } 10^{14} \,{}^{\text{W}}\!/\!_{\text{cm}^2}$. Clearly, the transient absorption signal of the 68.3 eV ${}^1\Sigma_g^+, \sigma^{*-1} \rightarrow 3d_{5/2}^{-1}$ appears close to time zero at slightly lower transition energies than the average over all time delays, indicating the wave packet is prepared at the outer turning point. The phase measurements for the pump intensities of $1.0 \text{ x } 10^{14} \,{}^{\text{W}}\!/\!_{\text{cm}^2}$ and $1.6 \text{ x } 10^{14} \,{}^{\text{W}}\!/\!_{\text{cm}^2}$ also indicate the wave packet is prepared on the outer turning point. A phase of 0π for the vibrational wave packet transient absorption indicates preparation at the outer turning point, while a phase of π indicates the wave packet is initially localized on the inner turning point. The ${}^1\Sigma_g^+, \sigma^{*-1} \rightarrow 3d_{5/2}^{-1}$ XUV transition energy around time zero and the measured phase of the vibrational wave packet support the supposition of preferential ionization at short internuclear separations for the two examined field intensities.

Strong-field ionization at $2.0 \text{ x } 10^{14} \,{}^{\text{W}}\!/\!_{\text{cm}^2}$ reveals a ground state vibrational wave packet phase indicating the superposition is prepared between the inner and outer turning point, closely akin to Franck-Condon ionization. The bond length corresponding to the preparation of the vibrational wave packet is further confirmed by the Br_2 ${}^1\Sigma_g^+, \sigma^{*-1} \rightarrow 3d_{5/2}^{-1}$ transition energy around time zero. The phase and transition energy indicate the loss of preferential ionization with R at this intensity, facilitating Raman pumping of the ground state to higher vibrational levels. At $4.0 \text{ x } 10^{14} \,{}^{\text{W}}\!/\!_{\text{cm}^2}$, the XUV transient absorption signal shows the Br_2 ground state vibrational wave packet is prepared closer to $R_e^{Br_2}$, shifting from the outer turning point toward the inner turning point, which is confirmed by the measured phase of the Br_2 ${}^1\Sigma_g^+, \sigma^{*-1} \rightarrow 3d_{5/2}^{-1}$ transition at 68.3 eV. The phase and XUV transition energy measurements indicate that as field intensity is increased, the mechanism of preferential ionization begins to switch from being well-explained by R_v-ADK ionization for the field-free potentials to increased ionization at R_c due to distortion of the ion potential curve. Essentially, the dominant ionization mechanism is determined by the distortion of the molecular potentials as illustrated in Fig. 5.3.

Utilizing R_v-ADK as well as the Franck-Condon factors, a vibrational wave packet is expected to be prepared in the ion by a broad distribution of vibrational levels centered on the ν_1 and ν_2. This calculation matches the experimental results quite well as a broad FFT peak is observed at 360 cm^{-1} as seen in Fig. 5.9. Franck-Condon excitation of the ion vibrational wave packet from strong-field ionization has been determined to misrepresent the accessed vibrational levels due to the strong dependence of the ionization rate with R.[61] For strong-field ionization, the distribution of superimposed vibrational states is not limited by the bandwidth of the driving laser pulse, but rather the accessible vibrational levels comparing the ionization energy from the ground state and the strength of the laser's electric field. As the field intensity increases, the distribution of vibrational levels composing the ion wave packet is expected to broaden.

For completeness, it is necessary to consider the impact of bond-softening on the ground state vibrational wave packet formation at the experimental field intensities. The contribution of bond-softening is typically retrieved through decomposition of the vibrational wave packet phase corresponding to the leading and tail edge of the pulse, i.e. a 0.5π phase mismatch in systems where the minimum ionization energy is on the outer turning point. The phase mismatch arises from the physical picture of bond-softening decreasing the dissociation energy of the ground state potential energy curve, allowing the vibrational amplitude to initially move toward the outer turning point, while preferential ionization at elongated bond lengths forms the amplitude toward the inner turning point. Unfortunately, under the experimental conditions the wave packet is always launched toward the outer turning point. Furthermore, effective bond softening wave packet preparation is accomplished with pump pulses of duration longer than the vibrational period, allowing the vibrational amplitude to move to long R before the potential relaxes.[59,63] For the experimental conditions employed here, there is not significant time within the pump pulse to allow this dynamic to dictate the vibrational wave packet preparation.

Interpreting the overall phase of the prepared vibrational wave packet with increasing field intensity as a function of the change in the energy of the ion ${}^2\Pi_{g,\frac{3}{2}}$ state presents an issue in interpreting the impact of bond-softening. At low field intensity, a wave packet phase close to zero is observed, indicating the wave packet is prepared near the outer turning point. As the field intensity is increased, the phase increases toward 0.5π and is eventually slightly larger. In the strict interpretation of the phase of the vibrational wave packet, where a phase of 0 and π indicate the wave packet has been prepared at the outer or inner turning point, respectively, while a phase of 0.5π indicates bond softening, then at the highest measured field intensity bond softening could be determined to dominant. This conclusion is counterintuitive to the current understanding of strong-field mechanisms, where bond softening is expected to dominate at low field intensities, while tunnel ionization governs dynamics as the field intensity increases. From the experimental results here, the phase of the ground state vibrational wave packet is found to be determined by the internuclear separation where ionization is preferred and the resulting hole in the vibrational amplitude caused by the strong-field ionization. Instead, Raman pumping of the vibrational energy to higher levels is found to increase with the field intensity. Therefore, the phase of the ground state vibrational wave packet phase may not be as clear an indicator of the preparation mechanism as expected with respect to Lochfraß and bond-softening.

5.6 Conclusions

Experiments investigating the formation of ground state wave packet by strong-field ionization reported to date have utilized a second strong-field probe pulse to ionize the ground state wave packet and subsequently detect the resulting ions as a function of ion-yield and kinetic energy release to map the time-dependence of the internuclear separation. This strongly interacting probe may affect the wave packet dynamics. Here, we have employed femtosecond XUV transient absorption spectroscopy as a weakly interacting probe to monitor the Br_2 wave packet preparation and determine the composition of the superposition in real-time. A new connection between Lochfraß ionization mechanisms and Raman pumping for vibrational wave packet preparation has been illuminated as a function of field intensity and the distortion of molecular potentials. The ground state vibrational wave packet may be prepared at various internuclear separations, dependent on the distortion of the ion potential and the resulting ionization energy between the Br_2 ${}^1\Sigma_g^+$ and the Br_2^+ ${}^2\Pi_{g,3/2}$ states. At $2.0 \text{ x } 10^{14}\, \mathrm{W}/\mathrm{cm}^2$, relatively equal ionization rates are realized across all bond lengths occupied by the Br_2 wave function, allowing non-selective ionization of the ground state and Raman pumping of the vibrational population to higher lying levels. The resulting vibrational superposition is composed of vibration beats up to and including $\nu_3\nu_4$.

The experiment data presented here indicates that XUV transient absorption spectroscopy is a bond-length-specific probe also capable of deconvolving multiple beat vibrational superpositions. These measurements pave the way for fully retrieving the wave packet vibrational level populations by utilizing shorter XUV pulses to measure the overtone beats at higher frequencies. The full extent of Raman pumping at various field intensities may then be determined directly.

Chapter 6

Ongoing Experiments and Conclusions

The strong-field dynamics of atoms and molecules presents a field of rich physics and chemistry with subtle nuances based on field intensity. Here, the framework and experimental capabilities of extreme-ultraviolet (XUV) transient absorption have been extended to include the accurate determination of vibrational wave packet dynamics as a function of field intensity. While the investigations of strong-field ionized Br_2 elucidated a novel link between previous experiments in I_2 and H_2, the potential of the technique has not been fully exploited. In particular, the inherent elemental specificity of the probe was not utilized, nor was the dependence of the absorption on the relative polarization of the pump and probe beams. Current work beyond the experiments presented here is focusing on the vibrational wave packet dynamics in iodine monobromide and the polarization dependent absorption of strong-field ionized xenon (Xe^{2+}) and Br_2.

6.1 Ongoing Experiments

Three experiments are ongoing at the moment investigating the strong-field ionization dynamics by XUV transient absorption spectroscopy. Ionization of IBr by an intense 800 nm pulse reveals the formation of a ground state vibrational wave packet, which may be detected by core-level absorption of iodine as well as bromine atoms. Quantitative determination of the $\left|j, m\right\rangle$ state distribution of xenon has been extended from Xe^{+} to Xe^{2+}. And finally, the alignment of neutral Br_2 with the polarization of the 800 nm pump beam after strong-field ionization is observed.

6.1.1 Strong-Field Ionization and Vibrational Wave Packet Dynamics in IBr

Probing of the strong-field ionization of Br_2 illuminated the capability of XUV transient absorption to detect and interpret vibrational wave packets. The experiment did not however exploit the elemental sensitivity intrinsically afforded by core-level absorption. Extending the studies started with Br_2 to IBr allows investigation of vibrational superpositions from an atomic perspective through probing of the bromine (*3d*) and iodine (*4d*) core-levels simultaneously. Currently, experiments have begun to determine if XUV absorption at multiple atomic sites is sensitive to vibrational motion in a correlated manner, i.e. if the iodine and bromine core-level absorption are equally dependent on the internuclear separation.

Figure 6.1 shows the XUV transient absorption spectrum for IBr at $4 \text{ x } 10^{14} \, {}^{\text{W}}\!/\!{}_{\text{cm}^2}$ and 500 fs pump-probe time delay. The iodine and bromine core-level windows are highlighted at 47-52 eV and 64-73 eV, respectively. Neutral depletions are observed for the IBr molecule in both atomic windows for both spin-orbit states: $nd_{5/2}$ and $nd_{3/2}$, where *n* is the principal quantum number. The IBr$^+$ molecular ion is also observed by the $\pi^{*-1} \longrightarrow nd_{5/2}^{-1}$ transition in both windows at 47.6 eV and 66.7 eV for iodine and bromine, respectively. In addition, the IBr$^+$ ion is also observed at 72.1 by the bromine $\sigma^{*-1} \longrightarrow 3d_{5/2}^{-1}$ transition. The dominant dissociation channel of the IBr$^+$ molecule is observed to yield I$^+$ as well as neutral atomic Br in the ${}^2P_{3/2}$ state, as there is no evidence for fragmentation to neutral atomic iodine, bromine in the ${}^2P_{1/2}$ state, or atomic bromine ions. Without fragmentation to either neutral atomic iodine or bromine atomic ions, dissociative ionization of neutral IBr is considered to be unlikely, while dissociation of IBr$^+$ is determined to be the dominant fragmentation channel.

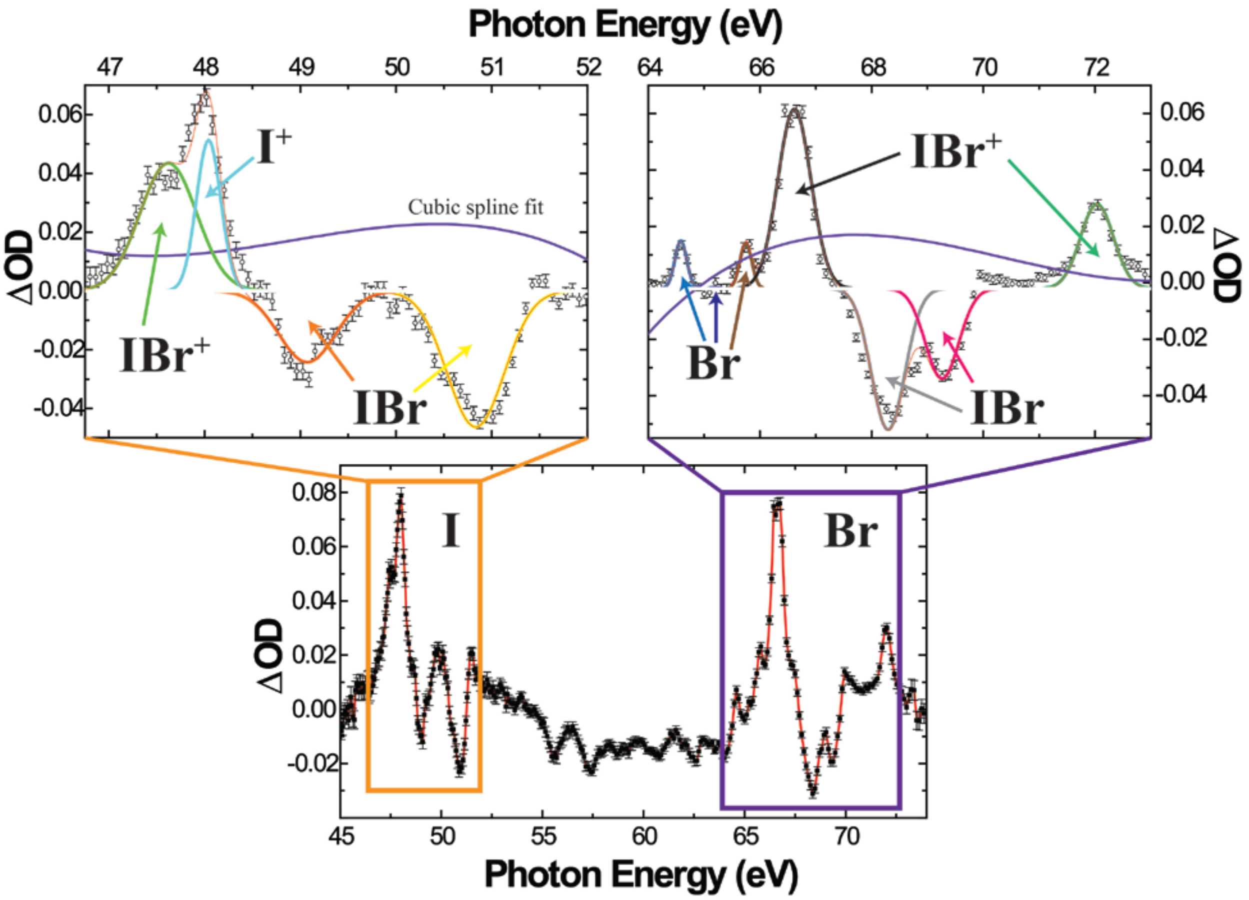

Figure 6.1: XUV transient absorption spectrum for IBr at a pump-probe time delay of 500 fs and a pump field intensity of $4 \text{ x } 10^{14} \, {}^{\text{W}}\!/_{\text{cm}^2}$. (Bottom) Complete transient absorption spectrum from 45-73 eV with the iodine and bromine spectral windows highlighted in orange and purple, respectively. In the region of 52-64 eV a broad depletion is observed due to the shift of the iodine giant resonance of the neutral due to the interaction with the strong-field. (Top Left) Iodine spectral window from 46-52 eV. Formation of IBr$^+$ is observed at 47.6 eV corresponding to the $\pi^{*-1} \longrightarrow 4d^{-1}_{5/2}$ transition, while I$^+$ is observed at 48 eV. The neutral IBr depletions are observed at 49.2 eV $\left(\sigma^{*-1} \longrightarrow 4d^{-1}_{5/2}\right)$ and 50.9 eV $\left(\sigma^{*-1} \longrightarrow 4d^{-1}_{3/2}\right)$. (Top Right) Bromine spectral window from 64-73 eV. Dissociation of atomic bromine is observed at 64.4 eV $\left({}^2P_{3/2} \longrightarrow {}^2D_{5/2}\right)$, 65.1 eV $\left({}^2P_{1/2} \longrightarrow {}^2D_{3/2}\right)$, and 65.4 eV $\left({}^2P_{3/2} \longrightarrow {}^2D_{3/2}\right)$. Formation of IBr$^+$ is observed at 66.7 eV $\left(\pi^{*-1} \longrightarrow 3d^{-1}_{5/2}\right)$ and 72.1 eV $\left(\sigma^{*-1} \longrightarrow 3d^{-1}_{5/2}\right)$. The neutral IBr depletions are observed at 68.3 eV $\left(\sigma^{*-1} \longrightarrow 4d^{-1}_{5/2}\right)$ and 69.4 eV $\left(\sigma^{*-1} \longrightarrow 4d^{-1}_{3/2}\right)$. The baseline of the entire spectrum is fit to a cubic spline function to account for the change in the non-resonant absorption, which is shown in both the iodine and bromine spectral windows. The cubic spline fit is then subtracted from the spectrum so the resonant features could be fit independently of the non-resonant absorption.

Examining the temporal dynamics of IBr after strong-field ionization $\left(2 \text{ x } 10^{14} \, {}^{\text{W}}\!/_{\text{cm}^2}\right)$ presented in false color plots in figure 6.2, it is clear that both the iodine and bromine transitions provide information about the vibrational motion and dissociation timescales of the photoionization. First, the vibrational dynamics are considered. The IBr neutral depletions time traces at 50.9 eV $\left(\text{I}, \sigma^{*-1} \longrightarrow 4d^{-1}_{5/2}\right)$ and 68.3 eV $\left(\text{Br}, \sigma^{*-1} \longrightarrow 3d^{-1}_{5/2}\right)$ are shown in figure 6.3, where the iodine and bromine core-level absorptions are observed to be in phase. Correlated detection of the IBr ${}^1\Sigma_g^+$ ground state vibrational wave packet by absorption at the iodine *4d* and bromine *3d* core-levels is thereby established. From the false color plots, the iodine $\sigma^{*-1} \longrightarrow 4d^{-1}_{3/2}$ as well as the bromine $\sigma^{*-1} \longrightarrow 3d^{-1}_{5/2}$ and $\sigma^{*-1} \longrightarrow 3d^{-1}_{3/2}$ transitions are all observed to appear at the same time delay around 50 fs. The iodine $\sigma^{*-1} \longrightarrow 4d^{-1}_{5/2}$ transition appearance time is not as clear due to the low signal-to-noise of the resonance, possibly due to an overlapping spectral feature. For this experiment, time zero was not accurately established due to the necessity to heat the sample chamber in order to maintain the IBr gas density in the target cell. The thermal expansion of the chamber thereby shifted time zero to positive time relative to the calibrated zero obtained from the strong-field ionization of xenon. Therefore, time zero for pump-probe overlap is interpolated by the appearance time of the IBr neutral depletions. Future measurements will correct for this offset by calibrating the pump-probe overlap via the strong-field ionization of xenon with the chamber at the operational temperature for the IBr experiments.

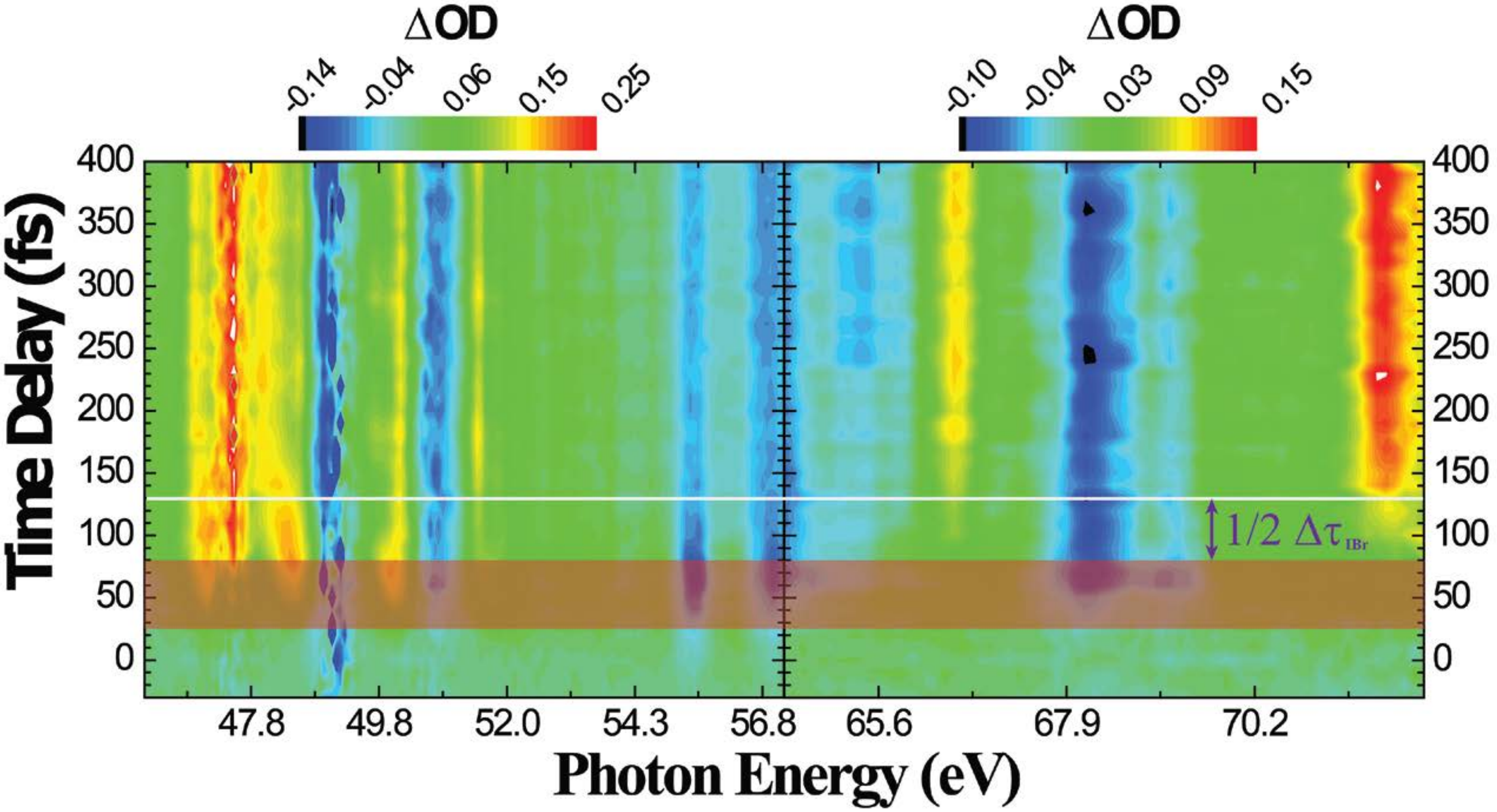

Figure 6.2: False color plots of the temporal dynamics of IBr. The transparent red line represents the ionizing 800 nm pump with a pulse duration of approximately 40 fs. (Left) Iodine spectral window from 46-57 eV with comparable features to figure 6.1. Clear features can be observed for the IBr $^{1}\Sigma_{g}^{+}$ ground state vibrational wave packet which are comparable to those observed for Br_2. (Right) Bromine spectral window from 64-73 eV. The white line shows the delay of the IBr^{+} resonance in the bromine spectral window compared to the iodine absorption.

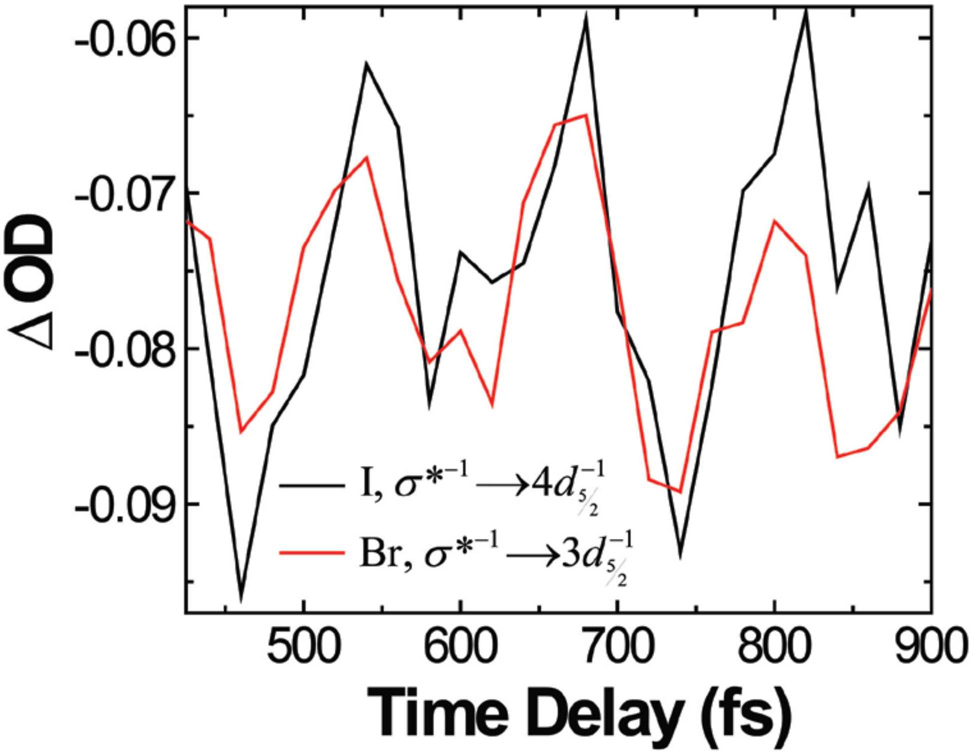

Figure 6.3: Time trace for the I, $\sigma^{*-1}\longrightarrow 4d^{-1}_{5/2}$ (50.9 eV) and Br, $\sigma^{*-1}\longrightarrow 3d^{-1}_{5/2}$ (68.3 eV) transitions, which are observed to be in phase demonstrating the capability of XUV transient absorption to detect correlated vibrational dynamics at two atomic absorbers.

Both the iodine IBr ${}^{1}\Sigma_{g}^{+}$ $\sigma^{*-1}\longrightarrow 4d^{-1}_{5/2}$ (49.2 eV) and $\sigma^{*-1}\longrightarrow 4d^{-1}_{3/2}$ (50.9 eV) transitions are observed to have the same spectral signature of a ground state vibrational wave packet as seen in Br_2. A dominant neutral depletion is observed at the peak of the static absorption feature for the respective spin-orbit states (presented in Appendix A), but unlike bromine, positive features present at both positive and negative energies relative to the neutral depletion. These features are observed in IBr due to the larger spin-orbit separation of iodine (1.7 eV) as well as the increased spectrometer resolution at the observed photon energies.[152] The localization of the ${}^{1}\Sigma_{g}^{+}$ wave packet may therefore be resolved at both the inner and the outer turning point as presented in figure 6.4 for the $\sigma^{*-1}\longrightarrow 4d^{-1}_{5/2}$ transition. A similar signature is expected for the bromine *3d* core-level transitions of IBr, but due to the spectrometer resolution and the spin-orbit splitting of the core-levels, the signature is not resolved.

The phase of the observed vibrational wave packet in IBr is dependent on both the preparation of the superposition as well as the curvature of the core-hole excited state. Previous experiments in Br_2 have shown the $3d^{-1},\sigma^{*}$ core-hole state is repulsive, and it is assumed that the similar $3d^{-1},\sigma^{*}$ and $4d^{-1},\sigma^{*}$ core-hole states are similarly repulsive in IBr. Should the curvature of the core-hole state be attractive in the region of excitation, the actual physical phase of the wave packet would be unaffected, but the experimentally detected phase would change as the XUV transition energy would then increase as the bond length increases, i.e. a π phase shift would be observed in comparison to the current result. For this reason, the qualitative shape of the core-hole excited state is critical. REW-TD-DFT calculations will be conducted in the future to confirm the curvature of the core-hole excited state.

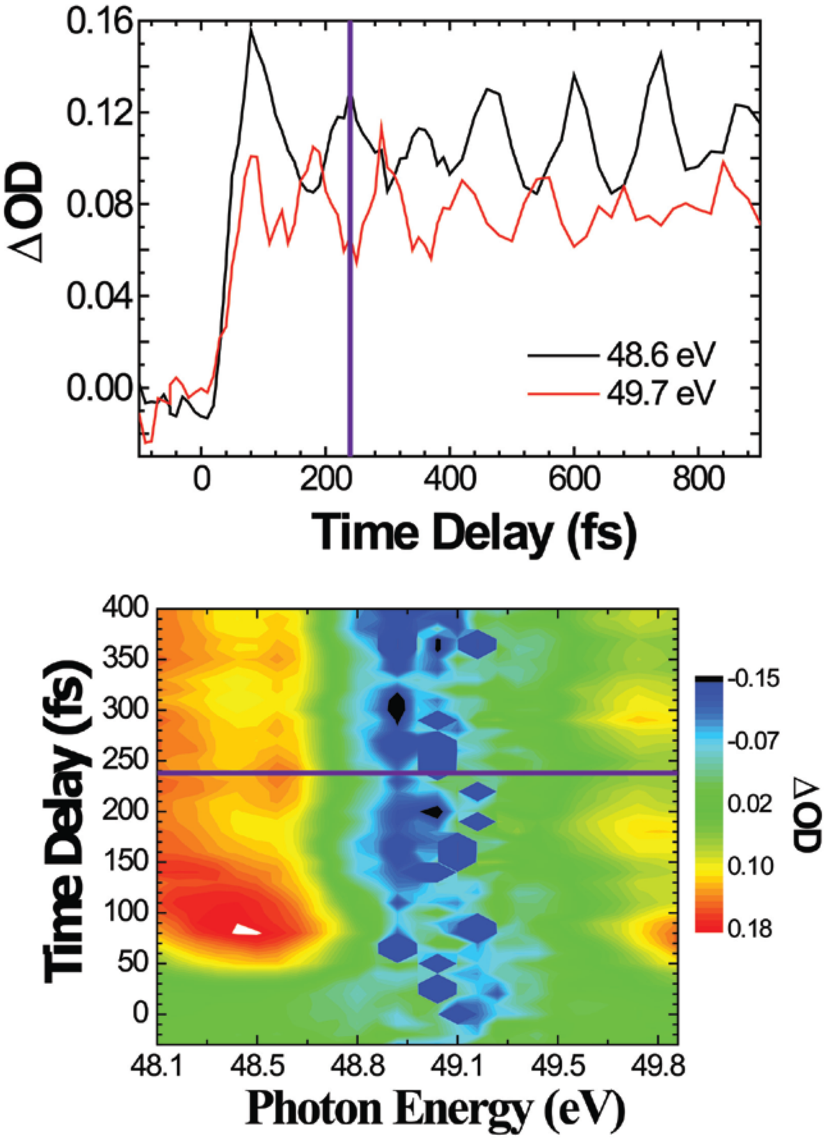

Figure 6.4: Vibrational motion of IBr as observed at the iodine $\sigma^{*-1} \longrightarrow 4d^{-1}_{5/2}$ (50.9 eV) transition. Alternating, out of phase positive features are observed at 48.6 eV and 49.7 eV as clearly observed in the line-out spectra presented on top of the false color plot. These features show the oscillation of the ${}^1\Sigma_g^+$ $\nu_0\nu_1$ vibrational superposition from the inner (49.7 eV) to outer (48.6 eV) turning point. The signal-to-noise of the neutral depletion obscures the vibrational dynamics of the negative ΔOD feature. The shift of the IBr^+ ion transient is observed from 48.5 eV to 48.1 eV around 75 fs, the falling edge of the 800 nm pump pulse.

By fitting the transient absorption signal of the IBr depletions, a vibrational period for the ${}^1\Sigma_g^+$ wave packet is determined to be 126 ± 2 fs and 124 ± 2 fs, fitting the 50.9 eV $\left(\mathrm{I}, \sigma^{*-1} \longrightarrow 4d_{5/2}^{-1}\right)$ and 68.3 eV $\left(\mathrm{Br}, \sigma^{*-1} \longrightarrow 3d_{5/2}^{-1}\right)$ transitions, respectively. This indicates that quantitative resolution of the vibrational motion is capable at both atomic core-levels, both of which match with good agreement to the literature value of 124 fs for a ${}^1\Sigma_g^+$ $\nu_0\nu_1$ vibrational beat.[170] Unfortunately, due to the signal-to-noise of the measurement a vibrational period for IBr^+ is not resolved, but a time delay is measured between the appearances of the IBr^+ signature as observed by the bromine core-level absorption with respect to iodine resonances. The time delay is found to be approximately half of the IBr vibrational period, 62 fs. Moreover, a distinct shift is observed in the IBr^+ iodine core-level absorption during the time delays when the pump and probe are overlapped, indicating that ionization is occurring on the molecular field-dressed potentials as was observed from bromine at high peak laser intensities.

Due to the lower ionization energy of IBr in relation to Br_2, it is expected that field dressing of the nuclear potentials occurs at lower peak intensities. For Br_2, moderate onset of field-dressing of the potential curves occurred at $2 \times 10^{14}\,\mathrm{W/cm^2}$, as evident from the bending of the Br_2^+ ${}^2\Pi_{g,3/2}$ potential curve observed by the change in the $3d_{5/2} \longrightarrow \pi^*$ transition energy. Therefore, observation of strong perturbation of the IBr molecular potentials at the same field intensity is not unexpected. Examining the IBr^+ $\pi^{*-1} \longrightarrow 4d_{5/2}^{-1}$ transition at 47.6 eV, a 0.5 eV shift in transition energy is observed at the trailing edge of the ionizing 800 nm pulse suggesting, as in Br_2, the ${}^2\Pi_{g,3/2}$ potential curve is lowered by the strong-field pulse. Lowering of the ion potential energy surface has the effect of increasing the *4d* core-level transition energy. Furthermore, ionization is determined to occur from the HOMO, which is comprised mainly of the iodine lone pair electrons. The delay in the detection of the IBr^+ formation by the bromine core-level absorption is suspected to relate to the localization of the valence hole from strong-field ionization on the iodine atom which then delocalizes across the molecular bond as the internuclear separation changes. Further experiments will focus on increasing the signal-to-noise of the measurement to confirm the results presented here, while theoretical calculations will focus on elucidating the time-scale for electron delocalization across the molecular bond as well as interpreting the correlated detection of vibrational motion.

6.1.2 Quantum State Distribution in Xe^{2+}

Previous studies by the Leone group demonstrated the capabilities of table-top high harmonic XUV transient absorption spectroscopy by determining the quantum state distribution of strong-field ionized xenon.[20] Probing of the Xe^{+} *4d* core-levels allowed direct interrogation of the *5p* hole for retrieval of the $\left|j,m\right\rangle$ population distribution with femtosecond resolution. Current experiments are pushing to retrieve the $\left|j,m\right\rangle$ state distribution after sequential ionization to Xe^{2+} at a field intensity of $4.6\text{ x }10^{14}\,{}^{\text{W}}\!/\!_{\text{cm}^2}$ to determine whether the m_j states are also aligned as in Xe^{+}.

Figure 6.5 shows the transient absorption spectrum for the strong-field ionization of xenon at a field intensity of $4.6\text{ x }10^{14}\,{}^{\text{W}}\!/\!_{\text{cm}^2}$ with the pump and probe polarizations aligned and orthogonal. The xenon depletions are observed at 65.1 eV $\left(4d_{5/2}\longrightarrow 6p\right)$, 66.4 eV $\left(4d_{5/2}\longrightarrow 7p\right)$, 67.03 eV $\left(4d_{3/2}\longrightarrow 6p\right)$, and 68.3 eV $\left(4d_{3/2}\longrightarrow 7p\right)$, and the Xe^{+} resonances are seen at 55.4 eV $\left(5p_{3/2}^{-1}\left({}^2P_{3/2}\right)\longrightarrow 4d_{5/2}^{-1}\left({}^2D_{5/2}\right)\right)$, 56.1 eV $\left(5p_{1/2}^{-1}\left({}^2P_{1/2}\right)\longrightarrow 4d_{3/2}^{-1}\left({}^2D_{3/2}\right)\right)$, and 57.1 eV $\left(5p_{3/2}^{-1}\left({}^2P_{3/2}\right)\longrightarrow 4d_{3/2}^{-1}\left({}^2D_{3/2}\right)\right)$. The additional transitions between 56 eV and 60 eV in the inset of figure 6.5 correspond to Xe^{2+} transitions. By scanning the polarization angle of the pump relative to the probe, the complete angular dependence of the XUV absorption may be determined as seen in figure 6.6 and also in Appendix B. For the Xe^{+} resonances, a clear angular dependence is observed for the polarization and is best fit by $P_2\left(\cos[\theta]\right)$, while the Xe^{2+} signatures are best fit by $P_4\left(\cos[\theta]\right)$. $P_2\left(\cos[\theta]\right)$ and $P_4\left(\cos[\theta]\right)$ are the second and fourth order Legendre polynomials, respectively. Each Legendre polynomial fit also includes an angular distribution asymmetry parameter constant, which is typically referred to as the beta parameter. Each beta parameter may be utilized to extract the complete $\left|j,m\right\rangle$ state populations. The extension of the number of required asymmetry parameters from Xe^{+} to Xe^{2+} is consistent with an increase of the total angular momentum *J* of the ion. In previous experiments, the ratio of Xe^{+} in the ${}^2P_{3/2}$ to ${}^2P_{1/2}$ states is found to be 5.5 ± 0.6 and 6.5 ± 1.1 depending on the field intensity, while in the current experiment a much smaller ratio is observed as calculated by $\dfrac{I^{\parallel}_{3/2\rightarrow 5/2}}{I^{\parallel}_{1/2\rightarrow 3/2}}$.[20,188] A distinct preference for ionization of ${}^2P_{3/2}$ Xe^{+} to ${}^3P_2$ and ${}^1D_2$ Xe^{2+} is thereby determined from the transient absorption signal.

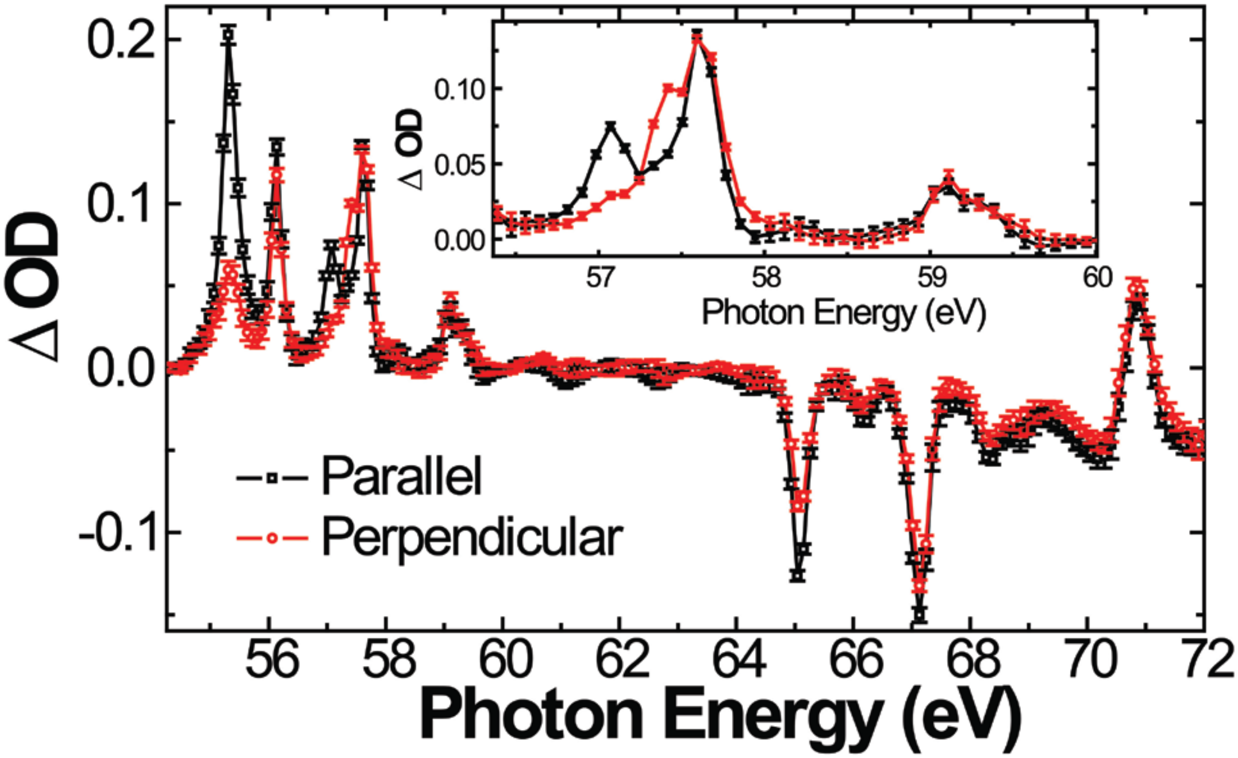

Figure 6.5: XUV transient absorption spectrum of the strong-field ionization of xenon at a field intensity of $4.6 \text{ x } 10^{14}\, {}^{W}\!/_{cm^2}$ and a pump-probe time delay of 500 fs. Xenon depletions are observed at 65.1 eV $\left(4d_{5/2} \longrightarrow 6p\right)$, 66.4 eV $\left(4d_{5/2} \longrightarrow 7p\right)$, 67.03 eV $\left(4d_{3/2} \longrightarrow 6p\right)$, and 68.3 eV $\left(4d_{3/2} \longrightarrow 7p\right)$. The Xe^{+} resonances are seen at 55.4 eV $\left(5p_{3/2}^{-1}\left({}^{2}P_{3/2}\right) \longrightarrow 4d_{5/2}^{-1}\left({}^{2}D_{5/2}\right)\right)$, 56.1 eV $\left(5p_{1/2}^{-1}\left({}^{2}P_{1/2}\right) \longrightarrow 4d_{3/2}^{-1}\left({}^{2}D_{3/2}\right)\right)$, and 57.1 eV $\left(5p_{3/2}^{-1}\left({}^{2}P_{3/2}\right) \longrightarrow 4d_{3/2}^{-1}\left({}^{2}D_{3/2}\right)\right)$. The Xe^{2+} transitions are observed at 57.1 eV $\left({}^{3}P_{2} \longrightarrow {}^{3}D_{3}\right)$, 57.6 eV $\left({}^{1}D_{2} \longrightarrow {}^{1}F_{3}\right)$, and 59.1 eV $\left({}^{3}P_{2} \longrightarrow {}^{3}D_{2}\right)$. The Xe^{2+} transitions are shown more clearly in the inset. The pump-probe configuration where the pump and probe polarizations are aligned parallel and perpendicular are presented in black and red, respectively. The assignment of the Xe^{2+} states is based in Flexible Atomic Code[218] calculations as well as previous spectroscopic measurements.[190]

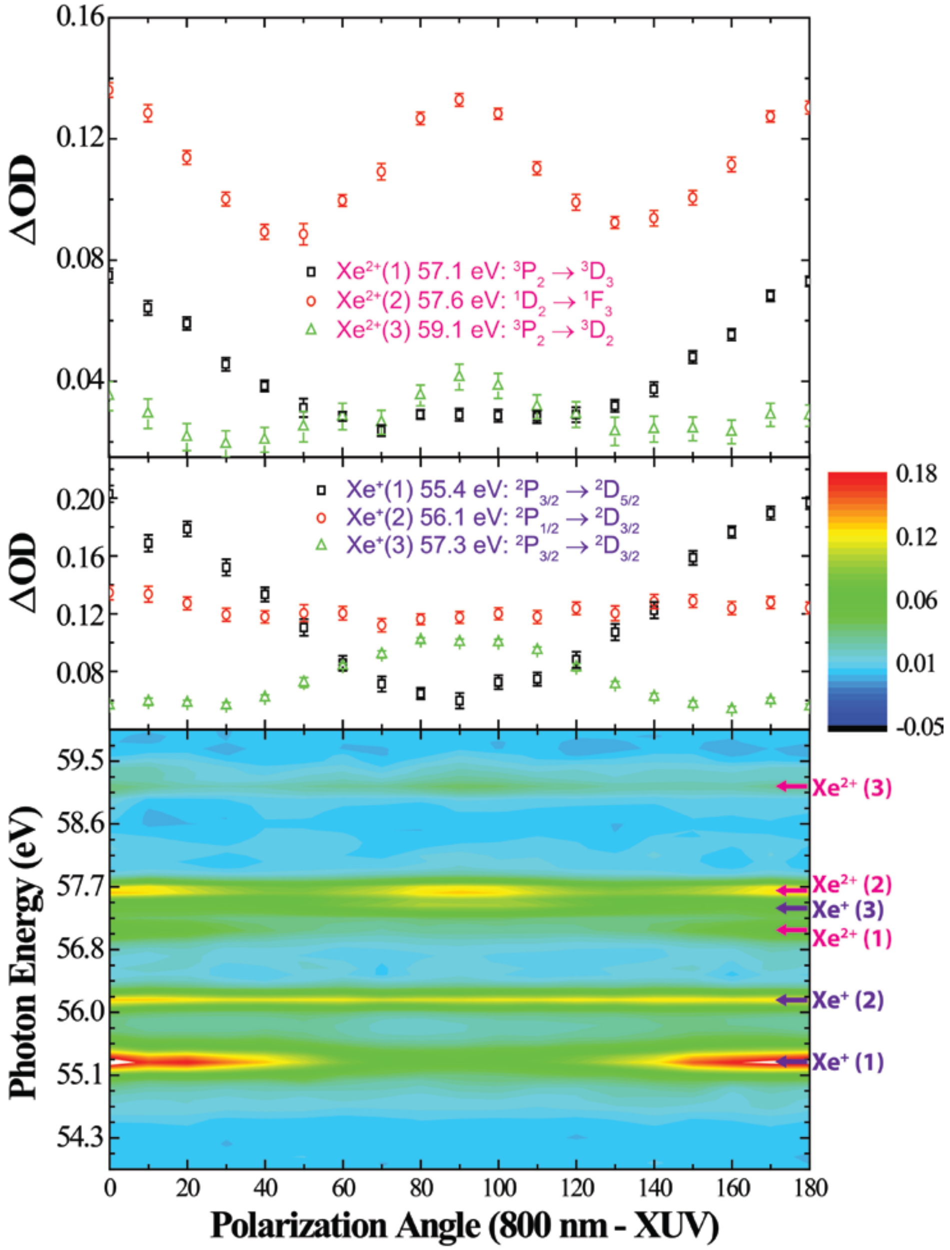

Figure 6.6: Polarization dependent transient absorption of Xe ions following strong-field ionization in 10° increments from 0°→180° at a field intensity of $4.6 \text{ x } 10^{14}\, \mathrm{W}/\mathrm{cm}^2$ and a pump-probe time delay of 500 fs. (Bottom) False color plot of the polarization dependent absorption with the relevant Xe^{+} and Xe^{2+} features labeled in purple and pink, respectively. (Top) Xe^{2+} energy line-out spectra and (Middle) Xe^{+} energy line-out spectra show the polarization angle dependence of the XUV absorption. No polarization dependence is observed for the Xe^{+} $\left(5p_{1/2}^{-1}\left({}^{2}P_{1/2}\right)\longrightarrow 4d_{3/2}^{-1}\left({}^{2}D_{3/2}\right)\right)$ as expected due to the spherical symmetry of the hole density, while the remaining transitions may be described by a $P_2\left(\cos[\theta]\right)$ Legendre polynomial due to the cylindrical symmetry of the holes. The Xe^{2+} transitions are best described by a $P_4\left(\cos[\theta]\right)$ Legendre polynomial.

Current efforts are focused on analyzing the angular dependent measurements to determine the exact $\left|j, m\right\rangle$ state populations for Xe^{2+} following strong-field ionization. Furthermore, future measurements of the Beta parameters as a function of field intensity look to reveal the dependence of the quantum state distribution on the strength of the laser electric field. These experiments look to illuminate the quantum state alignment of doubly charge atoms as a pathway for investigating correlated electron dynamics by attosecond XUV transient absorption spectroscopy.

6.1.3 Alignment of Br_2 Following Strong-Field Ionization

Determination of the complete $\left|j, m\right\rangle$ state distribution of Xe^{2+} lends credence to the capability of XUV transient absorption spectroscopy as an accurate polarization dependent detection technique. In particular, the alignment of non-polar molecules has gained interest recently due to the dependence of ionization on the angle between the polarization of the ionizing laser field and the molecular axis.[60,66,86,219,220] Partial alignment of an ensemble may be accomplished by the interaction of the molecular polarizability with the strong laser field as was outlined in Chapter 1. Alignment of neutral Br_2 is observed at low field intensities, but is lost as the field intensity is increased.

Strong-field ionization of Br_2 at $9 \text{ x } 10^{13}\, {}^{\text{W}}\!/_{\text{cm}^2}$ shows alignment of neutral molecules by probing the $\sigma^{*-1} \longrightarrow 3d^{-1}_{5/2}$ and $\sigma^{*-1} \longrightarrow 3d^{-1}_{3/2}$ core-level transitions. The alignment is induced by the partial ionization of the molecular ensemble at short internuclear separations, which subsequently results in the superposition of the ground state occupied vibrational states. As the polarization of the 800 nm ionizing pump is rotated from 0° relative to the XUV probe to 90°, a change in the XUV absorption is observed in figure 6.7 at 69.5 eV and 67.6 eV at a pump-probe delay of 160 fs and 210 fs, respectively. As the vibrational wave packet moves from the inner to the outer turning point, the polarization dependent absorption is observed relative to the static absorption transition energy at the corresponding positive features as described in Chapter 4. Plotting the XUV transient absorption as a function of polarization angle at 69.5 eV (outer turning point) and 67.6 eV (inner turning point) shows a clear $P_2\left(\cos[\theta]\right)$ shape indicating the neutral Br_2 molecular ensemble is partially aligned with the pump laser field polarization. Finally, as the field intensity is increased to $1.5 \text{ x } 10^{14}\, {}^{\text{W}}\!/_{\text{cm}^2}$, alignment of the neutral molecules with the field is lost. Future experiments and analysis will focus on determining why alignment dependent absorption is observed for the vibrational motion of Br_2 on the ${}^1\Sigma_g^+$ potential curve.

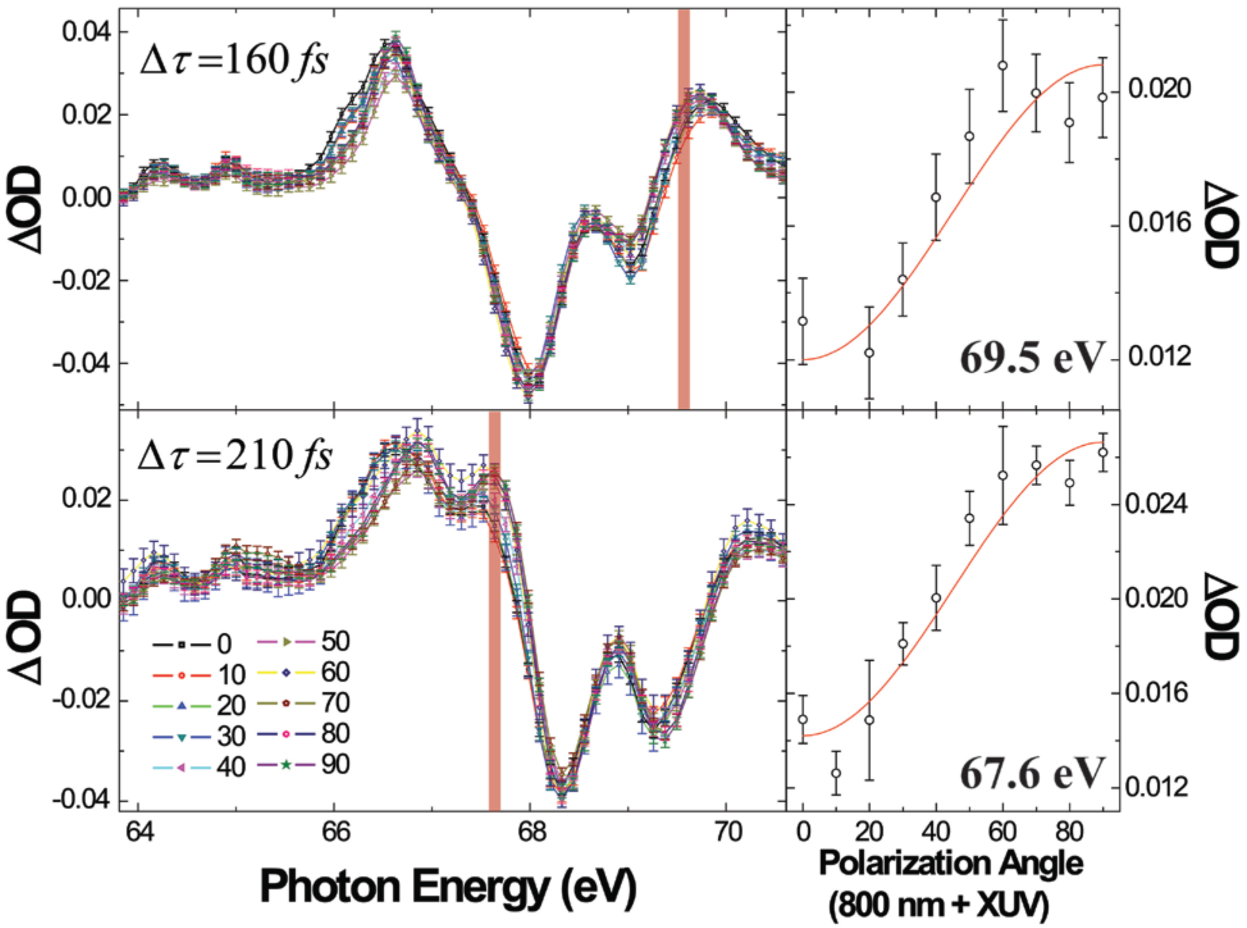

Figure 6.7: Polarization dependent transient absorption of Br_2 following strong-field ionization in 10° increments from 0°→90° at a field intensity of $9 \times 10^{13}\, ^{W}\!/_{cm^2}$ and a pump-probe time delay of 160 fs (Top Left) and 210 fs (Bottom Left) corresponding to localization of the vibrational amplitude on the Br_2 $^1\Sigma_g^+$ potential energy curve on the inner and outer turning points, respectively. Energy line-out spectra are presented for the two pump-probe delays to the right of each transient absorption spectrum. The polarization dependence for the inner (67.6 eV) and outer (69.5 eV) turning points can clearly be described by a $P_2(\cos[\theta])$ Legendre polynomial.

6.2 Conclusions

Strong-field ionization and the subsequent manipulation of molecular electronic and nuclear potentials by an intense laser field of few electron molecules is a complex regime of chemistry based on the strong dependence of the dynamics on the field intensity. Perturbation of the potentials beyond the Born-Oppenheimer curves further adds to the complexity of the dynamics launched within the strong-field pump or probe. Here, the introduction of weak-field XUV probe removes the complication of a strong-field probe, allowing interrogation of any induced dynamics or photofragments of the strong-field pump along the field-free potential curves. Application to the preparation of ground state vibrational wave packets in diatomics has demonstrated the sensitivity of XUV absorption to bond length as well as the composition of the generated superpositions as controlled by the strong-field pump intensity. Through the analysis of strong-field ionization rates and core-hole excitation energies, as well as the upgrading of the apparatus stability, the strong-field vibrational dynamics of Br_2 were explored at an unprecedented level of resolution for table-top femtosecond XUV experiment.

Previous to the studies presented here, the interpretation of XUV transient absorption spectra was difficult owing to the lack of literature on the core-level absorption of radicals and charged species. Calculations of core-level transitions by Restricted Excitation Window time-dependent Density Function Theory (REW-TD-DFT) allows for a relative determination of the XUV excitation energies of the expected transients in a given experiment, greatly reducing the ambiguity in spectral analysis. Furthermore, these calculations provide a novel route for characterizing the core-hole states of molecules and their photofragments, which would otherwise require the use of a synchrotron coupled with mass/charge selection apparatuses. Computational time on the order of hours is required for these calculations as opposed to the experimental time of days at a synchrotron. As the size of the analyte molecule increases moving toward more complex scientific problems, the results of these types of calculations will be invaluable.

A simple theoretical framework for determining the dynamic XUV transient absorption signal with pump-probe time delay beyond the complete photoabsorption formulation was presented for the determination of ground state vibrational wave packet formation and detection. Ammosov-Delone-Krainov (ADK) tunnel ionization calculations provided an accurate interpretation for the depletion mechanism responsible for the superposition of the ground state vibrational levels, while REW-TD-DFT calculations imparted the bond length dependent core-level transition energy for the range of internuclear separations explored by the wave packet. By combining the ADK tunnel ionization and REW-TD-DFT results, an intensity dependent XUV transient absorption spectrum was determined and found to agree with the experimental results.

Initially, the capabilities of the described apparatus were limited by the fluctuations in the high harmonic source as well as the apparatus construction. Being the prototype for femtosecond high harmonic XUV transient absorption spectroscopy, this is understandable. Improvements to the apparatus described here, especially the conversion to a semi-infinite gas cell source, have facilitated the extension of the technique to the detection of vibrational wave packet beats with better than 1.5 cm^{-1} resolution. Experiments on the timescale of several days may now be executed without appreciable deterioration in the apparatus's figures of merit.

Strong-field ionization of Br_2 and the subsequent formation of correlated ground state neutral and ion vibrational wave packets provided a unique opportunity to examine the sensitivity of XUV transient absorption to vibrational motion as well as investigate the field intensity dependence of the superposition preparation. The XUV transition energies from the bromine neutral $\left({}^1\Sigma_g^+\right)$ or ion $\left({}^2\Pi_{g,3/2}\right)$ ground states to the $3d_{5/2}^{-1}$ core-hole excited state are both found to decrease as the molecular internuclear separation increases. Bond-length-specific XUV probing reveals the neutral ground state vibrational wave packet is prepared near the outer turning point primarily composed of the $\nu_0\nu_1$ beat at low field intensities $\left(1\text{ x }10^{14}\text{ W}/\text{cm}^2\right)$ by Lochfraß. As the field intensity is increased, the bond length of preferential ionization of Br_2 is shifted to longer separations. Typical, Lochfraß ionization reduces the overall vibrational energy of the molecular ensemble, but due to the strong-field distortion of the nuclear potentials, the effect of preferential ionization of higher vibrational levels decreases and allows Raman pumping to coherently excite a large manifold of vibrational levels in the ground state. Perturbation of the potentials is evident in the Br_2^+ core-level absorption, showing the bending of the potential curve by approximately 0.5 eV at the peak of the strong-field pump.

Investigation of heteronuclear diatomics has demonstrated the feasibility of correlated XUV probing of multiple single atom absorbers. Strong-field ionization of IBr shows dissociation across multiple potential curves yielding both neutral and ion atomic bromine and iodine. A ground state vibrational wave packet is prepared and observed to oscillate as observed by the iodine *4d* and bromine *3d* core level transitions to the neutral IBr $\sigma*$ molecular orbital with the period of the superposition. Examination of the oscillation looks to further elucidate the sensitivity of XUV core-level absorption to vibrational motion.

Quantum state resolved probing of xenon has been extended to the doubly charged cation utilizing polarization dependent absorption. Alignment of the m_j quantum state distribution is observed for both Xe^+ and Xe^{2+}, and preferential ionization of the Xe^+ ${}^2P_{3/2}$ state is seen for the formation of the double charged species. Further analysis will reveal polarization anisotropy as well as the complete Xe^{2+} $\left|j, m\right\rangle$ quantum state distribution.

Alignment studies in Xe^{2+} have also been extended to molecules, in particular the alignment of Br_2 after strong-field ionization. As with the ionization mechanism and wave packet formation, the degree of alignment is found to be dependent on field intensity, i.e. at low field intensity, $\left(9\text{ x }10^{13}\text{ W}/\text{cm}^2\right)$ indications of alignment are observed, while at high field intensities $\left(1.5\text{ x }10^{14}\text{ W}/\text{cm}^2\right)$ alignment is lost due to the insensitivity of ionization to the angle the intermolecular axis makes with the laser polarization. Analysis of the experimental results looks to quantify the degree of alignment.

6.3 Outlook

Femtosecond XUV transient absorption spectroscopy has laid the foundation for examining electronic and now nuclear coherences in real-time, not only in the strong-field but also in the perturbative regime. Investigations of the strong-field generated vibrational wave packet dynamics in IBr are establishing the necessary understanding for extending the same measurement to the attosecond regime to investigate correlated nuclear and electronic coherences simultaneously, in real-time. Studies of coupled nuclear and electronic dynamics is not solely limited to diatomics, but may be easily extended to polyatomic halogen containing molecules as well transition metal complexes with the current high harmonic source capabilities.

An open ended question remains unanswered with respect to ground state vibrational wave packet preparation: What is the exact mechanism for formation of the vibrational coherence with respect to the contributions of impulsive stimulated Raman scattering, Lochfraß, R-critical ionization, and bond-softening? Several experiments have examined all of these mechanisms, and it is logical that all of the processes are occurring simultaneously in the strong-field regime. One mechanism, or at least mechanism establishing the same phase between the states of the superposition, must dominate for the preparation of a vibrational coherence with a measurable phase between states. Otherwise, the result would be an incoherent mixture of phases based on the contribution of opposing mechanisms. Previously, the contribution of opposing mechanisms has been established by the difference between the calculated phases based on the preferential depletion of the vibrational amplitude at an extreme of the molecular potential,[136] but in the present experiments it is seen that the phase of the coherence is dictated primarily by the exact internuclear separation of the ionization in terms of the potential energy curves of the ground and ion states. The increasing contribution of a Raman mechanism has been observed for the various field intensity measurements of Br_2, and building off the success of that experiment, future investigations look to quantify the contribution of each of the wave packet preparation mechanisms as a function of increasing field intensity, temperature, and ionization energy. Within this three-fold parameter space, each mechanism is affected in a different manner as seen in Table 6.1, which may be exploited to determine the contribution of each.

Table 6.1: Parameters for Determining Mechanism Contribution for Wave Packet Preparation

Mechanism	Field intensity	Temperature	Ionization Energy
Raman	Peak at particular intensity	Decrease	No Change
Bond-Softening	Increase	Decrease	No Change
Lochfraß (Field-Free)	Decrease	Increase	Increase
R-Critical	Increase	Increase	Decrease

XUV probing of transition metal oxide films has also been demonstrated very recently in the Leone lab. The prospect of investigating electronic and nuclear dynamics in materials involving metal active sites is very promising, facilitating an avenue of investigation into site specific oxidation state sensitivity. For example, the investigation of vibrational dynamics near the metal active site of dye-sensitized solar cells may lend to further physical understanding of the charge transfer dynamics required to increase the efficiency of such devices. Furthermore, extension of the established absorption techniques to investigating hole migration in heterostructure nanomaterials is likewise straightforward.

An unrecognized potential of femtosecond transient absorption is the characterization of core-level absorptions of exotic fragments and charged states of molecules produced by strong-field ionization and dissociation. By virtue of the disruptive nature of the strong-field pulse, a myriad of photofragments in various quantum and charge states are produced at high field intensities $\left(>10^{14}\,{}^{\mathrm{W}}\!/_{\mathrm{cm}^2}\right)$, and the broadband nature of the XUV probe allow detection of each species simultaneously. The experimental apparatus employed here has, by comparison to synchrotron sources, incredibly poor spectral resolution, but recently within the Leone lab, a spectral resolution of approximately 10 meV has been demonstrated. Given the proper instrumental configuration and sample source, a robust XUV transient absorption apparatus for investigating radicals and their dynamics with high spectral and temporal resolution could be envisioned.

Over the past decade, XUV transient absorption has brought some of the capabilities of national user facility synchrotrons to table-top experiments with the use of high harmonic sources. The range of experimental paths offered by such a platform is truly staggering. To-date, experiments have primarily been demonstrated in the gas phase with femtosecond resolution, but moving forward, the applications to condensed phase dynamics at faster timescales are becoming more apparent and feasible with the development of the technique. High harmonic generation sources have traditionally been heralded as a means to access experiments beyond the restrictions of large user facilities. With the recent advances in both source and experimental techniques, the field of table-top XUV spectroscopy stands poised to tackle these pinnacle experiments in the not-so-distant future.

Appendix

Here, additional measurements not discussed in the previous chapters relating to ongoing experiments as well as the computational calculations for strong-field ionization, vibrational wave packet formation, and wave packet propagation are presented.

A. IBr Static Absorption

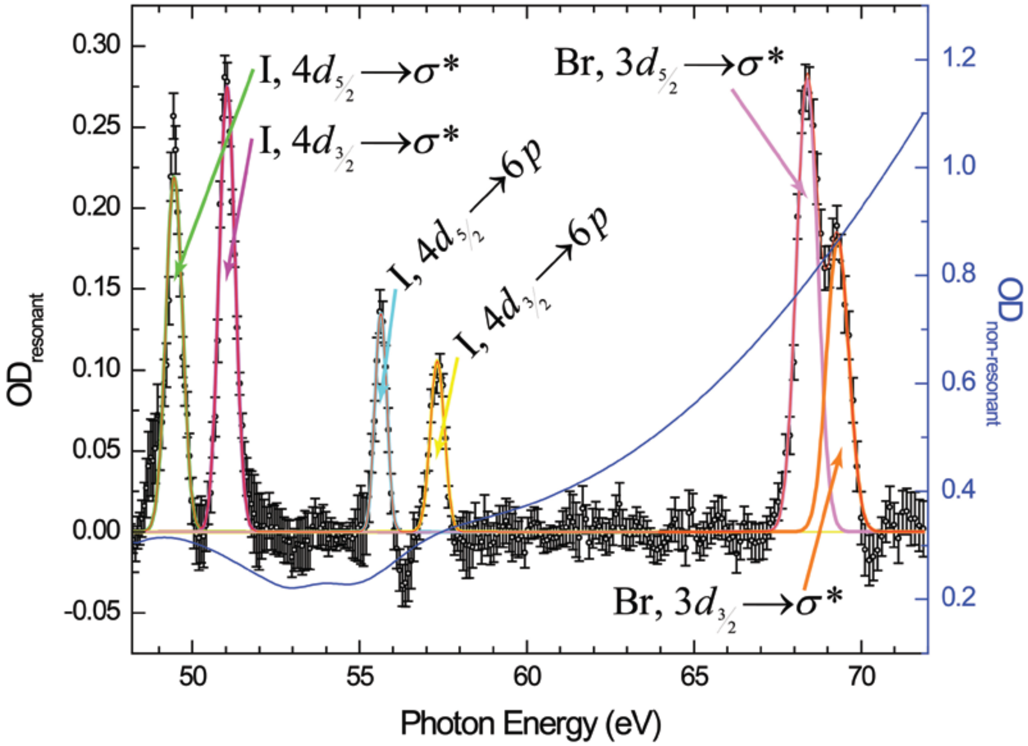

Figure A.1: Static XUV absorption spectrum for IBr. The IBr molecular transitions for absorption of the iodine *4d* electrons are observed at 49.5 eV $\left(\text{I, }4d_{5/2}\longrightarrow\sigma^*\right)$, 51.1 eV $\left(\text{I, }4d_{3/2}\longrightarrow\sigma^*\right)$, 55.6 eV $\left(\text{I, }4d_{5/2}\longrightarrow 6p\right)$, and 57.3 eV $\left(\text{I, }4d_{3/2}\longrightarrow 6p\right)$, while the IBr bromine transition are seen at 68.4 eV $\left(\text{Br, }3d_{5/2}\longrightarrow\sigma^*\right)$ and 69.3 eV $\left(\text{Br, }3d_{3/2}\longrightarrow\sigma^*\right)$. The dark blue line represents a cubic spline fit to the non-resonant absorption of IBr.

B. Xe^{2+} Beta Parameter Fits

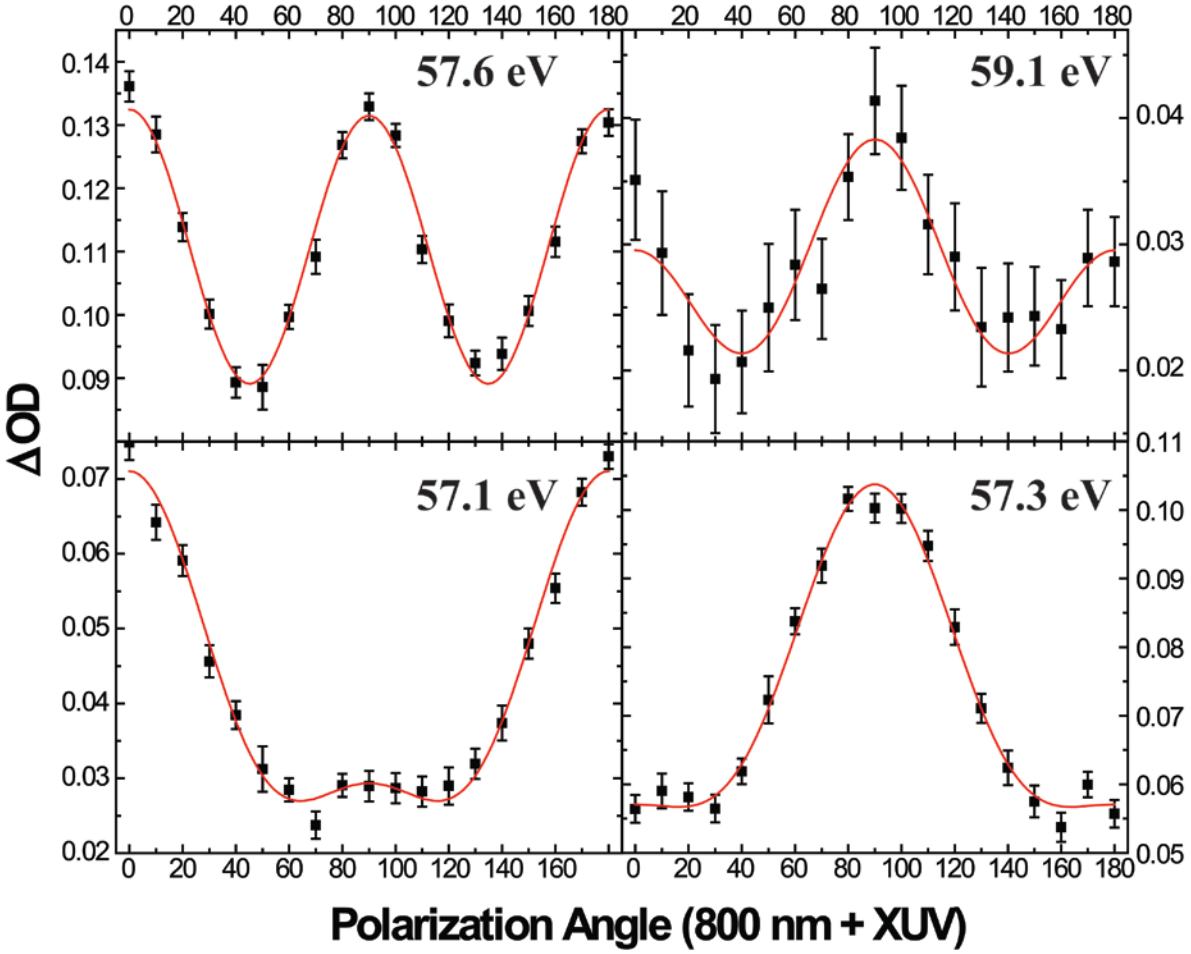

Figure B.1: Asymmetry parameter fits to the Xe^{2+} transient absorption signal at various transition energies corresponding to the different created Xe^{2+} spin-orbit states, expect the bottom right plot which is the $P_2(\cos[\theta])$ parameter fit of the Xe^{+} ${}^2P_{3/2} \longrightarrow {}^2D_{3/2}$ transition. (Top Left) XUV polarization dependent fit of the Xe^{2+} ${}^1D_2 \longrightarrow {}^1F_3$ transition showing strong $P_4(\cos[\theta])$ character. (Bottom Left) XUV polarization dependent fit of the Xe^{2+} ${}^3P_2 \longrightarrow {}^3D_3$ transition showing weak $P_4(\cos[\theta])$ character. (Top Right) XUV polarization dependent fit of the Xe^{2+} ${}^3P_2 \longrightarrow {}^3D_2$ transition showing strong $P_4(\cos[\theta])$ character. (Bottom Right) XUV polarization dependent fit of the Xe^{+} ${}^2P_{3/2} \longrightarrow {}^2D_{3/2}$ transition showing strong $P_2(\cos[\theta])$ character, but also some slight β_4 as observed by the delayed onset of the increase in XUV absorption as the polarization angle is tuned from 0° to 40° and 180° to 140°.

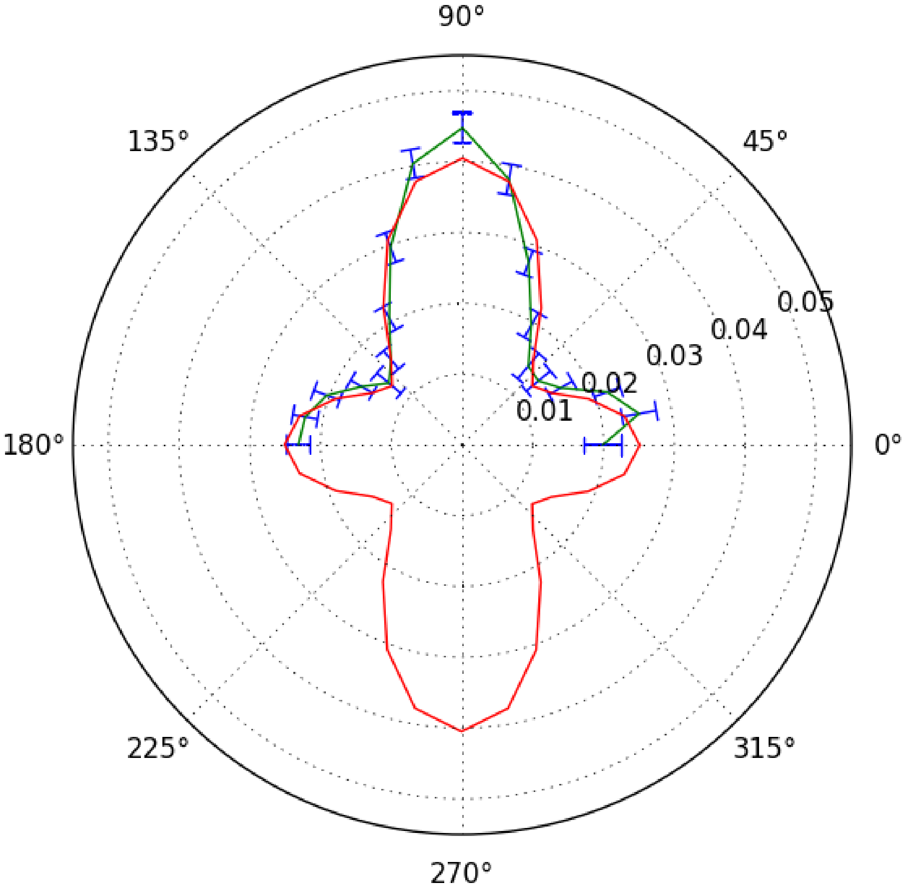

Figure B.2: Polar coordinate plot of the XUV transient absorption signal (blue data points with one standard error of the mean) versus the simulated m_j state distribution from strong-field ionization calculations (red) for the Xe^{2+} $^1D_2 \longrightarrow {}^1F_3$ transition at 57.6 eV. The ΔOD increases radially from the center.

C. ALS Photoabsorption Measurements

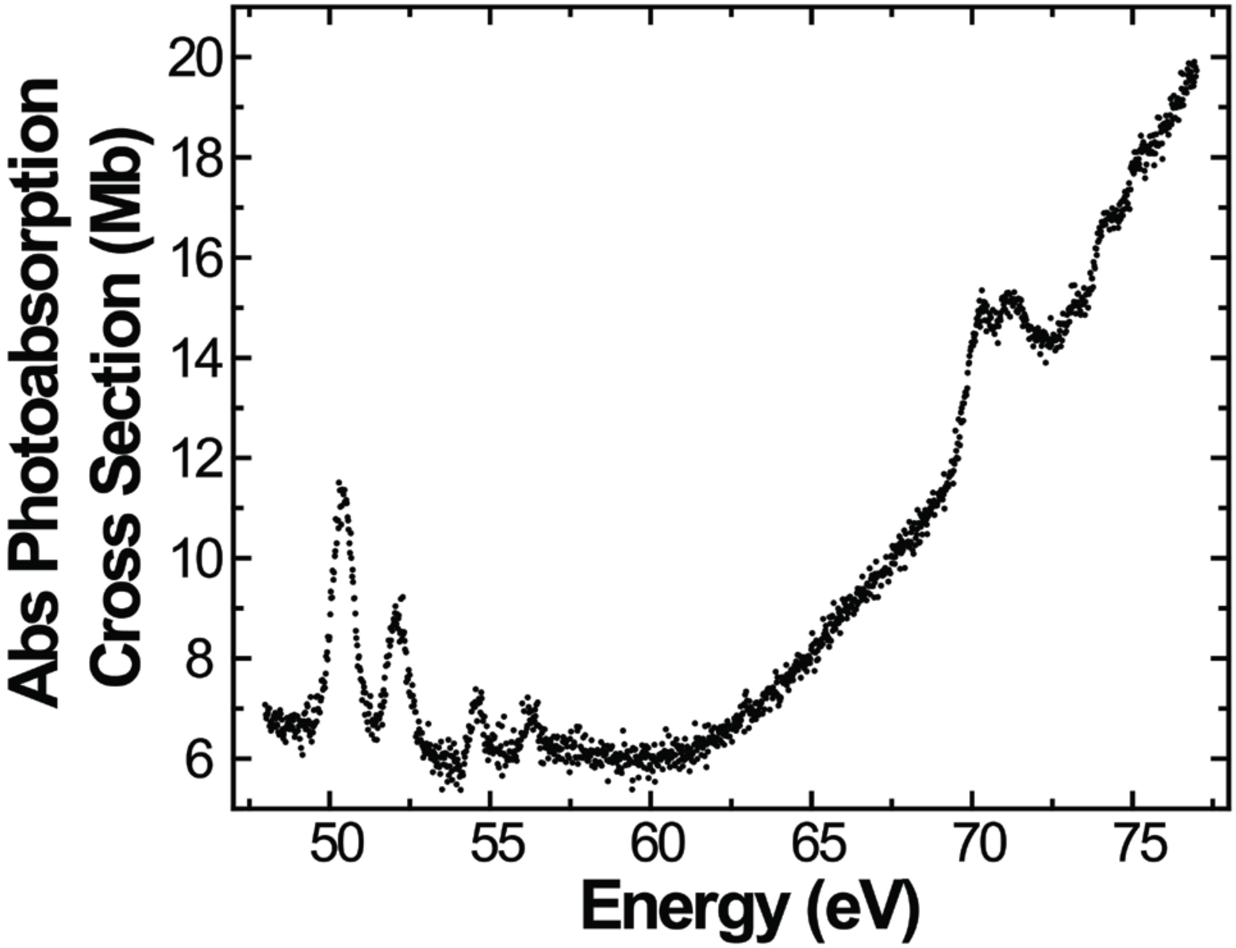

Figure C.1: Absolute photoabsorption cross section measurement of bromoiodomethane as measured at the Advance Light Source Beamline 10.0.1 utilizing a double ion chamber designed by J.A.R. Samson.[221] Ionization is accomplished by photoabsorption of extreme ultraviolet light produced by synchrotron radiation. The iodine core level transitions are observed between 49 eV to 57 eV, while the bromine core level transitions are observed from 69 eV to 76 eV.[222]

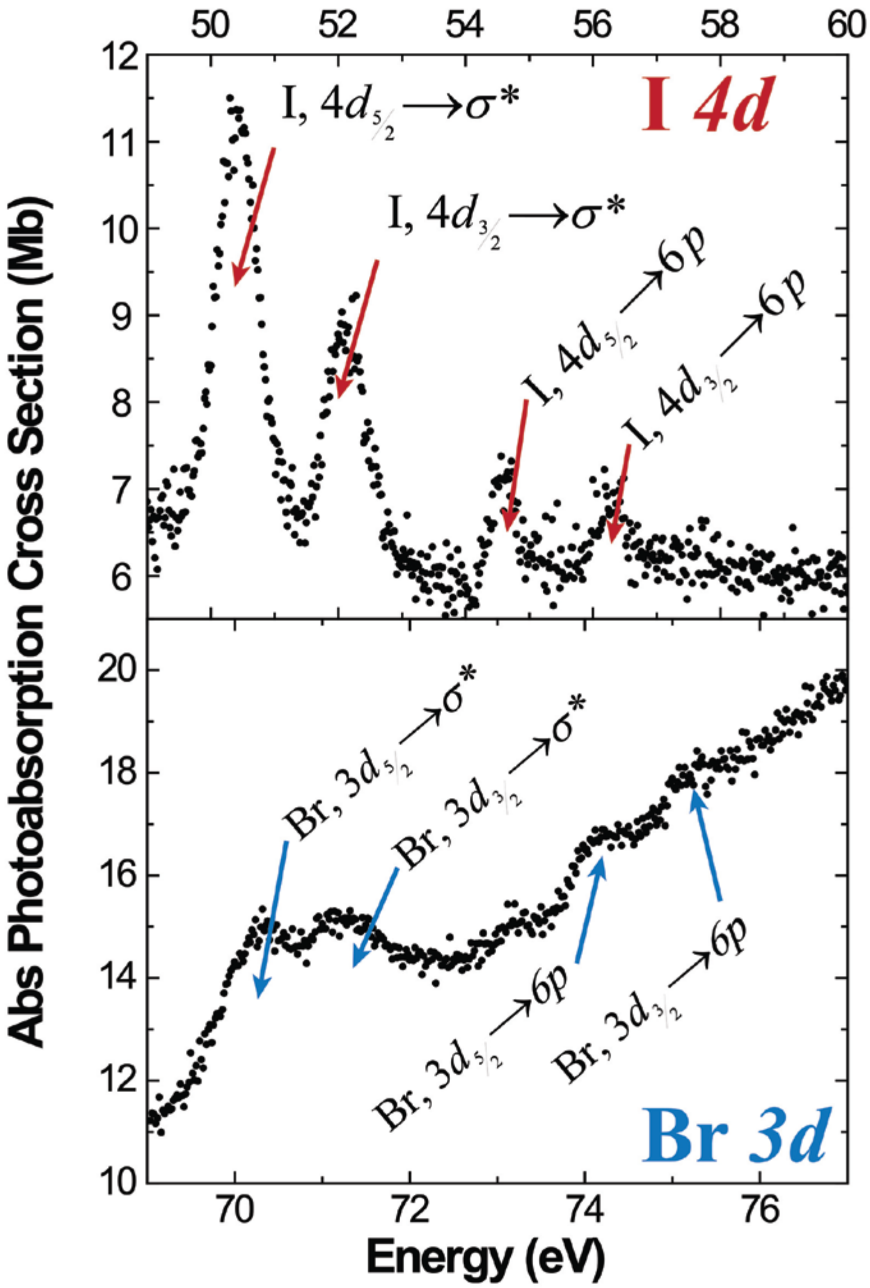

Figure C.2: Absolute photoabsorption cross section for bromoiodomethane measured by a double ionization chamber in the iodine and bromine core-level transition windows. (Top) Iodine *4d* core-level transitions at 50.4 eV $\left(4d_{5/2} \longrightarrow \sigma^*\right)$, 52.1 eV $\left(4d_{3/2} \longrightarrow \sigma^*\right)$, 54.6 eV $\left(4d_{5/2} \longrightarrow 6p\right)$, and 56.3 eV $\left(4d_{3/2} \longrightarrow 6p\right)$ as marked by the maroon arrows. (Bottom) Bromine 3*d* core-level transitions at 70.3 eV $\left(3d_{5/2} \longrightarrow \sigma^*\right)$, 71.2 eV $\left(3d_{3/2} \longrightarrow \sigma^*\right)$, 74.1 eV $\left(3d_{5/2} \longrightarrow 6p\right)$, and 75.1 eV $\left(3d_{3/2} \longrightarrow 6p\right)$ as marked by the red arrows.[221,222] The total photoabsorption measurements will be utilized in the study of the strong-field ionization of bromoiodomethane.

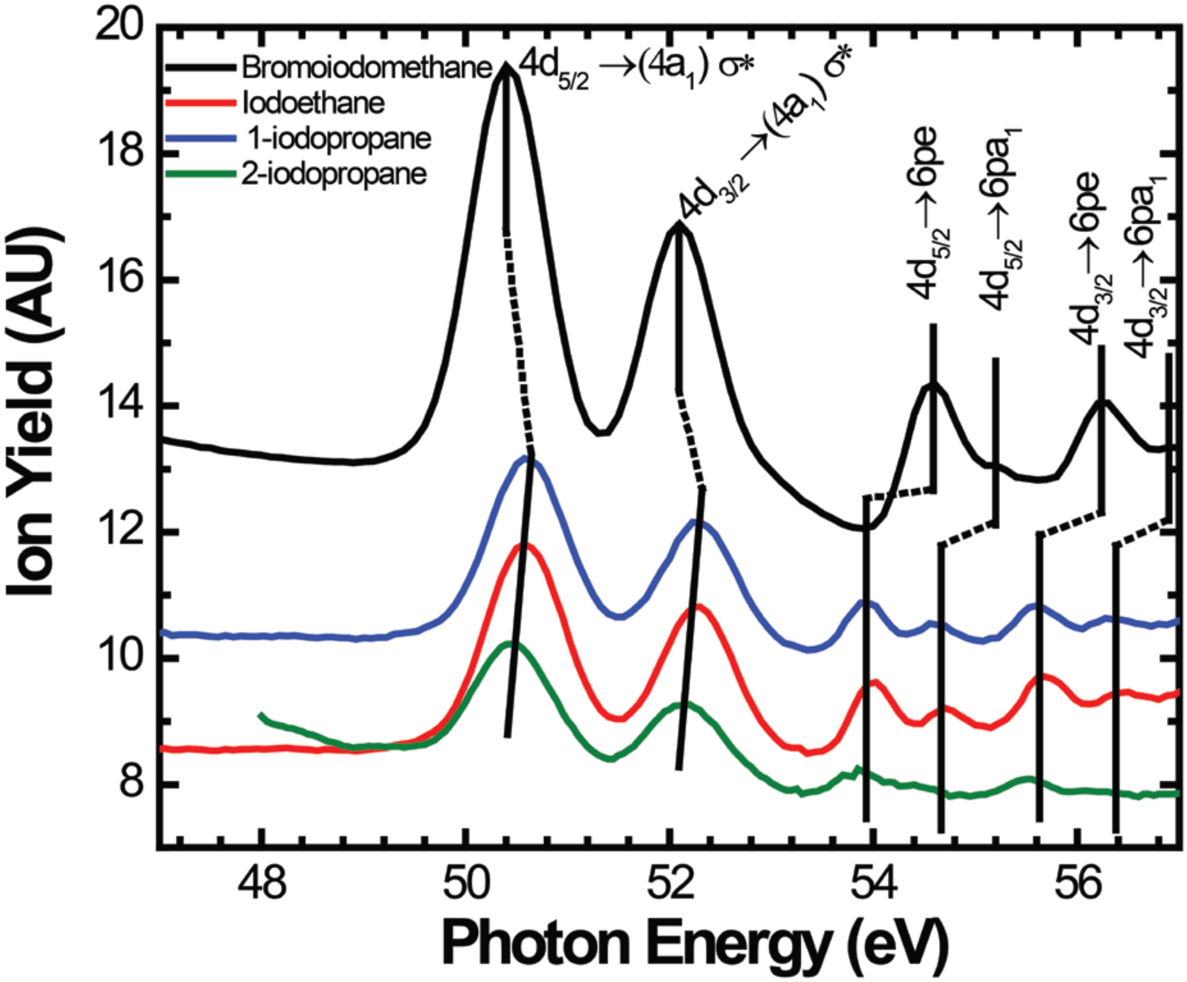

Figure C.3: Total ion yield measured in an ionization chamber at Beamline 10.0.1 for the extreme ultraviolet photoionization of bromoiodomethane, iodoethane, 1-iodopropane, and 2-iodopropane as measured around the iodine *4d* resonance absorptions. These photoabsorption measurements will be utilized in assigning the spectral features of the strong-field ionization of these molecules.

D. ALS HBr$^+$ Photoabsorption Measurement

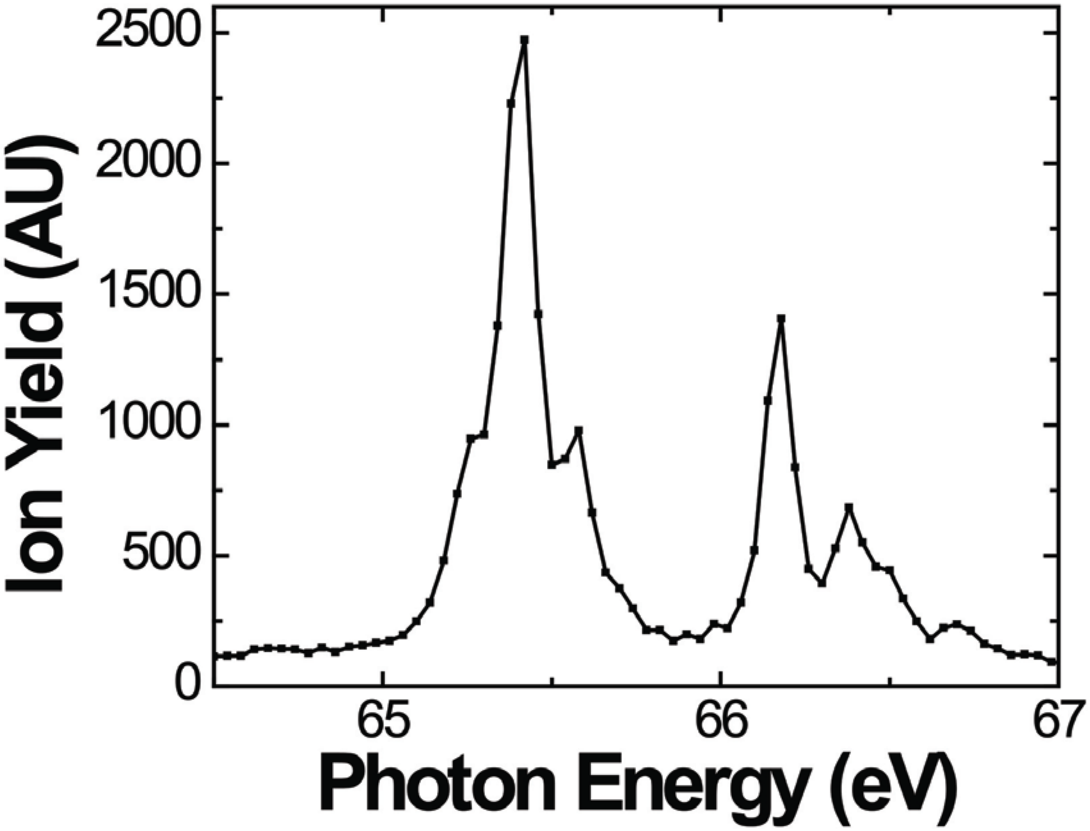

Figure D.1: Photoabsorption measurement of the *3d* core-levels of ion selected HBr$^+$ at the High-Resolution Atomic and Molecular Optical Ion-Photon Beamline at the Advanced Light Source Beamline 10.0.1. The assignment of these features will be completed utilizing concurrent measurements of bromine atomic ions and will be utilized in future experiments of the strong-field ionization of methyl halides containing bromine.

E. Mathematica Code

Here, we present the necessary Mathematica Code to calculate the XUV transient absorption signal for R_ν-ADK created vibrational wave packets. First, the ADK tunneling rates are calculated at the relevant R and vibrational states. Then the neutral vibrational amplitude is determined after ionization and the XUV transient absorption signal is determined. Finally, the created ground state vibrational wave packet is propagated according to the superimposed states and the evolving XUV transient absorption signal is determined at all times assuming a delta probe pulse.

E.1. ADK Calculations

Peak Field Intensity Calculation:

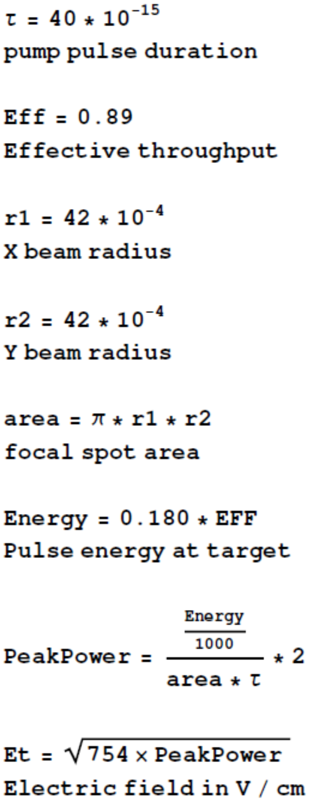

```
τ = 40 * 10^-15
pump pulse duration

Eff = 0.89
Effective throughput

r1 = 42 * 10^-4
X beam radius

r2 = 42 * 10^-4
Y beam radius

area = π * r1 * r2
focal spot area

Energy = 0.180 * EFF
Pulse energy at target

PeakPower = (Energy/1000)/(area * τ) * 2

Et = √(754 × PeakPower)
Electric field in V / cm
```

Calculation of ADK Tunneling probability with bond length and Vibrational Level:

Et is the electric field in V / cm, Ea is the atomic unit of electric field in V / cm,
n is the effective quantum number, v is the vibrational level,
W is the tunnel ionization rate using the expression in the paper by S. L. Chin & friends [J. Opt. Soc. Am. B **8**, 858 (1991)].

```
Clear[r, Ei, v, t, m, f, Et, Ea, l, Z, W]
Default[π]
```

$$\text{Intensity} := 1\times 10^{13}\ \text{Exp}\left[-\frac{4\ \text{Log}[2]\ t^{2}}{40^{2}}\right]$$

$$\text{Et} = \sqrt{754\times\text{Intensity}}$$

$$\text{Ei} := \left(3.26 * \left(\left(1 - e^{(-1.50155)*((r-2.18))}\right)\text{^}2\right) + 10.52 - (v\,/\,8065)\right)\Big/\,27.211$$

$$Z := 1$$

$$n := \frac{1}{\sqrt{2\ \text{Ei}}}$$

$$l := 1$$

$$m := 0$$

$$f := \frac{(2\ l + 1)\ (l + \text{Abs}[m])\,!}{2^{\text{Abs}[m]}\ (\text{Abs}[m])\,!\ (l - \text{Abs}[m])\,!}$$

$$\text{Ea} := 5.142\times 10^{9}$$

$$W = 41.34\times f\times\left(\frac{2\,e}{n}\right)^{2n}\frac{1}{2\,\pi\,n}\ \text{Ei}\ \sqrt{\frac{3\ \text{Et}\,/\,\text{Ea}}{\pi\ (2\ \text{Ei})^{3/2}}}\ \left(\frac{2\ \text{Ea}}{\text{Et}}\ (2\ \text{Ei})^{3/2}\right)^{2n-\text{Abs}[m]-1}\ \text{Exp}\left[-\frac{2\ \text{Ea}}{3\ \text{Et}}\ (2\ \text{Ei})^{3/2}\right]$$

E.2. R_v-ADK Calculations

Boltzmann Distribution:

$T = 298$

Temperature

$k_b = 1.380648 * 10^{-23}$

Boltzmann Constant

$\omega_e = 323 * 2.998 * 10^{10} * 6.626 * 10^{-34}$

Fundamental Vibrational Frequency

$\chi_e = 1 * 2.998 * 10^{10} * 6.626 * 10^{-34}$

Anharmonicity

$x = \{0, 1, 2, 3, 4, 5, 6, 7\}$

Vibrational Level

$$\frac{e^{\frac{-\left(\omega_e\,(x+0.5)-\omega_e\,\chi_e\,(x+0.5)^2\right)}{k_b\,T}}}{\sum_{x=0}^{10} e^{\frac{-\left(\omega_e\,(x+0.5)-\omega_e\,\chi_e\,(x+0.5)^2\right)}{k_b\,T}}}$$

Boltzmann Distribution

Calculation of ADK Vibrational Wave Packet and Propagation:

$r = \left(\left((-3.6195 * M) + \left(0.02582 * M^2\right) + 128.81403\right) * 10^{-10}\right)$

Conversion from R to transition energy as fit from REW - TD - DFT calculations

$x = 1$

Adjustement to field intensity (typically 1)

$b_0 = -34.80304$

$a_{01} = 44.56394 * 1 * 10^{10}$

$a_{02} = -18.82413 * 1 * 10^{20}$

$a_{03} = 2.62995 * 1 * 10^{30}$

$w_0 = b_0 + a_{01} * (r) + a_{02} * (r)^2 + a_{03} * (r)^3$

$b_1 = -37.49335$

$a_{11} = 48.00247 * 1 * 10^{10}$

$a_{12} = -20.27295 * 1 * 10^{20}$

$a_{13} = 2.83178 * 1 * 10^{30}$

$w_1 = b_1 + a_{11} * r + a_{12} * r^2 + a_{13} * r^3$

$b_2 = -40.32426$

$a_{21} = 51.61954 * 1 * 10^{10}$

$a_{22} = -21.79635 * 1 * 10^{20}$

$a_{23} = 3.04389 * 1 * 10^{30}$

$w_2 = b_2 + a_{21} * r + a_{22} * r^2 + a_{23} * r^3$

$b_3 = -43.29362$

$a_{31} = 55.4122 * 1 * 10^{10}$

$a_{32} = -23.39293 * 1 * 10^{20}$

$a_{33} = 3.26607 * 1 * 10^{30}$

$w_3 = b_3 + a_{31} * r + a_{32} * r^2 + a_{33} * r^3$

$b_4 = -46.3976$

$a_{41} = 59.37527 * 1 * 10^{10}$

$a_{42} = -25.06036 * 1 * 10^{20}$

$a_{43} = 3.49796 * 1 * 10^{30}$

$w_4 = b_4 + a_{41} * r + a_{42} * r^2 + a_{43} * r^3$

$b_5 = -49.63041$

$a_{51} = 63.50106 * 1 * 10^{10}$

$a_{52} = -26.79523 * 1 * 10^{20}$

$a_{53} = 3.73906 * 1 * 10^{30}$

$w_5 = b_5 + a_{51} * r + a_{52} * r^2 + a_{53} * r^3$

$b_6 = -52.98411$

$a_{61} = 67.77909 * 1 * 10^{10}$

$a_{62} = -28.59293 * 1 * 10^{20}$

$a_{63} = 3.9887 * 1 * 10^{30}$

$w_6 = b_6 + a_{61} * r + a_{62} * r^2 + a_{63} * r^3$

$b_7 = -56.44836$

$a_{71} = 72.19576 * 1 * 10^{10}$

$a_{72} = -30.44752 * 1 * 10^{20}$

$a_{73} = 4.24602 * 1 * 10^{30}$

$w_7 = b_7 + a_{71} * r + a_{72} * r^2 + a_{73} * r^3$

a and b are the fit parameters for the ADK tunneling rate
w_n is the tunneling rate for each vibrational state n

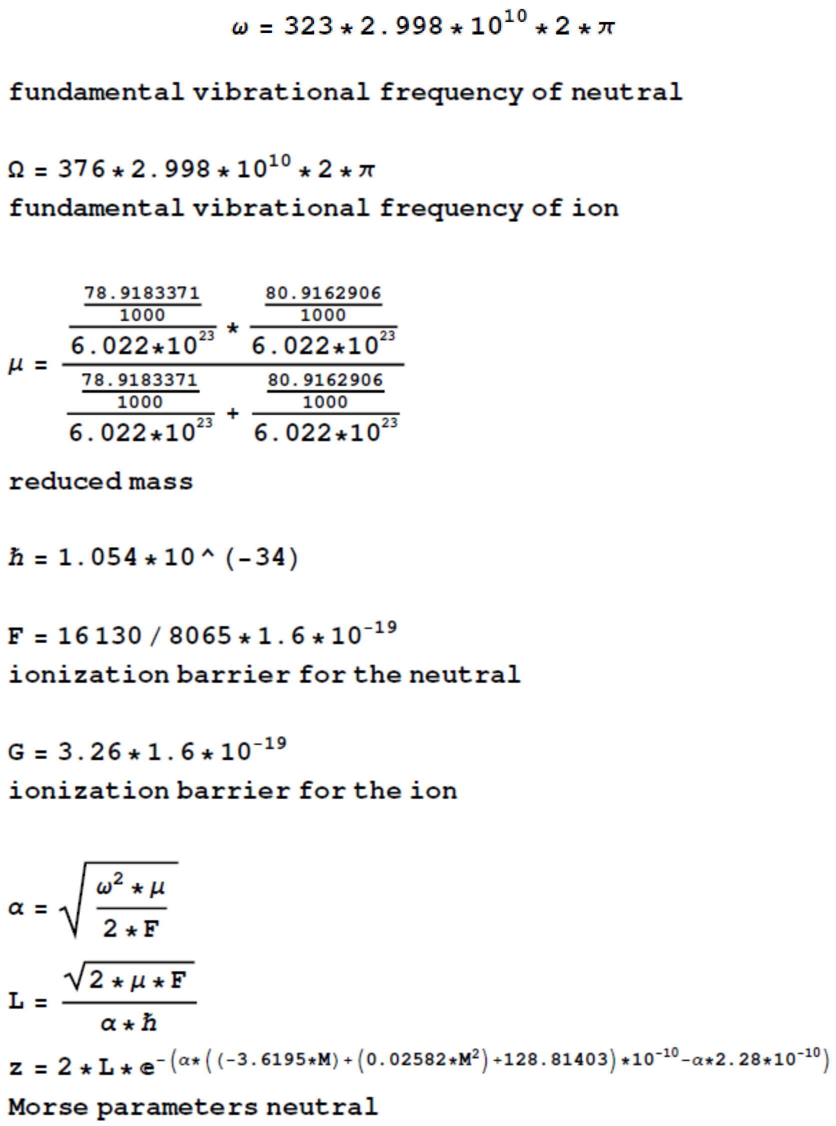

$$\omega = 323 * 2.998 * 10^{10} * 2 * \pi$$

fundamental vibrational frequency of neutral

$$\Omega = 376 * 2.998 * 10^{10} * 2 * \pi$$

fundamental vibrational frequency of ion

$$\mu = \frac{\frac{\frac{78.9183371}{1000}}{6.022*10^{23}} * \frac{\frac{80.9162906}{1000}}{6.022*10^{23}}}{\frac{\frac{78.9183371}{1000}}{6.022*10^{23}} + \frac{\frac{80.9162906}{1000}}{6.022*10^{23}}}$$

reduced mass

$$\hbar = 1.054 * 10\wedge(-34)$$

$$F = 16130 / 8065 * 1.6 * 10^{-19}$$

ionization barrier for the neutral

$$G = 3.26 * 1.6 * 10^{-19}$$

ionization barrier for the ion

$$\alpha = \sqrt{\frac{\omega^2 * \mu}{2 * F}}$$

$$L = \frac{\sqrt{2 * \mu * F}}{\alpha * \hbar}$$

$$z = 2 * L * e^{-\left(\alpha * \left(\left(-3.6195 * M\right) + \left(0.02582 * M^2\right) + 128.81403\right) * 10^{-10} - \alpha * 2.28 * 10^{-10}\right)}$$

Morse parameters neutral

$$\beta = \sqrt{\frac{\Omega^2 * \mu}{2 * G}}$$

$$l = \frac{\sqrt{2 * \mu * G}}{\beta * \hbar}$$

$$Z = 2 * l * e^{-\left(\beta * \left((-3.6195 * M) + \left(0.02582 * M^2\right) + 128.81403\right) * 10^{-10} - \beta * 2.18 * 10^{-10}\right)}$$

Morse parameters ion

$$B = \left(0.22918 * \left((-3.6195 * M) + \left(0.02582 * M^2\right) + 128.81403\right)\right) + \left(-0.04549 * \left((-3.6195 * M) + \left(0.02582 * M^2\right) + 128.81403\right)^2\right) - 0.20719$$

Oscillator strength from REW - TD - DFT

$c_0 = 0.78976$

$c_1 = 0.166039$

$c_2 = 0.0349082$

$c_3 = 0.00733911$

$c_4 = 0.00154298$

$c_5 = 0.000324396$

$c_6 = 0.0000682013$

$c_7 = 0.0000143387$

Boltzmann distribution

$$h = \frac{1}{3.5 * 10^{5} \sqrt{\sum_{n=0}^{7} (c_n)^2}}$$

Normalization constant

$$J_0 =$$

$$\left(16130 - \left(\left((L - 0 - 0.5)^2\right) * \frac{\frac{\alpha^2 * \hbar^2}{2*\mu}}{1.6 * 10^{-19}} * 8065\right)\right) * 2.998 * 10^{10} * 2 * \pi$$

$$J_1 = \left(16130 - \left((L - 1 - 0.5)^2 * \frac{\frac{\alpha^2 * \hbar^2}{2*\mu}}{1.6 * 10^{-19}} * 8065\right)\right) * 2.998 * 10^{10} * 2 * \pi$$

$$J_2 = \left(16130 - \left((L - 2 - 0.5)^2 * \frac{\frac{\alpha^2 * \hbar^2}{2*\mu}}{1.6 * 10^{-19}} * 8065\right)\right) * 2.998 * 10^{10} * 2 * \pi$$

$$J_3 = \left(16130 - \left((L - 3 - 0.5)^2 * \frac{\frac{\alpha^2 * \hbar^2}{2*\mu}}{1.6 * 10^{-19}} * 8065\right)\right) * 2.998 * 10^{10} * 2 * \pi$$

$$J_4 = \left(16130 - \left((L - 4 - 0.5)^2 * \frac{\frac{\alpha^2 * \hbar^2}{2*\mu}}{1.6 * 10^{-19}} * 8065\right)\right) * 2.998 * 10^{10} * 2 * \pi$$

$$J_5 = \left(16130 - \left((L - 5 - 0.5)^2 * \frac{\frac{\alpha^2 * \hbar^2}{2*\mu}}{1.6 * 10^{-19}} * 8065\right)\right) * 2.998 * 10^{10} * 2 * \pi$$

$$J_6 = \left(16130 - \left((L - 5 - 0.5)^2 * \frac{\frac{\alpha^2 * \hbar^2}{2*\mu}}{1.6 * 10^{-19}} * 8065\right)\right) * 2.998 * 10^{10} * 2 * \pi$$

$$J_7 = \left(16130 - \left((L - 5 - 0.5)^2 * \frac{\frac{\alpha^2 * \hbar^2}{2*\mu}}{1.6 * 10^{-19}} * 8065\right)\right) * 2.998 * 10^{10} * 2 * \pi$$

Beat energies

$$\psi[\text{n\_},\ \text{r\_}] := \text{n}\,!*\left(\frac{\alpha*((2*\text{L})-(2*\text{n})-1)}{\text{Gamma}[\text{n}+1]*\text{Gamma}[(2*\text{L})-\text{n}]}\right)^{\frac{1}{2}}*$$
$$\left(2*\text{L}*e^{-\left(\alpha*\text{r}-\alpha*2.28*10^{-10}\right)}\right)^{(\text{L}-\text{n}-0.5)}*e^{-0.5*2*\text{L}*e^{-\left(\alpha*\text{r}-\alpha*2.28*10^{-10}\right)}}*$$
$$\text{LaguerreL}\left[\text{n},\ ((2*\text{L})-(2*\text{n})-1),\ 2*\text{L}*e^{-\left(\alpha*\text{r}-\alpha*2.28*10^{-10}\right)}\right]$$

$$\phi[\text{n\_},\ \text{r\_}] := \text{n}\,!*\left(\frac{\beta*((2*\text{l})-(2*\text{n})-1)}{\text{Gamma}[\text{n}+1]*\text{Gamma}[(2*\text{l})-\text{n}]}\right)^{\frac{1}{2}}*$$
$$\left(2*\text{l}*e^{-\left(\beta*\text{r}-\beta*2.18*10^{-10}\right)}\right)^{(\text{l}-\text{n}-0.5)}*e^{-0.5*2*\text{l}*e^{-\left(\beta*\text{r}-\beta*2.18*10^{-10}\right)}}*$$
$$\text{LaguerreL}\left[\text{n},\ ((2*\text{l})-(2*\text{n})-1),\ 2*\text{l}*e^{-\left(\beta*\text{r}-\beta*2.18*10^{-10}\right)}\right]$$

$$\Xi[\text{n\_},\ \text{M\_}] := \text{h}*\text{x}*\text{w}_\text{n}*\text{c}_\text{n}*\text{n}\,!*\left(\frac{\alpha*((2*\text{L})-(2*\text{n})-1)}{\text{Gamma}[\text{n}+1]*\text{Gamma}[(2*\text{L})-\text{n}]}\right)^{\frac{1}{2}}*$$
$$\left(2*\text{L}*e^{-\left(\alpha*\left((-3.6195*\text{M})+\left(0.02582*\text{M}^2\right)+128.81403\right)*10^{-10}-\alpha*2.28*10^{-10}\right)}\right)^{(\text{L}-\text{n}-0.5)}*$$
$$e^{-0.5*2*\text{L}*e^{-\left(\alpha*\left((-3.6195*\text{M})+\left(0.02582*\text{M}^2\right)+128.81403\right)*10^{-10}-\alpha*2.28*10^{-10}\right)}}*$$
$$\text{LaguerreL}\Big[\text{n},\ ((2*\text{L})-(2*\text{n})-1),$$
$$2*\text{L}*e^{-\left(\alpha*\left((-3.6195*\text{M})+\left(0.02582*\text{M}^2\right)+128.81403\right)*10^{-10}-\alpha*2.28*10^{-10}\right)}\Big]$$

$$\Theta[\text{n\_},\ \text{M\_}] := \text{h}*\text{c}_\text{n}*\text{n}\,!*\left(\frac{\alpha*((2*\text{L})-(2*\text{n})-1)}{\text{Gamma}[\text{n}+1]*\text{Gamma}[(2*\text{L})-\text{n}]}\right)^{\frac{1}{2}}*$$
$$\left(2*\text{L}*e^{-\left(\alpha*\left((-3.6195*\text{M})+\left(0.02582*\text{M}^2\right)+128.81403\right)*10^{-10}-\alpha*2.28*10^{-10}\right)}\right)^{(\text{L}-\text{n}-0.5)}*$$
$$e^{-0.5*2*\text{L}*e^{-\left(\alpha*\left((-3.6195*\text{M})+\left(0.02582*\text{M}^2\right)+128.81403\right)*10^{-10}-\alpha*2.28*10^{-10}\right)}}*$$
$$\text{LaguerreL}\Big[\text{n},\ ((2*\text{L})-(2*\text{n})-1),$$
$$2*\text{L}*e^{-\left(\alpha*\left((-3.6195*\text{M})+\left(0.02582*\text{M}^2\right)+128.81403\right)*10^{-10}-\alpha*2.28*10^{-10}\right)}\Big]$$

$$\chi[\text{n\_},\ \text{M\_},\ \text{t\_}] := (\Theta[\text{n},\ \text{M}]-\Xi[\text{n},\ \text{M}])*e^{-\left(i*\text{J}_\text{n}*\text{t}*10^{-15}\right)}$$

Wave functions

E.3. Wave Packet Propagation

Propagation of the Ground State Vibrational Wave Packet from R_v-ADK Calculations:

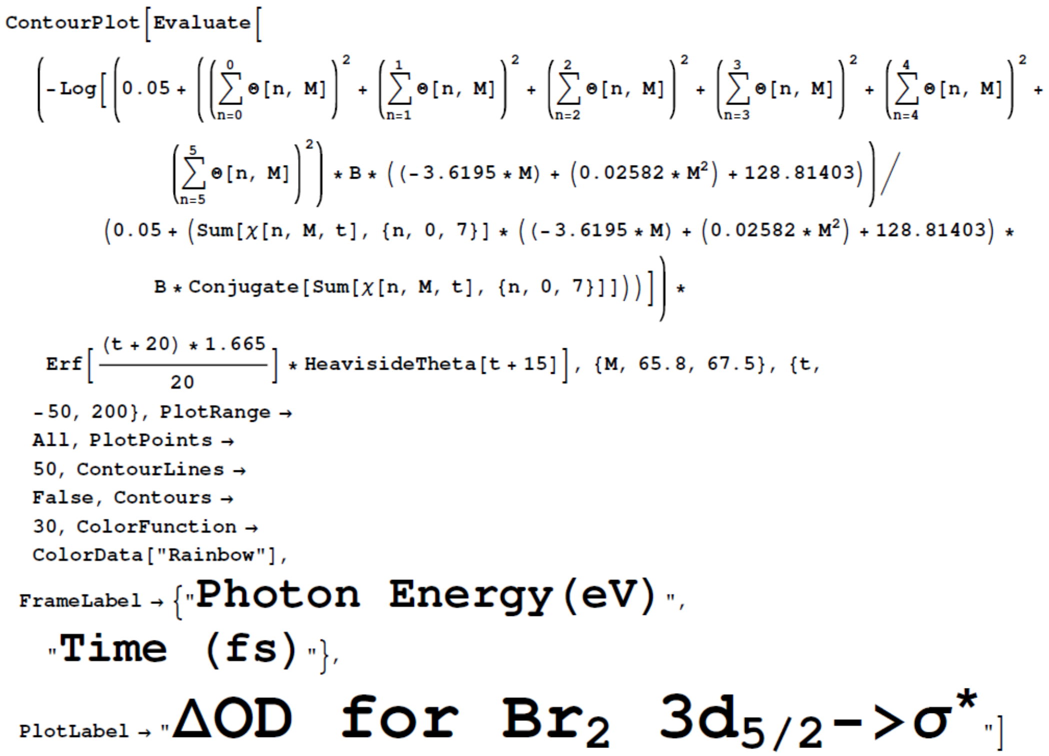

```
ContourPlot[Evaluate[
  (-Log[(0.05 + (((∑_{n=0}^{0} Θ[n, M])^2 + (∑_{n=1}^{1} Θ[n, M])^2 + (∑_{n=2}^{2} Θ[n, M])^2 + (∑_{n=3}^{3} Θ[n, M])^2 + (∑_{n=4}^{4} Θ[n, M])^2 +
          (∑_{n=5}^{5} Θ[n, M])^2) * B * ((-3.6195 * M) + (0.02582 * M^2) + 128.81403)) /
       (0.05 + (Sum[χ[n, M, t], {n, 0, 7}] * ((-3.6195 * M) + (0.02582 * M^2) + 128.81403) *
            B * Conjugate[Sum[χ[n, M, t], {n, 0, 7}]])))] *
   Erf[((t + 20) * 1.665)/20] * HeavisideTheta[t + 15]], {M, 65.8, 67.5}, {t,
  -50, 200}, PlotRange ->
  All, PlotPoints ->
  50, ContourLines ->
  False, Contours ->
  30, ColorFunction ->
  ColorData["Rainbow"],
 FrameLabel -> {"Photon Energy(eV)",
   "Time (fs)"},
 PlotLabel -> "ΔOD for Br₂ 3d₅/₂->σ*"]
```

Bibliography

1 T. H. Maiman, Nature **187**, 493 (1960).
2 J. P. Gordon, H. J. Zeiger, and C. H. Townes, Physical Review **95**, 282 (1954).
3 J. P. Gordon, H. J. Zeiger, and C. H. Townes, Physical Review **99**, 1264 (1955).
4 D. R. Herschbach, Discussions of the Faraday Society **33**, 149 (1962).
5 D. R. Herschbach, in *Advances in Chemical Physics* (John Wiley & Sons, Inc., 1966), p. 319.
6 Y. T. Lee, J. D. McDonald, P. R. LeBreton, and D. R. Herschbach, Review of Scientific Instruments **40**, 1402 (1969).
7 G. Karl and J. C. Polanyi, The Journal of Chemical Physics **38**, 271 (1963).
8 K. G. Anlauf, P. J. Kuntz, D. H. Maylotte, P. D. Pacey, and J. C. Polanyi, Discussions of the Faraday Society **44**, 183 (1967).
9 G. Karl, P. Kruus, and J. C. Polanyi, The Journal of Chemical Physics **46**, 224 (1967).
10 G. Karl, P. Kruus, J. C. Polanyi, and I. W. M. Smith, The Journal of Chemical Physics **46**, 244 (1967).
11 R. D. Levine, *Molecular reaction dynamics* (Cambridge University Press, Cambridge, UK; New York, 2005).
12 R. L. Fork, C. H. B. Cruz, P. C. Becker, and C. V. Shank, Optics Letters **12**, 483 (1987).
13 R. L. Fork, B. I. Greene, and C. V. Shank, Applied Physics Letters **38**, 671 (1981).
14 C. V. Shank and E. P. Ippen, Applied Physics Letters **24**, 373 (1974).
15 M. Dantus, R. M. Bowman, and A. H. Zewail, Nature **343**, 737 (1990).
16 A. H. Zewail, F. C. d. Schryver, S. D. Feyter, and G. Schweitzer, *Femtochemistry : with the Nobel lecture of A. Zewail* (Wiley, Weinheim; New York, 2001).
17 A. H. Zewail, The Journal of Physical Chemistry A **104**, 5660 (2000).
18 W. T. Pollard, S.-Y. Lee, and R. A. Mathies, The Journal of Chemical Physics **92**, 4012 (1990).
19 Z. H. Loh, M. Khalil, R. E. Correa, and S. R. Leone, Review of Scientific Instruments **79**, 073101 (2008).
20 Z. H. Loh, M. Khalil, R. E. Correa, R. Santra, C. Buth, and S. R. Leone, Physical Review Letters **98**, 143601 (2007).
21 Z.-H. Loh, C. H. Greene, and S. R. Leone, Chemical Physics **350**, 7 (2008).
22 Z.-H. Loh and S. R. Leone, The Journal of Chemical Physics **128**, 204302 (2008).
23 Z.-H. Loh and S. R. Leone, The Journal of Physical Chemistry Letters **4**, 292 (2012).
24 E. Goulielmakis, et al., Nature **466**, 739 (2010).
25 N. H. Burnett, H. A. Baldis, M. C. Richardson, and G. D. Enright, Applied Physics Letters **31**, 172 (1977).
26 A. McPherson, G. Gibson, H. Jara, U. Johann, T. S. Luk, I. A. McIntyre, K. Boyer, and C. K. Rhodes, Journal of the Optical Society of America, B **4**, 595 (1987).
27 R. W. Schoenlein, S. Chattopadhyay, H. H. W. Chong, T. E. Glover, P. A. Heimann, C. V. Shank, A. A. Zholents, and M. S. Zolotorev, Science **287**, 2237 (2000).

[28] C. Steier, D. Robin, F. Sannibale, R. Schoenlein, W. Wan, W. Wittmer, and A. Zholents, in *Particle Accelerator Conference, 2005. PAC 2005. Proceedings of the*, 2005), p. 4096.

[29] T. Brabec and F. Krausz, Reviews of Modern Physics **72**, 545 (2000).

[30] T. Popmintchev, M.-C. Chen, P. Arpin, M. M. Murnane, and H. C. Kapteyn, Nature Photonics **4**, 822 (2010).

[31] T. Popmintchev, M.-C. Chen, A. Bahabad, M. Gerrity, P. Sidorenko, O. Cohen, I. P. Christov, M. M. Murnane, and H. C. Kapteyn, Proceedings of the National Academy of Sciences **106**, 10516 (2009).

[32] R. Bartels, S. Backus, E. Zeek, L. Misoguti, G. Vdovin, I. P. Christov, M. M. Murnane, and H. C. Kapteyn, Nature **406**, 164 (2000).

[33] Y. Oishi, M. Kaku, A. Suda, F. Kannari, and K. Midorikawa, Optics Express **14**, 7230 (2006).

[34] A. Rundquist, C. G. Durfee, Z. Chang, C. Herne, S. Backus, M. M. Murnane, and H. C. Kapteyn, Science **280**, 1412 (1998).

[35] D. S. Steingrube, T. Vockerodt, E. Schulz, U. Morgner, and M. Kovacev, Physical Review A **80**, 043819 (2009).

[36] J. Sutherland, E. Christensen, N. Powers, S. Rhynard, J. Painter, and J. Peatross, Optics Express **12**, 4430 (2004).

[37] W. Li, X. Zhou, R. Lock, S. Patchkovskii, A. Stolow, H. C. Kapteyn, and M. M. Murnane, Science **322**, 1207 (2008).

[38] B. K. McFarland, J. P. Farrell, P. H. Bucksbaum, and M. Gühr, Science **322**, 1232 (2008).

[39] N. L. Wagner, A. Wüest, I. P. Christov, T. Popmintchev, X. Zhou, M. M. Murnane, and H. C. Kapteyn, Proceedings of the National Academy of Sciences **103**, 13279 (2006).

[40] V. Ramamurthy and Y. Inoue, *Supramolecular photochemistry controlling photochemical processes* (Wiley, Hoboken, NJ, 2011).

[41] N. J. Turro, *Modern molecular photochemistry* (Benjamin/Cummings Pub. Co., Menlo Park, Calif., 1978).

[42] C. Cohen-Tannoudji, B. Diu, and F. Laloë, *Quantum mechanics* (Wiley, New York, 1977).

[43] M. Born and R. Oppenheimer, Annalen der Physik **389**, 457 (1927).

[44] P. A. M. Dirac, Proceedings of the Royal Society of London. Series A **114**, 243 (1927).

[45] J. Orear, E. Fermi, A. H. Rosenfeld, and R. A. Schluter, *Nuclear physics : a course given by Enrico Fermi at the University of Chicago* (University of Chicago Press, [Chicago], 1950).

[46] M. Protopapas, C. H. Keitel, and P. L. Knight, Reports on Progress in Physics **60**, 389 (1997).

[47] P. Agostini, F. Fabre, G. Mainfray, G. Petite, and N. K. Rahman, Physical Review Letters **42**, 1127 (1979).

[48] T. Brabec, *Strong-Field Laser Physics* (Springer, New York, 2008).

[49] L. Keldysh, Soviet Physics JETP **20**, 1307 (1965).

[50] M. V. Ammosov, N. D. Delone, and V. P. Krainov, Soviet Physics JTEP **64**, 1191 (1986).

[51] S. Augst, D. D. Meyerhofer, D. Strickland, and S. L. Chint, Journal of the Optical Society of America, B **8**, 858 (1991).

[52] P. B. Corkum, Physical Review Letters **71**, 1994 (1993).

53 M. Bashkansky, P. H. Bucksbaum, and D. W. Schumacher, Physical Review Letters **60**, 2458 (1988).

54 F. Mauger, C. Chandre, and T. Uzer, Physical Review Letters **104**, 043005 (2010).

55 H. Niikura, F. Legare, R. Hasbani, A. D. Bandrauk, M. Y. Ivanov, D. M. Villeneuve, and P. B. Corkum, Nature **417**, 917 (2002).

56 G. N. Gibson, M. Li, C. Guo, and J. P. Nibarger, Physical Review A **58**, 4723 (1998).

57 K. Codling and L. J. Frasinski, Journal of Physics B: Atomic, Molecular and Optical Physics **26**, 783 (1993).

58 J. H. Posthumus, A. J. Giles, M. R. Thompson, and K. Codling, Journal of Physics B: Atomic, Molecular and Optical Physics **29**, 5811 (1996).

59 J. H. Posthumus, J. Plumridge, P. F. Taday, J. H. Sanderson, A. J. Langley, K. Codling, and W. A. Bryan, Journal of Physics B: Atomic, Molecular and Optical Physics **32**, L93 (1999).

60 F. Rosca-Pruna, E. Springate, H. L. Offerhaus, M. Krishnamurthy, N. Farid, C. Nicole, and M. J. J. Vrakking, Journal of Physics B: Atomic, Molecular and Optical Physics **34**, 4919 (2001).

61 X. Urbain, et al., Physical Review Letters **92** (2004).

62 A. Saenz, Physica Scripta **2004**, 126 (2004).

63 P. H. Bucksbaum, A. Zavriyev, H. G. Muller, and D. W. Schumacher, Physical Review Letters **64**, 1883 (1990).

64 A. Saenz, Physical Review A **66**, 063407 (2002).

65 G. Yao and S.-I. Chu, Physical Review A **48**, 485 (1993).

66 H. Chen, V. Tagliamonti, and G. N. Gibson, Physical Review A **86**, 051403 (2012).

67 E. Constant, H. Stapelfeldt, and P. B. Corkum, Physical Review Letters **76**, 4140 (1996).

68 L. Fang and G. N. Gibson, Physical Review A **75** (2007).

69 A. Manohar and S. Alejandro, Journal of Physics B: Atomic, Molecular and Optical Physics **39**, S389 (2006).

70 E. Goll, G. Wunner, and A. Saenz, Physical Review Letters **97**, 103003 (2006).

71 A. Saenz, Journal of Physics B: Atomic, Molecular and Optical Physics **33**, 4365 (2000).

72 T. Tajima and G. Mourou, Physical Review Special Topics - Accelerators and Beams **5**, 031301 (2002).

73 R. J. Levis, G. M. Menkir, and H. Rabitz, Science **292**, 709 (2001).

74 K. J. Schafer, M. B. Gaarde, A. Heinrich, J. Biegert, and U. Keller, Physical Review Letters **92**, 023003 (2004).

75 M. Lezius, S. Dobosz, D. Normand, and M. Schmidt, Physical Review Letters **80**, 261 (1998).

76 H. Liu, Z. Yang, Z. Gao, and Z. Tang, The Journal of Chemical Physics **126**, 044316 (2007).

77 D. Bauer and P. Mulser, Physical Review A **59**, 569 (1999).

78 M. Uiberacker, et al., Nature **446**, 627 (2007).

79 P. Eckle, A. N. Pfeiffer, C. Cirelli, A. Staudte, R. Dörner, H. G. Muller, M. Büttiker, and U. Keller, Science **322**, 1525 (2008).

80 J. S. Prauzner-Bechcicki, K. Sacha, B. Eckhardt, and J. Zakrzewski, Physical Review A **78**, 013419 (2008).

81 T. Pfeiffer, Wurzburg, 2004.

82 A. Saenz, Physical Review A **66**, 063408 (2002).

[83] G. N. Gibson, R. N. Coffee, and L. Fang, Physical Review A **73** (2006).
[84] J. P. Nibarger, S. V. Menon, and G. N. Gibson, Physical Review A **63**, art. no. (2001).
[85] R. Torres, R. de Nalda, and J. P. Marangos, Physical Review A **72**, 023420 (2005).
[86] B. Friedrich and D. Herschbach, Physical Review Letters **74**, 4623 (1995).
[87] C. Ellert and P. B. Corkum, Physical Review A **59**, R3170 (1999).
[88] O. Smirnova, S. Patchkovskii, Y. Mairesse, N. Dudovich, and M. Y. Ivanov, Proceedings of the National Academy of Sciences **106**, 16556 (2009).
[89] M. Magrakvelidze, F. He, S. De, I. Bocharova, D. Ray, U. Thumm, and I. V. Litvinyuk, Physical Review A **79**, 033408 (2009).
[90] A. S. Alnaser, et al., Physical Review Letters **93**, 113003 (2004).
[91] A. S. Alnaser, et al., Physical Review A **71**, 031403 (2005).
[92] M. Busuladžić, A. Gazibegović-Busuladžić, D. B. Milošević, and W. Becker, Physical Review Letters **100**, 203003 (2008).
[93] J. Itatani, J. Levesque, D. Zeidler, H. Niikura, H. Pepin, J. C. Kieffer, P. B. Corkum, and D. M. Villeneuve, Nature **432**, 867 (2004).
[94] A. L. Huillier, K. J. Schafer, and K. C. Kulander, Journal of Physics B: Atomic, Molecular and Optical Physics **24**, 3315 (1991).
[95] T. Morishita, A.-T. Le, Z. Chen, and C. D. Lin, New Journal of Physics **10**, 025011 (2008).
[96] D. D. Hickstein, et al., Physical Review Letters **109**, 073004 (2012).
[97] D. Shafir, H. Soifer, B. D. Bruner, M. Dagan, Y. Mairesse, S. Patchkovskii, M. Y. Ivanov, O. Smirnova, and N. Dudovich, Nature **485**, 343 (2012).
[98] M. Lewenstein, P. Balcou, M. Y. Ivanov, A. L'Huillier, and P. B. Corkum, Physical Review A **49**, 2117 (1994).
[99] A. Zaïr, et al., Physical Review Letters **100**, 143902 (2008).
[100] E. Benedetti, J.-P. Caumes, G. Sansone, S. Stagira, C. Vozzi, and M. Nisoli, Opt. Express **14**, 2242 (2006).
[101] A. Willner, et al., New Journal of Physics **13**, 113001 (2011).
[102] R. Paschotta, *Encyclopedia of laser physics and technology* (Wiley-VCH ; [John Wiley, distributor], Weinheim; Chichester, 2008).
[103] P. A. Franken, A. E. Hill, C. W. Peters, and G. Weinreich, Physical Review Letters **7**, 118 (1961).
[104] A. J. Paul, Doctor of Philosohpy, University of Colorado, Boulder, 2007.
[105] E. Snitzer, J. Opt. Soc. Am. **51**, 491 (1961).
[106] E. A. J. Marcatili and R. A. Schmeltzer, Bell System Technical Journal **43**, 1783 (1964).
[107] C. G. Durfee Iii, S. Backus, M. M. Murnane, and H. C. Kapteyn, Optics Letters **22**, 1565 (1997).
[108] C. G. Durfee Iii, A. Rundquist, S. Backus, Z. Chang, C. Herne, H. C. Kapteyn, and M. M. Murnane, Journal of Nonlinear Optical Physics & Materials **08**, 211 (1999).
[109] R. L. Abrams, Quantum Electronics, IEEE Journal of **8**, 838 (1972).
[110] E. Samsøe, P. Malm, P. E. Andersen, P. M. Petersen, and S. Andersson-Engels, Optics Communications **219**, 369 (2003).
[111] E. Gagnon, et al., Review of Scientific Instruments **79**, 063102 (2008).
[112] E. Takahashi, Y. Nabekawa, T. Otsuka, M. Obara, and K. Midorikawa, Physical Review A **66**, 021802 (2002).

[113] Y. Tamaki, J. Itatani, M. Obara, and K. Midorikawa, Physical Review A **62**, 063802 (2000).

[114] K. Midorikawa, Y. Nabekawa, and A. Suda, Progress in Quantum Electronics **32**, 43 (2008).

[115] N. Brimhall, J. C. Painter, N. Powers, G. Giraud, M. Turner, M. Ware, and J. Peatross, Optics Express **15**, 1684 (2007).

[116] J. C. Painter, M. Adams, N. Brimhall, E. Christensen, G. Giraud, N. Powers, M. Turner, M. Ware, and J. Peatross, Optics Letters **31**, 3471 (2006).

[117] E. Schulz, D. S. Steingrube, T. Binhammer, M. B. Gaarde, A. Couairon, U. Morgner, and M. Kova?ev, Optics Express **19**, 19495 (2011).

[118] I. J. Kim, C. M. Kim, H. T. Kim, G. H. Lee, Y. S. Lee, J. Y. Park, D. J. Cho, and C. H. Nam, Physical Review Letters **94**, 243901 (2005).

[119] R. Budriunas, Lund University, 2010.

[120] X. He, J. M. Dahlström, R. Rakowski, C. M. Heyl, A. Persson, J. Mauritsson, and A. L'Huillier, Physical Review A **82**, 033410 (2010).

[121] O. Cohen, T. Popmintchev, D. M. Gaudiosi, M. M. Murnane, and H. C. Kapteyn, Physical Review Letters **98**, 043903 (2007).

[122] L. Misoguti, I. P. Christov, S. Backus, M. M. Murnane, and H. C. Kapteyn, Physical Review A **72**, 063803 (2005).

[123] H. Eichmann, A. Egbert, S. Nolte, C. Momma, B. Wellegehausen, W. Becker, S. Long, and J. K. McIver, Physical Review A **51**, R3414 (1995).

[124] R. A. Ganeev, C. Hutchison, A. Zaïr, T. Witting, F. Frank, W. A. Okell, J. W. G. Tisch, and J. P. Marangos, Optics Express **20**, 90 (2012).

[125] M. J. Abel, T. Pfeifer, P. M. Nagel, W. Boutu, M. J. Bell, C. P. Steiner, D. M. Neumark, and S. R. Leone, Chemical Physics **366**, 9 (2009).

[126] T. Pfeifer, L. Gallmann, M. J. Abel, P. M. Nagel, D. M. Neumark, and S. R. Leone, Physical Review Letters **97**, 163901 (2006).

[127] H. Mashiko, S. Gilbertson, C. Li, S. D. Khan, M. M. Shakya, E. Moon, and Z. Chang, Physical Review Letters **100**, 103906 (2008).

[128] T. Popmintchev, et al., Science **336**, 1287 (2012).

[129] M. C. Chen, P. Arpin, T. Popmintchev, M. Gerrity, B. Zhang, M. Seaberg, D. Popmintchev, M. M. Murnane, and H. C. Kapteyn, Physical Review Letters **105**, 173901 (2010).

[130] J. J. Sakurai and S. F. Tuan, *Modern quantum mechanics* (Benjamin/Cummings, Menlo Park, Calif., 1985).

[131] L. Dhar, J. A. Rogers, and K. A. Nelson, Chemical Reviews **94**, 157 (1994).

[132] A. M. Weiner, D. E. Leaird, G. P. Wiederrecht, and K. A. Nelson, Science **247**, 1317 (1990).

[133] F. Légaré, S. Chelkowski, and A. D. Bandrauk, Chemical Physics Letters **329**, 469 (2000).

[134] A. Rudenko, T. Ergler, B. Feuerstein, K. Zrost, C. D. Schroter, R. Moshammer, and J. Ullrich, Chemical Physics **329**, 193 (2006).

[135] L. Fang and G. N. Gibson, Physical Review A **78**, 051402 (2008).

[136] L. Fang and G. N. Gibson, Physical Review Letters **100**, 103003 (2008).

[137] K. Yamanouchi, M. Nisoli, and W. T. Hill, *Progress in ultrafast intense laser science VIII* (Springer, Berlin; New York, 2012).

[138] H. Stapelfeldt, E. Constant, and P. B. Corkum, Physical Review Letters **74**, 3780 (1995).
[139] T. Ergler, B. Feuerstein, A. Rudenko, K. Zrost, C. D. Schroter, R. Moshammer, and J. Ullrich, Physical Review Letters **97** (2006).
[140] H. Chen, V. Tagliamonti, and G. N. Gibson, Physical Review Letters **109**, 193002 (2012).
[141] J. I. Steinfeld, J. S. Francisco, and W. L. Hase, *Chemical kinetics and dynamics* (Prentice Hall, Englewood Cliffs, N.J., 1989).
[142] W. T. Pollard, S. L. Dexheimer, Q. Wang, L. A. Peteanu, C. V. Shank, and R. A. Mathies, The Journal of Physical Chemistry **96**, 6147 (1992).
[143] W. T. Pollard and R. A. Mathies, Annual Review of Physical Chemistry **43**, 497 (1992).
[144] A. S. Sandhu, et al., Science **322**, 1081 (2008).
[145] G. Doumy, et al., Physical Review Letters **106**, 083002 (2011).
[146] L. Young, et al., Nature **466**, 56 (2010).
[147] M. Hoener, et al., Physical Review Letters **104**, 253002 (2010).
[148] N. Rohringer and R. Santra, Physical Review A **76**, 033416 (2007).
[149] R. Berlasso, et al., Physical Review B **73**, 115101 (2006).
[150] E. Seres, J. Seres, and C. Spielmann, Applied Physics Letters **89**, 181919 (2006).
[151] U. Becker and D. A. Shirley, *VUV and soft X-ray photoionization* (Plenum Press, New York, 1996).
[152] L. Nahon, L. Duffy, P. Morin, F. Combet-Farnoux, J. Tremblay, and M. Larzilliere, Physical Review A **41**, 4879 (1990).
[153] D. L. Ederer and M. Manalis, Journal of the Optical Society of America **65**, 634 (1975).
[154] C. Buth, R. Santra, and L. Young, Physical Review Letters **98**, 253001 (2007).
[155] N. Rohringer and R. Santra, Physical Review A **79**, 053402 (2009).
[156] R. Santra, R. W. Dunford, and L. Young, Physical Review A **74**, 043403 (2006).
[157] R. Santra and A. Gordon, Physical Review Letters **96**, 073906 (2006).
[158] L. Young, et al., Physical Review Letters **97**, 083601 (2006).
[159] R. Santra, V. S. Yakovlev, T. Pfeifer, and Z.-H. Loh, Physical Review A **83**, 033405 (2011).
[160] R. N. Zare, *Angular momentum : understanding spatial aspects in chemistry and physics* (Wiley, New York, 1988).
[161] M. Valiev, et al., Computer Physics Communications **181**, 1477 (2010).
[162] K. Lopata, B. E. Van Kuiken, M. Khalil, and N. Govind, Journal of Chemical Theory and Computation **8**, 3284 (2012).
[163] T. Zuo and A. D. Bandrauk, Physical Review A **52**, R2511 (1995).
[164] T. Seideman, M. Y. Ivanov, and P. B. Corkum, Physical Review Letters **75**, 2819 (1995).
[165] D. M. Volkov, Z. Physik **94**, 250 (1935).
[166] J. P. Brichta, W. K. Liu, A. A. Zaidi, A. Trottier, and J. H. Sanderson, Journal of Physics B: Atomic, Molecular and Optical Physics **39**, 3769 (2006).
[167] P. M. Morse, Physical Review **34**, 57 (1929).
[168] D. A. McQuarrie and J. D. Simon, *Physical chemistry : a molecular approach* (University Science Books, Sausalito, Calif., 1997).
[169] T. Harris, J. H. D. Eland, and R. P. Tuckett, Journal of Molecular Spectroscopy **98**, 269 (1983).
[170] K.-P. Huber and G. Herzberg, *Constants and diatomic molecules* (Van Nostrand Reinhold, New York; London [etc.], 1979).

[171] J. A. Horsley and R. F. Barrow, Transactions of the Faraday Society **63**, 32 (1967).

[172] F. H. M. Faisal, Journal of Physics B: Atomic and Molecular Physics **6**, L89 (1973).

[173] H. R. Reiss, Physical Review A **22**, 1786 (1980).

[174] A. M. Perelomov, V. S. Popov, and M. V. Terent'ev, Soviet Physics JTEP **23**, 924 (1966).

[175] X. M. Tong, Z. X. Zhao, and C. D. Lin, Physical Review A **66**, 033402 (2002).

[176] S.-F. Zhao, C. Jin, A.-T. Le, T. F. Jiang, and C. D. Lin, Physical Review A **81**, 033423 (2010).

[177] C. Guo, Physical Review Letters **85**, 2276 (2000).

[178] H. R. Reiss, Physical Review A **82**, 023418 (2010).

[179] E. Runge and E. K. U. Gross, Physical Review Letters **52**, 997 (1984).

[180] P. Hohenberg and W. Kohn, Physical Review **136**, B864 (1964).

[181] A. D. Becke, The Journal of Chemical Physics **98**, 5648 (1993).

[182] C. Lee, W. Yang, and R. G. Parr, Physical Review B **37**, 785 (1988).

[183] D. Merritt (private communication).

[184] A. E. Siegman, *Lasers* (University Science Books, Mill Valley, Calif., 1986).

[185] E. M. Gullikson, P. Denham, S. Mrowka, and J. H. Underwood, Physical Review B **49**, 16283 (1994).

[186] B. L. Henke, E. M. Gullikson, and J. C. Davis, Atomic Data and Nuclear Data Tables **54**, 181 (1993).

[187] T. Campbell, R. K. Kalia, A. Nakano, P. Vashishta, S. Ogata, and S. Rodgers, Physical Review Letters **82**, 4866 (1999).

[188] M.-F. Lin, A. N. Pfeiffer, D. M. Neumark, S. R. Leone, and O. Gessner, The Journal of Chemical Physics **137**, 244305 (2012).

[189] M. Sano, et al., Journal of Physics B: Atomic, Molecular and Optical Physics **29**, 5305 (1996).

[190] P. Andersen, T. Andersen, F. Folkmann, V. K. Ivanov, H. Kjeldsen, and J. B. West, Journal of Physics B: Atomic, Molecular and Optical Physics **34**, 2009 (2001).

[191] C.-J. Lai and F. X. Kärtner, Optics Express **19**, 22377 (2011).

[192] J. Seely and B. Kjornrattanawanich, Applied Optics **42**, 6374 (2003).

[193] C. F. d. M. Faria, T. Shaaran, and M. T. Nygren, Physical Review A **86**, 053405 (2012).

[194] H. Akagi, T. Otobe, A. Staudte, A. Shiner, F. Turner, R. Dörner, D. M. Villeneuve, and P. B. Corkum, Science **325**, 1364 (2009).

[195] S. Augst, D. Strickland, D. D. Meyerhofer, S. L. Chin, and J. H. Eberly, Physical Review Letters **63**, 2212 (1989).

[196] O. Takahashi, K. Matsuyama, K. Tabayashi, and K. Yamasaki, Journal of Physics B: Atomic, Molecular and Optical Physics **42**, 245102 (2009).

[197] D. P. Stevenson, Journal of the American Chemical Society **82**, 5961 (1960).

[198] C. E. Carroll and F. T. Hioe, Physical Review Letters **68**, 3523 (1992).

[199] A. Aguillar (private communication).

[200] M. Holler, F. Schapper, L. Gallmann, and U. Keller, Physical Review Letters **106**, 123601 (2011).

[201] H. Wang, M. Chini, S. Chen, C.-H. Zhang, F. He, Y. Cheng, Y. Wu, U. Thumm, and Z. Chang, Physical Review Letters **105**, 143002 (2010).

[202] A. W. Jasper, S. Nangia, C. Zhu, and D. G. Truhlar, Accounts of Chemical Research **39**, 101 (2005).

[203] G. Sansone, et al., Nature **465**, 763 (2010).

[204] B. J. Sussman, D. Townsend, M. Y. Ivanov, and A. Stolow, Science **314**, 278 (2006).

[205] P. Kukura, D. W. McCamant, S. Yoon, D. B. Wandschneider, and R. A. Mathies, Science **310**, 1006 (2005).

[206] H. Schwoerer, R. Pausch, M. Heid, and W. Kiefer, Chemical Physics Letters **285**, 240 (1998).

[207] Z. W. Shen, T. Chen, M. Heid, W. Kiefer, and V. Engel, The European Physical Journal D - Atomic, Molecular, Optical and Plasma Physics **14**, 167 (2001).

[208] Z. Shen, V. Engel, R. Xu, J. Cheng, and Y. Yan, The Journal of Chemical Physics **117**, 6142 (2002).

[209] H. Stammreich, Physical Review **78**, 79 (1950).

[210] D. Pavičić, A. Kiess, T. Hänsch, and H. Figger, Physical Review Letters **94** (2005).

[211] E. R. Hosler and S. R. Leone, *Characterization of Vibrational Wave Packets by Core-Level High Harmonic Transient Absorption Spectroscopy*

[212] J. Johnson, J. N. Cutler, G. M. Bancroft, Y. F. Hu, and K. H. Tan, Journal of Physics B: Atomic, Molecular and Optical Physics **30**, 4899 (1997).

[213] W. H. Press, *Numerical recipes in C. [Hauptbd.]* (Cambridge Univ. Press, Cambridge [u.a.], 1996).

[214] A. Cummings and G. O'Sullivan, Physical Review A **54**, 323 (1996).

[215] U. Fano and J. W. Cooper, Reviews of Modern Physics **40**, 441 (1968).

[216] O. P. J. Vieuxmaire, M. G. D. Nix, J. A. J. Fitzpatrick, M. Beckert, R. N. Dixon, and M. N. R. Ashfold, Physical Chemistry Chemical Physics **6**, 543 (2004).

[217] B. Schmidt and U. Lorenz, (2011).

[218] M. F. Gu, Canadian Journal of Physics **86**, 675 (2008).

[219] H. Sakai, C. P. Safvan, J. J. Larsen, K. M. Hilligsoe, K. Hald, and H. Stapelfeldt, The Journal of Chemical Physics **110**, 10235 (1999).

[220] S. Petretti, Y. V. Vanne, A. Saenz, A. Castro, and P. Decleva, Physical Review Letters **104**, 223001 (2010).

[221] J. A. R. Samson, Z. X. He, L. Yin, and G. N. Haddad, Journal of Physics B: Atomic, Molecular and Optical Physics **27**, 887 (1994).

[222] T. N. Olney, G. Cooper, and C. E. Brion, Chemical Physics **232**, 211 (1998).